CIVIL ENGINEERING JOURNAL

číslo 2/2022

Obsah:

CIVIL ENGINEERING JOURNAL

Article no. 18

THE CIVIL ENGINEERING JOURNAL 2-2022

THERMAL PERFORMANCE ASSESSMENT OF WALL ASSEMBLIES: CRITERIA IMPORTANCE THEORY AND AHP APPROACH

Yuriy Biks[1], Olga Ratushnyak[2], Georgiy Ratushnyak[1] and Andriy Lyalyuk[2]

1. *Vinnytsia National Technical University, Faculty of Construction, Heat Power Engineering and Gas Supply, Department of Construction, Architecture and Municipal Economy, Vinnytsia, Voiniv Internatsionalistiv 7, Ukraine; biksyuriy@gmail.com, ratusnakg@gmail.com*
2. *Vinnytsia National Technical University, Faculty of Management and Information Security, Department of Enterprise Economics and Production Management, Vinnytsia, Khmelnyts'ke shosse 95, Ukraine; ogratushnyak@gmail.com, 1b16b.lyalyuk @gmail.com*

ABSTRACT

The problem of the "best" choice in terms of the ecological, durable, cheap and energy-effective material of envelope construction has been considered in the paper. For the numerical assessment of the thermal performance, the Multi-Criteria Decision Analysis (MCDA) techniques as Analytical Hierarchy Process (AHP) and Criteria Importance Theory (CIT) were used. There were proposed eight types of wall assemblies from a natural material, namely: hempcrete, adobe, strawbale panel, earthbag, cordwood, structured insulated panel (SIP) (plywood + ecofiber), hempcrete + straw and compositional building thermo-block. As an objective function for the search of the best alternative the integral index was proposed which consist of thermo-physical and economic criteria. As the thermo-physical criteria component of the index were taken the u-value of the envelope W/m^{2}K, the dimensionless decrement factor of the envelope f and the internal areal heat capacity of the envelope k1, kJ/m^{2}K according to ISO 13786:2017. As economic criteria of the integral index, the authors proposed the cost of the wall material Q, UAH/m^2 and the mass of the wall m, kg/m^2. The analysis of the conducted research has shown, that from the one hand there is no absolute "leader" in the ranking of the wall assemblies according to the proposed criteria and considered type of MCDA technique, but from the other hand by comparison of the results, there were revealed that the top three alternatives in both AHP and CIT technique are walls of "B", "D" and "E" type with different point order, achieved in each MCDA calculation technique.

KEYWORDS

Thermal performance, Multi-criteria assessment, Subjective method, Multi-layered wall assembly.

INTRODUCTION

The modern level of the damage from anthropogenic footprint activity and global climate changes caused by such influence born the essential demand to minimize hypothetical damage in short-term and long-term perspectives.

As one of the key strategies presented nowadays, there is a shortening of the building energy consumption's sector as one of the major energy consumers. According to Xiaodong, Dai and Junjie [1] building energy use consumes over 40% of total primary energy in the U.S. and E.U.

Meanwhile, the problem of the “best” choice for the ecological, durable, cheap and energy-effective material of envelope construction from the one hand and compromise/optimal type from the other hand is a big challenge, even today[2]. That is why such state of the art motivates the researchers to use modern tools of the multi-criteria decision analysis (MCDA) methods in attempts to do make this choice. A huge amount of MCDA techniques for energy efficiency problems in general, and in the field of sustainable energy decision-making (DM) particularly have been proposed in the last two decades [3]-[6].

All MCDA techniques, in general, could be conditionally divided into two groups –subjective weighting methods and objective weighting ones [3].

In the present paper, has been conducted the comparison between two subjective weighting techniques of MCDA applying to the problem of thermal performance assessment of multi-layered wall assemblies by the most used in DM practice – the Analytical Hierarchy Process (AHP) method [7] and the method based on the Criteria Importance Theory (CIT) [8]-[14].

The MCDA process involves different criteria to be compared comprehensively. The variety of influence factors that could be taken into consideration in the DM problem model of thermal assessment are very broad and what is the "correct” one in the decision-making process is still a big issue [2], [17]. The most used factors in the specific research of energy supply, sustainable and energy-efficient problems are technical, economic, environmental, social ones [3]. The economic criterion usually is one of the main ones when DM chooses an appropriate alternative. As F. Stazi has shown [2] “… the internal areal heat capacity *k*1 and decrement factor *f* are the main influencers of the summer behaviour, while the steady-state thermal transmittance *U* and the decrement factor *f* of the winter performance”. On the other hand, the economic criterion is considered as the most important in terms of problem decision making.

Besides, the influence factors should be simply calculable and have interpretable value. For this reason, the integral index for the thermal performance assessment of multi-layered assemblies, which combines several multidimensional key criteria, was proposed.

As the thermo-physical criteria component of the index were taken the u-value of the envelope W/m^{2}K (steady-state criterion), the dimensionless decrement factor of the envelope f and the internal areal heat capacity of the envelope *k*1, kJ/m^{2}K (unsteady-state criteria according to ISO 13786:2017 [19]. As economic criteria of the integral index, the authors proposed the cost of the wall material, UAH/m^2 and the mass of the wall kg/m^2 (as an indirect parameter of the building fundaments cost). All of the above-mentioned criteria could be calculated simply and could be a good marker for thermal performance assessment of specific envelope type.

TASK OF THE RESEARCH

To assess the thermal performance of multi-layered wall assemblies from natural materials in terms of integral index values by two independent methods – AHP and CIT, which applied for the assessment procedure.

MATERIALS AND RESEARCH METHODOLOGY

This study proposed three thermal performance parameters, which are a key influencer of summer and winter behaviour, according to the research of F. Stazi [2]. The parameters are the u-value of the envelope W/m^{2}K, the decrement factor f of the envelope and the internal areal heat capacity of the envelope k1, kJ/m^{2}K. The above-mentioned criteria have been calculated in “Thermal mass calculation tool according to EN ISO 13786” [18], by assuming the values of internal heat transfer resistance as well as external heat transfer resistance according to Ukrainian National Building Standard DSTU B.V. 2.6-189:2013 [20] and Ukrainian Building Code DBN V. 2.6-31: 2016 [21]. The cost of the 1m^2 of the wall assembly’s material Q, UAH/m^2 was calculated by multiplying the width of the wall in meter to the specific material cost UAH/m^3 as an up to dated median one from Ukrainian marketplaces. The mass of the wall m, kg/m^2 have been calculated by multiplying the width of the wall in meter to the material’s density ρ, kg/m^3 respectively.

To assess and compare the results of thermal performance by proposed techniques, the eight types of wall assemblies from eco-friendly materials were taken into consideration in this research after data analyzing [2], [17], [20], [23], [24]. Represented wall types are Wall type “A” (Hempcrete), Wall type “B” (Adobe), Wall type “C” (Strawbale panel), Wall type “D” (Earthbag), Wall type “E” (Cordwood), Wall type “F” (SIP plywood + ecofiber), Wall type “G” (Hempcrete + straw) and Wall type “H” (Compositional building thermo-block [22]) (see Figure 1).

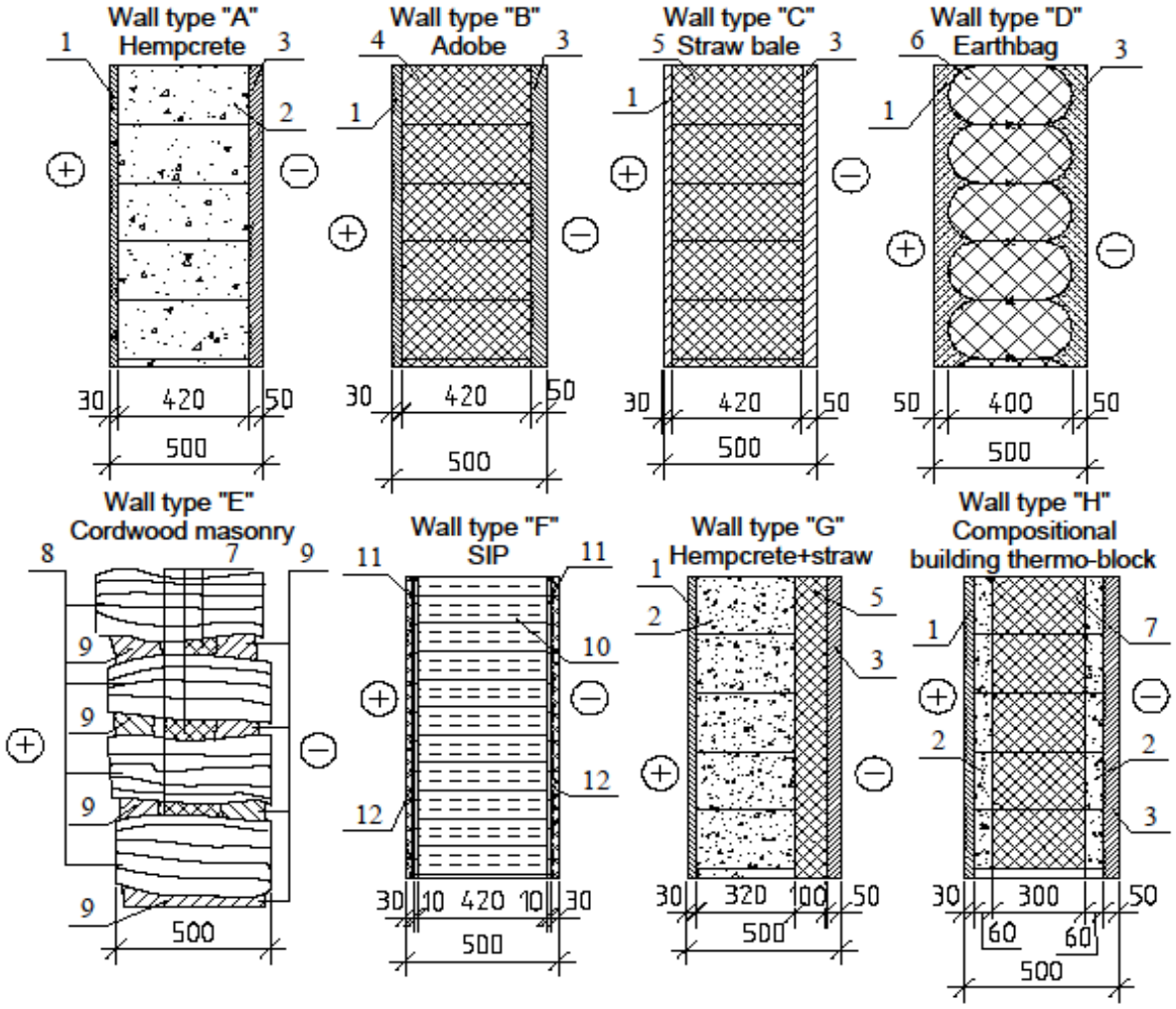

Fig. 1 – Cross-section of investigated wall assemblies
(1 - internal lime-sand plaster, 2 - hempcrete, 3 - external lime-sand plaster, 4 - adobe, 5 - strawbale panel, 6 - earthbag, 7 - chopped straw as an insulator, 8 - cordwood, 9 - lime-sand plaster, 10 - eco fibre, 11 - lime-sand plaster, 12 - plywood)

All of the dimensions in Figure 1 are in mm. Under the accepted dimensions of wall assemblies (Figure 1) and their thermo-physical and economic parameters, general input data for further assessment is calculated in Table 1.

Tab. 1 - The thermo-physical, physical and economic characteristics of the wall assemblies

Assembly type	*Q*	*m*	*u-value*	*f*	*k*1
Wall "A"	1146.00	275.00	0.15	0.0067	45.61
Wall "B"	358.50	716.00	0.77	0.0586	59.46
Wall "C"	1154.40	161.60	0.16	0.2336	41.77
Wall "D"	360.00	880.00	1.51	0.1219	68.53
Wall "E"*	810.00	272.00	0.24	0.0506	64.20
Wall "F"	918.00	131.10	0.14	0.2225	57.00
Wall "G"	1148.00	248.00	0.15	0.0119	45.59
Wall "H"	1152.00	194.00	0.16	0.1394	46.77

* All calculations for this wall design are made by taking the following assumptions into account:

the ratio of the volumes of clay V_{cl} and wood V_w of the outer and inner layer is 1/3 to 2/3,
wood chocks are from the pine (the fibres parallel to the heat flow), clay – sand mortar,
specific heat capacity of the cordwood mixed layer construction is found as

$$c_{cordwood} = (c_w \cdot V_w + c_{cl} \cdot V_{cl}) / (V_w + V_{cl}), \quad (1)$$

where c_w, c_{cl} – the specific heat capacity of the wood and the clay respectively,
V_w, V_{cl} – the volume of the wood and the clay respectively.

Other parameters as well as the density and the average thermal conductivity are found by the same dependencies.

AHP

The methodology of creating a hierarchical model for the thermal performance assessment in terms of the integral index is listed below. By pairwise comparisons [7] the advantages of each influence factors have been weighed on the value of the integral index of thermal performance. The AHP methodology calculation steps of the integral index are as follows.

Step 1. Each of the influence factors is a matrix, which is filled in a next way [7] as in Equation 2:

$$A = \begin{bmatrix} 1 & \frac{r_1}{r_2} & \frac{r_1}{r_3} & \dots & \frac{r_1}{r_n} \\ \frac{r_2}{r_1} & 1 & \frac{r_2}{r_3} & \dots & \frac{r_2}{r_n} \\ \dots & \dots & \dots & \dots & \dots \\ \frac{r_n}{r_1} & \frac{r_n}{r_2} & \frac{r_n}{r_3} & \dots & 1 \end{bmatrix}, \quad (2)$$

where r_1, r_2, r_3, r_n are the corresponding values of the priorities of the evaluated parameters of the matrix, which characterize the values of five included criteria (the internal areal heat capacity *k*1, the decrement factor *f*, the u-value (thermal transmittance), the mass of the wall and costs of the wall materials).

By the known line elements of the matrix in Equation (2), elements of all other lines have been calculated. The arbitrary element $a_{jj} = r_i / r_j$, with known elements $a_{kj} = r_k / r_j$, k, and $i = 1,...,n$. of a certain n-th line, is calculated as $a_{jj} = a_{kj} / a_{ki}$, and $j,k = 1,...,n$.

Step 2. The priority vector of each i-th parameter m_i as the average geometric value of each line of matrix elements divided by the sum of all mean geometric values for the estimated parameters is calculated as it presents in Equation (3) below through [7].

$$\sqrt[n]{1 \times \frac{r_1}{r_2} \times \frac{r_1}{r_3} \times ... \times \frac{r_1}{r_n}} = m_1. \quad (3)$$

Step 3. The vector of priorities of the first, second, n-th line of the matrix x_1, x_2, ... x_n should be obtained in Equation (4) as

$$m_1 / (m_1 + m_2 + ... + m_n) = x_1, \quad (4)$$

The components of the eigenvector and the vector of priorities for other m_n lines are determined in the same way.

Step 4. As the set of relative weights of the alternative, we use the components of our eigenvector λ_{max} corresponding to the maximal characteristic number. Moreover, to evaluate the coherence of the matrix, the condition must be fulfilled. As an indicator of the consistency degree of A matrix' elements, the consistency index (CI) is calculated as [7]:

$$CI = \left(\lambda_{max} - n\right) / n - 1, \quad (5)$$

where n is the rank of the matrix.

Step 5. To evaluate the consistency degree adequacy, the consistency ratio (CR) is used and it is calculated as

$$CR = CI / \text{MRCI}, \quad (6)$$

where $MRCI$ – mean random consistency index, is the average value that is randomly calculated for a large number of pairwise matrices that were generated on a fundamental scale [7].

The resulting vector of the priorities of a certain matrix of pairwise comparisons is considered acceptable if the CR does not exceed the coherence threshold in the range of 0.10 ... 0.20 [7].

Step 6. The resulting value V of j-th wall's assembly alternative integrated index in form of normalized additive composition [7] is calculated in the following manner:

$$V = \sum_{i=1}^{n} a_i \cdot w_i, \quad (7)$$

where a_i – i-th criterion priority, $i = 1,...,n$ $n = 5$; w_i – priority vector of alternatives by the i-th criterion.

THEORY OF CRITERIA IMPORTANCE

The Criteria Importance Theory (CIT) was developed in the USSR in the 1970s by prof. Podinovski V.V. [8], [9] and continues to evolve [10], [14]. The theory is based on formal definitions of the relative importance of criteria, which makes it possible to work with incomplete and inaccurate information about the preferences of the decision-maker (DM).

In this paper, we use a simple ordering of criteria according to their importance and consider two types of criteria scales. Based on this information about the preferences of the DM, conclusions will be drawn about which wall alternatives should be excluded from the candidates for the final choice. Employing the CIT methods, it is possible to obtain a quantitative assessment of the value function of each alternative, specifying quantitative information about the importance of criteria and their scale [11]. However, this is a more laborious process, therefore, in this article, to estimate the value function, we use the approach proposed in [12].

The CIT methodology calculation steps are as follows.

Step 1. The individual criteria $C_1,...,C_n$ must be reduced to a homogeneous form with a general scale $Z = \{1,...,q\}$, which can only be ordinal. In the problem under consideration, could be used

a 10-point scale: the higher the score, the more valuable (useful, preferable) the values of the criterion for the DM. Each alternative of the compared can be associated with its vector estimate from the set Z^n.

Step 2. The preferences of the DM are modelled using the non-strict preference relation R on the set Z^n: the notation yRz means that the vector estimate y is no less preferable than z. The relation R is reflexive and transitive; it defines the relations of indifference I and (strict) preference P: $yIz \Leftrightarrow yRz$ and zRy, $yPz \Leftrightarrow yRz$ and $\neg\, zRy$.

Since the DM's preferences increase along the criteria scale Z, the Pareto relation is defined on the set of vector estimates Z^n as follows:

$$yR^{\varnothing}z \;\Leftrightarrow y_i > z_i, i = 1, \ldots, n. \tag{8}$$

Alternatives with vector estimates dominated by $P^{\varnothing}$ should be excluded from the contenders for the best solution.

Step 3. The qualitative importance information Ω is introduced according to basic definitions [10]. Denote y^{ij}, the vector obtained from vector $y = (y_1, \ldots, y_n)$, by permuting its components y_i and y_j.

Definition 1. The statement "criteria C_i and C_j are equally important", which is denoted as $i : j$ means that any two vector estimates y and y^{ij} are indifferent.

Definition 2. The statement "criterion C_i is more important than criterion C_j", which is denoted as $i \succ j$, means that any vector estimate y, such that $y_i > y_j$, is preferred to y^{ij}.

Complete and consistent information Ω allows us to order criteria following their importance. For notational simplicity, let the criteria be numbered in order of nonincreasing importance in the following manner:

$$1 : \ldots : n_1 \text{ f } n_1 + 1 : \ldots : n_1 + n_2 \text{ f } \ldots \text{f } n_1 + \ldots n_{l-1} + 1 : \ldots : n, \tag{9}$$

where l is the number of groups of equally important criteria, so that $n_1 + n_2 + \ldots + n_l = n$.

To fulfil the relation $yR^{\Omega}z$ for arbitrary vector estimates y and z from Z^n, there must be a sequence of vector estimates $u^1, u^2, \ldots, u^L$ from Z^n, for which $yR^{\omega 1}u^1R^{\omega 2}u^2 \ldots R^{\omega L}u^LR^{\omega L}z$. Here, the relations $R^{\omega k}$ can be the relations $P^{i \succ j}$, $I^{i \succ j}$ or $P^{\varnothing}$. Such sequences are called explanatory chains [10]. Alternatives with vector estimates dominated by P^{Ω} should be excluded from the contenders for the best solution.

Step 4. In [12] the DM's preferences are represented in the form of numerical parameters $\alpha = (\alpha_1, \ldots, \alpha_n)$ and $v = (v_1, \ldots, v_q)$, and imprecise information about these preferences determines the sets A and V of potentially possible values of these parameters. Then, to estimate the value function of an alternative with vector estimate y, the centroid values of the parameters on the resulting sets A and V are taken as follows:

$$F(y) = \sum_{i=1}^{n} \alpha_i^c v_{y_i}^c. \tag{10}$$

The centroid coefficients of the criteria importance are calculated by the following formulas [12]:

$$\alpha_i^c = \frac{1}{l} \sum_{j=k}^{l} \frac{1}{\sum_{m=1}^{j} n_m} \tag{11}$$

where $k = 1, \ldots, l$ is the criteria group number, and i is the number of any criterion belonging to this group.

For the ordinal scale of criteria:

$$v_1 < v_2 < \ldots < v_q \tag{12}$$

Therefore, the centroid values of the scale estimates are:

$$v_s^c = \frac{s-1}{q-1},\ s = 1,\dots,\ q. \tag{13}$$

Step 5. In addition to Equation 12, we can assume the rate of growth of preferences along with the criteria scale Z. In practice, the law of diminishing marginal utility is often fulfilled, which means:

$$v_2 - v_1 > v_3 - v_2 > \dots > v_q - v_{q-1}. \tag{14}$$

We denote such Information by Δ. The information $\Omega\Delta$ does not contradict but clarifies the information Ω. The preference relations $P^{\varnothing}$ and P^{Ω} are supplemented by the relation $P^{\Omega\Delta}$, the definition and method of calculation of which are described in [12], [14]. Alternatives with vector estimates dominated by $P^{\Omega\Delta}$ should be excluded from the contenders for the best solution.

Step 6. To estimate the value function as it described in Equation 10 based on information $\Omega\Delta$ we can use centroid coefficients of the criteria importance, as described in Equation 11. Wherein, the centroid values of the scale estimates calculated as follows [12]:

$$v_1^c = 0;\ v_{s+1}^c = v_s^c + d_s^c,\ s = 1,\ \dots,\ q-1, \tag{15}$$

Where:

$$d_s^c = \frac{1}{q-1}\sum_{j=s}^{q-1}\frac{1}{j},\ s = 1,\ \dots,\ q-1. \tag{16}$$

NUMERICAL MODELLING OF THE THERMAL PERFORMANCE ASSESSMENT IN TERMS OF THE INTEGRAL INDEX' CRITERIA

AHP. To provide the research according to AHP methodology, the three-level hierarchy structure was proposed. As an objective function was chosen the integral index of thermal performance of the multi-layered envelopes from natural materials, which is presented in Figure 2.

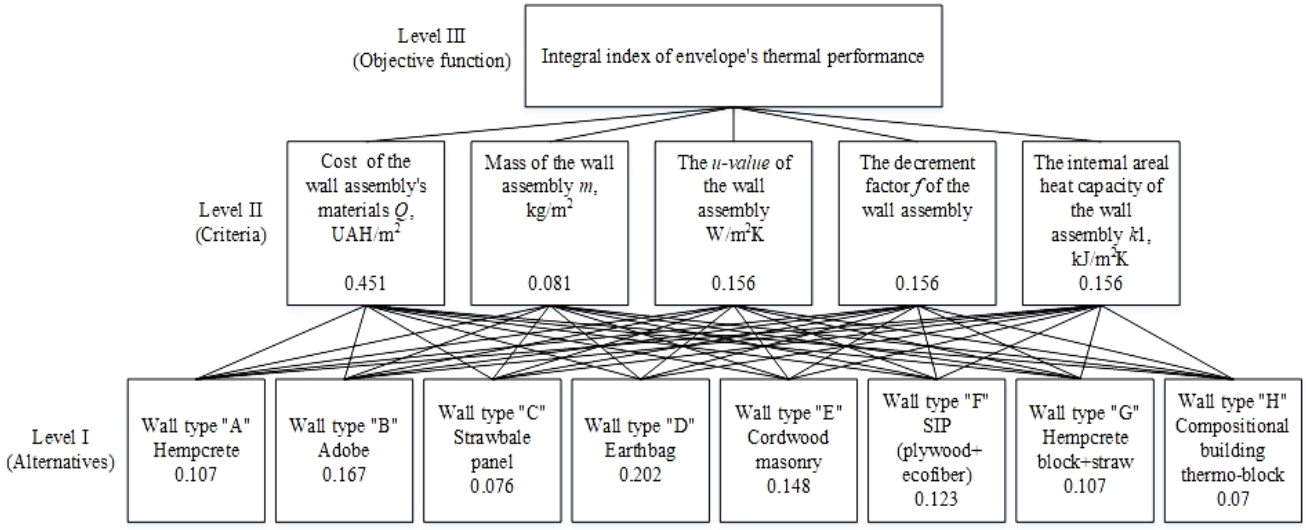

Fig. 2 – Three-level hierarchy for assessment of the envelope's thermal performance

The procedure of calculating according to the AHP methodology is commonly known and widely used [3], [4], [7], [15], [17].

Therefore, the authors allowed themselves to give only the resulting values of the alternatives criteria weights (numbers in rectangles in Figure 2, according to the step-by-step description of this apparatus [7] methodology presented in Equations (1)-(7).

For better visualization of results, the chart bar graph is presented in Figure 3.

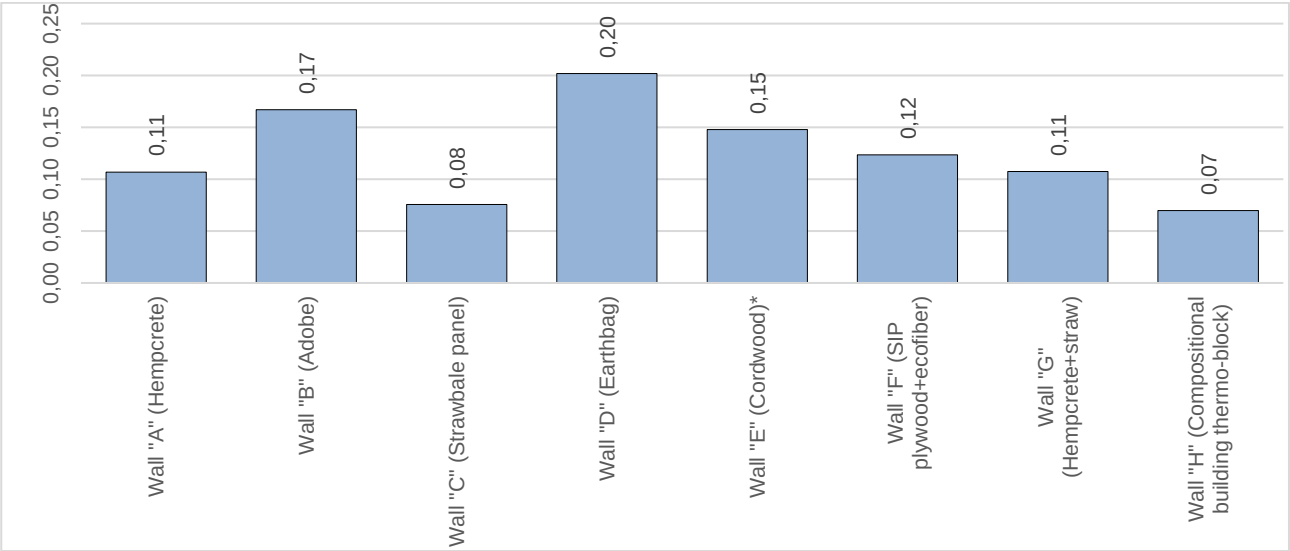

Fig. 3 – Thermal performance assessment of envelopes in terms of integral index' criterion according to AHP

According to Figure 3, the best multi-layered alternative in terms of integral index of thermal performance is the Wall "D" (Earthbag). Such an unobvious solution could be explained by the significant weight of the *Q* criterion (0.451 from Fig. 2). However, from terms of thermal performance parameters, this wall has a contradictive rank (the worst *u-value* from the eights alternatives – 1.51 W/m^{2}K, the average value of the decrement factor *f* = 0.1219 and the best value of the internal areal heat capacity *k*1= 68.53 kJ/m^{2}K) according to the Table 1.

Cost criterion *Q* has a dominating influence on the best alternative, according to the obtained evaluation of proposed criteria by AHP assessment methodology. Therefore, the second place of the ranking took the Adobe Wall "B" with 0.167 points. The worst solutions got Wall "C" from strawbale panel (0.076 points and Wall "H" from Compositional building thermo-block (0.07) which have excellent thermal performance parameters according to Table 1.

CIT. To make the criteria homogeneous, the simplest method is used, which involves a uniform change in preferences along with the numerical scales of the criteria. First, the linear normalization of the criteria values to the interval from 0 to 1 is used. Then, the value of the numerical values of the criteria is transformed to the 10-point scale. For the minimized criteria, the correspondence is used: [1; 0.9] $\rightarrow$ 1 point, (0.9; 0.8] $\rightarrow$ 2 points, …, (0.1; 0] $\rightarrow$ 10 points. For the maximized criteria, the opposite correspondence is used: [0; 0.1] $\rightarrow$ 1 point, (0.1; 0.2] $\rightarrow$ 2 points, ..., (0.9; 1] $\rightarrow$ 10 points.

Table 2 contains the calculated values of the criteria according to normalizing and transforming to the 10-point scale CIT methodology [12].

Tab. 2 - Normalized and 10-point scale values of the criteria

Assembly type	Normalized criteria					Normalized criteria transformed to the 10-point scale				
	Q	*m*	*u-value*	*f*	*k*1	*Q*	*m*	*u-value*	*f*	*k*1
Wall "A"	0.989	0.192	0.010	0.003	0.144	1	9	10	10	2
Wall "B"	0.001	0.780	0.458	0.231	0.661	10	3	6	8	7
Wall "C"	0.999	0.040	0.018	0.998	0.000	1	10	10	1	1
Wall "D"	0.003	0.999	0.999	0.508	1.000	10	1	1	5	10
Wall "E"	0.567	0.188	0.079	0.196	0.838	5	9	10	9	9
Wall "F"	0.703	0.000	0.001	0.950	0.569	3	10	10	1	6
Wall "G"	0.991	0.156	0.012	0.026	0.143	1	9	10	10	2
Wall "H"	0.996	0.084	0.016	0.585	0.187	1	10	10	5	2

Using the Pareto relation

According to the Pareto relation $R^{\varnothing}$ according to Equation 8 defined on the set of vector estimates Z^5, we can immediately distinguish the Wall “C”, which is dominated by the Walls “F” and “H”: $y(\text{"F"})P^{\varnothing}y(\text{"C"})$, $y(\text{"H"})P^{\varnothing}y(\text{"C"})$. This means that the Wall “C” cannot claim to be the best.

Consideration of the criteria relative importance

Let us order the criteria by importance in accordance with the Equation 1 and Equation 2. The qualitative criteria importance information $\Omega = \{1\text{f}\ 3 :\ 4 :\ 5\text{f}\ 2\}$ corresponds to the preferences used in the AHP method. After introducing the preference relation R^{Ω} the Wall “H” has become dominated (Table 3). For example, the relation $y(\text{"A"})P^{\Omega}y(\text{"H"})$ can be checked by constructing the following explanatory chain:

$$y(\text{"A"}) = (1,\underline{9},10,\underline{10},2)P^{4\succ 2}(1,10,10,9,2)P^{\varnothing}(1,10,10,5,2) = y(\text{"H"}).$$

Tab. 3 - Applying the Pareto domination for the alternatives

Assembly type	*Q*	*m*	*u-value*	*f*	*k*1	Is dominated by P^{Ω}
Wall “A”	1	9	10	10	2	
Wall “B”	10	3	6	8	7	
Wall “C”	1	10	10	1	1	“A”, “D”, “F”, “G”,”H”
Wall “D”	10	1	1	5	10	
Wall “E”	5	9	10	9	9	
Wall “F”	3	10	10	1	6	
Wall “G”	1	9	10	10	2	
Wall “H”	1	10	10	5	2	“A”, “F”, “G”

At this step, we can calculate the centroid values of the preference parameters and evaluate the value functions by Equation 10 of the alternatives on their basis. According to Equation 9, the information $\Omega = \{1\text{f}\ 3 :\ 4 :\ 5\text{f}\ 2\}$ breaks down the criteria into $l = 3$ groups of equally important criteria, where $m_1 = 1$, $m_2 = 3$, $m_3 = 1$. Therefore, we can calculate the centroid coefficients of the criteria importance using the Equation 11:

$$\alpha_1^c = \frac{1}{3}\left(1+\frac{1}{4}+\frac{1}{5}\right) = 0.483,$$

$$\alpha_3^c = \alpha_4^c = \alpha_5^c = \frac{1}{3}\left(\frac{1}{4}+\frac{1}{5}\right) = 0.15,$$

$$\alpha_2^c = \frac{1}{3}\left(\frac{1}{5}\right) = 0.067.$$

For the ordinal scale of criteria (see Equation 11), the centroid values of the scale estimates by Equation (13) are as follows:

$$v_1^c = 0,\ v_2^c = 1/9,\ v_3^c = 2/9,\ \ldots,\ v_{10}^c = 1.$$

Thermal performance assessment of envelopes in terms of integral index' criterion according to CIT is calculated according to Equation 10-13 and DASS software [15] and presented in Table 4.

Tab. 4 - Thermal performance assessment of envelopes according to the relative importance criteria by CIT

Assembly type	Integral index of envelope's thermal performance
Wall "A"	0.376
Wall "B"	0.798
Wall "C"	0.217
Wall "D"	0.700
Wall "E"	0.691
Wall "F"	0.407
Wall "G"	0.376
Wall "H"	0.300

It should be noted, that obtained results in Table 4 of the centroid values of the integral index of envelope's thermal performance are quite close to the ones of the AHP method. Thus, the first criterion is about 3 times more important than the third (and the fourth with the fifth), and the third is about 2 times more important than the second is. So, in this problem, we can limit ourselves to qualitative information Ω and not try to refine it quantitatively. Nevertheless, at the next step, when refining the scale, it is possible to reduce the number of non-dominated alternatives to two.

Clarification of information on the scale of criteria

Initially, it was only assumed that preferences grow along the scale of criteria as in Equation 12. Additionally, we can assume about the rate of growth of preferences along the criteria scale Z. In practice, the law of diminishing marginal utility is often fulfilled as in Equation 14. We denote such Information by Δ. The information $\Omega\Delta$ does not contradict, but clarifies the information Ω. The preference relations $P^{\varnothing}$ and P^{Ω} are supplemented by the relation $P^{\Omega\Delta}$, the definition and method of calculation of which are described in [12],[14]. As a result, there are only two non-dominated Walls

"B" and "E" (Table 5). Also, value functions 10 were evaluated in DASS software in accordance with Equation 12, 15, 16.

Tab. 5 - Thermal performance assessment of envelopes according to the clarified information about criteria scale by CIT

Assembly type	Is dominated by $P^{\Omega\Delta}$	Integral index of envelope's thermal performance
Wall "A"	"B", "E"	0.413
Wall "B"		0.929
Wall "C"	"A", "B", "D", "E", "F", "G", "H"	0.217
Wall "D"	"B"	0.750
Wall "E"		0.887
Wall "F"	"B", "E"	0.596
Wall "G"	"B", "E"	0.413
Wall "H"	"A", "B", "E", "F", "G"	0.380

Obtained results in Table 5 reveals that the best alternative of the multi-layered envelope is the Wall "B" from adobe - 0.929 points, the second place is taken by Wall "E" from cordwood masonry with 0.887 points. This fact could be explained by a comprehensive consideration of both thermal performance and economic criteria.

From the data presented in Table 1, it could be seen, that both of the "best" assembly type alternatives has a moderate level of performance in the terms of their thermal parameters (*u-value*, *f* and *k*1). Furthermore, Wall "B" has a *u-value* of 0.77 W/m^{2}K, which is significantly higher than all envelope types, except for Wall "D" with 1.51 W/m^{2}K with approximately the same order of the decrement factor *f*. In other words, even without taking into consideration the economic criteria, Wall "E" is considered the best alternative, according to the scale range in Table 3.

Applying the CIT method of MCDA assessment of integral index of envelope's thermal performance, which comprehensively considers assumed relative importance criteria and clarified information about criteria scale (Table 4, 5) the bar chart, is given in Figure 4.

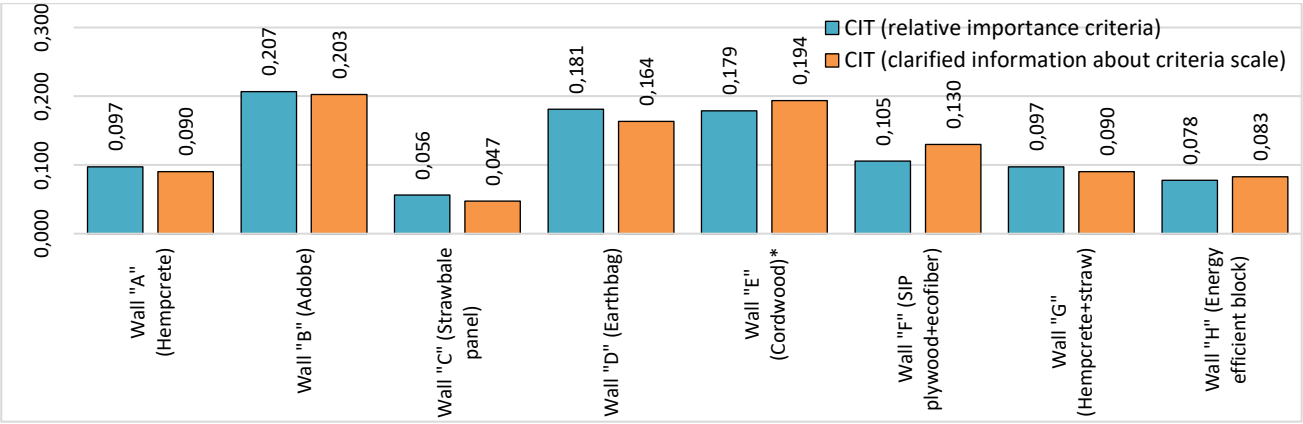

Fig. 4 – Thermal performance assessment of envelopes in terms of integral index' criterion according to CIT

Presented comparison in Figure 4 shown that both CIT attitudes as relative importance criteria and clarified information about criteria scale demonstrate the same ranking priority of alternatives.

More interest has the comparison of the result by AHP and CIT technique, which is given in Figure 5.

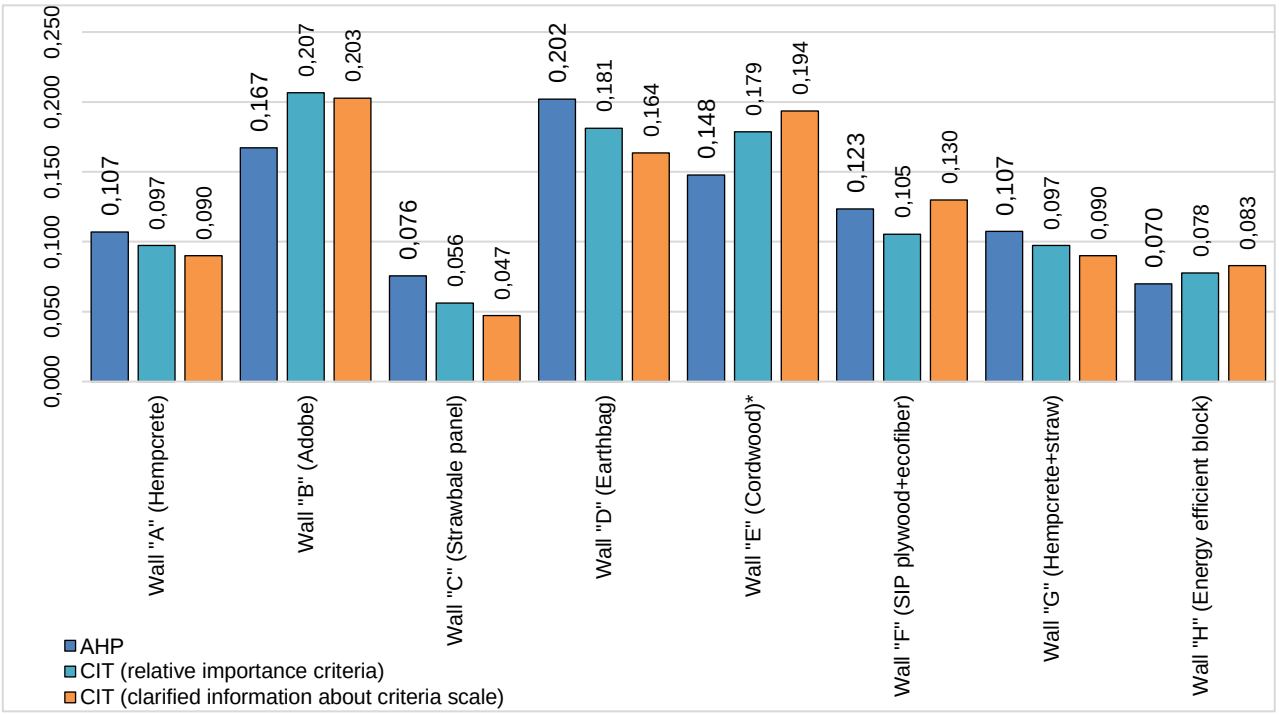

Fig. 5 – Thermal performance assessment of envelopes in terms of integral index' criterion according to AHP and CIT

DISCUSSION OF THE RESULTS

From Figure 5 it could be noted that there is no absolute "leader" in terms of the integral index of thermal performance assessment according to the above-mentioned techniques. Thus, the wall type "D" takes first place by the AHP with 0.202 points, but it is only the third, according to CIT (0.164 points by the clarified information about the criteria scale). However, if decision-maker needs to know the top three envelopes alternatives (from the highest evaluation to the smaller one, it would be: wall "D" – wall "B" – wall "E" by AHP, wall "B" – wall "D" – wall "E" by CIT (relative importance criteria scale) and wall "B" – wall "E" – wall "D" by CIT (clarified information about criteria scale). The final decision by the decision-maker should be made after comprehensive consideration of additional data, which can be determinative in terms of assessed criteria.

Despite a ranking difference of wall assemblies by AHP and CIT techniques, the top three assemblies of each technique are the same variants. It means that both Wall type "D" or "B" could not be the best ones, but they could be with high probability. Also, it could be considered, that any additional information about the assemblies, which does not correlate with assumed criteria should be taken into consideration in each MCDA technique.

To summarize the above-mentioned, it could be noted, that at least several MCDA techniques should be applied for verifying the best alternative of a multi-layered wall assembly in terms of thermal performance assessment by proposed criteria. As a reference point in decision making according to the result analysis by different MCDA techniques the correlation coefficient could be taken as a yardstick – the more result's correlation is obtained by different methods, the more trustable are results.

CONCLUSIONS

The analysis of the conducted research has shown that:

there is no absolute “leader” in the ranking of the wall assemblies according to the proposed criteria and MCDA technique,

there is no universal “right” method or technique for MCDA assessment, but it could be considered, that the more comprehensive and objective analysis of real, simply measurable and interpretable influence factors, with no correlation between each other, will be conducted the more correct and trustable will result,

non-contradictional, balanced decision making according to the results, obtained by different MCDA techniques should be considered as a reasonable one if the correlation between results, obtained by different MCDA techniques for all alternatives in terms of proposed criteria, has maximized values,

the common top three alternatives in both AHP and CIT technique are wall “B”, “D” and “E” type with different values of integral index’ criterion, achieved in each MCDA technique calculation,

with the high level of probability, it could be noted that the best wall assembly according to the proposed criteria of integral index’ criterion would be Wall “D” (Earthbag) or/and Wall “B” (Adobe), but in this case, the *u-value* must meet Building code requirement and have to be reviewed.

As a further step of the investigations, authors see in supplementing of the results by Building Energy Modelling (BEM) of the case study house. Also, at the next step, the optimization model for the best wall assembly could be designed, which should meet the requirement of minimum value of the decrement factor *f, u-value* of the wall, mass *m* and cost *Q* and maximum value of the internal areal heat capacity *k*1.

REFERENCES

[1] Xiaodong C., Dai X., Junjie L., 2016. Building energy-consumption status worldwide and the state-of the-art technologies for zero-energy buildings during the past decade. Energy and Buildings, vol. 128: 198-213. https://doi.org/10.1016/j.enbuild.2016.06.089.

[2] https://doi.org/10.1016/j.buildenv.2013.07.019. STAZI F., 2017. Thermal inertia in energy-efficient building envelopes. (Butterworth-Heinemann) 367 pp.

[3] Wang J. J. et al., 2009. Review on multi-criteria decision analysis aid in sustainable energy decision-making. Renewable and Sustainable Energy Reviews, vol. 13: 2263-2278. https://doi.org/10.1016/j.rser.2009.06.021.

[4] Shimray B. A., Singh K. M., Mehta R. K., 2017. A survey of multi-criteria decision-making technique used in renewable energy planning. International Journal of Computer, vol. 4523: 124-140.

[5] Kheiri F. 2018. A review on optimization methods applied in energy-efficient building geometry and envelope design. Renewable and Sustainable Energy Reviews, vol. 92: 897-920. https://doi.org/10.1016/j.rser.2018.04.080.

[6] Arce M. E. et al., 2015. The use of grey-based methods in multi-criteria decision analysis for the evaluation of sustainable energy systems: A review. Renewable and Sustainable Energy Reviews, vol. 47: 924-932. https://doi.org/ 10.1016/j.rser.2015.03.010.

[7] Saaty Thomas L., 1996. Multicriteria Decision Making: The Analytic Hierarchy Process. (RWS Publications) 479 pp.

[8] Podinovski V.V., 1976. Multicriterial problems with importance-ordered criteria. Automation and remote control, vol. 37: 1728-1736.

[9] Podinovski V. V., 1994. Criteria importance theory. Mathematical Social Sciences, vol. 27: 237-252.

[10] Podinovski V. V., 2019. Ideas and methods of the Criteria Importance Theory in multicriteria decision-making problems (Nauka Moscow) 103 pp. (in Russian).

[11] Podinovski V. V., 2002. The quantitative importance of criteria for MCDA. Journal of multi-criteria decision analysis, vol. 11: 1-15. https://doi.org/10.1002/mcda.312.

[12] Nelyubin A. P., Podinovski V.V., 2017. Multicriteria Choice Based on Criteria Importance Methods with Uncertain Preference Information. Computational Mathematics and Mathematical Physics, vol. 57: 1475-1483. https://doi.org/10.1134/S0965542517090093.

[13] Podinovski V.V., 2009. On the use of importance information in MCDA problems with criteria measured on the first ordered metric scale. Journal of multi-criteria decision analysis, vol. 15: 163-174. https://doi.org/10.1002/mcda.433.
[14] Nelyubin A. P., Podinovski V.V., 2012. Analytical decision rules using importance ordered criteria with a scale of the first ordinal metric. Automation and Remote Control, vol. 73: 831-840. https://doi.org/10.1134/S0005117912050074.
[15] Decision Analysis Support System DASS [computer program] Available at: URL http://mcodm.ru/soft/dass/ [Accessed: date 25.02.2021].
[16] Biks Y., Ratushnyak G., Ratushnyak O., Ryapolov P., 2020. Application of AHP and GRA methods in energy efficiency potential's assessment of envelopes from natural materials. Theory and building practice, № 2: 48-62. https://doi.org/10.23939/jtbp2020.02.048.
[17] Biks Y., Ratushnyak G., Ratushnyak O., 2019. Energy performance assessment of envelopes from organic materials. Architecture Civil Engineering Environment, vol. 3: 55-67. https://doi.org/10.21307/ACEE-2019-036.
[18] A brief guide and free tool for the calculation of the thermal mass of building components, [online]. Available at: URL https://www.htflux.com/en/free-calculation-tool-for-thermal-mass-of-building-components-iso-13786/. [Accessed: date 17.02.2021].
[19] ISO 13786:2017 Thermal performance of building components – Dynamic thermal characteristics – Calculation methods, [online] Available at: URL https://www.iso.org/standard/65711.html [Accessed: date 16.02.2021].
[20] Ukrainian National Standard DSTU B.V. 2.6-189:2013, 2014. Methods of choosing insulation material for insulation of buildings (Minregion Kyiv) 46 pp. (in Ukrainian).
[21] National Building Code DBN V. 2.6-31: 2016, 2017.Thermal insulation of buildings (Ministry of Regional Development, Construction and Housing and Communal Services of Ukraine, Kyiv) 33 pp. (in Ukrainian).
[22] Biks, Y.S., Ratushnyak G. S., Ratushnyak O. G., *Compositional building thermo-block*. Ukraine. IPC: E04B 1/00 E04C 2/16 (2006.01). Utility model u201808845. Available at: URL: https://base.uipv.org/searchINV/search.php?action=viewdetails&IdClaim=253299 [Accessed: date 09.05.2021].
[23] Asdrubali F., D'Alessandro F., Schiavoni S., 2015. "A review of unconventional sustainable building insulation materials". Sustainable Materials and Technologies, vol. 4:1-17. https://doi.org/10.1016/j.susmat.2015.05.002.
[24] Gan W. et al., 2019. "Energy-Saving Design of Building Envelope Based on Multiparameter Optimization". Mathematical Problems in Engineering, vol. 2019: 1-12. https://doi.org/10.1155/2019/5261869 .
[25] Hopfe C. J., Augenbroe G. L., Hensen J. L., 2013. Multi-criteria decision making under uncertainty in building performance assessment. Building and environment, № 69: 81-90.

CIVIL ENGINEERING JOURNAL

Article no. 19

THE CIVIL ENGINEERING JOURNAL 2-2022

EQUIVALENT THICKNESS COEFFICIENT OF COLD CENTRAL PLANT RECYCLING PAVEMENT STRUCTURE

Yanhai Yang[1], Liang Yue[1], Huaizhi Zhang[1] and Ye Yang[1,2]*

1. *School of Transportation and Geomatics Engineering, Shenyang Jianzhu University, Shenyang 110168, China; YHYang@sjzu.edu.cn; YueLiang@stu.sjzu.edu.cn; huaizhi.zhang@163.com*
2. *College of Transportation Engineering, Dalian Maritime University, Dalian 116026, China; yangye@sjzu.edu.cn*

ABSTRACT

In order to promote the development of cold central plant recycling technology and realize the recycling of road solid waste. This research focuses on the equivalent relationship between cold central plant recycling mixture and hot mix asphalt. A large number of on-site investigations were undertaken to collect relevant data. The thickness of the structural layer of the trunk road was obtained by sampling the core. The pavement surface condition index (PCI) was calculated by the road surface conditions investigating, which was used as the evaluation standard. The unreasonable data were removed by SPSS software. The existing decay equation of pavement performance was simplified by MATLAB and optimized by the Marquardt and global optimization methods. The survey data were fitted nonlinearly by 1stOpt software. The multivariate nonlinear regression optimization equation of the equivalent thickness coefficient was established. Ultimately, the equivalent thickness coefficients of cold central plant recycling with emulsified asphalt (CREA) and cold central plant recycling with foamed asphalt (CRFA) were calculated and proposed. The relationship between cold central plant recycling pavement and traditional hot mix asphalt pavement was established.

KEYWORDS

Road engineering, Cold central plant recycling, Pavement surface condition index, Decay equation, Equivalent thickness coefficient

INTRODUCTION

In recent years, with the rapid development of highway construction in China, the roads begin to enter the maintenance phase. A large amount of waste of asphalt mixture was produced. These materials occupied a mass of land and polluted the environment. Generally, cold central plant recycling technology could recycle these old materials [1-2]. Although the technology has been widely used in China, the recycling rate of road pavement materials is less than 30%. However, the utilization in the United States is more than 90%. Obviously, the recycling rate of road pavement materials is far lower than that of developed countries. Now, road milling and reconstruction tasks are becoming more and more prevalent. The cold central plant recycling technology is to break and sift the recycled asphalt pavement. The cold recycling mixture is mainly made up of emulsified asphalt or foamed asphalt, new aggregates, old aggregates, cement, water and so on. The technology is generally applied to binder course and base course of the pavement. The technology could be divided into CREA and CRFA [3]. It has the remarkable advantages of saving resources, low-carbon environmental protection and cost savings. In order to achieve harmonious coexistence of road maintenance and the ecological environment, the national green development concept should be implemented.

Under the combined effect of traffic load and environmental factors, pavement performance during road operation would exhibit different degrees of decay [4-5]. The pavement performance decay model is the theoretical basis for pavement analysis, design, management, construction. Therefore, it is an integral part of pavement research. Additionally, the use of the decay equation is a quantitative description of the process. For example, the service life of pavement is about to end when the performance drops to a certain value. Therefore, it is necessary to describe the decay process of pavement performance accurately. The present service ability index (PSI) pavement performance evaluation model was first proposed by AASHTO [6], which marked the beginning of the research of the pavement performance evaluation technology worldwide. Moreover, the pavement surface condition index (PCI) and international roughness index (IRI) were used by the governments of Alberta and Ontario, Canada in studying the decay performance equation of pavement performance [7-8]. In addition, the maintenance control index (MCI) was proposed as an evaluation model for pavement maintenance quality evaluation index by Japan's Ministry of Construction [9]. Meanwhile, the domestic road performance degradation equation was proposed by Sun Lijun et al [10-11].

According to the method of AASHTO guidelines, different pavement structures have the same service life and performance as long as the number of structures is the same, regardless of the combination of pavement structures. The layer coefficient of pavement structure layer was proposed to measure the performance provided by the unit thickness of the layer material. And the reference equivalent thickness coefficient was 0.6-0.7. Van Wijk et al [12] obtained that the equivalent thickness coefficient of cold recycling mixture with foamed asphalt was between 0.45 and 0.95. And the equivalent thickness coefficient of cold recycling mixture with emulsified asphalt was between 0.39 and 0.93. On the basis of road roughness decay equation established by Sun Lijun, Xu Jun obtained that the equivalent thickness coefficient of the CREA was 0.82.

At present, because of the characteristics of small traffic volume, low technical standards and good economic conditions, cold central plant recycling technology is being applied to the binder course of the pavement. However, the research on the equivalent thickness of this technology and hot mix asphalt under the same pavement performance is still in a nascent stage. According to the research status at home and abroad, PCI was determined as the evaluation standard. The characteristics of typical road selection were put forward. Then, road age, traffic load and surface thickness were taken as the influencing factors. Additionally, the nonlinear optimization equation of the equivalent thickness coefficient was established. Ultimately, the equivalent thickness coefficient was obtained through the data acquired by investigation of the regenerative and comparison sections of a road. Therefore, it provided the theoretical basis for the development of maintenance and repairing decisions during the life cycle of the road.

MATERIALS AND METHODS

Related Variable Data Acquisition

A large number of on-site investigations were undertaken to collect relevant data in a survey covering 13 cities in Liaoning Province, China. In addition, cold central plant recycling technology was selected as the method in this paper. Meanwhile, 36 typical sections were compared after taking more than 300 core samples. Finally, the physical investigation project distribution map was shown in Figure 1. The investigation areas were marked by stars.

The evaluation criteria should be determined by the level of detail of the basic data and management level when constructing the pavement performance decay equation. In detail, the maintenance quality indicator (MQI) was used as an indicator to evaluate road pavement status. PCI is an important component of pavement maintenance quality index (PQI). It comprises 0.7% of MQI [13]. Additionally, PCI was used as a predictor for pavement performance by Sun Lijun and the government of Alberta, Canada. Meanwhile, the research of the performance decay equation determining the PCI was a priority among these comprehensive indicators. Therefore,

comprehensive indicators such as PCI and PSI were used as the object, the road integrity could be better reflected.

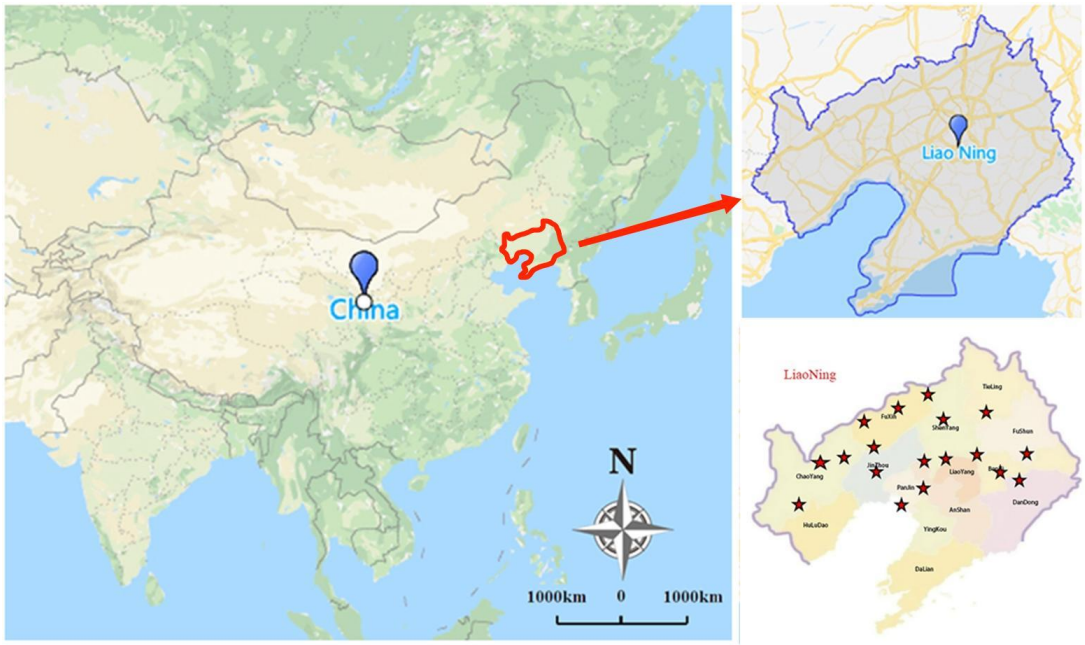

Fig. 1 – Entity survey project distribution (Drawing review No:GS（2019）1685)

Besides, the basic data of PCI could be investigated. Researchers were required to stay within a certain length of road, referring to the relevant guidelines to identify and record the types of road damage [14]. As shown in Figure 2 and Figure 3, the PCI values were obtained based on road surface usage conditions. In order to better reflect the integrity of the road surface and the representativeness of the indicators, the basic data acquisition methods were considered. PCI was used as the evaluation standard for studying the road surface performance decay equation in this research.

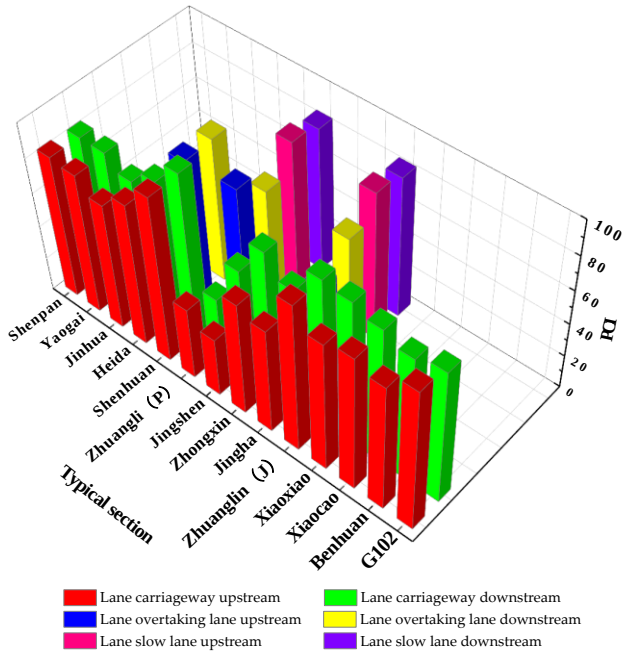

Fig. 2 – PCI of CREA road

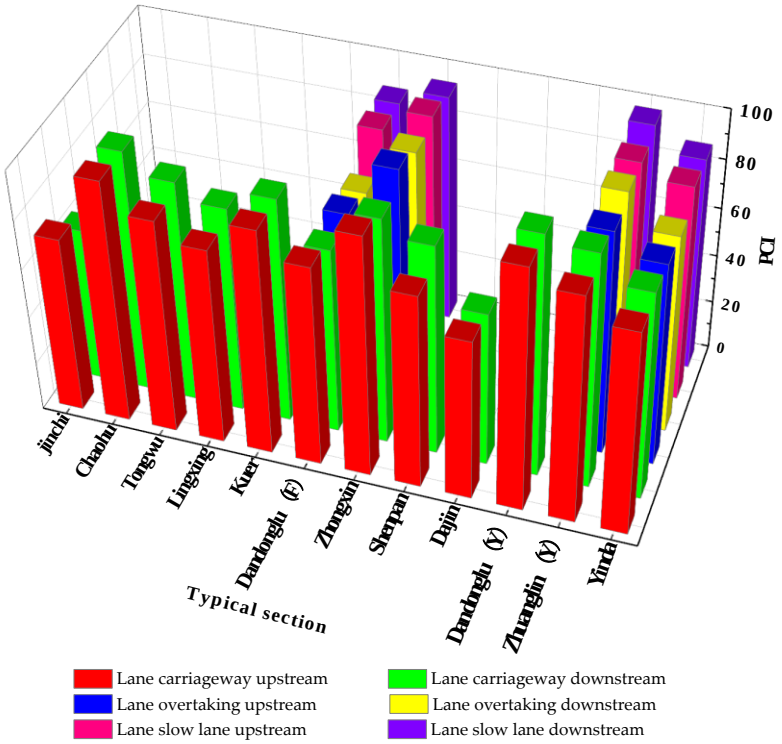

Fig. 3 – PCI of CRFA road

Traffic volume, road age, surface course thickness and other related information were collected to ensure the reliability of the simplified decay equation. On the premise of meeting the requirements of traffic volume data acquisition in relevant norms [15], detailed investigation of traffic volume was carried out for the specific situation of the area where the trunk road was located. As shown in Figure 4 and Figure 5, the traffic volume was obtained by the survey.

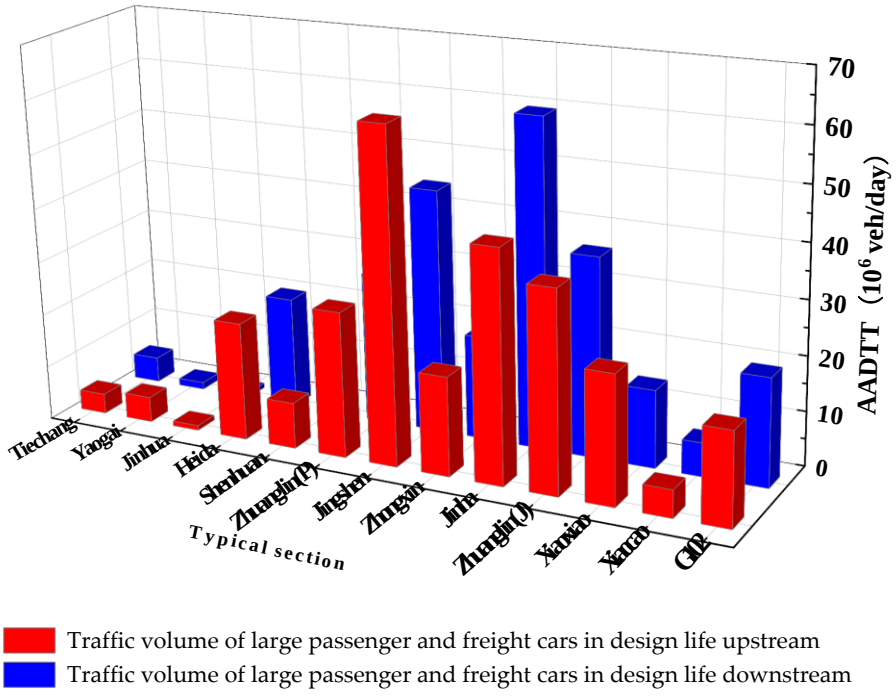

Fig. 4 – Traffic volume of CREA road traffic volume

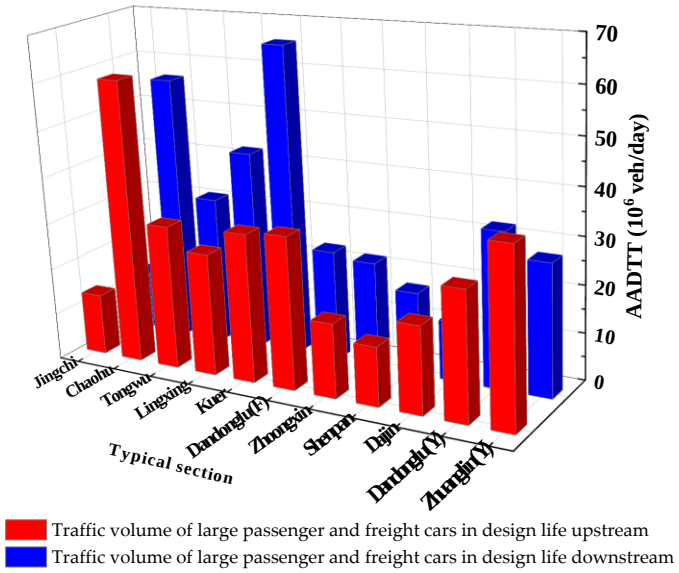

Fig. 5 – Traffic volume of CRFA road traffic volume

Road age, structural layer thickness, road paving materials and maintenance history were obtained by questionnaires and accessing to the construction documents.

In addition, the thickness of the structural layer of the trunk road was obtained by sampling the core to obtain the surface layer thickness under the influence of multiple factors. Considering the extensiveness of the thickness data, the core was sampled according to the following three criteria.

- The core of the decay-free hard shoulder was selected to obtain the thickness of the structural layer close to the initial state of the road surface.
- The core at the wheel track was selected to obtain the thickness of the structural layer under the wheel pressure state.
- Considering the subsequent road performance research, the core at the site of the decay was selected. After the core sample was dried, the thickness of each layer was measured.

Pavement Performance Decay Equation

At present, the pavement structural number (SN) method provided by AASHTO is the most common method for cold regenerative equivalent thickness research [16]. Therefore, the pavement performance of the unit thickness of the structural layer material could be measured by the stratification coefficient in the PSI model proposed by the SN method. Meanwhile, extensive use of performance survey data was simplified. Finally, the decay equation [17-19] was established by Sun Lijun and others. The simplification and equivalent thickness coefficient of the performance decay equation of cold central plant recycling pavement would be studied below based on the performance and experience.

The decay process of PCI is determined by the pavement life factor α and the curve shape factor β uniquely. So, the research of the two parameters is a prerequisite for simplification. In addition, road age, traffic load, type of base layer, type of materials, surface layer thickness and environmental conditions are involved by the two parameters α and β. However, type of base layer, environmental conditions and type of materials could be ignored for the following reasons.

- The structure of the surveyed road section is basically same. For example, the structure of the CREA pavement is basically 3 cm of modified asphalt mixture + 6 cm of cold recycling mixture with emulsified asphalt + the semi-rigid base layer. Therefore, the influence of the base type was ignored.

- The reclaimed section selected in the survey and the corresponding comparison section are located in the same climate conditions of Liaoning Province. Therefore, the impact of environmental conditions was neglected.

- Materials for paving the investigation section are all from the local area of Liaoning Province. The performance of the paving materials at each level is similar. Therefore, the influence of the material type was neglected.

Therefore, only the factors of traffic load, road age and surface layer thickness were considered. Because of the complexity of the original equation, only the pavement life factor α was researched in this paper. Meanwhile, the curve shape factor β was used as the regression coefficient in the simplified equation. According to the PCI data of several trunk highways in Liaoning Province, the road age, the surface layer thickness and traffic load were taken as the influencing factors. Formula (1) is obtained by MATLAB and taking related experience into account:

$$\mathrm{PCI} = \mathrm{PCI}_0 \left\{ 1 - \exp\left[-\left(\frac{a \times h^b \times \mathrm{AADTT}^c}{y} \right)^d \right] \right\} \quad (1)$$

Where PCI_0 is the initial pavement surface condition index, PCI is the pavement surface condition index, y is the road age, H is the surface layer thickness, AADTT is the total number of large passenger trucks and a, b, c and d are the regression coefficients of road life.

In formula (1), the value of PCI_0 was 100. The two parts of the hard shoulder and the lane were organized to use the original data properly. As shown in Table 1, the lane data were processed. Firstly, the SPSS software was used to screen and remove the irrational data obtained from small and medium scale conservation in recent years. Then, 1stOpt fitting software was used for secondary development [20] and for multivariate nonlinear regression. Besides, the Marquardt and global optimization methods [21] was used for optimization. Finally, the results of fitting parameters were shown in Table 2 and the fitting regression coefficients were shown in Table 3. As shown in Table 3, the regression coefficient b corresponding to the thickness was greater than 0. In contrast, the regression coefficient c corresponding to the traffic level was less than 0. Obviously, PCI increased gradually with the increase of the thickness, the traffic level decreases. Therefore, according to experience and understanding, the rationality of the regression results was explained from this level. Meanwhile, PCI value could be predicted by 1stOpt. As shown in Figure 6, the correlation curve between the predicted value and measured value could be obtained by simplifying the equation. It could be seen from Figure 6 that the correlation between the PCI prediction value and measured value was good. Meanwhile, the basic extension y=x curve presents a symmetrical discrete distribution. According to the fitting results of R=0.916, R^2=0.839 and Figure 6, formula (1) was ideal. It could reflect the quantitative relationship among PCI, PCI_0, road age, traffic load and surface layer thickness to a certain extent. In addition, it also could provide a basis for the research of the equivalent thickness coefficient.

Tab. 1 - Partial data used for fitting

Route name	Regeneration method	Average thickness (cm)	Average daily traffic (vehicle/day)	Road age (year)	−ln(1−PCI/100)
G102	CREA	6.233	3313.289	3	1.801810
Benhuan	CREA	8.127	513.688	3	1.452434
Jinhua	CREA	7.920	205.475	3	1.400393
Yaogai	CREA	10.225	719.163	1	1.774902
Xiaoxiao	CREA	10.722	4215.070	7	1.723167
Jinshen	CREA	10.850	3159.183	4	0.980829
Heida	CREA	10.244	3698.555	2	1.917323
Xiaocao	CREA	7.533	1348.432	3	1.698269
Zhuangli n	CREA	13.633	6392.855	6	1.161066
Zhongxin	CREA	9.033	3319.710	1	3.194183
Tongwu	CRFA	11.250	734.860	1	2.277892
Lingxing	CRFA	8.800	819.047	2	1.760261
Jinchi	CRFA	8.200	3051.451	5	1.139434
Zhongxin	CRFA	14.025	3346.108	1	3.194183
Shenpan	CRFA	8.400	3664.310	2	1.786772
Dajin	CRFA	10.625	3701.409	3	1.049822
Kuer	CRFA	10.425	1164.360	1	2.617296
Dandong	CRFA	9.620	500.539	6	1.683623
Tongwu	CRFA	11.250	734.856	1	2.277892

Tab. 2 - Fitting calculation results

Regeneration method	RMSE (root mean square error)	SSE (sum of squares for error)	R (correlation coefficient)	R^2 (coefficient of determination)
CREA	0.4141	1.8864	0.9160	0.8390
CRFA	0.3089	0.7631	0.8911	0.7941

Tab. 3 - Fitting regression coefficients

Regeneration method	a	b	c	d
CREA	1.699	0.795	−0.072	0.752
CRFA	0.135	2.407	−0.127	0.326

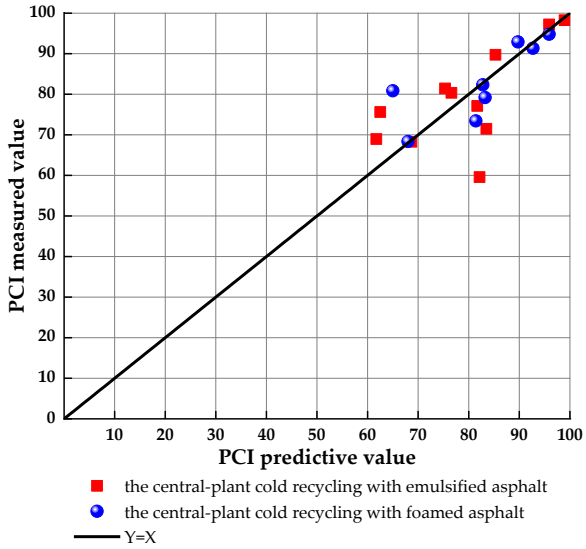

Fig. 6 – Measured and predicted values correlation curve

Equivalent Thickness Coefficient Calculation

The equivalent thickness coefficient of the cold regenerated layer is defined as the ratio between the thickness of the structural layers of the conventional hot mix asphalt and the cold recycling mixture on the same road surface performance. Based on the established PCI prediction equation, formula (1), the nonlinear optimization equation formula (2) of the equivalent thickness coefficient was obtained:

$$\mathrm{PCI} = \mathrm{PCI}_0\left\{1-\exp\left[-\left(\frac{a\times\left(h_{surfacelayer}+K_{equivalent}h_{lowerlayer}\right)^{b}\times\mathrm{AADTT}^{c}}{y}\right)^{d}\right]\right\} \quad (2)$$

As shown in Table 4, the research data for hot mix asphalt were given. Firstly, the regression coefficient of Table 3 was substituted into formula (2). Then, the PCI data obtained by the survey were fitted by 1stOpt. Moreover, the parameters were optimized by the Marquardt method. Finally, as shown in Table 5, the equivalent thickness coefficient of the CREA was 0.587. In addition, the equivalent thickness coefficient of the CRFA was 0.632.

Tab. 4 - Hot mix asphalt survey data

Route name	Lower layer thickness (cm)	Average daily traffic (vehicle /day)	Road age (year)	−ln(1−PCI/100)
G102	5.35	4083.822	3	1.812792
Lingxing	4.45	829.0357	2	1.743096
Tongwu	4.40	1582.445	1	2.249550

Tab. 5 - Fitting calculation results

Regeneration method	RMSE	SSE	R	R^2
CREA	0.4365	0.7623	0.9097	0.8275
CRFA	0.1657	0.1098	0.8919	0.7954

AASHTO conducted research on cold recycling pavement based on the more suitable method of medium and light traffic roads. And the reference equivalent thickness coefficient of 0.6-0.7 based on the horizon coefficient was provided by AASHTO. Meanwhile, the roads targeted by this research were mostly trunk highways with medium and light traffic. And under the conditions of the binder course of the pavement, the equivalent thickness coefficient of the CREA was 0.587 in this research. In addition, the CRFA was 0.632. Obviously, these values were close to the reference value given by AASHTO. Therefore, the rationality of the results was further explained in this research. However, the equivalent thickness coefficient of the CREA pavement obtained by Xu Yan based on physical engineering was 0.82 [22]. Because the project of applying regeneration technology to the base course was investigated by Xu Yan. And the stress and environmental impact of the base course was weaker than that of the surface course. Obviously, the equivalent thickness coefficient obtained by Xu Yan was larger than the equivalent thickness coefficient provided by this research and AASHTO. Therefore, it was concluded that, when the cold central plant recycling technology was applied to the binder course of the pavement, the performance of 10 cm cold central plant recycling pavement was equivalent to that of 6 cm the traditional hot mix asphalt pavement.

As shown in Figure 7, the equivalent thickness coefficient of the measured and predicted values of the CREA and CRFA were obtained by formula (2). Apparently, the correlation between the predicted and measured values was good. Furthermore, the CREA technology is controlled by many indexes. Such as, the construction technology is difficult and the variability of construction is large. Therefore, the road performance of different road sections shows differences. On the contrary, the CRFA construction process is less difficult than the CREA. In addition, its variability is much smaller. So the road performance of CRFA is relatively stable. To sum up, compared with the CRFA, the dispersion of the CREA is more significant.

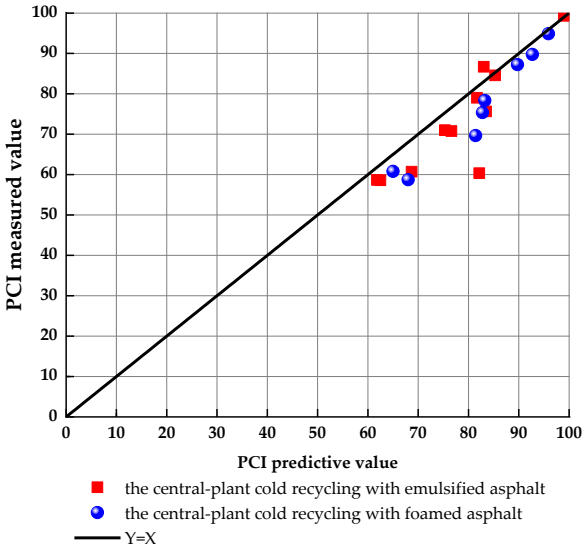

Fig. 7 – Measured and predicted values correlation curve

CONCLUSION

- Under the conditions of the actual situation, the quantitative relationship between road age, surface layer thickness, traffic load and the PCI is obtained as follows:

$$\mathrm{PCI} = \mathrm{PCI}_0 \left\{ 1 - \exp\left[-\left(\frac{a \times h^b \times \mathrm{AADTT}^c}{y} \right)^d \right] \right\}$$

- According to the simplified decay equation of pavement performance, the equivalent thickness coefficient of the CREA is calculated to be 0.587 (R=0.9097, R^2=0.8275). In addition, the

equivalent thickness coefficient of the CRFA is 0.632 (R=0.8919, R^2=0.7954). That is, the performance of 10 cm cold central plant recycling pavement is equivalent to 6 cm the traditional hot mix asphalt.

- The dispersion of CREA is significantly greater than that of CRFA. Because of the construction process, the cold regeneration variability of the CREA is greater than that of the CRFA. Therefore, the road performance of CRFA is relatively stable.

ACKNOWLEDGEMENTS

Thanks are due to the platform support provided by Shenyang Jianzhu University and professors' guidance for this research. This study was supported by Liaoning Distinguished Professor Program [grant numbers tpjs2017003]; the key Program of Basic Scientific Research of Higher Education of Liaoning Province [grant numbers LJZ2017001].

REFERENCES

[1] Yang Y H, Yang Y, Qian B T, 2019. Performance and Microstructure of Cold Recycled Mixes Using Asphalt Emulsion with Different Contents of Cement, Materials, vol. 12(16): 2548.
[2] Yang Y H, Wang H B, Yang Y, et al, 2021. Evaluation of the Evolution of the Structure of Cold Recycled Mixture Subjected to Wheel Tracking Using Digital Image Processing, Construction and Building Materials, vol. 304(2): 124680.
[3] Tang F L, Zhu S C, Xu G J, et al, 2019. Influence by Chemical Constitution of Aggregates on Demulsification Speed of Emulsified Asphalt Based on UV-spectral Analysis, Construction and Building Materials, vol. 212: 102-108.
[4] Iwanski M, Chomicz-Kowalska A, 2011. The Effects of Using Foamed Bitumen and Bitumen Emulsion in the Cold Recycling Technology//Environmental Engineering, Proceedings of the International Conference on Environmental Engineering, ICEE, Vilnius Gediminas Technical University, Department of Construction Economics & Property, (8): 1089-1096.
[5] Zhang Y Q, Jia S Y, 2005. Evaluation Method for Asphalt Pavement Performance of Freeway, Journal of Chang'an University (Natural Science Edition), vol. 25(2): 11-15.
[6] American Association of State Highway and Transportation Officials (AASHTO), 1993. AASHTO Guide for Design of Pavement Structures, AASHTO.
[7] Humphries J A, Ma E, 2004. Optimization of Pavement Preservation Activities//2004 Annual Conference and Exhibition of the Transportation Association of Canada-transportation Innovation-accelerating the Pace.
[8] Hein D, Croteau J M, 2004. The Impact of Preventive Maintenance Programs on the Condition of Roadway Networks//Proceedings: 2004 Annual Conference of the Transportation Association of Canada, 19-22.
[9] Lou Z Y, John L J, Gunaratne M, et al, 2000. Forecasting of Pavement Crack Performance with Adaptive Filter Model, Transportation Research Record Journal of the Transportation Research Board, vol. 1699(1): 95-100.
[10] Sun L J, Liu X P, 1995. General Deterioration Equation for Pavement Performance, Journal of Tongji University (Natural Science), vol. 23(5): 512-518.
[11] Li F, Huang S C, Xu J, 2011. Foamed Bitumen Decay Equation and Bitumen Foaming Characteristics Evaluation, Journal of Tongji University (Natural Science), vol. 39(7): 1031-1039.
[12] Van W, Adriaan J, 1984. Structural Comparison of Two Cold Recycled Pavement Layers, National Research Council, Washington, DC, (No. 954).
[13] Ministry of Transport of the People's Republic of China, 2018. Highway Performance Assessment Standards. JTG 5210-2018, Beijing: China Communications Press.
[14] British Transport Research Institute, 2001. A Guide to the Pavement Evaluation and Maintenance of Bitumen-surfaced Roads in Tropical and Sub-tropical Countries, People's Communications Press.
[15] Ministry of Transport of the People's Republic of China, 2017. Specification for Design of Highway Asphalt Pavement, JTG D50-2017, Beijing: China Communications Press.

[16] Kandhal P S, Mallick R, 1997. Pavement Recycling Guidelines for State and Local Governments: Participant`s Reference Book. Final Report, September 1995--December 1997. National Center of Asphalt Technology.
[17] Ye J, Chen C, Sun L J, 2008. Deterioration Equation for Pavement Performance Based on Self-adaptive of Parameters, Shanghai Highways, vol. (04): 21-23.
[18] Sun L J, Liu L P, 2006. Determination of Material Influence Coefficient in Asphalt Pavement Structural Behavior Equation, Journal of Highway and Transportation Research and Development, vol. 23(12): 6-9.
[19] Liu X P, Sun L J, 1996. Effects of Environmental Factors on Performance in Distress, Journal of Tongji University (Natural Science), vol. 24(04): 398-404.
[20] He Z, Yu H, 2013. Data Fusion Based on First Optimization and its Comparison with the Traditional Algorithms//2013 6th International Congress on Image and Signal Processing (CISP), IEEE, 3: 1432-1436.
[21] Yu G Y, Zheng S X, Liu G X, et al, 2000. Study on Global Optimization Algorithms for Complex Engineering Problem, Journal of South China University of Technology (Natural Science Edition), vol. 28(8): 104-110.
[22] Xu Y, 2016. Performance-based Cold Recycling Pavement Structure Design Method, Shanghai Highways, vol. (4): 14-18+97.

CIVIL ENGINEERING JOURNAL

Article no. 20

THE CIVIL ENGINEERING JOURNAL 2-2022

DEFORMATION AND FAILURE BEHAVIOR OF OPEN-GRADED FRICTION COURSE AT LOW TEMPERATURES

Baoyang Yu[1,2], Zongguang Sun[1] and Lin Qi[3]

1. *College of Transportation Engineering, Dalian Maritime University, Dalian 116026, China; yubaoyang12380@126.com sun@dlmu.com*
2. *School of Transportation Engineering, Shenyang Jianzhu University, Shenyang 110168, China;*
3. *Department of Civil Engineering, Shenyang Urban Construction Institute, Shenyang 110167, China; qilin6126@126.com*

ABSTRACT

To study the deformation and failure behavior of the open-graded friction course (OGFC) before cracking at low temperatures, a four-point bending test of the trabecula was conducted, and the deformation process was monitored by the digital surface model (DSM). The distribution law of the strain field of the trabecular specimens was analyzed. The horizontal strain field gradually changed from a uniform distribution to a strain concentration area with loading. The crack initiation time, crack initiation strain, and deformation period were obtained from the strain curve. The combination of stress reconstruction and DSM makes the stress measurement of the OGFC more authentic.

KEYWORDS

Open-graded friction course (OGFC), Four-point bending test, Digital surface model (DSM), Strain field, Stress reconstruction

INTRODUCTION

The open-graded friction course (OGFC) has been popular since 1950 and has been used because of its advantages, such as strong drainage capacity, improved road surface friction, and low noise [1–2]. Compared with other types of mixtures, OGFC has a higher porosity and coarse aggregate content. However, owing to this unique structure, its spatial distribution has a significant influence on the deformation and failure behavior [3].

Low-temperature deformation and failure are common issues associated with asphalt pavements and have important impacts on the road function of the OGFC. Typically, the deformation and failure behavior of materials are evaluated as a whole by the nominal stress and strain in multiple macroscopic tests [4–5]. However, material properties are evaluated according to the assumption of isotropy; the anisotropic properties of the mixture are neglected [6–7]. In addition, the deformation process prior to failure is ignored. It is impossible to obtain the deformation of the sample surface or the concerned part. The actual strain field of materials must be obtained to understand their macroscopic behavior, irrespective of whether it is the surface of the sample or the place of interest [8]. Therefore, it is of great significance to study the deformation and failure behavior of OGFCs by considering comprehensively the anisotropy properties of materials.

The digital surface model (DSM) can realize full-field, noncontact measurements. Through the deformation measurement experiment of 0.1-500m scale, Maas et al. [9] determined that digital image correlation (DIC) can analyze deformation with a precision of 1:1000000. Kovačič et al. [10] found that the photogrammetry results also maintained high accuracy compared with the results

obtained by geodetic and hydraulic piston methods. Stewart et al. [11] found that cracks are sensitive to mesostructural features using DSM combined with macro tests. Bjorn et al. [12] found that a DIC system overcomes the shortcomings of traditional strain measuring equipment and has satisfactory accuracy compared with strain gauges. Through the failure test of concrete wall, Teo [13] studied that there is a high correlation between photogrammetry displacement and linear variable differential transformer (LVDT) displacement. Lyons et al. [14] studied the ability of DIC computer vision technology to measure in-plane deformation at temperatures as high as 650 °C.

Considering the above analysis, in this study, the deformation and failure behavior of OGFC is studied using DSM in conjunction with a four-point bending test to obtain the full-field displacement and strain information of the OGFC mixture. Additionally, we propose stress reconstruction, obtain the stress change during loading, and recognize the full-field deformation and failure behavior of the OGFC mixture.

METHODS

Gradation design of OGFC

OGFC is an open-graded asphalt mixture composed of asphalt and aggregates. Basalt was used as the coarse aggregate, alkaline machine-made sand was used as the fine aggregate, and the mineral powder was made of ground limestone. The gradation is illustrated in Figure 1.

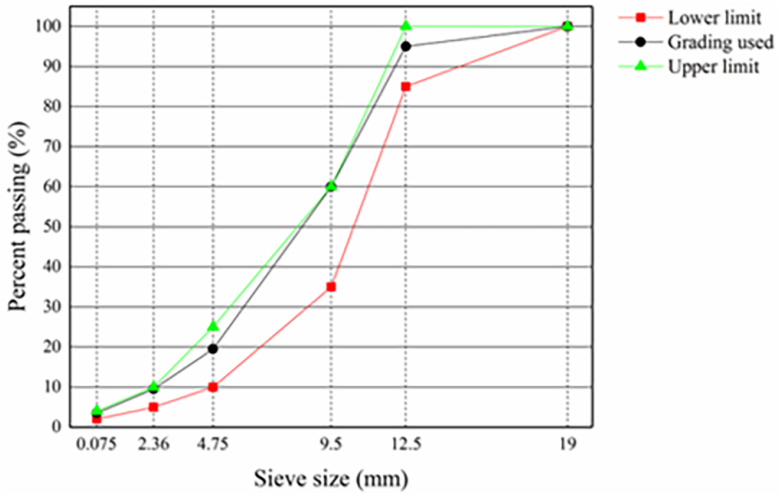

Fig. 1 – Gradation design of open-graded friction course

To verify the high-temperature stability, low-temperature crack resistance, and water stability of the OGFC, the dynamic stability was measured by conducting a rutting test at 4160 times/mm. The freeze-thaw splitting strength ratio measured by the freeze–thaw splitting test was 90.86%, and the flexural tensile strain measured by the low-temperature bending test was 3178.34 × 10^{-6}.

Test methods

Basic principle of DSM

This study mainly uses the MatchID system, comprising a camera, computer, and light source, to execute the DSM test. The DSM test system is shown in Figure 2.

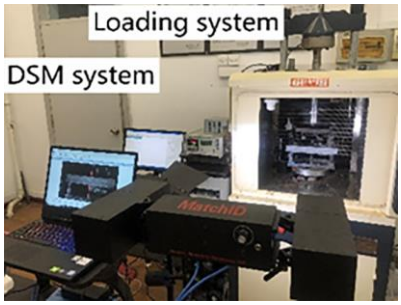

Fig. 2 – Digital speckle method test system

Basic principle of DSM [15]: Through correlation matching of speckle images before and after deformation (the images before and after deformation are reference and deformed images, respectively), the gray field of an image subregion is obtained, and the displacement and strain of sample are calculated according to the gray changes of pixel points. The algorithm principle is depicted schematically in Figure 3. The gray values of the reference and deformed images are *f(x, y)* and *g(x', y')*, respectively. Consider a point *P(x, y)* in the reference image, and a subset s of pixel points with a size of (2M +1) × (2M+1) as the reference image matching subarea. After loading, when point *P* moves to point *P'(x', y')*, the speckle in *S* moves to the corresponding position in the *S'* subregion centered on the point *P'(x', y')*. Based on the principles of probability and statistics, the deformed point *P'* can be determined by the position of the point with the maximum correlation coefficient after matching with point *P* [16]. After matching the corresponding points, the coordinate differences between these two points are the displacement components attributed to the deformation of point *P* [17].

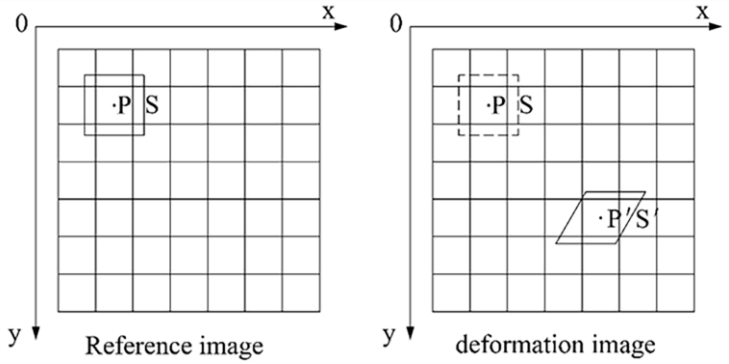

Fig. 3 – Basic principle diagram explaining the implementation of the correlation algorithm

The zero-mean normalized sum-of-squared differences (ZNSSD) correlation function [18] is used to calculate the correlation coefficient of the OGFC beam specimen before and after deformation,

$$C_{ZNNSSD} = \sum_{x=-M}^{M}\sum_{y=-M}^{M}\left[\frac{f(x,y)-f_m}{\sqrt{\sum_{x=-M}^{M}\sum_{y=-M}^{M}[f(x,y)-f_m]^2}} - \frac{g(x',y')-g_m}{\sqrt{\sum_{x=-M}^{M}\sum_{y=-M}^{M}[g(x',y')-g_m]^2}}\right] \quad (1)$$

where *f(x,y)* is the gray value of reference image point *P* in Figure 3, *g(x', y')* is the gray value of the deformed image point in Figure 3, and f_m and g_m are the average gray values of the subregions of the reference and deformed images, respectively.

Preparation of test pieces

The rutting plate specimen with dimensions of 300 mm × 300 mm × 50 mm (length × width × height) was cut in beam specimens with dimensions of 250 mm × 30 mm × 35 mm (length × width × height). Speckles were made on the test piece. The bottom part was sprayed with matte white paint on one side in the up-and-down direction of molding, and black spots were added after air drying to form a speckled surface with black spots on a white background, as shown in Figure 4.

Fig. 4 – Speckled surface of the tested specimen

Test scheme

The four-point bending test is shown in Figure 5. A SANS universal testing machine was used as the loading device. The distance between the supports of the specimen placement device was 200 mm, the distance between adjacent chucks was 66.67 mm, the loading rate was 50 mm/min, the test temperature was -10 °C, and the image acquisition frequency was 10 ms/pair.

Fig. 5 – Four-point bending test

ANALYSIS AND DISCUSSION OF TEST RESULTS

Load–time curve analysis

The entire field deformation and failure behavior of the OGFC were studied using DSM combined with a four-point bending test. Figure 6 illustrates the load–time curve. At the initial stage of loading, the load on the specimen increases approximately linearly. At this time, the microcracks in the specimen are gradually compressed and deformed. Subsequently, the load growth rate decreases until the peak value is reached. Finally, the load decreases approximately linearly until the end of the test. To analyze the strain field evolution process of the OGFC beam specimens before complete failure, the strain fields at six representative time points (A–F) were selected to analyze the evolution process from the load–time curve and the evolution characteristics of the strain field nephogram. Point A is the initial loading of the specimen, point B is in the stage of linear load growth, point C is in the stage of slow-load growth, point D is near the peak load, point E is at the stage of load decline, and point F is the end of the load decline when the test is terminated.

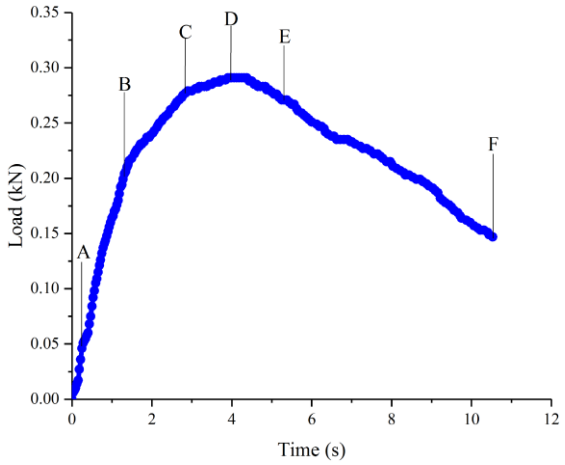

Fig. 6 – Load–time curve of four-point bending test

Strain-field evolution analysis

We focus on the evolution process of the strain field before the complete failure of the OGFC beam specimen and investigate the deformation and failure behavior by examining the evolution of the horizontal strain field [19], as shown in Figure 7(a)–(f).

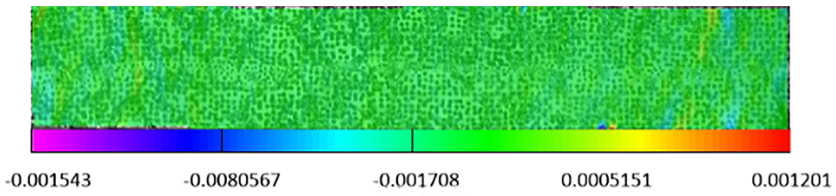

(a) Point A

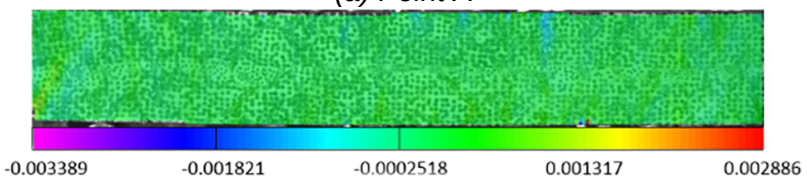

(b) Point B

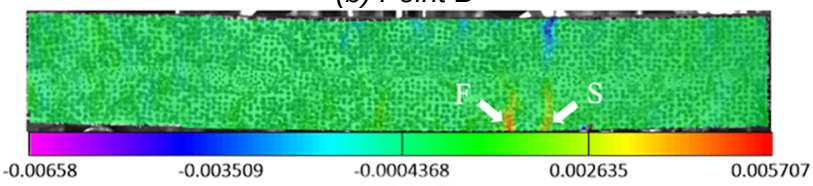

(c) Point C

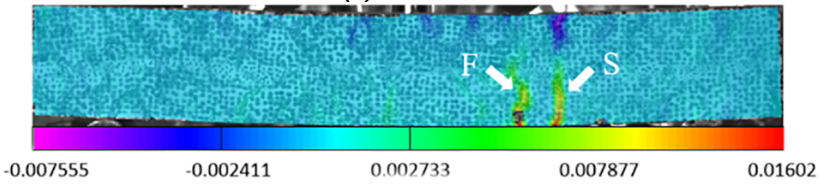

(d) Point D

Fig. 7 – Horizontal strain field at representative temporal points

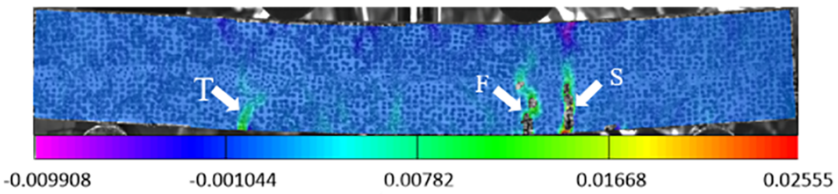

(e) Point E

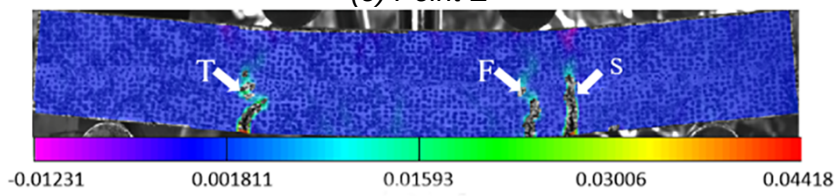

(f) Point F

Fig. 7 – Horizontal strain field at representative temporal points

Figure 7 demonstrates that:

① There is no notable difference between the strain fields at points A and B, and the nephogram of the horizontal strain field is uniformly distributed; however, there is a rather fuzzy ribbon area at point B. Compared with the position of the specimen, these areas are all distributed along the asphalt mortar owing to the uneven distribution of materials, and the flexible asphalt binder is prone to deformation. Thus, different positions generate different strain responses.

② When loaded to point C, the sample is in a stage of slow load growth. First, flame-like areas F and S, namely the strain concentration areas, appear at the bottom part of the right indenter and expand upward to form the strain concentration belt area (Figure 7(c)). As indicated, the degree of strain concentration in area F is higher than that in area S. Comparing Figures 7(c) and 7(b), we can observe that areas F and S are developed from the ribbon areas in Figure 7(b).

③ When loaded at point D, the strain concentration degree of area F is higher than that of area S, and the stress is concentrated. When the concentrated stress exceeds the ultimate strength that the OGFC can bear, area F cracks before area S, as shown in Figure 7(d). Concurrently, a crack tip is produced, and the strain concentration area moves up to the tip, thus promoting continuous expansion of cracks. In addition, the first generation of cracks in area F increases the tensile strain at point D by one order of magnitude compared with point C.

④ With the application of load, the cracks in area F continue to expand, and the strain concentration in area S increases synchronously. When the material limit is exceeded, the cracks in area S appear as shown in Figure 7(e). Simultaneously, a flame-like area T appears at the bottom of the left indenter owing to the strain concentration.

⑤ The strain concentration in the left indenter and cracking in area S disperse the stress in area F and decelerate the development of cracks. When loaded to point F, the strain concentration causes the crack at the bottom of the left indenter specimen to expand to a certain extent, which in conjunction with the two cracks on the right side, leads to the final failure form of the specimen shown in Figure 7(f).

According to the overall observation of the six pairs of strain field nephograms with different characteristics at different times, the drastic changes in the strain field distribution in the four-point bending test are mainly concentrated between two indenters. The strain field gradually changes from a uniform distribution to a considerable concentration, thus indicating the localization characteristics of the OGFC deformation. In addition, by comparing the strain concentration bands to the distribution positions of the specimen materials, it can be observed that the strain concentration bands in areas F, S, and T are all located between coarse aggregates, and the

materials at the positions are asphalt mortar formed by asphalt binder and fine aggregate. Furthermore, the cracks are distributed along the asphalt mortar and spread at the interface between the fine aggregate and asphalt binder.

Strain characteristics at strain concentration zone

To objectively and quantitatively investigate the evolution of the strain concentration zone, the horizontal strain of the concerned points (1, 2, 3, and 4; Figure 8) was measured using the point function of the MatchID system, as depicted in Figure 7(c), in which three points (1, 3, and 4) were located at the cracking point of the strain concentration zone, and point 2 was located at the middle bottom. Figure 9 demonstrates the change in the horizontal strain at each point with the number of collected frames.

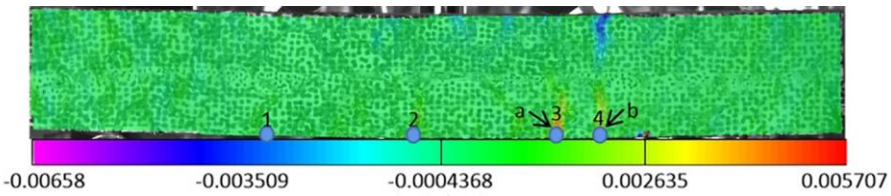

Fig. 8 –The horizontal strain of the Concerned points

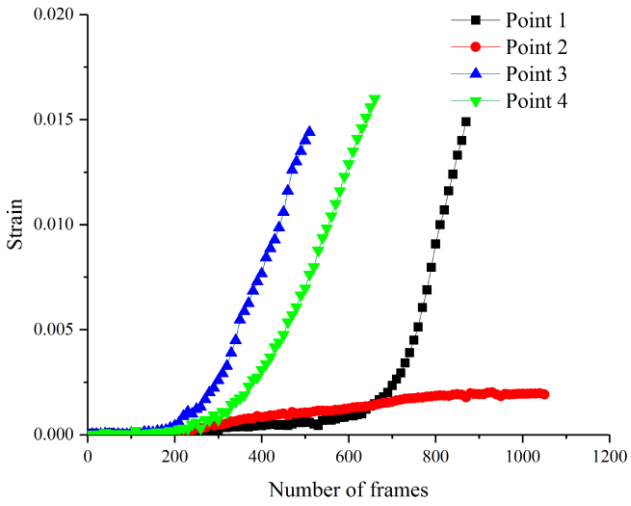

Fig. 9 – Changes of horizontal strain of concerned points with the number of frames collected

Figure 9 shows that the strain change trends of the concerned points are different, and the strain growth is slow in the early stage with no notable differences. The strain growth rate at points 3 and 4 is accelerated and tends to be linear at approximately 200 frames, but the growth rate at point 3 is faster than that at point 4 in the early stage. At approximately 600 frames at point 1, the strain begins to increase rapidly and tends to be linear. When cracks occurred at points 1, 3, and 4, the strain responses were disrupted. Considering that no cracks were formed at point 2, the curve changed steadily until the test stopped. Based on the number of frames at the turning point of the curve from slow growth to rapid growth, the cracking point sequence adheres to the order of points 3, 4, and 1, respectively. The corresponding time at the strain interruption at point 3 is the crack initiation time (4.33 s). Furthermore, the time before cracking (strain interruption) is the deformation period of the specimen, which is approximately 0–4.33 s (520 frames).

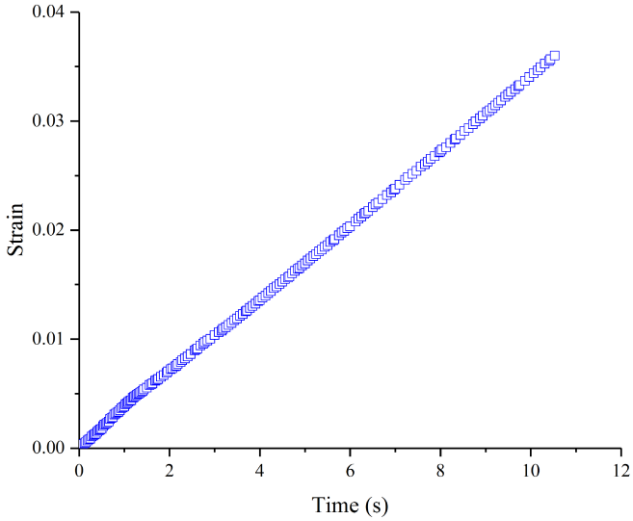

Fig. 10 – Nominal strain response of four-point bending test

The nominal strain of the four-point bending test is shown in Figure 10. Comparing Figures 9 and 10, the strain change trends present nonlinear growths and not the approximate linear growth trends of the nominal strain, although the strain change trends of the concerned points are different. This is because OGFC exhibits anisotropic properties, as verified by the distribution of the strain field and strain changes of the concerned points. The nominal strain was the ideal strain obtained by homogenizing the specimen. The DSM calculates the strain values of the points on the surface of the specimen. Therefore, the strain calculated using the DSM is the true strain value of each point.

Stress reconstruction and evolution analysis

To study the material stress variation law, a theoretical formula is generally used to calculate the stress; however, this method does not consider the change in the material's cross-section owing to load. In addition, the theoretical formula can only calculate the representative stress and cannot obtain the stress change of the concerned area or point. Previously, the stress change was studied using the finite element method (FEM) [20-21]. However, the FEM is too idealistic; thus, using DSM to estimate the stress of materials can provide more accurate results. Therefore, based on the FEM and material properties, this study reconstructs the stress of the OGFC deformation process through the stress–strain inverse mechanical analysis method based on the strain measurement results of DSM.

Stress reconstruction

The four-point bending test used in this study was performed at -10 °C. Assuming that OGFC produces elastic deformation during loading, the stress–strain relationship at the deformation stage can be expressed using Equations 2–4, according to the elastic mechanics theory as follows,

$$\varepsilon_x = \frac{1-\mu}{E}\left(\sigma_x - \frac{\mu}{1-\mu}\sigma_y\right) \quad (2)$$

$$\varepsilon_y = \frac{1-\mu}{E}\left(\sigma_y - \frac{\mu}{1-\mu}\sigma_{yx}\right) \quad (3)$$

$$\gamma_{xy} = \frac{2(1-\mu)}{E}\tau_{xy} \quad (4)$$

where σ_x is the horizontal stress, σ_y is the vertical stress, τ_{xy} is the shear stress, μ is the Poisson's ratio of the material, and E is the elastic modulus.

Assuming that $a = \frac{1-\mu}{E}$ and $b = \frac{\mu}{1-\mu}$, the above equations can be simplified to Equations 5–7, as follows,

$$\varepsilon_x = a(\sigma_x - b\sigma_y) \tag{5}$$

$$\varepsilon_y = a(\sigma_y - b\sigma_x) \tag{6}$$

$$\gamma_{xy} = 2a(1+b)\tau_{xy} \tag{7}$$

Equations 8–10 of the stress reconstructions in the horizontal, vertical, and shear directions can be obtained by the simultaneous inversion of Equations 5–7, as follows.

$$\sigma_x = \frac{\varepsilon_x - b\varepsilon_y}{a(1-b^2)} \tag{8}$$

$$\sigma_y = \frac{\varepsilon_y - b\varepsilon_x}{a(1-b^2)} \tag{9}$$

$$\tau_{xy} = \frac{1}{2a(1+b)}\gamma_{xy} \tag{10}$$

Therefore, using the elastic modulus, Poisson's ratio, and strain data, the real stress can be obtained by stress reconstruction. The elastic modulus and Poisson's ratio were calculated from the DSM in the deformation stage. The starting and ending points of the deformation stage were determined; E_{av} and μ_{av} [22] of the specimen represent the elastic modulus and Poisson's ratio, respectively.

To obtain E_{av} and μ_{av}, the line function of the MatchID analysis system was adopted, and the lines were arranged in the obtained strain nephogram. The required strain values are given by Equations 11–14, as follows,

$$\varepsilon_{ha} = \frac{1}{n}\sum_{i=1}^{n}\varepsilon_{iha} \tag{11}$$

$$\varepsilon_{ea} = \frac{1}{n}\sum_{i=1}^{n}\varepsilon_{iea} \tag{12}$$

$$\varepsilon_{hb} = \frac{1}{n}\sum_{i=1}^{n}\varepsilon_{ihb} \tag{13}$$

$$\varepsilon_{eb} = \frac{1}{n}\sum_{i=1}^{n}\varepsilon_{ieb} \tag{14}$$

where a and b are the start and end marks of the deformation stage, respectively; ε_{ha} and ε_{hb}, and ε_{ea} and ε_{eb} are the average horizontal strains and average vertical strains at the beginnings and ends of the deformation stages, respectively; n is the number of measuring points on the measuring line; ε_{iha} and ε_{ihb}, and ε_{iea} and ε_{ieb} are the horizontal and vertical strains of the measurement point i of the measuring line at the start and end points, respectively.

According to the definition of the elastic modulus and Poisson's ratio, Equations 15 and 16 are obtained as follows,

$$E_{av} = \frac{\sigma_b - \sigma_a}{\varepsilon_{hb} - \varepsilon_{ha}} \tag{15}$$

$$\mu_{av} = \frac{\varepsilon_{eb} - \varepsilon_{ea}}{\varepsilon_{hb} - \varepsilon_{ha}} \tag{16}$$

where σ_a and σ_b are the stress values at the beginning and end of the deformation stage, respectively.

Stress analysis based on DSM

As observed earlier, the elastic deformation time of the OGFC beam specimen is in the range of 0–4.33 s (0–520 frames), and its horizontal and vertical strains are both zeroes because

there is no stress at the beginning. The horizontal and vertical strains at the end of the deformation stage can be obtained by combining the corresponding relationship between time and strain. The strain field is shown in Figure 11.

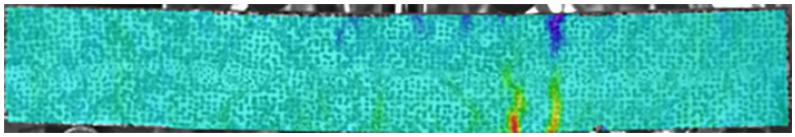

(a) Nephogram of horizontal strain field at the end point

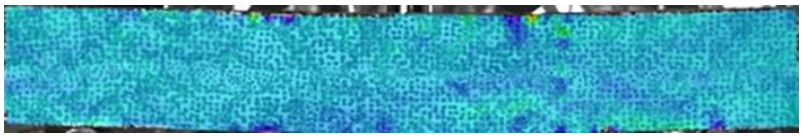

(b) Nephogram of vertical strain field at the end point

Fig. 11 – Nephogram of horizontal strain and vertical strain fields at the end point

Based on the stress condition, a measuring line was placed horizontally along the top and bottom edges of the test surface of the specimen to calculate the average horizontal strain. Further, a measuring line was placed vertically directly below the loading end to calculate the average vertical strain. A total of 51 points from each measuring line were used to obtain the strain change of the test piece, as shown in Figure 12. In Figure 12(a), the fluctuations of the top and bottom measuring lines are located at the middle measurement point, and the fluctuation of the top measuring line is much smaller than that of the bottom. This indicates that the deformation of the test piece occurs between the loading ends. The top is the compressive strain, and the bottom is the tensile strain, which plays a major role in the deformation. In Figure 12(b), the left measuring line is parallel to the right measuring line, exhibiting no significant changes. However, compared with Figure 12(a), vertical strain value is one order of magnitude smaller than the horizontal strain value, thus indicating that the horizontal strain primarily affects the test piece. The irregular fluctuation and peak value of the measuring lines in Figures 12(a) and 12(b) demonstrate the anisotropic characteristics of the OGFC; accordingly, the applicability of DSM to OGFC is verified.

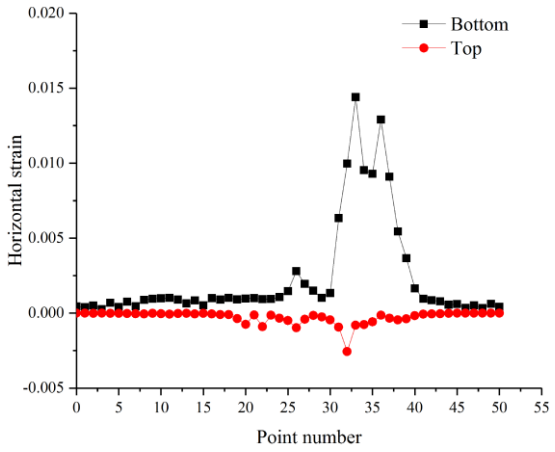

(a) Horizontal strain of the top and bottom measuring lines

Fig. 12 – Horizontal and vertical strains of the measuring lines

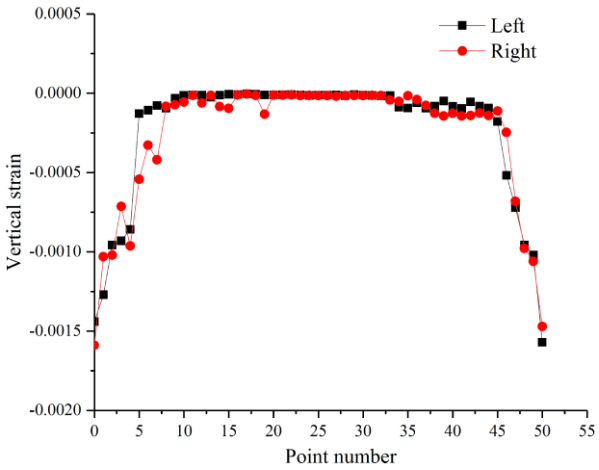

(b) Vertical strain of the measuring lines on the left- and right-sides at the end point

Fig. 12 – Horizontal and vertical strains of the measuring lines

The horizontal strain data of the top and bottom measured points were input in Equation 13, while the vertical strain data of measured points at the loading end were input in Equation 14. The following results were obtained based on calculations: $\varepsilon_{ha} = 0$, $\varepsilon_{ea} = 0$, $e_{hb} = 1.008 \times 10^{-3}$, and $e_{eb} = 2.467 \times 10^{-4}$. The stress value at the beginning and end of the deformation stage was determined based on the time correspondence. The above estimated data were input in Equations 15 and 16. The following results were obtained based on calculations: $E_{av} = 1580$ MPa and $\mu_{av} = 0.24$.

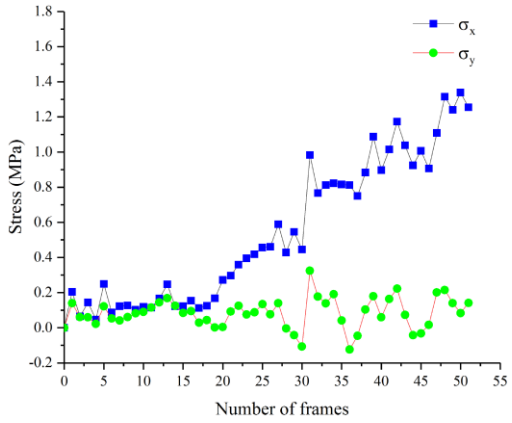

(a) Stress at point 1

Fig. 13 – Horizontal and vertical stress plots as a function of the number of frames

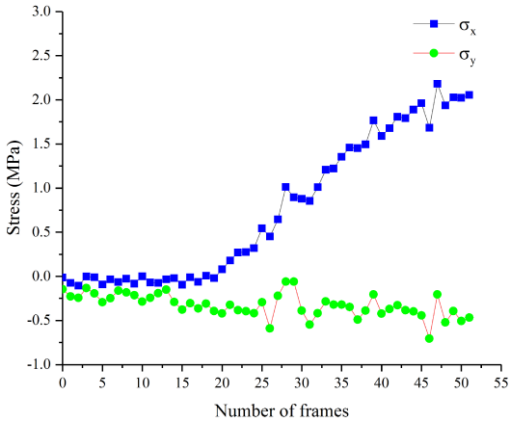

(b) Stress at point 2

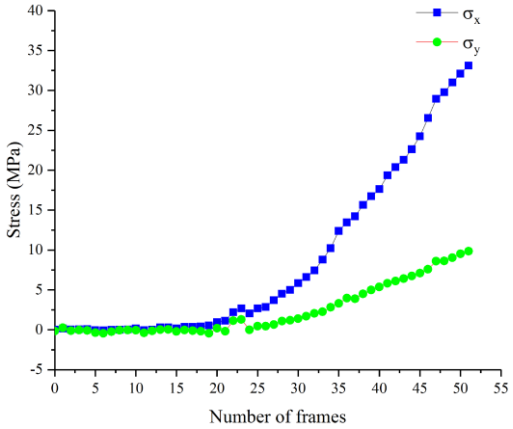

(c) Stress at point

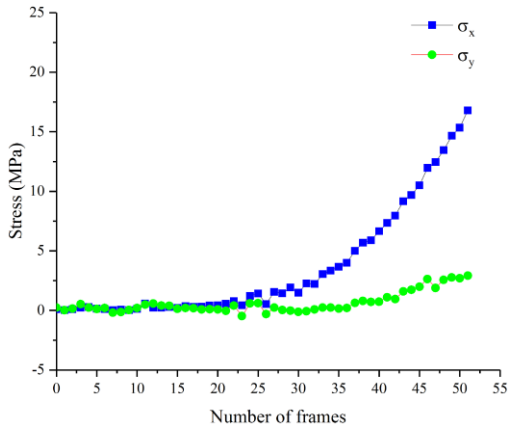

(d) Stress at point 4

Fig. 13 – Horizontal and vertical stress plots as a function of the number of frames

The horizontal and vertical stresses can be obtained by using the four points in Figure 8 as the concerned points for stress reconstruction and by inputting the horizontal and vertical strains and the calculated elastic modulus and Poisson's ratio in the deformation process in Equations 8 and 9 (Figure 13). The positive and negative values represent only the stress direction and not the value. As shown in Figure 13, the horizontal stress of the four points increased significantly compared with the vertical stress, indicating that the horizontal stress primarily affects the

specimen. In addition, by comparing the horizontal stresses at different points, it can be observed that the point order (from large to small stress values) is 3, 4, 2, and 1. In particular, the stress at point 3 is slightly greater than that at point 4 and far greater than those at points 1 and 2. Therefore, point 3 is the first crack point with the highest strain and stress concentration.

Therefore, the results of stress reconstruction are consistent with the macro phenomenon and DSM that verifies the feasibility of stress reconstruction for the analysis of the stress change law of the OGFC.

CONCLUSION

(1) During the four-point bending test of the OGFC, we observed a strain concentration zone in the horizontal strain field at the mortar distribution until a crack occurred at the highest strain concentration.

(2) The quantitative analysis of the strain of the concerned points showed that the strain increased nonlinearly, and the growth was initially slow, then accelerated, and then tended to be linear. Strain responses were disrupted owing to the cracking of the specimen at the strain concentration zone and tended to be stable at a later stage in the noncracking zone.

(3) The stress–strain inversion and stress reconstruction of the DSM confirm that the stress reconstruction is effective and feasible for the analysis of the stress variation law of the OGFC.

ACKNOWLEDGEMENTS

This research was supported by the General Project of Liaoning Provincial Department of Education (No. lnjc202014).

REFERENCES

[1] Qun Y., Guo Z.Y., 2005. Mixture Design of Fire-Retarded OGFC in Road Tunnel. Road Materials and Pavement design, vol. 6(2): 255-268.

[2] Xiong R., Fang J.H., Xu A.H., Guan B.W., Liu Z.Z., 2015. Laboratory Investigation on the Brucite Fiber Reinforced Asphalt Binder and Asphalt Concrete. Construction and building materials, vol. 83: 44-52.

[3] Tanzadeh R., Tanzadeh J., Honarmand M., Tahami S.A. , 2019. Experimental Study on the Effect of Basalt and Glass Fibers on Behavior of Open-graded Friction Course Asphalt Modified with Nano-silica. Construction and building materials, vol. 212:467-475.

[4] Lee L., Charles R., Nicola S., 2016. Stress-Strain Behaviour of Asphalt Concrete in Compression. Procedia structural integrity, vol. 2: 2913-2920.

[5] Pirmohammad S., Shokorlou Y.M., Amani B., 2020. Laboratory Investigations on Fracture Resistance of Asphalt Concretes Reinforced with Carbon and Kenaf Fibers at -15 degrees. Engineering fracture mechanics. vol. 230: 1-19.

[6] Ahmad M; Bairgi B.K.; Khan Z.H.; Tarefder R.A., 2020. Evaluation of the Fracture Resistance of Asphalt Concrete Mixes Including the Effect of Anisotropy. International journal of pavement research and technology, vol. 13(2): 121-128.

[7] Xu H.N., et al., 2019. Investigation of Anisotropic Flow in Asphalt Mixtures Using the X-ray Image Technique: Pore Structure Effect. Road materials and pavement design, vol. 20(3): 491-508.

[8] Huang Y.H., Liu L., Sham F.C., et al., 2010. Optical Strain Gauge vs. Traditional Strain Gauges for Concrete Elasticity Modulus Determination. Optik, vol. 121(18):1635-1641.

[9] Maas H., Hampel U., 2006. Photogrammetric techniques in civil engineering material testing and structure monitoring. Photogrammetric Engineering and Remote Sensing, vol. 72:39-45.

[10] Kovačič B., Kamnik R., Premrov M., Gubeljak N., Predan J., Tišma Z.,2008. Modern deformation measurement techniques and their comparison. Strojniški vestnik, vol. 54:364-371.

[11] Stewart C.M., Garcia E., 2018. Fatigue Crack Growth of a Hot Mix Asphalt Using Digital Image Correlation. International journal of fatigue, vol. 120: 254-266.
[12] Birgisson B., et al., 2009. An Optical Strain Measurement System for Asphalt Mixtures. Materials and structures, vol. 42(4): 427-441.
[13] Teo, T.,2020. 3D deformation measurement of concrete wall using close-range photogrammetry. ISPRS - International Archives of the Photogrammetry, Remote Sensing and Spatial Information Sciences, vol. 43:1175-1179.
[14] Lyons J.S., Liu J., Sutton M.A., 1996. High-temperature Deformation Measurements Using Digital-Image Correlation. Experimental mechanics, vol. 36(1): 64-70.
[15] Hu, Y., Wang, S., Cheng, X., Xu, C., Hao, Q., 2020. Dynamic Deformation Measurement of Specular Surface with Deflectometry and Speckle Digital Image Correlation. Sensors (Basel, Switzerland), vol. 20(5):1278.
[16] Lu H., Cary P.D., 2000. Deformation Measurements by Digital Image Correlation: Implementation of a Second-order Displacement Gradient. Experimental mechanics, vol. 40(4): 393-400.
[17] Šedina J., Pavelka K., Housarová E.,2016. Using of photogrammetric methods for deformation measurements and shape analysis. The 2nd International Conference on Engineering Sciences and Technologies, vol. 2016:859-864.
[18] Yuan Y., et al., 2014. Accurate Displacement Measurement via a Self-adaptive Digital Image Correlation Method based on a Weighted ZNSSD Criterion. Optics and lasers in engineering, vol. 52: 75-85.
[19] Li C., Wang L., Xiao-xiao W., 2017. Crack and Crack Growth Behavior Analysis of Asphalt Mixtures based on the Digital Speckle Correlation Method. Construction and building materials, vol. 147: 227-238.
[20] Xue Q., et al., 2013. Dynamic Behavior of Asphalt Pavement Structure under Temperature-stress Coupled Loading. Applied thermal engineering, vol. 53(1): 1-7.
[21] Underwood B.S., Kim Y.R., 2011. Experimental Investigation into the Multiscale Behaviour of Asphalt Concrete. International journal of pavement engineering. vol. 12: 357-370.
[22] Kumar M., Gaur K.K., Shakher C., 2015. Measurement of Material Constants (Young's Modulus and Poisson's Ratio) of Polypropylene Using Digital Speckle Pattern Interferometry (DSPI). Journal of the Japanese Society for Experimental Mechanics, vol. 15 (Special_Issue): s87-s91.

CIVIL ENGINEERING JOURNAL

Article no. 21

THE CIVIL ENGINEERING JOURNAL 2-2022

VALUING THE URBAN SPACE ACCORDING TO THE REHABILITATION OF GREEN SPACES

Tahri Djeloule

University of Mohamed Boudiaf M'sila, Institute of Urban Technology Management, Algeria; djeloule.tahri@univ-msila.dz

ABSTRACT

The nations of the ancient world paid special attention to the vegetation cover and made it units of different dimensions and different arrangements, and various types of life sciences, engineering, and art were used for these units. Nature, fresh air, and spacious spaces.

Algerian cities in general and their residential streets, in particular, know many aspects of deterioration, especially those associated with the preparation of external areas, foremost of which is the apparent lack of creation of green spaces within urban areas.

El Bayadh city, like others Algerians cities, complains of most of its residential streets of a complete absence of prepared green spaces, while the remaining streets contain green spaces in a deteriorating condition.

KEYWORDS

Urban rehabilitation, Green spaces, Urban spaces, Urban ecology

INTRODUCTION

Most of those interested in the city and its organization agree that it is a distinct style of social life, as it is the vivid image of its residents and the place of coexistence in which the various social, economic, and entertainment relationships interact.

It is noted that parks and green spaces are an important component of urban infrastructure, and sometimes their implementation may be delayed or canceled due to the need for land for other facilities, although green spaces of all kinds are considered an outlet that is equivalent to the rest of the city's components, including residential buildings, industrial areas, markets, streets, and squares. Green spaces reduce noise, as they can absorb 20-30% of the noise of machinery and help in a positive effect on human health and nerves. Trees also play an important role in providing shade for animals and humans, and this reduces the use of air conditioners.

It is known that the limited places of trees and green spaces, and congestion in some cities and villages are random, so that people suffer from high pollution in them, to the point that life becomes seriously threatened. The situation is almost completely changed by the presence of green spaces, where trees, vegetation, and green spaces are built. By supp lying the city air with the oxygen element necessary for the life of living organisms, it absorbs carbon dioxide for use in its photosynthesis. In other words, "a person (one person) needs 12 m3 of air per day and requires a green surface of 150 M2 to compensate for the oxygen consumed by living organisms and various combustion processes. However, we see the opposite in most third-world countries and Algeria is one of these countries on

the path of growth, which has witnessed great urban development in recent years, accompanied by a clear shortage in terms of the presence of green spaces.
The city of El Bayadh, like other Algerian cities, also suffers from several problems related to green spaces as a result of the accelerated urban growth, which resulted in negative effects on various economic, social, environmental, and even health aspects for the users of these areas, which affected the human psyche, comfortable living, and aesthetic image. The most important of these problems are:

- The numerical and cadastral shortage of these areas.
- The absence of an aesthetic visual image within the urban sphere.
- Lack of planning, misuse, and management.
- Limited user culture and lack of environmental awareness in the population.

In order to understand and know the various causes that have led to the deterioration of green spaces in preparation for providing solutions that help us improve the status of urban areas within the residential complexes, we raised the following questions:

- What are the most important reasons that led to the deterioration of green spaces?
- Was the design considered during the design of the planning standards for green spaces and their suitability for the area's specificity?
- Is there any involvement of the citizen in managing and monitoring green spaces in order to create spaces that fit the social characteristics of the city's residents?

And in order to be familiar with the topic in its various aspects, to direct the research according to a specific and purposeful path, and to answer the questions raised in the problem, we decided to put forward the following hypotheses:

Managing hypothesis:

- Lack of the level and quality of preparation and failure to consider the principles of designing green spaces has had a negative impact on the urban sphere.
- the hypothesis's schematic nature:
- The absence of a planning aspect that is consistent with the specificity of the region has led to the deterioration of green spaces, and its negative reflection on the visual image and the urban sphere of the city.
- The hypothesis of a cultural character:
- The residents' lack of urban sense toward green spaces caused the deterioration of their current situation.

Each study has a goal that it aspires to as a mechanism to uncover the mystery sweeping it. In the midst of these research principles, the study included the following objectives:

The main objective:

- Attempting to upgrade the urban sphere of the city by improving and rehabilitating green spaces.

Partial goals:

- Work to find the real causes that led to the deterioration of green spaces, and try to reduce them to improve the visual image of the city.

- Spreading environmental awareness among the population and trying to involve the citizen in running and making decisions and designing projects, especially those related to the preparation and green spaces within the urban sphere.

METHODS

Green space:

The term green spaces are considered to be a recent creation, as it was used for the first time in the French real estate directive law in 1967 AD, as the first article of it defined it as a space devoted to barns and gardens in urban areas. [1].
As for the Algerian legislator, despite his use of this term in several laws, he did not know green areas except in accordance with Article 04 of Law No. 07/06. [2]. Relating to the management, development and protection of green spaces as: areas or part of urban areas that are not built, that are totally or partly covered by plants, and that are located within urban areas or areas to be built that are the subject of classification. [3] What follows from this definition is the consideration of green spaces as national, public, economic properties. Because they require classification in order to give them the character of green space. In the sense of violation, every green space is not subject to classification that comes out of the framework of the implementation of Law No. 06/07.

Historical Approaches to Green Spaces:

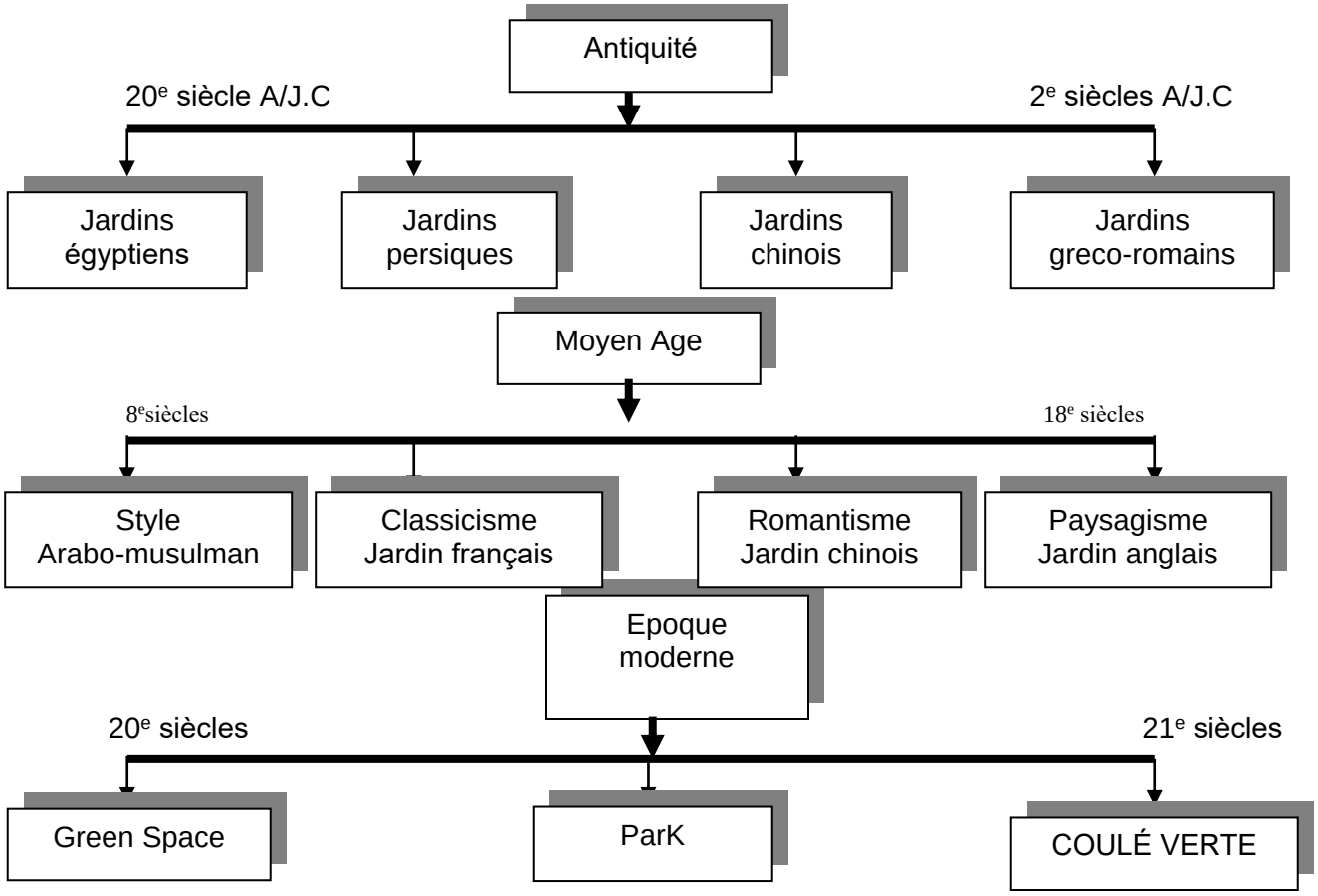

Fig. 1- Restructuring historical approaches to green spaces.

The status of green spaces in Algeria:

Thanks to the Islamic civilization. The Arabs returned and settled on this difficult land to build cities and gardens. Because of the desert and the nomadic Bedouins. The Arabs were not directed to create gardens. And it is not like their inherited traditions. In Algeria this urbanization and the inherited tradition of building cities with its gardens. What remains for us today. This does not reflect the nomadic people living in cities and villages. This is what is considered a break in the rhythm of our green spaces at the level of each region in our urban areas. We begin to embody Algerian traditions, in the year 1970 AD and in particular and the authority. The public is empowered to remove trees in our urban areas. Wipe out the lungs of cities and villages. For the benefit of the ugly concrete encroachment. What led to an urban landscape that does not provide any connection to social communication. What led to the lack of green spaces. Today is one of our priorities in the field of landscaping. We can say that our cities will be threatened with deterioration and division in the event that we continue uprooting trees in order to build a place or expand the building, despite the doubling demographic growth in Jazaa by the end of the year 1970 AD, the legislation and laws that govern

green spaces in the Algerian urban environment have not changed. On the other hand, these spaces have become almost non-existent. And the amount allocated for their management has become completely absent. We did not say that it is not present. They are given to unqualified achievement institutions in preparing the spaces. Green. And it is led by architects in the building. Those who do not have any knowledge about plants and how to use them. Even on the technology of planting and tree planting.

In the spontaneous period of city expansion. We notice the rural displacement. The return of private green spaces and horticultural gardens. These two types of green spaces are added to colonial green spaces. ”But what is known as the great neglect and the almost total lack of interest in the reconstruction directorates, which also follow the absence of responsibility Peri-urban green spaces. The latter is considered to create parks and gardens in urban areas. Which are a good vital component and the quality of the urban environment. It is secondary compared to the basic function that it provides. Movement. Housing and trade. Algerian urban circles are currently suffering from a green deficit because Even our capital, compared to Paris, which amounted to 6 M2. wooded areas per inhabitant, without forests, and in Amsterdam, which is estimated at 36 M2., London, estimated at 45 M2., designated for green spaces in urban areas, which are exploited by 3 million inhabitants per week. Talking about our cities, which are distinguished by not continuing to build without greening, and in the absence of a green urban policy. What the National Economic and Social Council indicated. CNES. In recommendations in the form of a report put at disposal for environmental interests. At the community level. C. Local. Rehabilitation of the municipality according to its traditional activities. In order to protect the framework of life for the citizen in the field of green spaces and for the need for greenness. Which has become a necessity for the citizen who aspires to improve his life framework and see a comfortable environment with an appropriate design. [4]

The creation of landscapes. Accompanied by the creation of green spaces and spaces for hiking and entertainment in Algeria. It became a priority for local groups at the beginning of the 20th century AD due to an unavoidable urban structure. For the success of the large lines of the sustainable development strategy for tourism. In order to implement the presidential program and Follow-up by the Ministry of Tourism, which prepared an amount of nearly one billion dollars at the end of 2013 AD. In order to attract foreign tourists who left Algeria due to the deteriorating state of our cities, without any logical presence to prepare the landscapes with green spaces that are prepared temporarily for the visit of the President or Minister.

Tab. 1 -:Distribution of green spaces among the states in 1995.

THE STATE	ALGERIA	OM AL-BOUAGI	CONSTANTINE	MASCARA	ORAN, TIPAZA, AIN DEFLA	JIJEL	TIARET	OTHER STATES
/	20.6	8.1	6.8	6.7	5.4	4.7	3.7	40.6

Varieties for green space in Algeria:

Green areas within cities are classified according to the number of inhabitants in the area or street into:

Green spaces accompanying residential complexes:

- This kind of greenery is given a Share estimated at : 6.8m^2 / inhabitant.

- Green spaces within neighborhoods: estimated value: 4 M^2 / inhabitant.

- Peri-urban green spaces: estimated: 10 m^2 / inhabitant.
- Row trees.

These three items were distributed as follows:

The green spaces accompanying the residential compounds: which contain three elements as follows:

Wooded residential areas: ..... 1.8 m^2 / inhabitant.

Play spaces consist of areas divided as follows:

Gardens for children: less than 04 years ..... 0.20 m^2 / inhabitant.

Children's gardens: from 04 to 10 years: ..... 0.80 m^2 / inhabitant.

Sand areas for free play: ..... 0.50 m^2 / inhabitant.

Play areas: children over 10 years old: ..... 3.00 m^2 / inhabitants.

Free spaces coordinated in the form of spaces for recreation and leisure: .0.50 m^2 / inhabitant.

-Grand total: ..... 6.80 m^2 / inhabitants [5].

Green spaces within streets

It consists of public gardens, squares, and small gardens that have been completed

Allocation of share: 4.00 m^2 / inhabitant.

These two types of green spaces have been present in Algerian cities since the colonization. It was recommended by the ministerial department to preserve this type of green space and try to integrate it into the new urban fabric.

The planning of green spaces must consider the physical characteristics, the climate, the region, and which are in line with the environmental specificity. The summary of these types of green spaces examined together was estimated at 10.80 m^2 / inhabitant. For urban green spaces.

Peri-urban green spaces:

contain barns and hiking forests.

Barns and Picnic Forests: ....10.00m^2 / inhabitant.

Barns and hiking forests are placed for balance and as one of the most important and distinguished varieties. The site is chosen on a specially prepared base. It comes according to the shape of the site and the distance, the degree of the frequency with it, and the roads leading to it. All these numbers are distributed over the circle. Of lower standards that provide indications for designating public green spaces.

Row trees or wooded rows:

Which contains all the wooded formations found along roads and highways and other types of roads in their parts located in urban areas and adjacent to the city, or what is expressed as the green belt that connects to the main roads and maybe a link between countries and regions or a protective belt to isolate urban areas from sources of pollution and noise, as the green belt acts as a source of winds .[6].

Tab. 2 - Green space standards. "Unitary needs".

N°	Designation Of Green Areas Varieties	Individual Needs
01	Green spaces in the residential neighborhood	6.8m² / inhabitant
02	Green spaces within neighborhoods	4m² / inhabitant
03	Green spaces outside the city	10m² / inhabitant
	Total green space standards	20.8 m² / inhabitant
04	Row trees: Inside the urban center In the semi-urban center	01trees every 05 meters 01trees every 10 meters

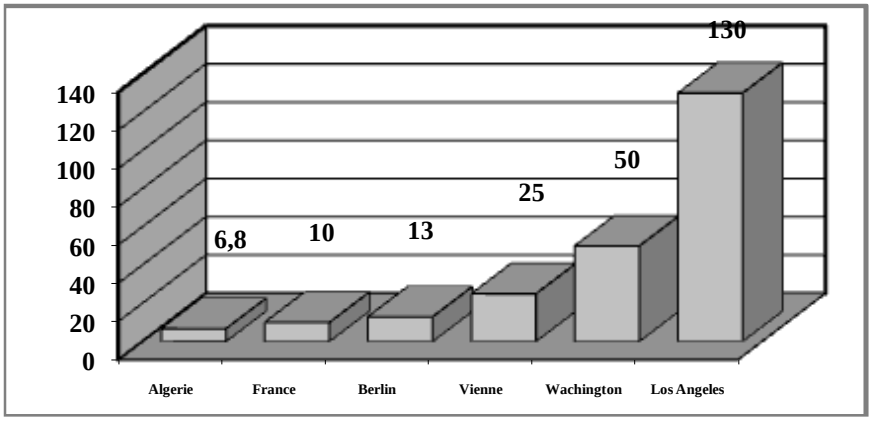

Fig. 2- Percentage of green spaces in Algeria and some countries of the world.

Laws regulating green spaces in Algeria:

It implemented Ministerial Instruction No. 29256 dated 11/29/1983, which included the upgrade and creation of green spaces. Then several laws were issued referring to green spaces .[7].
First: Law No. 90/25 containing the real estate directiv. [8].
It is considered the first law to determine the technical strength of real estate by classifying it and determining the provisions that apply to each category, dividing the property into private and state property and property belonging to the state, state, and municipality, and determining the last types to the following: Agricultural lands with an agricultural destination Pastoral lands. Desert lands. Durable and sustainable lands. Forestlands and areas with protected sites. As for the provisions related to the regulation of green spaces, they are regulated by Law No. 90/29 related to planning and reconstruction and Law No. 90/30. Law 90/29 stipulates in Article 11 of it that the preparation and reconstruction tools determine the basic directions for preparing the lands. It also sets the directions

and expectations of reconstruction and specifies in particular the conditions that allow the protection of sensitive areas, sites, and green spaces. In Article 31 of the same law, the legislator asserts that the land occupation plan is determined in detail within the framework of the directives of the master plan for development and reconstruction, the rights of land use and construction, and specifies the locations of public spaces and green spaces. This is also confirmed by Executive Decree No. 91/178. Which specifies the procedures for preparing a land occupation plan in Article 08 thereof. Planning green spaces is a process that cannot be separated from the context of the overall planning of the city due to its importance in maintaining the environmental balance.

What is to be noted about the provisions contained in the Law of Development and Reconstruction: That the law obligated every municipality to cover its territory with reconstruction plans. However, the reality indicates that most of the municipalities until recently did not return these plans, and therefore the reconstruction operations were carried out in accordance with the general rules for reconstruction. Executive No. 175/91, meaning that the absence of these two tools means the absence of green spaces of all kinds in cities and neighborhoods. [9].

Law No. 30/90 containing national properties: This law is considered in Article 16 thereof. Green spaces are public national properties. It defines two types of them which are prepared gardens and public gardens, without knowing any of them. They may be subordinate to the state, state, or municipality, because the text is general, and in order for these gardens and orchards to be established, they must first be included in the national public property by classification.

Executive Decree No. 91/454 issued on 11/23/1991 defines the conditions for managing private and public properties belonging to the state by classifying green spaces. This decree was repealed by Executive Decree No. 427/12.

Law No. 03/10 was issued on 07/19/2003. [10]. Relating to the protection of the environment in the context of sustainable development, this law is included

A single text related to green spaces within the sixth chapter on the protection of the living environment is the text of Article 65 thereof, which states: Without prejudice to the legislative provisions in force related to urbanization and considering environmental protection considerations. Small forests, public parks, recreational spaces, and each area are classified It has a collective benefit that contributes to improving the living framework and determines the modalities of this classification through regulation. It is noticeable that the executive decree has not been issued and this article has been explicitly canceled according to Law No. 07/06 related to the management of green spaces.

Law No. 07/06. Dated 05/13/2007 related to managing, protecting, and valuing green spaces and it is the first law related to green spaces. Hence, the legislator obligated every architectural or urban production to establish green spaces, considering the character of the site and the scenes that should be preserved and valued. And the varieties and types of plants and the preservation of the architectural heritage of the region. He also stressed the need to consider the allocation of green space sites within urban areas when preparing or reviewing construction tools according to the standards of each city or urban group. All this is in line with the green space management plans. The per capita share of the area of recreational areas in large cities has been estimated to be between 10 to 15 meters as an acceptable limit, as these spaces are of utmost importance to the psyche of urban residents and their daily activities. [11] Article 02 of it stipulates that the management, protection, and development of green spaces in the context of sustainable development, in particular, require the following: Improving the urban living environment.

 Maintaining and improving the quality of existing urban green spaces
 Upgrade the creation of green spaces of every kind.
 Upgrading the expansion of green areas in relation to the built areas.
 It is mandatory to include green spaces in every building project that is covered by public and private urban and architectural studies. Article 29: The public or private achievement is required upon completion of each

A green space must consider, in order to achieve the homogeneity and quality of the landscape, the following factors:

The character of the site, the views that should be preserved and valued or those that should be hidden, the land resources, the plant species and varieties of the area concerned the architectural heritage of the area or sub-district, agreements, and obstacles related to the neighborhood, the water system, the right of crossing, the separation of boundaries, the rows of the road network, the leveling of lands, afforestation and the network of underground canals And underground electrical installations.

Executive Decree No. 67-09 of Safar 11, 1430, corresponding to February 7, 2009, defines the nominal list of urban trees and row trees.

Executive Decree No. 101/09 issued on 03/10/2009 specifies the organization and modalities for granting the National Award for the Green City.

Restrictive measures to protect green spaces:

The privacy of green spaces justifies the preservation of their components by means of restraining protection against various attacks. Therefore, physical assault on green spaces has been criminalized at the level of unlawful behavior against this property:

1. Criminalization of physical assault on green spaces:

Pursuant to the provisions of Article 40 of Law 06/07, the aforementioned person shall be punished with a penalty of five hundred thousand dinars to one million dinars who totally or partially demolishing a green space with the intention to acquire the place and direct it to another activity. F. A penalty of fewer than 03 months to a year applies to anyone who causes the degradation of green areas or uprooting of shrubs. [12].

2. Criminalization of illegal disposition of green spaces:

Green spaces of all kinds, like other open spaces, may be subject to illegal actions, especially with the phenomenon of occupying the public domain without capacity. The legislator has subjected the exploitation of parks to the necessity of obtaining prior licenses from the will administration. Any change in the green space or every occupation thereof shall be punished. He violates the laws and regulations in force, with imprisonment from six months to a year, and a fine from fifty thousand to one hundred thousand dinars, and the places are returned to what they were.

As for the person who wears billboards in green spaces without the knowledge and approval of the concerned administration, he is subject to a prison sentence of two to four months, and a fine of ten thousand to twenty thousand dinars, which is the same penalty applied to every person seeking to cut down trees in urban areas without a prior permit. In order to strengthen these procedures and work to implement and implement them on the ground, the law authorizes some qualified employees the authority to investigate and search for crimes. It gave them the capacity for judicial seizure. These violations are examined according to records sent to the public prosecutor. The criminal judge has broad powers with regard to measures that can be adjudicated in addition to the original penalty.

Obstacles to creating green spaces in Algerian legislation:

The protection of green spaces has become these days one of the most important priorities that countries set in their programs, policies, and plans. They allocate important funds for them and recruit enormous human resources for them. But this care for green spaces differs in different cities. It appears prominent in some areas of the country. Throughout the number of prepared and protected spaces, they appear dim in other cities, as they notice a fading color due to the loss of green in them. This is due to the uneven efficacy of the protection mechanisms adopted by the state. The process of protecting green spaces faces many difficulties and negative repercussions stemming mainly from the planning stage of these spaces' deficiencies. Good and organized planning is one of the elements of the plan's success in achieving its aspirations. Poor urban planning is also considered one of the most important shortcomings of the planning situation besides these Areas with his adoption of chaotic buildings threatening green spaces. [13].

Difficulty controlling the real estate field:

Controlling the real estate field is the basis of the preparation process, as it is the framework on which local groups undertake the preparation operations. Through it, what has been programmed for, for example, urban planning is implemented. And what the example assumes in terms of allocating land may often conflict with the boundaries of real estate that are constructed. For different owners. This calls for the management to intervene in order to resist the monopoly of land by acquiring it and preparing it so that it is suitable for construction. However, in most cases, the administration is unable to follow this policy due to the real estate difficulties it faces. As the transfer of ownership often occurs from one party to another in a way. It is difficult to define the real owner; therefore, these lands must be removed from the stalemate and the credibility of the real estate registry, its unity and the homogeneity of its components must be sought. [14].

Cluttered buildings threaten green spaces.

Despite the multiplicity of laws that explicitly stated the construction permit and the necessity to respect this procedure. However, the phenomenon of chaotic construction remained in place. Neither the procedures nor the restraining arrangements were able to prevent this type of construction that harms our cities and obscures their aesthetics. It tries to reduce the often-messy structures built on undeveloped lands that can be designated as green spaces.

The inability to deter the citizen:

The environmental dimension represents an important axis in the preparation and reconstruction process. Therefore, emphasis has been placed on effective tools to reduce the abuses that exist in green spaces. In addition to the need to provide supervisors, this is not sufficient. No matter how intense the monitoring is, the citizen, if he is not aware of the importance of spaces. Green is in its living environment, and its role in bringing closer and strengthening social relations and combating air pollution, it will not improve its use and exploitation, which leads to its extinction. [15].
or pictures should be clear black and white prints. Supply the best quality illustrations or pictures possible.

RESULTS AND DISCUSSION

Introducing the EL bayadh City:

Historical overview:

EL BAYADH Department rose to a state during the administrative division of 1984, as it was previously affiliated with a SAIDA state, and it is considered one of the oldest departments, it was called" GERRY VILLE."[16] .Relative to a French officer.

As for the EL BAYADH as a region, its history can be traced back to six thousand years of history and archeology scholars. This is embodied by the stone drawings extending from the north and south of the desert Atlas, as well as the spread of prehistoric human cemeteries, especially in the regions of "Karakada" and "brizina", in addition to the palaces located there.

Popular narratives differed as to the significance of the name of the eggs, but the most likely analysis of the name is due to the presence of white soil that was used to wash white clothes, such as bernous, and this soil is called “the BAYADH.”

Location and space:

The state of El Bayadh is located in the southwest of Algeria and is one of the states of the high plateaus, with an altitude of 1400 meters above sea level, interspersed with mountains such as "Boungta" and "Bouderga". The city’s topography combines three aspects:

High plateaus: to the north, the desert atlas: in the center, the desert: to the south

The location of the wilaya makes it a steppe region in the first place.

Astronomical site:

Al-Bayadh city is located astronomically between latitude (40-33) north and longitude (00-01) to the east.

Administrative site:

El Bayadh is located in the southwest of Algeria, bordered by:

On the north: Saida, Tiaret, Sidi Bel Abbas, south: Adrar, east: Laghouat, Ghardaia. West: Naama, Bashar.

Area:

The state of El Bayadh occupies an area of 71,697 km^2 and represents 3% of the area of Algeria, made up of 08 departments and 22 municipalities.

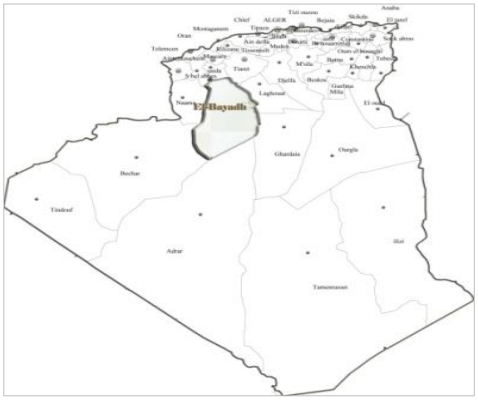

Fig. 3 - El Bayadh State website.

Natural study:

- The climate:

The region is generally characterized by a semi-arid climate, which is very harsh, cold in winters and mild in summer.

- Temperature:

It is considered one of the most important influencing climatic elements as it enables us to know and choose the building materials used and to use mechanical means such as "cooling means". Therefore, the city knows different temperatures according to the seasons of the year.

Tab. 3 - shows the temperature changes.

Months	January	February	March	April	Mai	June	July	August	September	October	November	December
Maximum temperature	4,83	11	12,5	13	27	32	34	34	18	20	13	11,2
Minimum temperature	4,24	5,4	5,72	6,7	23	27	30,2	29	15,2	16	10,6	4,58

According to Table 3, we note that the month of January is the coldest with an estimate of 4.10 degrees and the month of July is the warmest with an estimate of 34 degrees Celsius, which requires the use of devices to humidify the air. Unusually, the city of El-Bayadh is known to be very cold in winter and summer. This confirms the city's lack of green spaces that It is considered as an average temperature. After a study carried out by some researchers on the oasis of Laghouat, on the impact of the lack of green areas on the temperature, and after the lack of palm oases in the city of Laghouat between 1984 and 2015, the average maximum temperature recorded in August increased from 30 ° This is due to the retreat of palm oases that provided a microclimate thanks to the shade of the palms, trees, and watering channels that ensured the adjustment of the high temperature.[17].

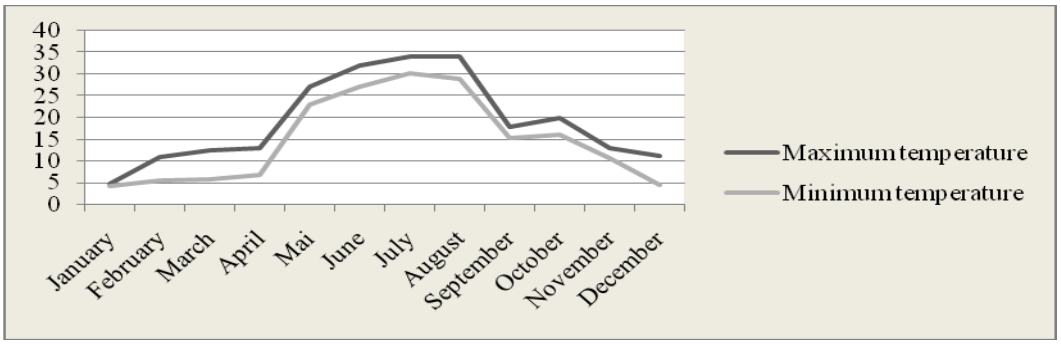

Fig. 4 - shows the temperature changes.

PRECIPITATIONS:

Is a precipitation factor climatically specific agricultural activities sometimes be a major factor in the soil destruction, and is also considered specific to the size of networks (VRD). According to meteorology, the city eggs know the amount of precipitation is sandwiched between 200-300mm. During the year, there is frequent precipitation in the following months: January Avril, and December.

Vegetation:

The city of EL Bayadh belongs to the cities of high plateaus and is characterized by a semi-arid flank. Therefore, most of the existing plants are astropic plants such as the Allied and Artemisia, but they are in constant decline due to random grazing and the desertification factor.

Green spaces in the city of El Bayadh :

El-Bayadh City lacks green spaces within the urban fabric, as its percentage is estimated at 0.56%, or 4.67 hectares, while those destined for recreation do not exceed 0.45%. Of the total area of the city consumes an area of 3.72 hectares .

It can be said that all the green spaces that cover the city share the same problems:

- The recorded deficit in these areas at the city level (numerical and cadastral shortage) at the rate of two parks for the entire city, especially since the required rate per person from public parks within the residential neighborhood is about 0.6 m ^{2} / person, meaning that the recorded deficiency area in the city is about 47150.57 m ^{2}.
- An imbalance in its distribution in the city, where it serves a small population.
- Poor configuration and design quality.
- The lack of wooded area means that most of it are paved.
- The lack of covered areas, as well as the absence of their own furniture (kiosks, games.) .
- Lack of maintenance.

In order to understand the state of green spaces in the city, we must study Freedom Park as the only outlet for residents in the city, as an example of urban gardens, and in order to see the true reality of green spaces within the city of El Bayadh.

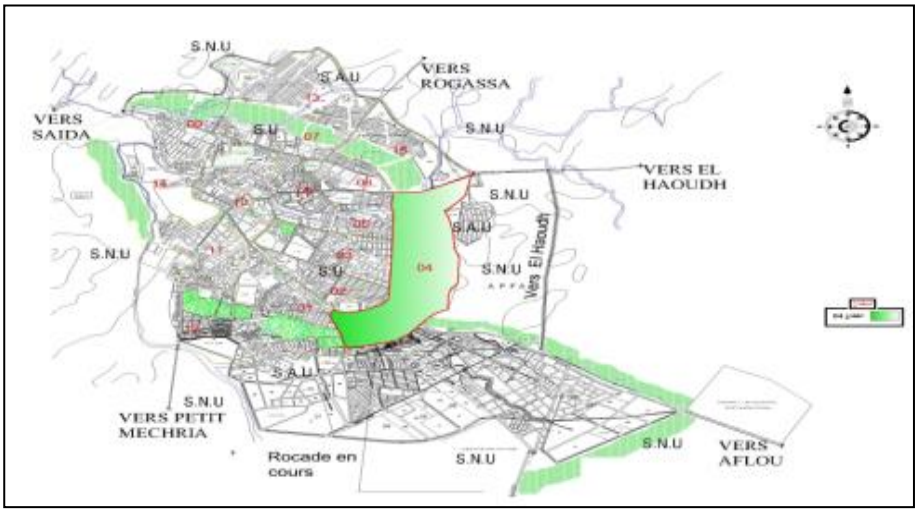

Fig. 5 - Distribution of green spaces in El Bayadh City.

Parks and public gardens in El Bayadh City,*The garden park*:

In order to revive the public spaces directed to entertainment and entertainment in the city of El bayadh. A financial envelope of 9.5 million Algerian dinars has been set aside for the rehabilitation work of the garden park. This process falls within the framework of the municipality's development plan for the year 2011, through its rehabilitation and equipping it with a number of entertainment and entertainment facilities, in addition to connecting it to the electrical network and exploiting the well located in the same garden. In order to water the plants, in addition to supplying them with an additional share of various trees, according to the head of the Municipal People's Council.

It should be noted that this park was inaugurated on May 20, 2011, but soon it was closed again after the end of the summer period so that the recorded deficit in recreational green spaces returned again.

Site:

The park is located in the southern side of the city of El Bayadh. It is distinguished by its strategic location, being located near the city center, about 450 m. In addition to its alignment with some of the important secondary roads in the city.

Situation:

The park is limited by a group of buildings of various functions and engineering, separated from it by a series of important roads from its three sides, so we find from: The northern side of the park: the court - the retirement fund.

The eastern side of the park: an urban façade consisting of three-story buildings - a temporary passenger terminal.

The western and southern sides of the park: an urban façade consisting of four-story buildings - the residence of the National Gendarmerie.

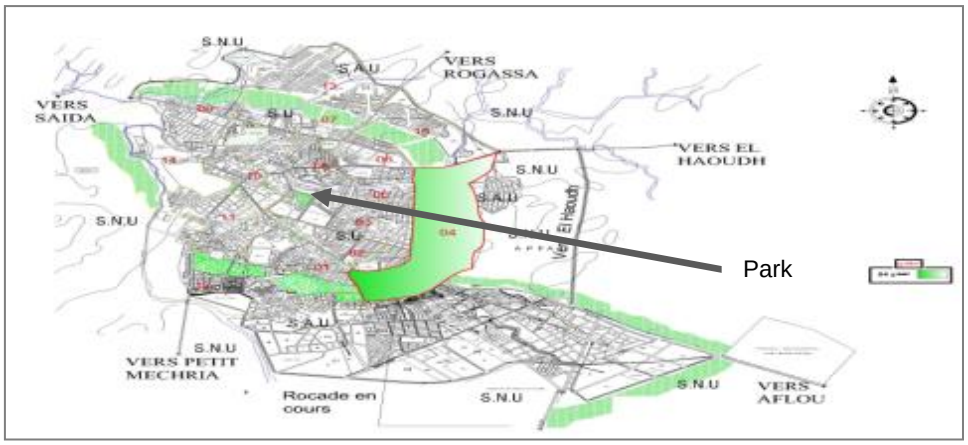

Fig. 6.- Location of Freedom Park in relation to the city of El bayadh.

Through the plan, we notice that the location of the Freedom Park was a strategic location compared to the rest of the green spaces within the city, as it came in the city center, which makes it exploited by all of the city's residents and serves the largest possible group in the city.

Department of Use (its effect on the city).

Based on the area of the park and its location in the city, we have drawn a usage cycle.

Existing tree varieties:

For this purpose, we dealt with the enumeration of tree species in the garden by studying each species separately.

- *The eucalyptus tree* - It is known for its effective role in the ecological balance, in addition to its rapid growth and distinctive size, so that it quickly forms a fence. To protect the field from external winds (cold – hot), the chart below shows the locations of its distribution in the garden.
- *Washingtonia tree* - The same palm leaves (palm fronds) are round in shape and green in color, with an average foot of 1.5 m .Addition of its decorative (cosmetic) property.
- *False pepper tree* - Slender evergreen tree, the compound feathery leaf includes about 25 leaves, it has a distinct aromatic smell, it is sensitive to cold. It is known for its overhanging branches that hinder the movement of pedestrians on the sidewalk, in addition to its irregular shapes in the absence of regular maintenance.
- *Acacia tree* - A perennial, fast-growing, evergreen shrub with a broad crown and a multi-branching stem, reaching a length of 3-7 meters. It is known for its strong resilience to the salinity of the soil and its predominantly dryness due to the lack of rain and its scarcity, and it is called “thistle” or “ginkgo”.

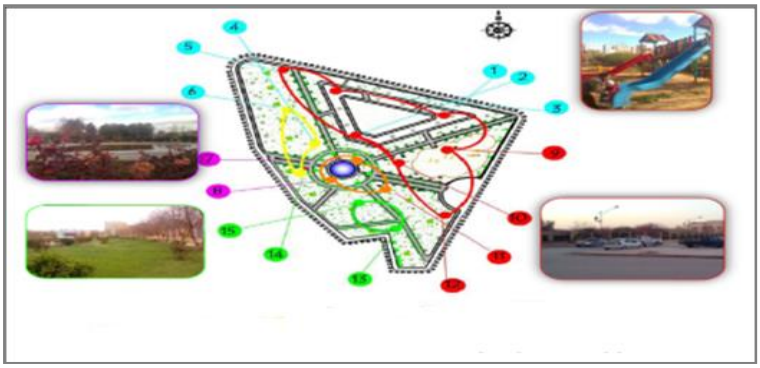

Fig. 7 - Garden noise intensity.

The lack of experience of some members of the technical staff in implementing agricultural service and maintenance operations, and is reflected in the status of forestation services, so we often notice the lack of pruning trees that are most in need of pruning and sometimes unfair pruning of some trees. This is confirmed by the inappropriate selection of plants in residential green spaces and

the inadequacy of the soil. A lot of residential green spaces are allocated for planting and spreading herbs.

The simple structure and preparation of the park do not match the variety and excitement required by such facilities.

The difference in the time periods for planting trees in the garden, in addition to their inappropriate orientation, negatively affected the process of producing shade, breaking the intensity of the wind and reducing its speed.

The ill-considered choice of the existing tree species makes the garden more vulnerable to wind and sunlight throughout the winter and fall seasons.

It is noticed that false pepper trees have lost their greenness as a result of frost waves due to lack of watering and periodic maintenance, especially since it is the most abundant tree in the garden.

The random and uneven distribution of trees in the garden and the lack of diversity in their use, in addition to not considering at least 3 m of the corridors to grow false peppers on the edges of the paths to avoid branches that hinder movement.

The park is surrounded on the north and east sides by two main roads and the absence of anti-external noise barriers, whether natural or artificial, on these two sides allows the passage of high sound waves resulting from mechanical movement in addition to the noise generated by users in the middle of the park.

CONCLUSIONS

El-Bayadh city lacks green spaces within the urban fabric, as its percentage is estimated at 0.56%, or 4.67 hectares, while those destined for recreation do not exceed 0.45% of the total area of the city, consuming an area of 3.72 hectares.

According to the hypotheses put forward at the beginning of our study, we presented the most important problems of green spaces in this intervention in three important aspects:

Management side:

Each institution holds the other responsible for the degradation and lack of green spaces. The inability of city governing bodies, especially the municipality, to create and establish effective and efficient management rules and mechanisms that guarantee a minimum of interest in green spaces.

Schematic aspect:

After an analytical study of green spaces at the general level of the city, we concluded that there is a clear shortage of these places on several levels, the most important of which are:

- The areal and numerical shortage of green spaces compared to the number of city streets and the number of residents.
- Absence of green floors.
- Lack of maintenance work and absence of protective barriers.
- Poor selection of plant and tree varieties.
- Lack of diversity is used tree varieties.
- The cultural awareness aspect:
- After analyzing the form addressed to the users of these spaces, it is found:

- The absence of a general program for awareness and information at the municipality level, as it is responsible for running these spaces.
- The absence of the role of association movements at the level of the city's streets in sensitizing the importance of parks and gardens.
- The user's personal and personal limits are dominant, as the responsibility does not exceed the limits of his personal benefits.

REFERENCES

[1] Toufik, a; 2012.approach to urban public spaces. case of the new city ali mendjeli. Memoire de magister, university mentouri.constantine., P 49.
[2] The Official Gazette; 2007.Article 34 of Law 7/6, Algeria,.
[3] Mustafa Aida; The role of green spaces in embodying sustainable urban development, Faculty of Law and Political Science, 2019.Journal of Studies and Research, Arab Journal of Humanities and Social Sciences, University of Blida 02,. p 159- 163
[4] Ammar, a; 2011 .green spaces has skikda. proposal for the development of the peri-urban zone of mouadher in green grid. Memoire magister., University badji mokhtar- faculte des sciences de la terre, annaba, ,P 50.
[5] Adra, a. K; 2011.urban public green space from Historicism to normativity case of Constantine, These de doctorat es-science , Department of architecture and town planning, Constantine, , P 183.
[6] Azzouzi, a; 2013.green spaces in skikda. Journal of man and society university of tebessa, , p. 95.
[7] Bekkouche, a. 2012. (n.d.); green spaces in oran, a component of the Mediterranean identity. Memoire magister, Oran, ,P 181.
[8] The Algerian Official JOURNAL; 1990.Law No. 29-90, Algeria..
[9] Hisham Al-Abed Al-Derawi; 2013.Obstacles to providing open areas and green spaces in the structural plans in the Gaza Strip and ways to develop them, Master Note in Architectural Engineering, Gaza, College of Engineering, Islamic University, Palestine,. p 34
[10] The Official JOURNAL; 2003.Law No. 03/10. Environmental protection within the framework of sustainable development, Algeria.p 53.
[11] Ali Salem Al-Shawawrah; 2012.Urban and rural urban planning, Amman, Maisarah House for Publishing and Distribution, First Edition. Jordan,. P 385.
[12] Dr. Dawar Jamila; 2019.Green spaces in Algeria: shortcomings and challenges, Faculty of Law and Political Science, University of Mohamed El Bashir Brahimi. Bordj Bou Arreridj. Journal of Legal and Social Sciences, Zian Ashour University, Djelfa, Issue 14,. P 14.
[13] Al-Jassi Samah; 2006.Protect green areas. Master's Memorandum, Faculty of Law and Political Science, Tunis,. P 06.
[14] Boris Zidane; 2000.Documentation relationship with urban activity. Authentic Magazine. Issue 1,. P 34.
[15] Bin Saad Haddah; 2004.Environmental protection as a restriction on the right to real property. Master's Memorandum, Faculty of Law and Political Science, University of Algiers,.. p 99.
[16] The master plan for preparation and reconstruction. 2012.El bayadh..p 145.

CIVIL ENGINEERING JOURNAL

Article no. 22

THE CIVIL ENGINEERING JOURNAL 2-2022

EXPERIMENTAL STUDY ON THE VERTICAL SELF-WEIGHT STRESS DISTRIBUTION LAW OF SLOPE WITH GRANULAR MATERIALS UNDER DIFFERENT CONDITIONS

Huijian Zhang, Gongning Liu, Weixiong Liu and Longgang Miao

Southwest Jiaotong University, Key laboratory of Transportation Tunnel Engineering. Ministry of Education, Chengdu, No. 111, North Section, Second Ring Road, Jinniu District, 610031, China; huijianz@163.com, 2995484603@qq.com, 695600270@qq.com, 695174032@qq.com

ABSTRACT

Topography is one of the important factors affecting the distribution of the self-weight stress field. However, granular materials are different from general continuum materials (such as fluids and solids). Only adopting the continuum theory research still has certain limitations, while the use of experimental methods can better reflect the actual stress state of the granular materials. Therefore, in order to further obtain the vertical self-weight stress distribution of single slope with granular materials, the indoor experimental study of quartz sand based on the point source method is carried out in this paper. The research results indicate that: The measured value of the vertical stress on the bottom surface of the quartz sand slope is generally smaller than the γh (Gravity × Buried depth) value of the corresponding point, and the closer the measuring point is to the slope top, the greater the difference between the test value and γh. Besides, the influence of slope heights and slope ratios on the vertical self-weight stress about slope with granular material is also analyzed. Stress depressions appear in some test conditions, that is, the measured stress peak on the bottom of the slope does not appear at the measuring point closest to the slope top. Whether there is a stress depression and the scope of the depression is mainly related to the slope height, while the slope ratio has little effect on it.

KEY WORDS

Granular material, Self-weight stress, Slope topography, Slope height, Slope ratio, Distribution law

INTRODUCTION

The self-weight stress field is the main initial stress field of most tunnel projects and slope projects, and its stress distribution law is very important to the stability analysis of related projects. The vertical self-weight stress is calculated through multiplying the buried depth by the gravity (γh) based on the premise that the ground is horizontal and the rock mass is a semi-infinite elastic body [1, 2]. In fact, there are many factors affecting the self-weight stress field. Xie et al. [3] studied the self-weight stress of the foundation considering sedimentation, and the results showed that the self-weight stress changed nonlinearly with the depth. Liu and Li [4] regarded the parallel layered rock mass as an equivalent transversely isotropic body, deduced the theoretical solution of the in-situ stress of the rock mass under its own weight, then analyzed the influence of the rock inclination angle and the elastic parameters about the rock mass on the horizontal principal stress. Liang [5] proposed the distribution characteristics of the ground stress about the deep-cut valley based on the research results of the rock mass stress in the Jinping Hydropower Project pivot area. Savage [6-7]

studied the in-situ stress field near the vertical cliff under the action of its own weight and put forward a theoretical solution suitable for the design of rock slope. In addition, the in-situ stress field of the finite elastic slope under self-weight load was also studied, the theoretical solution of the in-situ stress under the terrain was obtained and it can be used for the limited slope design with four kinds of slope angles. Yu et al [8] conducted numerical analysis on the ground self-weight stress field with the slope angles of 30°, 45° and 60°, respectively. The results showed that the difference between the slope vertical stress calculated by the direct buried depth and actual value of the slope was large under the self-weight condition. Qi and Wu [9] studied the stress field of the valley based on numerical simulation and in-situ stress measured data, and found that for a homogeneous elastic slope without unloading zone, the stress distribution from the slope surface to the inside slope can be divided into stress reduction area and stable stress area. While for the slope with unloading area, the stress distribution from the slope surface to the slope body can be divided into stress reduction area, stress rising area and stress stable area. Zhao et al [10] conducted statistical analysis on the distribution law of the in-situ stress field of China. For the stress field of the canyon slope, foreign scholars have also conducted a lot of theoretical and practical research [11-14]. In the literature [15], the self-weight stress was calculated according to the continuum mechanics assumption (finite element numerical simulation) of non-horizontal ground conditions. It was found that the vertical stress along the slope top line was smaller than the calculated value of “depth multiplied by severity”, especially when the slope was steep, the peak of the vertical stress was not even on the vertical line of the mountain top with the deepest buried depth, instead, the peak stress appeared at the two sides of the deepest buried depth section.

About the mechanical properties of granular materials, there have been certain studies at home and abroad. Vernay et al. [16] analyzed the unstable behavior of sand with different saturations under cyclic triaxial tests, and analyzed the influence of saturation on triggering these instabilities. It was found that even if the soil is not fully saturated initially, it can be liquefied. Wu et al. [17] used the discrete element method to study the mechanical properties of granular materials under various stress ratios and density conditions, and the respective ultimate states of different conditions were analyzed. Chen et al. [18] conducted three saturated cycle triaxial tests on granular material with high fines content, and further obtained its stable elastic modulus. It was found that with the increase of cyclic deviator stress, the elastic modulus of the granular material with high fine particle content first decreased and then gradually increased, and an improved non-monotonic relationship model for predicting the elastic modulus and the stress state was proposed. Based on discrete element software, the numerical model of the slope is established to analyze the stability and failure process of the slope [19-22], and the stability factors of the granular slope are also analyzed through experiments [23, 24].

Breaking through the continuum medium assumptions, it was found that there were some peculiar behaviors in the mechanical analysis based on the discrete particulate matter system. The famous granary effect [25] pointed out that when the height of grain accumulation was about twice the bottom diameter, the pressure on the bottom of the granary did not increase with the increase of grain. This was inconsistent with the conclusion that any buried depth pressure or vertical compressive stress was equal to the material weight multiplied by the buried depth in the traditional self-weight stress field. The German engineer Janssen explained that it was the silo wall supports part of the grain weight. Furthermore, removing the “silo” of the granary, in daily life, it was generally believed that when plenty of particles were naturally dumped on a level ground, the central pressure acting on the ground was the greatest. But this reality was not like this case, there was a stress value around the center, which was smaller than both sides and was the minimum value, and this phenomenon was called as stress depression [25]. The further research shows that the center of the sand heap may show a completely different stress distribution due to the different methods of forming the sand heap, the stress result of the falling rain method and the point source method was not the same [26]. Through the indoor falling rain method and PFC2D simulation software, Yao et al [27] analyzed the influence of particle size and friction coefficient on the stress characteristics of sand heap structure.

Granular materials have a wide range of applications in practice (such as embankment filling, grain piles, cofferdams, etc.), but the experimental research on the distribution of its vertical self-weight stress is still rarely involved. Besides, the mechanical properties of different soils are not the same, especially for slope with granular materials, there are still few studies. Therefore, on the basis of the above research, the further experimental research on the vertical self-weight stress distribution characteristics of the bottom surface of the quartz sand slope formed by the point source method is conducted in this paper, focusing on exploring the influence of slope height and slope ratio on the vertical self-weight stress about slope with granular material; further quantify the location and magnitude of the stress peak (the range of the stress depression), aiming to provide some theoretical support for the engineering design and construction of similar slope terrain.

INDOOR MODEL TEST DESIGN

Overall test scheme

In order to minimize the friction between the sand particles and the test box, glass test box is used in this test. As shown in Figure 1, the 2-4 mesh quartz sand is piled up by the point source method to form a unilateral slope in a glass box with the size of 1.5 m × 0.5 m × 0.55 m (length × width × height). A 10 cm thick cushion of the same material is set on the bottom of the slope in advance. To study the vertical stress distribution characteristics of sand slope under different conditions (various slope heights and slope ratios), vertical stress is obtained through several test sensors with the same size that are placed continuously on the cushion surface, the number of these test points is related to the horizontal length of the slope, ranging from 3 points to 8 points.

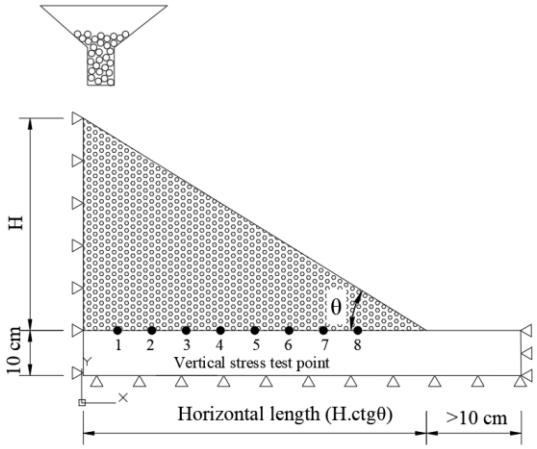

(a) Layout of self-weight stress measurement points of slope

(b) Test box

Fig. 1 – Indoor test scheme

Test conditions

In order to study the influence of various slope heights and slope ratios on the self-weight stress distribution of slope terrain with granular material, multi-condition tests with slope ratios of 1:1.5, 1:2.0, 1:2.5 and 1:3.0 as well as test conditions with slope heights of 30cm, 35cm, 40cm and 45cm are carried on, as shown in Table 1 (a total of 16 test cases).

Tab. 1 - Test conditions

Slope ratios	Slope heights /cm			
	30	35	40	45
1:1.5	√	√	√	√
1:2.0	√	√	√	√
1:2.5	√	√	√	√
1:3.0	√	√	√	√

Test sensor

In terms of pressure test sensors, as shown in Figure 2, a self-made “water bag pressure sensor” is made basing on the communicating vessels principle. Under the action of the upper pressure (the weight of the upper sand), the water in the bag will flow into the pipe, and the pressure is represented by recording the height of the water column. In order to easily observe the change of the water column height, red liquid is dropped into the water bag.

Fig. 2 – Water bag pressure sensor

Test procedure

(1) Level the test box. In order to ensure that the test box is in a horizontal state, level bubbles are placed in the length and width directions of the box bottom side, and the levelling work is completed before starting the test.

(2) Calibration of the water bag pressure sensors. The water bag pressure sensors are preloaded before starting the formal test. Firstly, make sure that the water bag is full, that is, no air bubbles remain. Then pave a 6cm thick quartz sand layer (approximately 2cm above the top surface of the water bag) on the water bags placed side by side, and read the liquid level height before and after paving the sand. On the one hand, it is to confirm whether the liquid level is working normally, on the other hand, it is to compare whether the hydraulic pressure difference of each water bag is consistent, and after the actual calibration, make sure the error is within 0.2mm. The formal test continues to be carried out based on the preload thickness, the test result is based on the difference of the liquid height before and after the formal test.

(3) Formation of quartz sand slope using point source method. The funnel is used to form the slope body by falling sand at the preset slope top position. Since the falling sand is difficult to form different slope ratio cases, the wooden slats are used for slight flattening. For each of the cases shown in Table 1, two sets of parallel tests have been carried out. If there are large deviations on the test results, the third set parallel tests will be supplemented.
(4) Data record. When the slope is formed, in order to reduce the experimental error, keep it stand for 10 minutes, and the reading cannot be carried out until the liquid height is stable. Use a transparent triangular ruler to measure the height of the vertical liquid column, move the liquid column tube slightly to the left and right to record the largest liquid height during the measurement.

ANALYSIS AND DISCUSSION OF THE TEST RESULTS

Vertical stress distribution characteristics of slope terrain

The test results of “slope height 30cm-slope ratio 1:1.5 (case I)”, “slope height 35cm-slope ratio 1:2.0 (case II)”, “slope height 40cm-slope ratio 1:2.5 (case III)” and “slope height 45cm-slope ratio 1:3.0 (case IV)” are extracted and analysed, as shown in Figure 3. The dotted lines in Figure 4 are the corresponding points of the corresponding cases, which are converted to the equivalent height of the water column (referred to the equivalent value of γh) through multiplying the gravity of the quartz sand by the buried depth (γh).

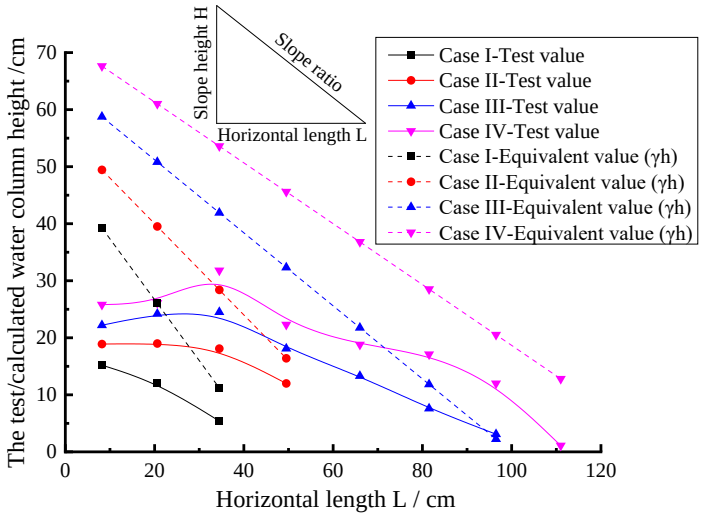

Fig. 3 – Comparison between the test value and the equivalent value γh

It can be seen from Figure 3 that the test value is generally smaller than the equivalent value of γh, and the closer the measuring point is to the top of the slope (namely, the smaller the measuring point number shown in Figure 3), the greater the difference between the test value and the γh equivalent value. At measurement point 1, which is closest to the top of the slope, the actual measured values of cases I ~ IV are only 38.7%, 38.2%, 37.8% and 38.1% of the equivalent value γh of the corresponding cases, respectively. The self-weight stress distribution on the bottom surface of the slope about case I and case II decreases monotonously from the top of the slope to the foot of the slope, that is, the peak stress appears at the measuring point 1; however, the self-weight stress of the slope bottom surface of case III and case IV increases first and then decreases from the top of the slope to the foot of the slope, that is, there is a phenomenon of stress depression, and the peak stress deviates from the actual slope top section to a certain range. In case III, the position where the stress peak appears is about 26.5%L from the top of the slope corresponding to the bottom surface point of the slope, and the peak stress is 58.1%γh of the corresponding point; the position where the stress peak appears in case IV is about 24.1%L from the top of the slope corresponding

to the bottom surface point of the slope, and the peak stress is 53.6% of the γh value of the corresponding point.

Influence of slope height on the distribution of vertical self-weight stress about slope

The experiment photo is shown in Figure 4 (for the condition: slope ratio = 1:1.5 and slope height =40cm) when the slope is formed. Since there are too many experiment conditions involved, in order to better describe in-situ stress distribution of the slope and the convenience of readers, the remaining experiment conditions are represented by curve graphs. The test results of different slope height conditions are extracted with the fixed slope ratio, as shown in Figure 5.

Fig. 4 – The experiment photo after the slope is formed (the condition: slope ratio = 1:1.5 and slope height =40cm)

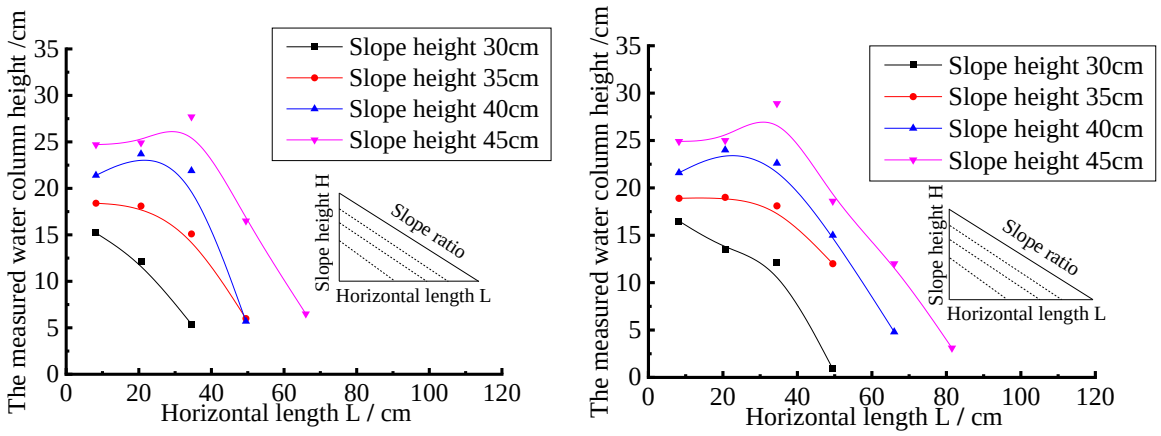

(a) Fixed slope ratio (1:1.5)

(b) Fixed slope ratio (1:2.0)

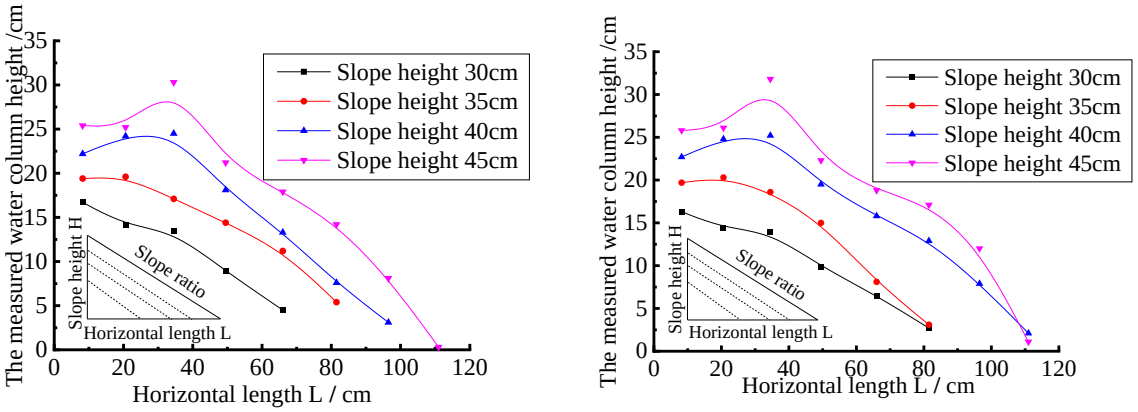

(c) Fixed slope ratio (1:2.5) *(d) Fixed slope ratio (1:3.0)*

Fig. 5 – Influence of slope heights on test results

Figure 5(a) shows that under the condition of the slope ratio 1:1.5, the self-weight stress distribution curve of the slope bottom surface with slope heights of 30cm and 35cm decreases monotonously from the top of the slope to the slope foot, while the curves for the slope heights of 40cm and 45cm appears as a single wave crest that rises first and then falls; the absolute data difference of the adjacent slope heights at measurement point 1 is similar, it is about 3.2cm water column height; the stress peaks of the four slope heights are respectively 31.7%, 32.8%, 35.9%, and 36.2% of the calculated γh value of the corresponding slope height. Figure 5(b) shows under the condition of slope ratio 1:2.0, the self-weight stress distribution curve of the slope bottom surface of the slope height of 30cm decreases monotonously from the top of the slope to the slope foot, while the curve of the slope heights 40cm and 45cm appears to rise first and then fall, showing a single wave crest shape. The data of measuring point 1 and measuring point 2 with the slope height 35cm are almost the same, which can be regarded as the transition state of the above two curve forms. The absolute data difference of the adjacent slope height at measurement point 1 is similar, about 2.8cm water column height. The stress peaks of the four slope heights are respectively 34.4%, 33.9%, 36.6% and 37.4% of the calculated γh value according to the corresponding slope height. Figure 5(c) shows that under the condition of the slope ratio 1:2.5, the self-weight stress distribution curve of the slope bottom surface with a slope height of 30cm decreases monotonously from the top of the slope to the slope foot, while the curves for the slope heights 40cm and 45cm appear to the single wave peak state of rising first and then decreasing, and there is small fluctuations in the slope curve after the peak of the case (slope height 45cm), and the case of slope height 35cm is still the transition state of the above two curve forms; the absolute data difference of the adjacent slope height at measurement point 1 is similar, about 2.9cm water column height; the stress peaks of the four slope heights are 34.8%, 35.0%, 38.0% and 39.0% of the calculated γh value according to the corresponding slope height, respectively. Figure 5(d) shows that under the case of the slope ratio 1:3.0, the self-weight stress distribution curve of the bottom surface of the slope with slope height of 30cm decreases monotonously from the top of the slope to the slope foot, while the curve of the slope heights 40cm and 45cm appears to the single wave peak state of rising first and then falling, and the slope of the post-peak curve of the two slope height cases shows small fluctuations. The data at measuring point 2 of the 35cm slope height case is slightly larger than the data at measuring point 1, and it is about to change from decreasing monotonically to single wave peak state; the absolute data difference of the adjacent slope heights at measuring point 1 is similar, it is about 3.2cm water column height; the stress peaks of the four slope heights are 34.0%, 35.7%, 38.8% and 40.8% of the calculated γh value of the corresponding slope heights.

It can be concluded that when the slope ratio is constant, with the increase of slope height, the self-weight stress distribution curve of the slope bottom surface changes monotonous decrease

from slope top to slope foot to a single peak wave state that first rises and then falls. Under the test conditions, the self-weight stress distribution curve of the slope bottom surface with slope height 30cm under different slope ratios shows a monotonous decreasing shape, while the slope heights of 40cm and 45cm shows a single wave peak shape that first increases and then decreases. The slope height of 35cm is the transitional case of the above two curve forms. The higher the slope height, the more obvious the wave crest, and the farther the wave crest (stress peak) appears from the top of the slope. The stress peak value of all cases is about 31.7%~40.8% of the calculated γh value of the corresponding slope height. If only the single wave peak shape case is considered, the value is 35.9%~40.8%. Affected by the slope heights, the slope of the curve with the same slope ratio does not show a good parallel relationship, but under the same slope ratio, the absolute data difference of the measuring point at the nearest slope top of the adjacent slope height is similar, it is about 2.8~3.2 cm water column height.

Influence of slope ratio on the distribution of vertical self-weight stress about slope

The test results of different slope ratios are extracted with the fixed slope heights, as shown in Figure 6.

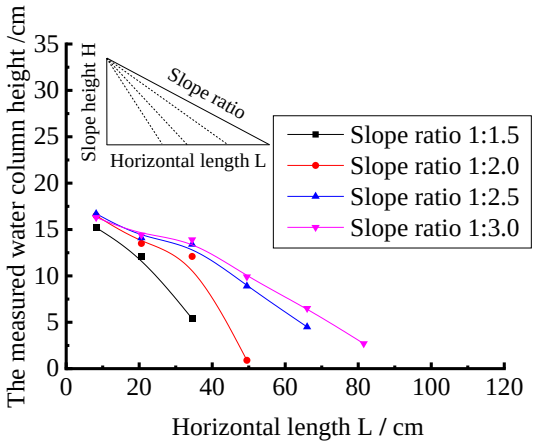

(a) Fixed slope height (30cm)

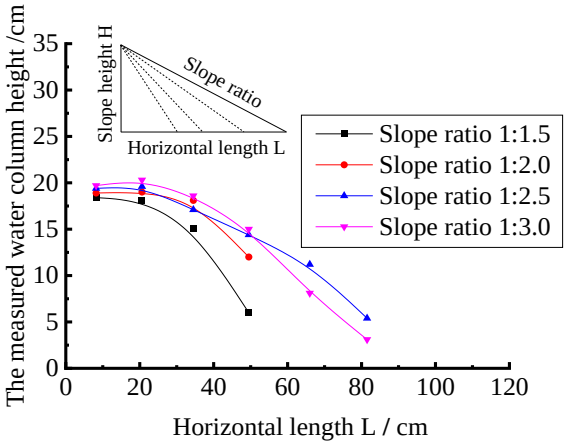

(b) Fixed slope height (35cm)

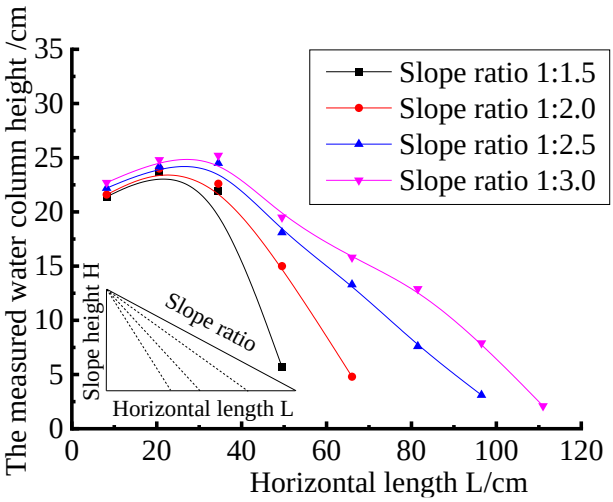

(c) Fixed slope height (40cm)

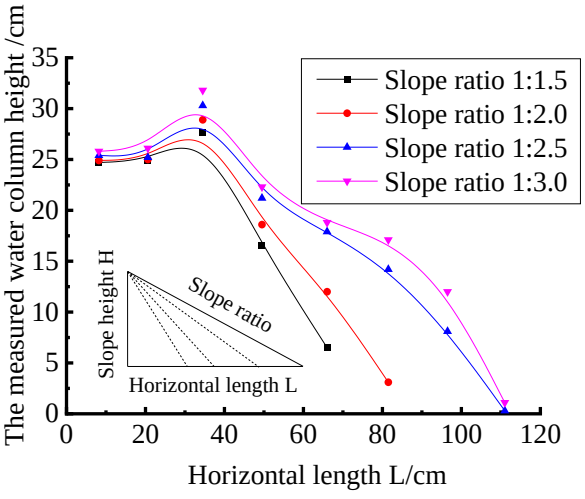

(d) Fixed slope height (45cm)

Figure 6 – Influence of slope ratio on test results

Figure 6(a) shows the measured curves of the four cases with slope ratios of 1:1.5, 1:2.0, 1:2.5 and 1:3.0 under the condition of fixed slope height 30cm. The curves of the above four slope ratios all show a monotonous decrease from the slope top the to the slope foot, and the peak stress point is the measuring point closest to the slope top (measurement point 1), the difference of these four cases is little, and the difference increases with the increase of the distance from the measuring point 1. Figure 6(b) shows the measured curves of the four cases with slope ratios 1:1.5, 1:2.0, 1:2.5 and 1:3.0 under the condition of the fixed slope height 35cm. The shapes of the four curves are similar, and all show that the measured value of measuring point 1 and measuring point 2 are close, that is, the curve of this section is close to horizontal, and then as the number of measuring points increases, the curve shows a downward trend; the curve with slope ratio 1:2.0 crosses the curve with slope ratio 1:2.5, and the curve with slope ratio 1:2.5 crosses the curve with slope ratio 1:3.0, but there is no significant difference in the data of measurement point 1, which is the peak stress. Figure 6(c) shows the measured curves of the 4 cases with slope ratios 1:1.5, 1:2.0, 1:2.5 and 1:3.0 under the condition of the fixed slope height 40cm.The four curves shows the same trend that as the number of the measuring point increases, the curve first increases and then decreases; the peak stress appears between the measuring point 2 and measuring point 3, as the slope ratio decreases (the slope becomes gentler), the more the deviation from the top of the slope is, the less significant is. The tilt rate of the curve after the peak becomes gentle as the slope ratio decreases. Figure 6(d) shows the measured curves of the 4 cases with slope ratios of 1:1.5, 1:2.0, 1:2.5, and 1:3.0 under the condition of a fixed slope height of 45cm. The four curves all appear to increase first and then decrease, presenting a more obvious single wave crest shape, with a stress depression at the top of the slope. In contrast, the curve before the wave crest with the slope height 40 cm is convex, and the curve before the wave crest in this case is concave. The stress peaks all appear between measuring point 2 and measuring point 3, the specific position is not affected by the slope ratio. The distance from the horizontal length 0 point is 29.0cm, 30.8cm, 32.3cm, 32.8cm, respectively; compared with the horizontal length of the corresponding slopes, the ratios are 43.0%, 34.2%, 28.7% and 24.3% respectively. The magnitude of the peak stress increases as the slope ratio decreases. If the maximum value of γh with the slope height 45 cm is used as the reference, the stress peaks of the slope ratios 1:3.0, 1:2.5, 1:2.0 and 1:1.5 are 40.8%, 38.9%, 37.4%, 36.2% of the benchmarks respectively.

It can be concluded that when the slope height remains unchanged, with the decrease of the slope ratio, the shape of the self-weight stress distribution curve at the bottom of the slope shows a good consistency, especially in the section near the slope top, and the data difference of the measurement point 1 closest to the top of the slope is minimal. For cases of the slope heights 40cm and 45cm where the distribution curve is in the form of a single wave peak, the smaller the slope ratio, the more obvious the wave crest, and the farther away the wave crest appears from the slope top, but it is not significant. For the curve section before the wave crest, the 40cm slope height case is convex, while the 45cm slope height case is concave. For the slope of the post-peak curve with the same slope height, the change law is roughly the same as the slope ratio. The smaller the slope ratio, the smoother the curve.

CONCLUSION

Based on the quartz sand slope formed by the point source method with granular material, the experimental research on the vertical self-weight stress distribution of the slope terrain under different conditions is carried out. The main conclusions are as follows.

(1) The test value is generally smaller than the γh equivalent value, and the closer the measuring point is to the slope top, the greater the difference between the test value and the γh equivalent value. At measurement point 1, which is closest to the slope top, the measured values are only 38.7% of the calculated equivalent value of γh in the corresponding cases. The vertical self-weight

stress distribution of granular material slope terrain may show the phenomenon of slope crest stress depression after the slope reaches a certain height, and the range of the stress depression is mainly related to the slope height, while the slope ratio has little effect on this.

(2) With the fixed slope ratio, as the slope height increases, the self-weight stress distribution curve on the bottom of the slope changes from a monotonous decrease to the state that: from the slope top to the slope foot being with a single wave crest that rises first and then drops, and the higher the slope height, the more obvious the wave crest, and the farther the wave crest (stress peak) appears from the slope top.

(3) With the fixed slope height, the shape and trend of the self-weight stress distribution curve of the bottom surface of the slope with different slope ratios are similar. When the slope height reaches a certain value, the crest of the self-weight stress distribution curve at the bottom of the slope is more prominent, and the farther the position of the wave crest deviates from the slope top section, but it is not significant.

ACKNOWLEDGMENTS

The authors would like to acknowledge the financial support of the National Natural Science Foundation of China (51578459).

REFERENCES

[1] Guan, B. S., 2003. Key Points of tunnel engineering design. China Communication Publishing, Beijing.

[2] Zhang, N., 2002. Study on the current crustal stress field in the rockmass. Master's thesis, Zhejiang University, Hangzhou.

[3] Xie, K. H., Hu, A. F., Liu, Y. M., 2004. On computation of overburden pressure and settlement for layered soil considering sedimentation. Chinese Journal of Rock Mechanics and Engineering, Vol. 23, 1585-1589.

[4] Liu, Y. and Li, W., 2001. Gravitational stresses in parallel stratified rock mass. Rock and Soil Mechanics, Vol. 22: 63-66. https://doi.org/10.16285/j.rsm.2001.01.017

[5] Liang, Y., 2008. The study of in situ stress and rock slope stability analysis in deep-incised valley. Ph.D thesis, Southwest Jiaotong University, Chengdu.

[6] Savage, W. Z., 1993. Gravity-induced stresses near a vertical cliff. International Journal of Rock Mechanics and Mining Science & Geomechanics Abstracts, Vol. 30: 325-330. https://doi.org/10.1016/0148-9062(93)91716-V

[7] Savage, W. Z., 1994. Gravity-induced stresses in finite slopes. International Journal of Rock Mechanics and Mining Sciences & Geomechanics Abstracts, Vol. 31: 471- 483. https://doi.org/10.1016/0148-9062(94)90150-3

[8] Yu, D. J., Zhu, W. S., Yong, M., et al., 2011. Initial geostress field characters in mountain with different slopes and its influence on underground projects. Rock and Soil Mechanics, Vol. 32: 609-613. https://doi.org/10.16285/j.rsm.2011.s1.060

[9] Qi, S. W. and Wu, F. Q., 2011. Stresses field characteristics of a valley slope in high geo-stress area. Rock and Soil Mechanics, Vol. 32: 1460-1464. https://doi.org/10.16285/j.rsm.2011.05.019

[10] Zhao, D. A., Chen, Z. M., Cai, X. L., et al., 2007. Analysis of distribution rule of geostress in China. Chinese Journal of rock mechanics and Engineering, 1265-1271.

[11] Savage, W. Z., Swolfs, H. S., Powers, P. S., 1985. Gravitational stresses in long symmetric ridges and valleys. International Journal of Rock Mechanics and Mining Sciences & Geomechanics Abstracts, Vol. 22: 291- 302. https://doi.org/10.1016/0148-9062(85)92061-3

[12] Mctigue, D. F. and Mei, C. C., 1981. Gravity-induced stresses near topography of small slope. Journal of Geophysical Research Solid Earth, Vol. 86: 9268-9278. https://doi.org/10.1029/JB086iB10p09268

[13] Mctigue, D. F. and Mei, C. C., 1987. Gravity-induced stresses near axisymmetric topography of small slope. International Journal for Numerical and Analytical Methods in Geomechanics, Vol. 11: 257-268.

[14] Mandal, P. and Singh, R. N., 1991. Gravity induced near-surface stresses in long-symmetric ridge-valley systems. Journal of Earth System Science, Vol. 100: 267-280.

[15] Wang, H. Y., Chen, S. M., Yan, Z. X., 2008. Principles of dynamic design of underground engineering. Chemical Industry Press, Beijing.
[16] Vernay, M., Morvan, M., Breul, P., 2020. Experimental study on the influence of saturation degree on unstable behavior within granular material. European Journal of Environmental and Civil Engineering, Vol. 24: 1821-1839. https://doi.org/10.1080/19648189.2018.1488623
[17] Wu, Q. X., Yan, L. Y., Yang, Z. X., 2021. Discrete element simulations of drained granular material response under multidirectional rotational shear. Computers and Geotechnics, Vol. 139: 104375(1-13) https://doi.org/10.1016/j.compgeo.2021.104375
[18] Chen, W. B., Feng, W. Q., Yin, J. H., 2020. Effects of water content on resilient modulus of a granular material with high fines content. Construction and Building Materials, Vol. 236: 117542(1-14). https://doi.org/10.1016/j.conbuildmat.2019.117542
[19] Chen, X. X., 2018. The research of stability of rock slope based on statistics and particle flow code. Master's thesis, Jilin University, Jilin.
[20] Tang, H. M., Yan, Z. Q., Chen, H. K., 2016. Numercial simulation on failure of Gongjiafang 2# bank slope in Wu Gorge of the three gorges based on discrete element method. Journal of Choingqin Normal University (Natural Science), 33(1): 40-46. https://doi.org/10.11721/cqnuj20160128
[21] Hou, J., Zhang, M. X., Chen, Q., et al, 2019. Failure-mode analysis of loose deposit slope in Ya'an-Kangding Expressway under seismic loading using particle flow code. Granular Matter, 21(1), 1-12. https://doi.org/10.1007/s10035-018-0859-1
[22] Li, X. X, Liu, J. S, Gong, W. P., et al, 2022. A discrete fracture network based modeling scheme for analyzing the stability of highly fractured rock slope. Computers and Geotechnics, 141, 104558(1-18). https://doi.org/10.1016/j.compgeo.2021.104558
[23] Bu, X. H., Fu, R. H., Li, J. D., et al, 2016. Internal Factors of the Failure of Granular Mixtures Slope, Journal of Yangtze River Scientific Research Institute, 33(9): 116-120. https://doi.org/10.11988/ckyyb.20150606
[24] Zhang, J. M., Luo, Y., Zhou, Z., et al, 2021. Effects of preferential flow induced by desiccation cracks on slope stability. Engineering Geology, 288, 106164(1-16). https://doi.org/10.1016/j.enggeo.2021.106164
[25] Sun, Q. C. and Wang, G. Q., 2009. Introduction to particle mechanics. Science Press, Beijing.
[26] Luo, W. Z., 2020. Experimental study and analysis on stress arch effect in sand. Master's thesis, South China University of Technology, Guangzhou.
[27] Yao, Y. X., Li, S., He, C., et al, 2019. Analysis on pressure characteristic at bottom of sand heap with laboratory experiment and PFC2D numerical simulation. Journal of Engineering Geology, Vol. 27: 1281-1289.

CIVIL ENGINEERING JOURNAL

Article no. 23

THE CIVIL ENGINEERING JOURNAL 2-2022

FEATURES OF THE MORPHOLOGY OF THE SHEAR FAILURE SURFACES OF COARSE-GRAINED SLIP ZONE SOILS

Zechuang Li [1], Qiyuan Cai[1] and Di Liu[2]

1. *School of Civil Engineering, Northeast Forestry University, Harbin 150040, Heilongjiang, China;lzc@nefu.edu.cn, caiqiyuannefu@163.com*
2. *Zhejiang Huadong Construction Engineering CO., LTD, Hangzhou 310014, Zhejiang, China; liu_d5@hdec.com*

ABSTRACT

Analyzing the change in the roughness of the shear failure surface under different particle composition is important to reveal the mesoscopic mechanism of strength change of coarse-grained slip zone soil. Slip zone soils were grouped according to different particle gradations and coarse particle contents for experiments. To collect shear surface coordinate data points, the customized shear surface measurement mold was examined to measure the shear surface. Then, the measured 3D elevation data are drawn into a 3D surface map by using the Surfer software to show the actual situation of the shear surface. The shear surfaces were analyzed by using box plots and ice crystal flower plots. Finally, the roughness of the shear surface was quantified by the root mean square of the relative undulation (Z_2). Findings indicate that the shear surface undulation characteristics of coarse-grained slip zone soil are obviously correlated with the proportion of particles with a size between 5–20 mm. Moreover, whether the gradation is good or poor has a significant effect on the shear surface characteristics. The well-graded shear surface is rougher and more undulated, whereas the poorly graded shear surface is the opposite. As the normal pressure increases, the roughness of the shear surface decrease. As the content of coarse particles increases, the roughness of the shear surface increases, and Z_2 has a highly positive linear correlation with the coarse particle content.

KEYWORDS

Slip zone soil, Shear surface, Roughness, Medium direct shear test, Meso-structure

INTRODUCTION

The shear strength of slip zone soils is one of the most important factors in landslide stability evaluation and landslide protection and management. Few studies have been conducted on shear surface characteristics, and most of them focus on structural plane of rock and soil aggregate and rock [1-2]. Currently, research on the shear surface characteristics of slip zone soil is still lacking.

Scholars who studied the shear properties of weathered schist residual soils found that the undulation of shear surface increases with increasing stone content. With the increase in the normal pressure, mostly tumbling and gnawing failure occur [3]. Some scholars also found through large-scale shear experiments of coarse grain soil that the shear surface has an obvious undulating shape

[4]. An experimental study of the shear character of rock and soil aggregate found that the shear surface has a good fractal property and calculated the fractal dimension of the shear surface [5]. In their study on gravelly slip zone soils, Ren et al. [6] found that the residual strength is determined by the contact properties of gravels on the shear surface and the shear surface undulation. Many studies have found that the morphological features of the shear surface have an effect on the strength, but no studies have been conducted on the effect of factors such as particle gradation and coarse particle content on the shear surface nor have they been able to establish a good relationship between shear surface undulation and shear strength. At present, no dedicated instrument for measuring the shear surface is available; the most common solution in this research field is to obtain the data point cloud of the shear surface by 3D laser scanning technology [7-8]. However, 3D laser scanning is an expensive technique for collecting point clouds of 3D data.

In this paper, the shear surface of slip zone soil is first measured by using the hanging wire method by studying the customized mold. The samples can be measured immediately after shearing, and the measurement accuracy can meet the requirements of analysis. Then, the Surfer software is used to draw the measured data into a 3D surface map to reflect the features of the shear surface more clearly. Analyze the 3D surface map, build meso-structural models to observe internal structures, and conduct further statistical analysis of shear surfaces through box plots and ice crystal flower plots. Finally, the roughness of the shear surface is quantitatively described by the root mean square of relative undulation, and the features of the shear surface of the slip zone soil with different particle compositions are analyzed.

TEST MATERIALS AND METHODS

Soil samples were taken from the landslide on the south slope of the West Open-pit Mine in Fushun [9]. Reconstituted test specimens consisted of dried and sieved soil samples of each particle size. The sieving particle size range is 0–0.075, 0.075–0.25, 0.25–0.5, 0.5–2, 2–5, 5-10, and 10–20 mm. The test does not consider particle breakage, and the coarse particles that are larger than 2 mm are replaced with white stones, as shown in Figure 3(a). The test uses a medium-sized direct shearing instrument. The direct shear box internal length and width are 200 mm, and the height of the upper and lower shear boxes is 100 mm.

(1) Shear test scheme: To investigate the effect of different particle compositions on the shear failure surface undulation of slip zone soil, coarse-grained slip zone soil was divided into seven groups according to different particle size distributions. The first, second, and third groups were poorly graded, and the fourth, fifth and sixth groups were well graded (particles with a size greater than 2 mm are considered coarse grains [10]). The soil was then divided into five groups according to the content of coarse particles, and groups 7, 8, 9, 10, and 11 have coarse particle contents of 40%, 50%, 60%, 70%, and 80%, respectively. In the group with coarse particle content, the gradation of coarse particles above 2 mm and the gradation of fine particles below 2 mm were equally divided. Here, 40% coarse particle content was taken as an example; 0–0.075, 0.075–0.25, 0.25–0.5, 0.5–2, 2–5, 5–10, and 10–20 mm accounted for 15.00%, 15.00%, 15.00%, 15.00%, 13.33%, 13.33%, and 13.33%, respectively. Each group was tested under three different normal pressures of 50, 100, and 150 kPa. The “Standard for Geotechnical Test Methods GB/T50123-2019” serves as a reference for the test shear process [11]. The topographic geometry of the sheared surface was measured

after shearing. The particle size distribution curve is shown in Figure 1.

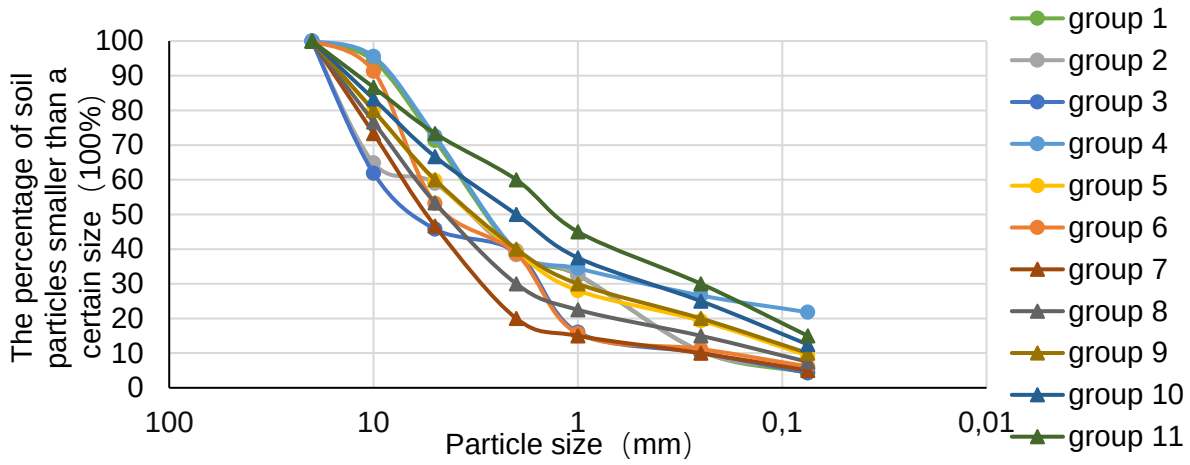

Fig.1 - Particle size distribution curve

(2) Shear surface 3D elevation data point acquisition: A measuring mold was made to extract the 3D data points of the shear surface. To make the mold fit well with the shear box, the length and width of the mold are designed to be consistent with the upper and lower shear boxes. The leg height is 60 mm. The mold schematic is shown in Figure 2(a), and the actual mold is shown in Figure 2(b). Two crawlers of the same width as the mold frame are fixed above the mold sides, The mold is equipped with a steel rod with indentations, as shown in Figure 2(c), and a hanging hammer with scale, as shown in Figure 2(d). The four legs of the mold are placed on the shear box, the steel rods are placed in the corresponding grooves on both sides of the crawlers in turn. And the hanging wire method is used for measurement, that is, the specific measurement method in the subsequent paragraph. The plane size of the soil sample is 200 mm × 200 mm. To exclude edge effects, only the 104 mm × 104 mm area in the center of the shear surface was measured (Figure 3a). The groove spacing of the mold crawler is 8 mm, that is, the Y-coordinate point spacing. The indentation spacing of the steel rod is 8 mm, that is, the X-coordinate point spacing. Thus, the coordinates of horizontal X and Y are determined (X is the shear direction). The hanging wire method is as (3).

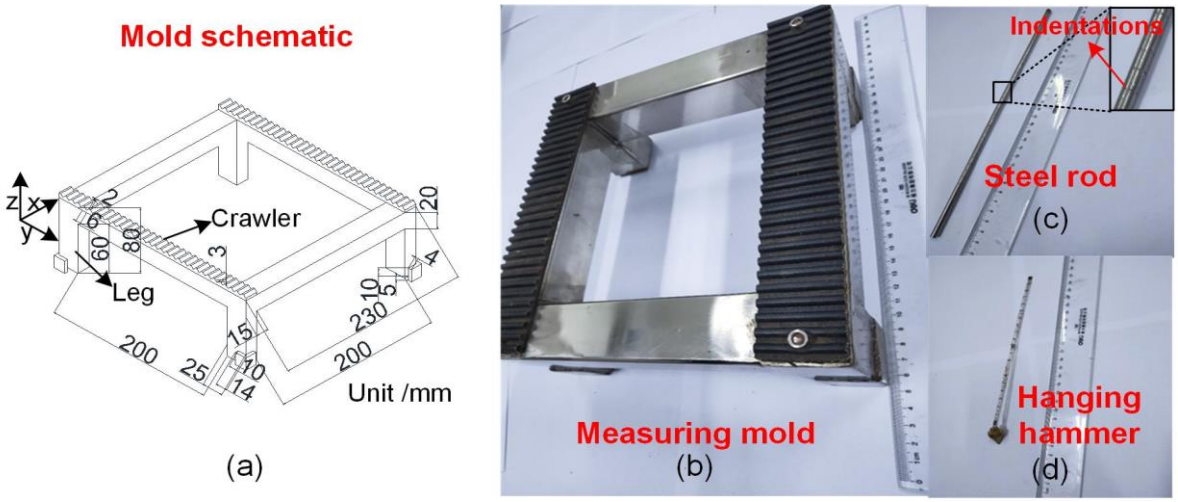

Fig.2- Drawing of the shear surface measurement mold: (a) schematic of mold; (b) actual mold; (c) actual steel rod; (d) actual hanging hammer

(3) The hanging hammer was dropped perpendicularly along the indentations of the steel rod, and the process was stopped when the hammer just touched the shear surface (i.e., shear failure surface). According to the scale of the thin line, the height of the drop of the hanging hammer from the upper surface of the steel rod is read and then marked as h_1. The vertical distance from the upper surface of the steel rod to the upper surface of the lower shear box is h_0. $Z = h_1 – h_0$ is the elevation of the measured point, that is, the coordinate Z represents the elevation of this point on the shear surface. The actual measurement process is shown in Figure 3(b).

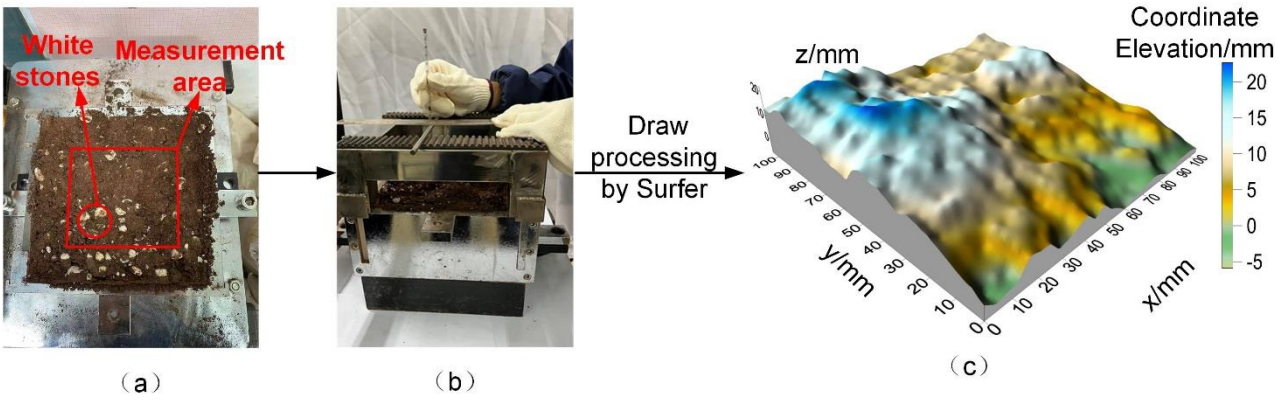

Fig.3- Extraction process of the 3D topography of the shear surface: (a) the actual shear surface after shearing; (b) the measurement diagram of the shear surface; (c) the 3D topography map of the shear surface

ESTABLISHMENT OF THE MESO-STRUCTURAL MODEL

The random filling algorithm is used to establish the meso-structure model by using MATLAB programming language. The established space size is consistent with the test shear box size, which is 200 mm × 200 mm, and the area is denoted as "*A*." According to the particle size gradation in the test scheme, the diameter range of each particle interval and the proportion of particles in each particle interval is set, and the proportion coefficient is recorded as "*p*." The principle is as follows: First, the sequence randomly picks a point "*O*" in the space, with the point as the center of the ellipse [12]. An ellipse with the length of the long semi-axis "*a*" and the length of the short semi-axis "*b*" is generated. "*a*" is the radius of the largest particle in the particle interval. After the ellipse is generated, a part of the arc is randomly picked to translate and deform inward at equal distances; it is regarded as a new particle after deformation. Then, a point in space is picked again. If the point is within the range of generated particles, then a new point is picked, and if it is outside the range of generated particles, then the minimum distance between the point and the outer surface of particles is calculated. If the distance is less than the maximum radius of the particle size interval, then a new point is picked, and if the distance is greater than the maximum radius of the particle size interval, then a particle is generated according to the above steps. The distance from any point in the plane to the boundary of the particle is shown in the literature [12-13].

The criterion of the position relation between points and particles on the plane is as follows:

Consider the function: $$\varphi(x,y)=(x-x_0,y-y_0)A\begin{pmatrix}\frac{1}{a^2} & 0\\ 0 & \frac{1}{b^2}\end{pmatrix}A'\begin{pmatrix}x-x_0\\ y-y_0\end{pmatrix}-1 \quad (1)$$

Let $P(x,y)$ be a point on the plane. If $\varphi(x,y)>0$, then $P(x,y)$ is outside the particle. If $\varphi(x,y)=0$, then $P(x,y)$ is on the particle. If $\varphi(x,y)<0$, then $P(x,y)$ is inside the particle.

The principle of particle deformation is as follows:

The interval of symmetry for "a_0" [13]: $[a_0-r_1,a_0+r_1]$ and $[a_0-r_2,a_0+r_2]$, among them $0\le r_1<r_2$,

let $t=(x-a_0)^2$. The C function is then created $$g(x,a_0,r_1,r_2)=g(t)=\begin{cases}e^{\frac{1}{(t-r_1^2)(t-r_2^2)}},0\le r_1^2<t\le r_2^2\\ 0,t\le r_1^2,t\ge r_2^2\end{cases} \quad (2)$$

Scaling factor: $$B(x,a_0,r_1,r_2)=\begin{cases}1, & t\le r_1^2\\ \int_{0.025r_1^2}^{r_2^2}g(s)ds\Big/(\int_{4r_1^2}^{r_2^2}g(s)ds+0.01), & r_1^2<t\le r_2^2\\ 0, & t>r_2^2\end{cases} \quad (3)$$

This factor is used to randomly translate inward at equal intervals to achieve a deformation effect.

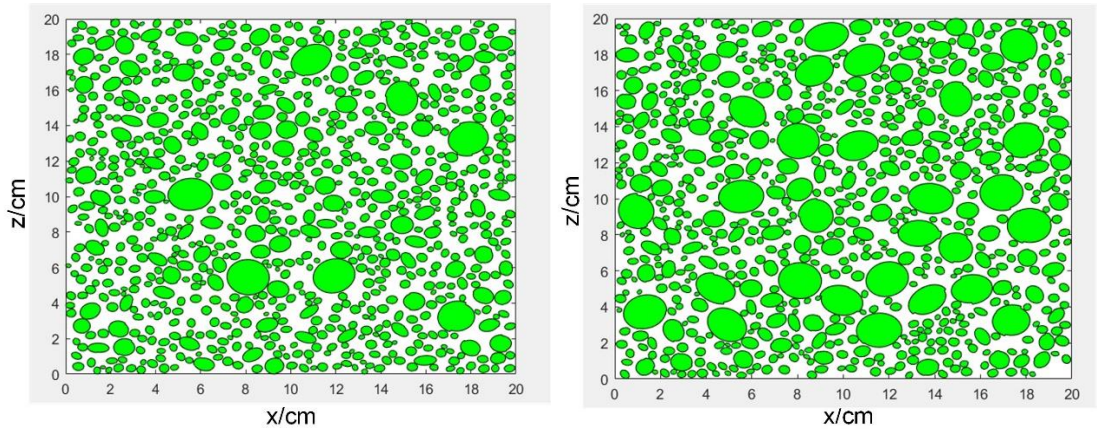

(a) *(b)*

Fig.4- Meso-structure model diagram: (a) first group of gradation; (b) gradation for group 9

In this way, the particles are generated cyclically, and the total area of the generated particles is calculated. The ratio of the sum of the areas of all particle sizes to the space area *A* is *q*, and the ratio of this particle size range to all particle sizes is p_1. When the area of generated particles exceeds $q\times p_1\times A$, the generation of the particle size is stopped. The next particle size is generated until all particle sizes have been generated. The generation of small particle sizes is too complicated; thus, only the particle size larger than 2 mm is simulated. The generated model is shown in Figure 4.

ANALYSIS OF TEST RESULT

Effects of particle gradation on shear surface undulation morphology

To more specifically reflect the morphology of the shear failure surface, the measured 3D data points were drawn with Surfer. The following is a comparative analysis:

Comparison between 3D topography map and actual shear surface

First, the actual shear surface is compared with the figure drawn by Surfer to show the actual situation corresponding to the 3D topography map more clearly.

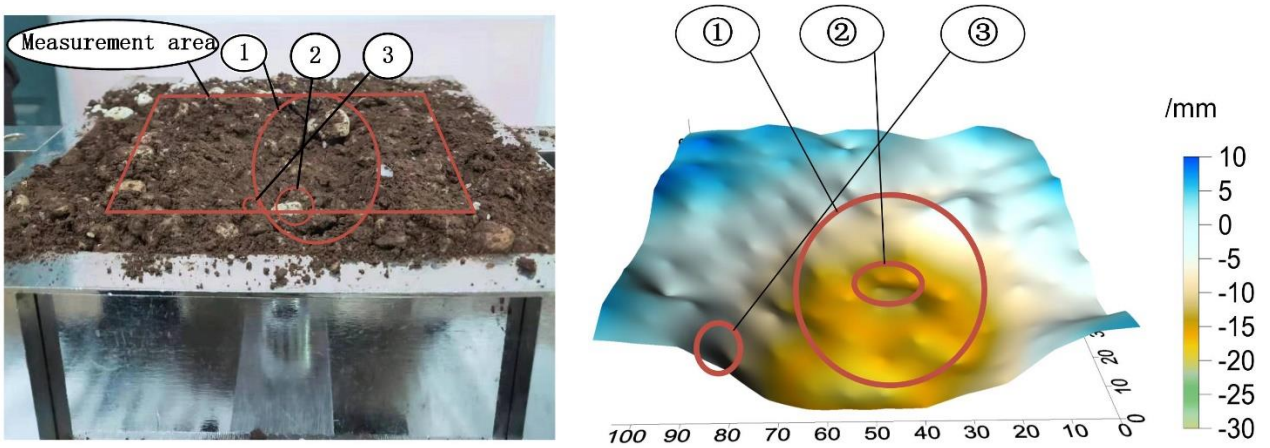

(a) (b)

Fig.5- Comparison between the shear surface 3D topography map and the actual shear surface: (a) the actual shear surface; (b) the shear surface 3D topographic map

①, ②, and ③ in Figure 5(a) correspond to ①, ②, and ③ in Figure 5(b). The ① in the two sub-figures is due to the fact that this part is relatively compact, with good particle interlocking, good internal structure integrity. In the shearing process, this part could not be cut off because of its strong shear resistance and appeared as a large regional depression. The ② is due to the protrusions being supported by coarse particles, and it has high strength. During shearing, the protrusions could not be cut off but passed over. After the upper shear box is removed, this part appears as a small protrusion. The ③ is due to the poor interlocking between a single coarse particle and the soil in the lower shear box, which is more firmly embedded with the upper shear box. During shearing, this particle pushes the particles around the inlay part of the lower shear box loose and move backward, forming small pits.

Comparative analysis of well-graded soil and poorly graded soil

Figure 6 compares well-graded and poorly graded groups: Three groups (2, 5 and 6) with similar contents of 5-20mm were selected for comparative analysis.

Comparison at 50 kPa: The figure shows many small protrusions and pits in all three figures. However, compared with the poorly graded group 2 (Figure 6c), the well-graded groups 6 (Figure 6a) and 5 (Figure 6b) have obviously protrusions and depressions. (i.e., obvious undulation)

Comparison at 100 kPa: Compared with the poorly graded group (Figure 6f), the well-graded

group in group 6 (Figure 6d) has more obvious undulation and is rougher. Group 5 (corresponding to Figure 6e) with good gradation has similar overall undulation to group 2 with poor gradation.

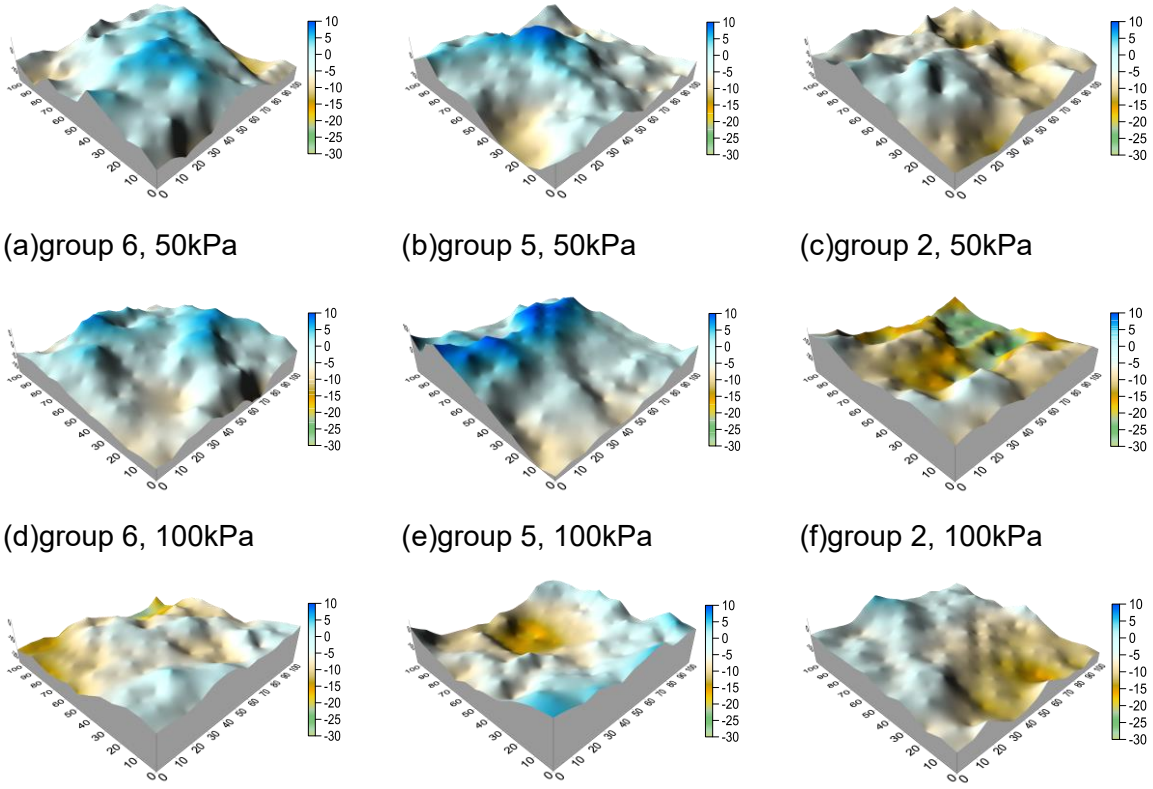

(a)group 6, 50kPa (b)group 5, 50kPa (c)group 2, 50kPa

(d)group 6, 100kPa (e)group 5, 100kPa (f)group 2, 100kPa

(g)group 6, 150kPa (h)group 5, 150kPa (i)group 2, 150kPa

Fig. 6- Comparison of shear surface topography (well- and poorly graded soil, Unit: mm)

Comparison at 150 kPa: Groups 6 (Figure 6g) and 5 (Figure 6h) are two well-graded test groups with different shear surface undulations, but both are more obvious than the poorly graded group 2 (Figure 6i). In addition, Figures 6(e), 6(g), and 6(i) all exhibit shear inclination. Thus, the gradation of coarse-grained soil has an obvious influence on the roughness of shear surface. The shear surface of the well-graded group has an obvious interlocking bond and is rougher than that of the poorly graded group. Most of the protrusions of the poorly graded groups were cut off and the shear surface was relatively smooth because the protrusions with an inclination angle >0° can act as resistance during shearing. The poorly graded group does not have a good interlocking bond, the protrusions are more likely to be sheared off, and the resistance to shear in the shearing process is relatively small. In contrast, the well-graded group has good particle interlocking, the protrusions are not easily sheared off, and the resistance to shear in the shearing process is relatively large. All the above-mentioned particle gradations were grouped separately at different normal pressures. The comparison derived that the shear surface is the smoothest under 150 kPa, the second under 100 kPa, and the roughest under 50 kPa. The comparative analysis of different normal pressure concluded that, with the increase in the normal pressure, the roughness of shear surface decreases and becomes smoother. During the shearing process, the occurrence of shear displacement needs to overcome the occlusion between the protrusions and the sliding friction resistance of the shearing surface. When the normal pressure is not enough, the upper soil sample climbs along the protrusions

of the shear surface so as to balance the vertical force caused by shear (it is characterized by shear expansion). When the normal pressure is large enough, the climbing movement is inhibited and the shear strength increases. When the shear force increases to a certain extent, the protrusion is sheared off. The shear failure of the protrusions is determined by its shear resistance.

Statistical analysis of coordinate elevation of shear failure surface

The elevation (Z) of 3D data points on the shear failure surface measured after shearing was statistically analyzed, and the box graph was drawn as follows. In Figure 7, “group 1, 50 kPa” represents the group 1 sample sheared under normal pressure of 50 kPa.

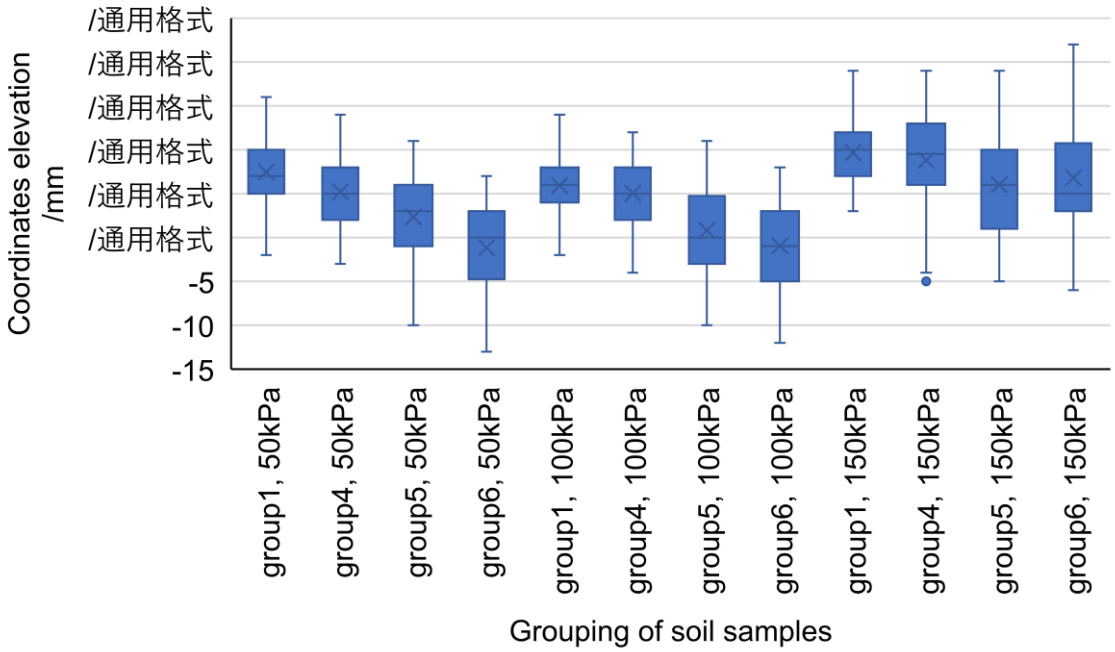

Fig.7- Elevation statistics of shear failure surface coordinates

To study the influence of particle proportion between 5–20 mm on the shear failure surface undulation morphology, the particle content in the interval was taken as a variable, and the test results under normal pressure of 50, 100, and 150 kPa were analyzed, taking one group of poor gradation and three groups of good gradation as examples (the proportion of 5–20 mm particles in groups 1, 4, 5, and 6 was 28.67%, 27.39%, 40.21%, and 46.79%, respectively). A large difference between the upper and lower edges of the box plot and difference between the upper and lower quartiles corresponds to a sparse elevation of the shear surface, that is, the probability of a rougher shear surface is greater. The figure clearly shows that under the normal pressure of 50 and 100 kPa, the box plot of the 3D coordinate points of the shear surface shows a downward trend as a whole with the increase in the proportion of particles between 5–20 mm. This finding does not mean that the roughness decreases, but that the elevation of the shear surface generally decrease with the increase of particles in the interval (i.e., 5-20mm). In addition, the difference between the upper and lower edges and the difference between the upper and lower quartiles gradually increase with the increase in the proportion of particles in the interval. This finding indicates that the shear surface becomes relatively rough and the undulation is larger with the increase in the proportion of particles

with a size between 5–20 mm. The overall decrease trend of the shear surface elevation with the increase in the particle size occurs because when the coarse particles are relatively few, a large part of the fine particles in the soil sample do not have enough coarse particles to combine and more fine particles combine; the combination of coarse and fine particles is stronger than that of fine particles. In the shear process, a regional zone is formed in the soil by the combination of many fine particles, and the protrusions supported by coarse particles near the shear zone have higher strength. Thus, the soil sample is cut apart along the regional zone where many fine particles are bound. Under the normal pressure of 150 kPa, although no sufficiently obvious rule is observed similar to that under the normal pressures of 50 and 100 kPa, the above changes still have a tendency to occur.

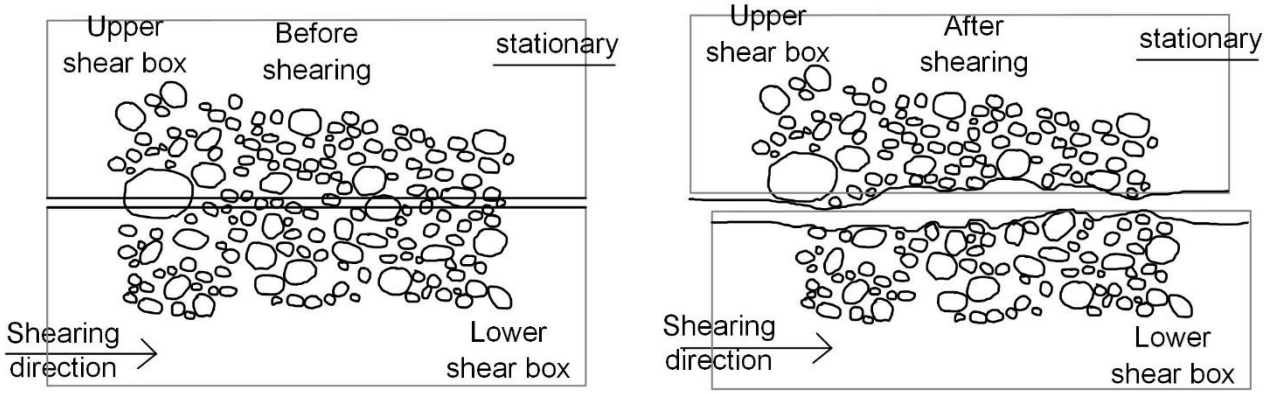

Fig.8- Schematic of the development of shear surface (the first group of grading)

In the first group of meso-structure, coarse particles are significantly fewer, and the distance between them is relatively large, so that they cannot form a good solid matrix. The pores between the coarse particles are filled with fine particles to form a solid matrix suspension structure. During the shearing process, most of the protrusions are easily sheared off, so the shear surface appears relatively flat.

Statistical analysis of undulation angle of shear surface profile along shear direction

A row of data points on the shear failure surface along the shear direction was statistically analyzed, and the angles between two adjacent points in a row of data were calculated, which were drawn in a polar coordinate system as an ice crystal flower diagram in the Figure 9. The proportion of particles between 5–20 mm is still used as the variable for comparison, and the normal pressure is 50 kPa as an example. Statistical analysis of all data points showed that an angle greater than 45° is very rare. Therefore, for the convenience of processing, the angle over 45° is calculated as 45°. In the figure, there is a column of shear surface data every 45°. Fourteen columns of shear surface data exist for each group of specimens, and 8 columns of the middle part are selected to draw a complete 360° graph. The first region in order is the most marginal column of data, arranged inward in order, and the fourth and fifth regions are the innermost two columns of data in the shear surface. In the actual shear surface, part of area 1 is relatively flat, and another part is undulating. The ice crystal flower diagram shows that part of the angle of area 1 is close to 0°, and most angles are close to 22.5°. In the actual shear surface, the shear zone of region 2 contains relatively few coarse particles, which have bad interlocking bond and are cut relatively smoothly. Region 2 is relatively flat

as a whole, and the ice crystal flower diagram shows that most of the angles of region 2 are close to 0°. In the actual shear surface, the first half of region 3 is relatively flat, and the second half is a relatively large depression. The ice crystal flower diagram shows that part of the angle of region 3 is close to 30°, and part of the data is close to 0°. In the actual shear surface, many small pits and protrusions are found in region 7, and most angles are close to 22.5° in the ice crystal flower diagram.

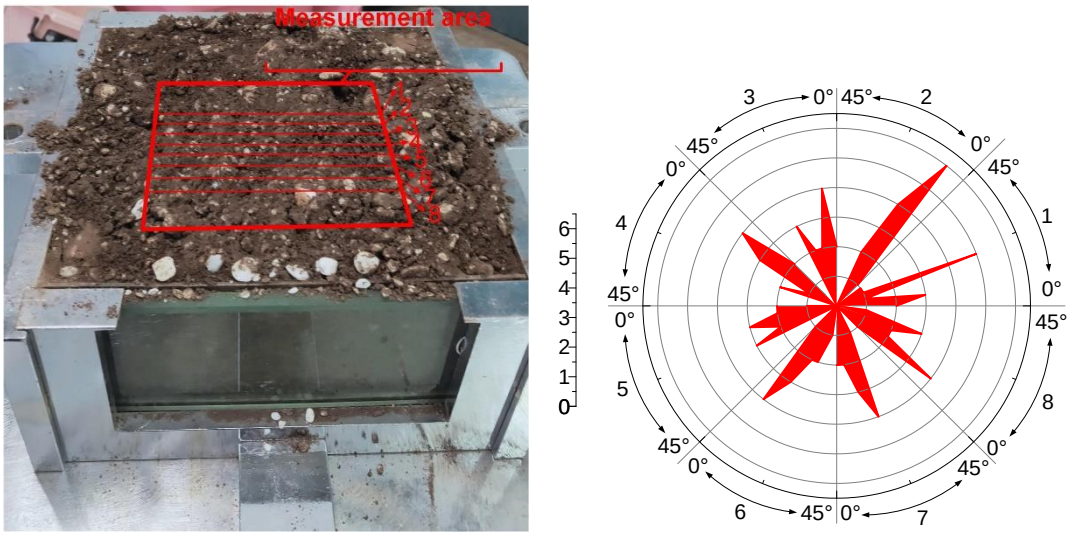

Fig.9- Comparison between actual shear surface and ice crystal flower diagram

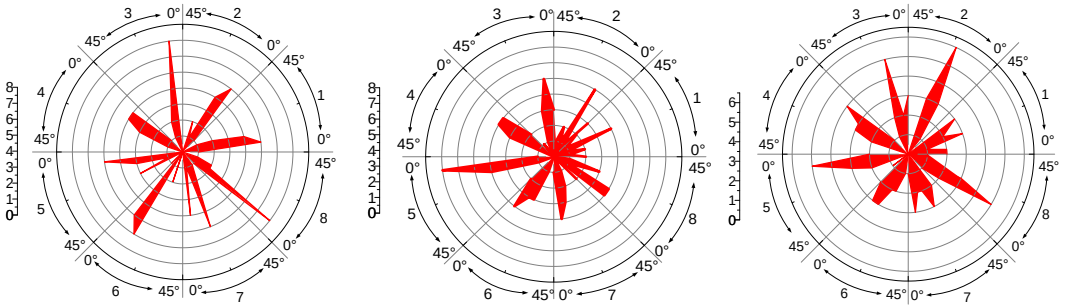

(a)group 1 (b)group 2 (c)group 3

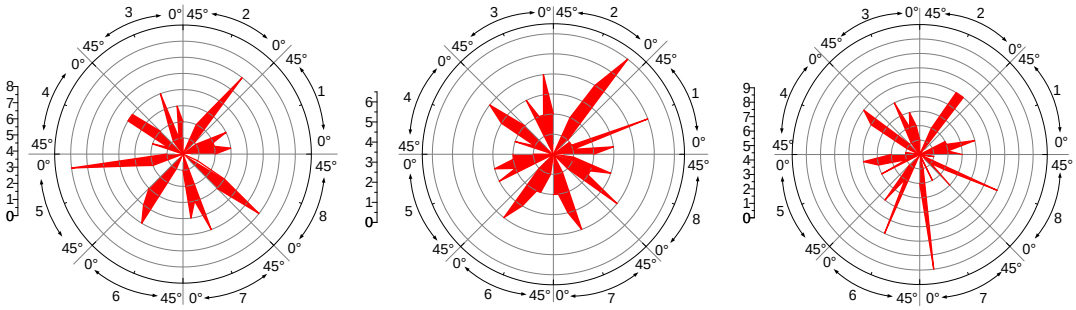

(d)group 4 (e)group 5 (f)group 6

Fig.10- Ice crystal flower diagram

As can be seen from Figure 10, when the proportion of particles in this interval is low, the ice

crystal flower diagram is generally closer to 0°, which shows that the angles of two adjacent points on the shear surface are mostly small, and the shear surface is relatively flat. With the increase in the particle size in this interval, the ice crystal flower diagram gradually approaches 45°, which means that with the increase in the particles in this interval, the angle between the two points of the shear surface generally increases, the shear surface is relatively rougher, and more obviously undulated.

Effect of coarse particle content on shear surface undulation morphology

Comparison of 3D topographic map of shear surface (coarse particle content group)

The content of coarse particles in slip zone soil was studied, and the groups are divided into 40%, 50%, 60%, 70%, and 80% according to the content of coarse particles, corresponding to groups 7, 8, 9, 10, and 11, respectively. For each group, three specimens were made at 50, 100, and 150 kPa, respectively.

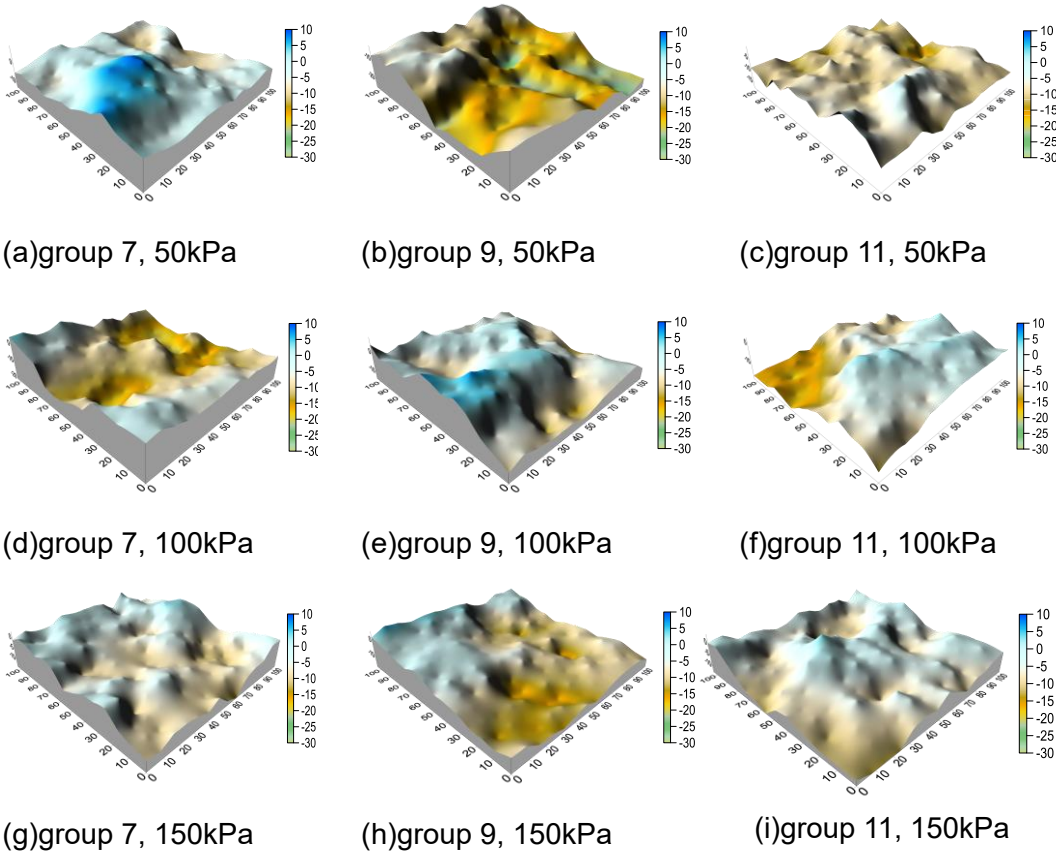

(a)group 7, 50kPa (b)group 9, 50kPa (c)group 11, 50kPa

(d)group 7, 100kPa (e)group 9, 100kPa (f)group 11, 100kPa

(g)group 7, 150kPa (h)group 9, 150kPa (i)group 11, 150kPa

Fig.11- Comparison of shear surface topographic map (coarse particle content, Unit: mm)

Figure 11 compares different coarse particle contents as variables and analyzes the three groups of 50, 100, and 150 kPa. Comparison at 50 kPa: The undulation of the group with 40% coarse particle content (Figure 11a) is smaller than that of the group with 60% coarse particle content (Figure 11b), and the roughness is lower. The two groups with 80% and 60% coarse particle content have more small protrusions and depressions and significantly more roughness compared with the 40%

shear failure surface. Comparison at 100 kPa: The two groups with coarse particle content of 80% and 60% (Figures 11f and 11e) are more undulating and relatively rougher. Although the shear surface of the group with coarse particle content of 40% (Figure 11d) has obvious protrusions and depressions, the undulation is smaller than that of the two groups. Comparison at 150 kPa: The shear surface morphologies of the two groups with 40% coarse particle content (Figure 11g) and 80% coarse particle content (Figure 11i) are similar, but the 80% group is rougher, and the 60% coarse particle content group (Figure 11h) has greater undulation than the 40% group. Thus, with the increase in the coarse particle content, the roughness of the shear surface of slip zone soil increases and the undulation increases. The mechanism is as follows: During the shearing process, the coarse particles in shear zone soil move and gradually rearrange along the shearing direction, forming an uneven shear surface. When the content of coarse particles is small, most coarse particles are completely wrapped by fine particles and fail to form effective contact, mainly relying on friction between particles to resist shearing. As the content of coarse particles increases, the solid matrix between coarse particles gradually forms, and the structural effect of the good interlocking bond is strong.

Statistical analysis of coordinate elevation of shear failure surface (coarse particle content group)

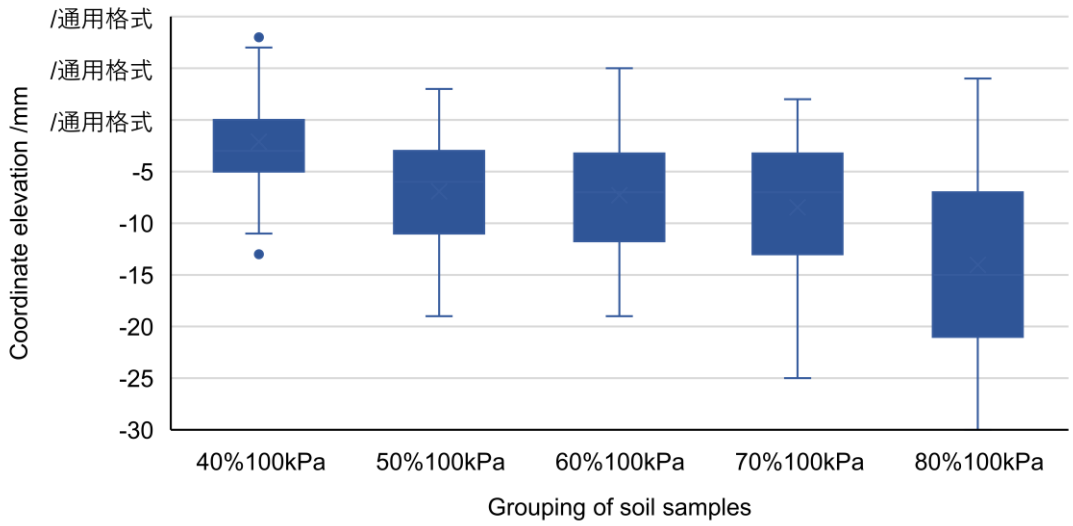

Fig.12- Elevation statistics of shear failure surface coordinate (coarse particle content group)

The shear failure surface elevation with different coarse particle contents was statistically analyzed and a box diagram was drawn. The test results under normal pressure of 100 kPa were taken as an example. The figure shows that the difference between the upper and lower edges and the difference between the upper and lower quartiles gradually increase with the increase in the coarse particle content. This finding means that the shear surface becomes relatively rough with the increase in the coarse particle content, and the undulation is more obvious. In addition, with the increase in the coarse particle content, the overall box plot of coordinate point elevation of the shear surface shows a decreasing trend.

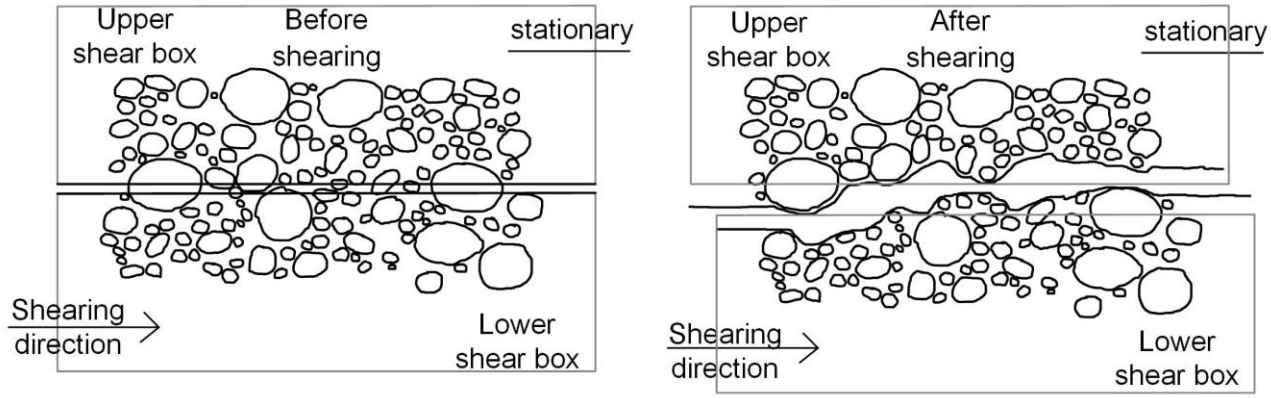

Fig.13- Schematic of the development of shear surface (group 9)

The structure in the figure (group with 60% coarse particle content) is relatively dense. The coarse particles are enough to fit well with each other and form a good solid matrix structure between them, and the fine particles are enough to fill the pores between the coarse particles, thus being a solid matrix dense structure. The protrusions in the shear zone of the structure are supported by coarse particles, which are not easily sheared off during the shear process. When the shear displacement increases continuously, the coarse particles continuously move and rotate under the action of the shear. As a result, the shear surface appears to be rougher.

Relative root mean square of undulation Z_2

According to the comparison of the calculated data (Z_2), no obvious rule exists for the particle gradation group (group 1-6), but an obvious correlation exists between the coarse particle content and the roughness of the shear surface as indicated by an analysis of the coarse particle content group. Therefore, with the coarse particle content taken as an example, quantitative analysis is conducted on the shear surface.

The roughness of the shear failure surface of slip zone soil is described by using the Z_2. A larger value corresponds to a rougher shear surface and a greater undulation. The parameter expression is as follows:

$$Z_2=\left\{\begin{array}{l}\dfrac{1}{\left(N_x-1\right)\left(N_y-1\right)}\left[\dfrac{1}{\Delta x^2}\displaystyle\sum_{i=1}^{N_x-1}\sum_{j=1}^{N_y-1}\dfrac{\left(Z_{i+1,j+1}-Z_{i,j+1}\right)^2+\left(Z_{i+1,j}-Z_{i,j}\right)^2}{2}\right. \\ \left.+\dfrac{1}{\Delta y^2}\displaystyle\sum_{j=1}^{N_y-1}\sum_{i=1}^{N_x-1}\dfrac{\left(Z_{i+1,j+1}-Z_{i+1,j}\right)^2+\left(Z_{i,j+1}-Z_{i,j}\right)^2}{2}\right]\end{array}\right\}^{1/2} \quad (4)$$

In the formula, $Z_{i,j}$ are the coordinates of the "*I*"-th data point on the X-axis and the "*j*"-th data point on the Y-axis on the Z-axis, and $Z_{i+1,j+1}$ are the coordinates of the "*i+1*"th data point on the X-axis and the "*j+1*"-th data point on the Y-axis on the Z-axis. N_x and N_y represent the number of measurement data points on the x-axis and y-axis, respectively. In this test, N_x=14, N_y=14. $\triangle x$ is the spacing of measured data points along the X-axis, and $\triangle y$ is the spacing of measured data points along the Y-axis. The spacing of data points measured in both the X-axis and Y-axis is 0.8 mm, so $\triangle x$=$\triangle y$ =0.8mm. The 3D elevation data points of the shear surface measured in the test are

substituted into the above formula to obtain the relative root mean square of undulation Z_2 which is used to represent the roughness of the shear surface.

According to the 3D shear surface data of different soil samples, the Z_2 obtained to represent the roughness of shear surface increases with the increase in coarse grain content under each normal pressure. Through data fitting, a highly positive linear correlation existed between Z_2 and the content of coarse grains, and the correlation was high under the normal pressure of 50, 100, and 150 kPa. In addition, in the case of the same gradation, Z_2 decreases with the increase in the normal pressure, which has obvious regularity.

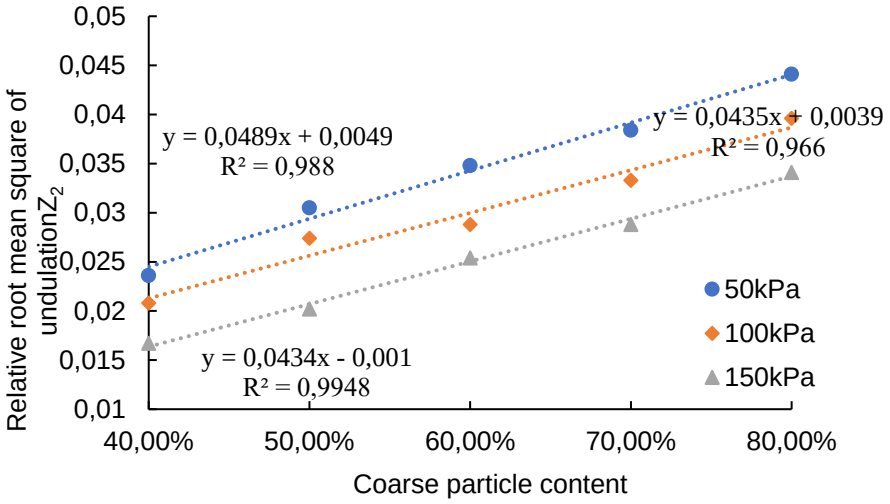

Fig.14- Relationship between shear surface roughness and coarse grain content of slip zone soil

CONCLUSION

(1) A significant correlation exists between the undulation morphology of shear surface of the coarse-grained slip zone soil and the proportion of particles with a size between 5–20 mm. Under the same normal pressure, with the increase of particles in the interval, the shear surface undulation gradually increases, and the roughness also becomes larger. The meso-structure model shows that when the proportion of coarse particles of 5–20 mm is small, a good solid matrix cannot be formed between each particle, and the protrusion strength is not enough. Most of the protrusions are cut off during the shear process, thus resulting in low roughness.

(2) The internal particles of well-graded soil samples have good internal structure and interlocking bond effect between coarse particles. Protrusions have high strength and are difficult to shear off. Therefore, the shear surface undulation and roughness of well-graded soil samples are more than those of poorly graded soil samples.

(3) The increase in the normal pressure inhibits the climbing movement of soil samples along the protrusions, and the most of protrusions are sheared off. Under the same particle gradation, a great normal pressure corresponds to a smaller shear surface undulation, and with a lower roughness, the shear surface is smoother.

(4) A highly positive linear correlation exists between Z_2 and coarse grain content. With the increase in the coarse grain content, the solid matrix between coarse particles is formed gradually, and the structural effect of the interlocking bond is strong, so the shear surface is rougher.

ACKNOWLEDGEMENTS

This work was supported by “the Fundamental Research Funds for the Central Universities” (Grant No. 2572018BJ02), Heilongjiang Provincial Natural Science Foundation of China (Grant No. LH2019D001)

REFERENCES

[1] Zhao Y. l, Zhang C. S, Wang Y. X, Lin H, 2020. Shear-related roughness classification and strength model of natural rock joint based on fuzzy comprehensive evaluation. International Journal of Rock Mechanics and Mining Sciences, Vol. 137: 104550.

[2] Liu Q. S, Tian Y. C, Liu D. F, Jiang Y. L, 2017. Updates to JRC-JCS model for estimating the peak shear strength of rock joints based on quantified surface description. Engineering Geology, Vol. 228: 282-300.

[3] Liu S. L, Chen S. X, Liu F, Luo H. M, Zhao W. G, 2013 Study of shear properties of weathered schist residual soil. Rock and Soil Mechanics, Vol. 34, No. 12: 3520-3526.

[4] Cheng D. X, Xu J, Liu Z. W, Ren J. W, 2017. Experiments on Large-scale Direct Shear Strength of Coarse-grained Saline Soil. Journal of Water Resources and Architectural Engineering, Vol. 15, No. 5: 149-153.

[5] Dong Y, Chai H. J, 2007. Experimental study on fractal character of shear surface of rock-soil aggregate mixture. Rock and Soil Mechanics, Vol. 28, No.5: 1015-1020.

[6] Ren S. S, Zhang Y. S, Xu N. X, Wu R. J, 2021. Mesoscopic response mechanism of shear surface roughness and residual strength in gravelly sliding zone soils. Chinese Journal of Geotechnical Engineering, Vol. 43, No. 8: 1473-1482.

[7] Singh S.K., Raval S., Banerjee B.P., 2021. Automated structural discontinuity mapping in a rock face occluded by vegetation using mobile laser scanning. Engineering Geology, Vol. 285: 106040.

[8] Rushikesh B, Masoud Z.N, Ebrahim E, Javad S, 2021. A state-of-the-art review of automated extraction of rock mass discontinuity characteristics using three-dimensional surface models. Journal of Rock Mechanics and Geotechnical Engineering, Vol. 13, No. 4: 920-936.

[9] Li Z.C., Liu Z.B., 2021. Influence of Particle Shape on the Macroscopic and Mesolevel Mechanical Properties of Slip Zone Soil Based on 3D Scanning and 3D DEM. Advances in Materials Science and Engineering, Vol. 2021: 9269652. DOI10.1155/2021/9269652.

[10] Jiang J.W., Xiang. W., Zhang X.Y., 2011. Research on mechanical parameters of intact sliding zone soils of huangtupo landslide based on ct scanning and simulation tests. Chinese Journal of Rock Mechanics and Engineering, Vol. 30, No. 5: 1025-1033.

[11] China Ministry of Housing and Urban-Rural Development. (2019),“Standard for geotechnical testing method(GB/T 50123 – 2019)” State Administration for Market Regulation, p: 344-348.

[12] Song L. Z, Song B. W, Shen T, and Yu B, 2015. A New Numerical Simulation Method for Three-Dimensional Mesoscale Analysis of Concretes, Mathematical Problems in Engineering, Vol. 2015: 627948.

[13] Sun Y.H., Song L.Z., Shen T., 2013. With Random Parametric Equation of Circle Inscribed Polygon Generation Algorithm and Analysis. Applied Mechanics and Materials I, Vol. 275-277: 2506-2510.

CIVIL ENGINEERING JOURNAL

Article no. 24

THE CIVIL ENGINEERING JOURNAL 2-2022

USE OF CALCINATION RESIDUE FROM RICE HUSK AS A SUBSTITUTE FOR CEMENT

Lyamine Briki, Loucif Ali Bouacida and Noureddine Lahbari

University of Batna 2, Faculty of Technology, Department of Civil Engineering, Batna, Algeria; l.briki@univ-batna2.dz, l.alibouacida@univ-batna2.dz, n.lahbarii@univ-batna2.dz

ABSTRACT

In this study, we have developed a new cement composed by a partial substitution of the clinker with artificial pozzolans rich in silica, obtained by treatment of lignocellulosic residues, in this case, ash from rice husk. This substitution is added to the clinker with percentages ranging from 25 to 75%. These substitutions were chosen on the basis of the presence of silica which can react with portlandite ($Ca(OH)_2$).

The results obtained show that these materials have, after activation, a great pozzolanicity that allows their addition to the Portland clinker with a percentage of up to 25% of the mass of the clinker.

The improvement of this reactivity is achieved by calcinating these additions at temperatures of 750°C. This significantly reduces the CO_2 emissions that accompany the production of Portland cement clinker.

KEYWORDS

Eco-cements, CPA cement, Rice husk ash, Calcination, resistance

INTRODUCTION

For many years, Portland cement has been the most widely used building material in the world because of its mechanical performance, fire holding and competitive cost.

However, its manufacture is very energy-intensive and emits a significant amount of carbon dioxide (CO_2) well known for its impact on the greenhouse effect [1-6].

The most effective strategy to reduce the carbon footprint of the cement industry on a worldwide scale is to reduce the clinker factor [7].

One of the alternatives to reduce the negative impact of the cement industry on the environment is to partially replace the clinker in Portland cement with pozzolanic materials to produce compound cements. Limestone calcined clay cements (LC3) are one of the promising alternatives for high performance sustainable cements [8-10]. Previous studies have focused on different stages of the processing of calcined clays, such as grinding [11-13] and color control [14]. These pozzolanic materials are either natural materials such as natural pozzolan [15], thermally treated materials such as metakaolin [16,17], or industrial by-products such as silica fumes and fly ash [18,19], as well as coal mash [20,21], silica fumes [22,23], flying ash [24-26], charred clay [27], limestone [28], mine tailings and polymeric waste [29], bauxite residue [30], river sediment [31,32]. These mineral additions, composed mainly of either silica or silica and alumina, exhibit a certain chemical activity called "pozzolanic" that allows them to react with lime to form compounds similar to cement hydrates.

B. Diana et al. [33] show that the use of 20% crushed mash as a partial substitution for CEM I reduces the cost of conventional concrete with Portland cement by 9.3%. In addition, these pozzolanic materials contribute to the improvement of the mechanical characteristics of concretes through the development of the pozzolanic activity [34].

Today, it is accepted that silica and alumina in the glass phases are reactive [35]. The incorporation of the rice husk as reinforcement in a cement matrix has been the subject of some work, notably those of Morsi [36] as well as those that essentially summarize the work of Julian Salas Serrano at the Eduardo Torroja Institute (Spain) [37,38].

The use of rice husk without calcination in combination with a mineral binder has been little studied. Only a few works open up prospects for the upgrading of this by-product in the manufacture of lighted mortars based on Portland cement [37-39]. However, most of this work involves a small fraction of rice husk in the matrix and mineral aggregates are sometimes retained.

In the building sector, ash from the burning of rice husk has been the subject of much research [40-42]. Rice husk is characterized by a lower organic matter content than most other lignocellulosic resources since it contains about 20% amorphous silica concentrated mainly on its outer surface (convex) [41,43]. As a result, when the rice husk is charred above 500°C, the organic matter disappears and gives way to a very silica-rich nanometric ash (SiO_2).

The ashes contain 95% silica and develop a very high pozzolanic reactivity [43,44]. They can therefore be used as a pozzolanic filler in Portland cements to improve the mechanical performance of ordinary concretes in the same way as fly ash or silica fumes [35].

This is a strategy emphasized in this paper. The aim is to study the pozzolanic quality of rice husk ash in mortar and the experimental work relates to the development of different mortar compositions integrating the rice husk ash, the mechanical strengths are then determined.

MATERIALS AND METHODS IN MECHANICAL APPROACH

Materials and mixtures

Cement

The Portland Cement used is type CEM I 42.5 N without any addition (95% clincker with 5% gypsum), produced by the GICA group of Ain-Touta located in Batna City (Algeria) and compliant with the standard NF EN 197-1 (NF EN 197-1, 2000) whose clinker is produced and ground in conjunction with gypsum by the GICA group. This cement is used for the formulation of mortars by setting the ratio E/C equal to 0.5. The dosage of natural gypsum (dehydrated calcium sulphate, $CaSO_4.\ 2H_2O$) was kept constant at 5%.

Properties of cement are mentioned in Table 1.

Tab. 1 – Physical properties of Portland Cement.

No	Property	Test results
1	Physical properties:	
	Apparent volumetric mass (g/cm^3)	1.100
	Absolute volumetric mass (g/cm^3)	3.190
	Fineness of grind (cm^2/g) [Specific surface]	4200
	Density	3.138
	Take time: Start (hours)	2h:12
	Take time: End (hours)	3h:08
2	Chemical composition (% mass):	
	SiO_2	20.34
	Al_2O_3	5.37
	Fe_2O_3	3.75
	CaO	63.83
	MgO	1.80
	SO_3	2.20
	K_2O	1.07
	Insoluble residue	1.12
3	Bogue's formula:	
	C_3S	57.83
	C_2S	16.75
	C_3A	8.03
	C_4AF	10.92
4	Compressive resistance:	
	2 days	31.70
	7 days	47.05
	28 days	50.30
5	Bending resistance:	
	2 days	5.90
	7 days	7.70
	28 days	8.85

Rice husk ash

Fig. 1 – Rice husks before and after calcining.

After combustion of rice husks, the ash was finely pulverized. Chemical composition and physical properties of the RHA are given in (Table 2).

Tab. 2 – Chemical composition and physical properties of the rice husk ash.

No	Property	Rice husk ash
1	Constituents (%):	
	SiO_2	86.98
	Al_2O_3	0.84
	Fe_2O_3	0.73
	Na_2O	0.11
	K_2O	2.46
	CaO	1.40
	MgO	0.57
2	Fire loss (%) [quantity of 45 grams]	
	T°p 200°C	8.26
	T°p 300°C	50.78
	T°p 400°C	62.46
	T°p 500°C	73.00
	T°p 600°C	73.34
	T°p 700°C	73.76
	T°p 800°C	73.04
	T°p 900°C	74.72
	T°p 1000°C	77.06
	T°p 1100°C	77.62
3	Specific surface (cm^2/g) [EN 196-6]	16455
4	Absolute density (g/cm^3)	2.635
5	Mean particle size (μm)	5
6	Water content (%)	16.50

The pozzolanic activity of ash is determined by the Chapel test, which was performed twice on each of the charred samples at a given temperature. The average values are shown in the following Figure 1:

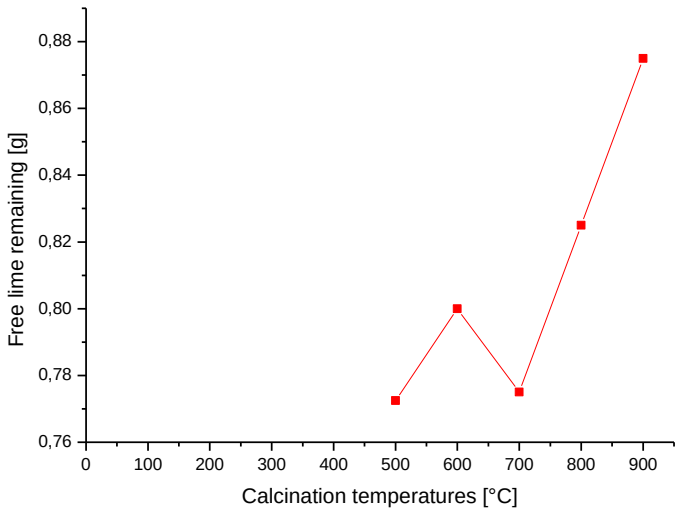

Fig. 2 – Chapel Test: Remaining Free Lime depending on temperature.

A second test measuring pozzolanic activity is Luxan, based on the measurement of the change of electrical conductivity in a solution saturated with $Ca(OH)_2$ lime after addition of pozzolanic ash.

The average values of electrical conductivity for different temperatures are shown in the following Figure 2.

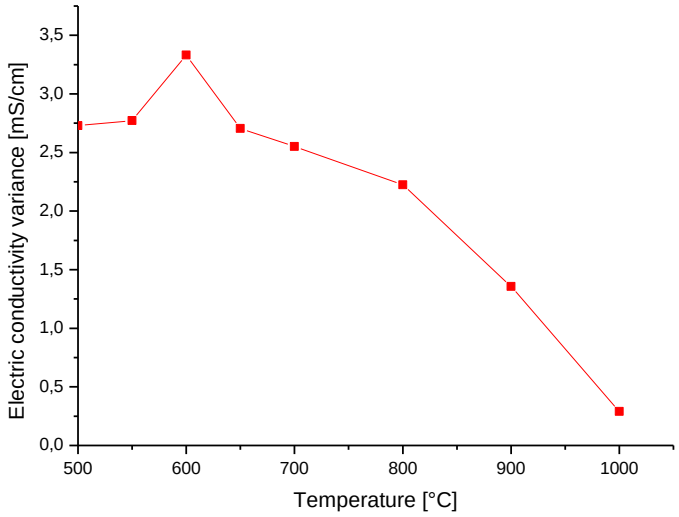

Fig. 3 – Luxan Test: the variation of conductivity based on temperature.

The mineralogical composition of the ash was determined by XRD. The XRD was carried out on three samples of rice husk ash calcined at different temperatures: 600, 700 and 800 ° C.

600°C

T W (	d-spacing (Å)		Angle (°2Theta)	Background (counts/s)		Significance
	12,85512	65,61	8,63719	18,24	172,79	0,28000	0,72
	5,69569	64,96	19,57060	18,06	131,03	0,12000	0,85
	5,03955	51,36	22,14895	14,28	155,20	0,48000	1,00
	4,20311	100,00	26,63066	27,80	214,44	0,12000	0,74
	3,34657	89,16	33,62696	24,79	147,38	0,20000	1,08

Fig. 4 – XRD results for rice husk ash – 600°C.

700°C

T W (	d-spacing (Å)		Angle (°2Theta)	Background (counts/s)		Significance
	4,07434	29,96	27,48859	15,25	230,06	0,10000	0,67
	3,99741	100,00	28,02837	50,89	228,59	0,10000	0,63
	3,33671	46,50	33,72937	23,66	148,26	0,48000	0,68

Fig. 5 – XRD for rice husk ash – 700°C.

800°C

T W (	d-spacing (Å)		Angle (°2Theta)	Background (counts/s)		Significance
	6,51061	16,81	17,10127	7,35	117,25	0,80000	0,75
	6,05491	71,39	18,39910	31,23	118,13	0,06000	0,60
	3,33680	100,00	33,72838	43,74	136,05	0,24000	1,66
	2,89753	19,36	39,03376	8,47	86,65	0,20000	0,61

Fig. 6 – XRD for rice husk ash – 800°C.

With reference to the tables of the results, only the sample calcined at 700°C. has a peak at 4.07434 Å characterizing the presence of crystobalite whose “d” is between 4.05 and 4.13. The sample of the ash obtained at 600°C. contains a “d” close to 4.2031 Å which can explain the presence of crystobalite. The intensity of this peak is lower than that representing crystobalite at 700°C. this therefore explains the formation of crystalline phases when the temperature increases.

Note that between the XRD characterizing ash calcined at 600°C. and the XRD for ash calcined at 800°C., the quantity of quartz decreases, so quartz is transformed into a crystalline phase.

Sand

The standard sand is packaged in polyethylene bags each containing 1350 g ± 5g. Physical properties and chemical composition are shown in Table 3.

Tab. 3 – Physical properties and chemical composition of standardized sand.

No	Property		Cumulative percentage retained (%)
1	Sieve size (mm):		
	0.08		99 ± 1
	0.16		87 ± 5
	0.50		67 ± 5
	1.00		33 ± 5
	1.60		7 ± 5
	2.00		0
2	Chemical constitute:		Constituents (%)
	CaO		1.090
	Al_2O_3		1
	SiO_2		94.789
	Fe_2O_3		0.650
	MgO		0.130
	K_2O		0.300
	Cl^-		0.030
	SO_3		0.080

Mixture proportioning

Four mixtures of thirty-six mortar test pieces prepared in this experimental work complying with the European standard NF EN 196-1.

A study conducted by Siline Mohammed and Omary Safiuallah [45] with the objective of experimentally searching for the optimum gypsum content of a Portland Cement CEMI was concluded that the optimum of this cement is 5.5%. So, we opted for a Portland Cement CEMI (PC) composed of 94.5% clinker and 5.5% gypsum with a characteristic 28-day strength of 50.3Mpa.

The chemical compositions of the gypsum are given by the following Table 4:

Tab. 4 – Chemical composition of gypsum.

Elements %	SiO_2	Al_2O_3	Fe_2O_3	CaO	MgO	SO_3	K_2O	Na_2O	CL
Gypsum	8.50	2.54	1.04	29.32	3.07	36.53	0.53	0.03	0.008

Preparation of test specimens

All mixtures with a constant water/binder ratio of 0.5 were manufactured with a binder content of 450g and a sand content of 1350 g, i.e. a C/S ratio 1/3.

The binder content of all other mixtures is kept fixed at 450 g. Of the four mixtures, the first is composed only of PC without using superplasticizer, it serves as a reference in this experimental program, the ashes of the rice husk (RHA) were used to replace 25%, 50% and 75% by mass of PC

without adding superplasticizer in order to study the influence of RHA on the practicability. These are three RHA1, RHA2 and RHA3 mixtures respectively.

Additional or less water may be substituted for certain compositions to provide sufficient workability. The proportions by mass of the various constituents of the cement are mentioned in Table 5.

Tab. 5 – Identification of different mixtures.

Type of cement	Constituents of Cement			Constituents of the mortar		
	Clinker [%]	Gypsum [%]	RHA [%]	Cement [g]	Water [ml]	Sand [g]
PC	94.50	5.50	00.00	450	129	1350
RHA1	69.50	5.50	25.00	450	165	1350
RHA2	44.50	5.50	50.00	450	240	1350
RHA3	19.50	5.50	75.00	450	260	1350

In the anhydrous state, the cements were subjected to chemical treatments to determine the density and density tests and Blaine Specific Surface BSS tests according to EN 196, NF EN 196-1 and EN 196-6 respectively.

The physical properties studied are: the normal consistency and the start and end time determined by the Vicat test of pure compound cement pastes used in accordance with NF 196-3.

The consistency of the mixtures will be tested as well as the compressive and bending strength on standardized test pieces 4x4x16 cm^3 according to the standards NF P-18-406 and NF P18-407.

After removal from the mold at 24 hours of age, the test pieces are kept in a humid environment (20° C. and 100% RH) until the age of the compressive and bending test at 2, 7 and 28 days according to the standard NF P15-402.

EXPERIMENTAL, RESULTS AND DISCUSSION

Workability

It is measured according to the standard NF EN 1015-3 and determined by means of shaking table. The spreading diameters for each of the mortars are mentioned in Table 6.

Tab.6 – Mortar Consistency Test Results.

Composition	D1 (mm)	D2 (mm)	Spreading diameter
PC	156	158	157
RHA1	113	119	116
RHA2	148	140	144
RHA3	-	-	-

RHA2 and RHA3 mortars each performed poorly in terms of consistency. For RHA3 mortar, there is no clear formation of a cake after the shaking. The mixture being too dry. It is obviously a lack of water.

Influence of normal consistency on synthesized cements

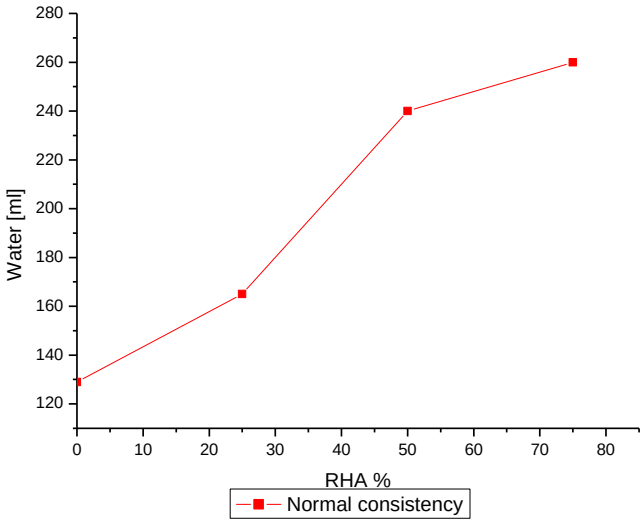

Fig. 7 – Normal Consistency Test Results.

The addition of RHA brings some challenges to the water demand and workability of clinker-based mortars. Water demand has been shown to be greater when cement is substituted with RHA. This is explained by the large specific surface area due to porous nature and giving a sponge role to the ash. This unfavorable effect is especially remarkable for RHA mixtures with finer cements with a long grinding time.

In addition, the demand for water is increased when there is a high carbon content in the ash, as carbon is as porous but finer than silica. The demand for water also increases with the grinding time to reach a maximum and then decreases with a pronounced grinding. This increase in water demand can offset the decrease in workability.

Influence of RHA substitution rate on the intake of the cement used

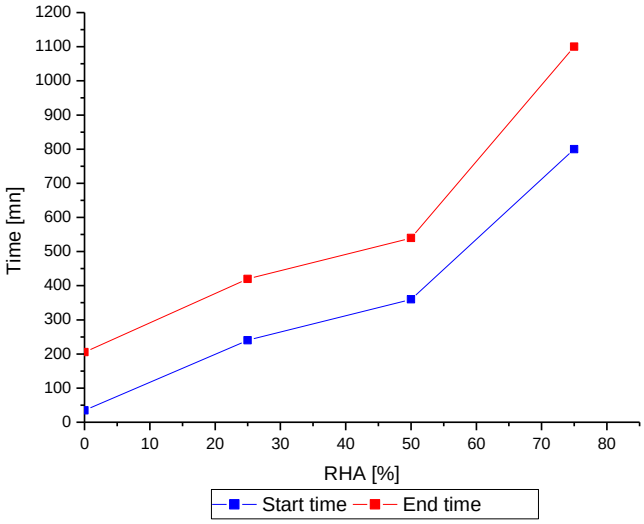

Fig. 8 – Start and End Results.

Figure 7 shows that RHA cements have a much longer time than standard Portland cement. The sitting time evolves in the same direction as the percentage of RHA.

This setting time is due to the addition of gypsum in the mixture of the synthesized cement. This delay can be explained by the existence of soluble extractables in RHA which reduces the rate of hydration of alite (C_3S). The latter forms an obstacle to the progress of hydration. This is due to the slow reaction of the pozzolanic [49].

Density Influence on the pulp of the cement used

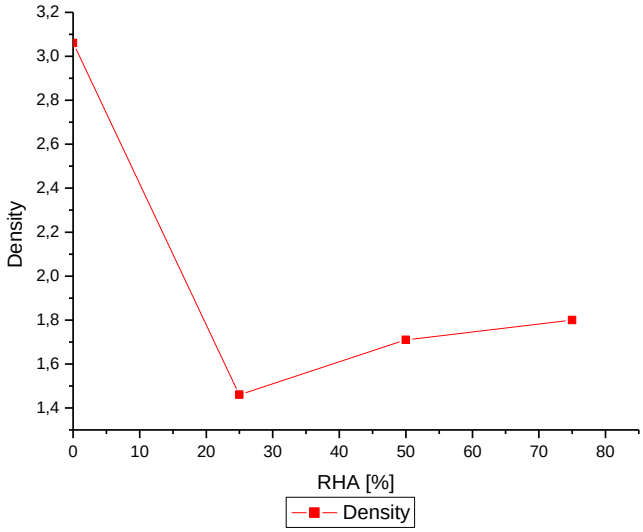

Fig. 9 – Effect of RHA addition rate on density.

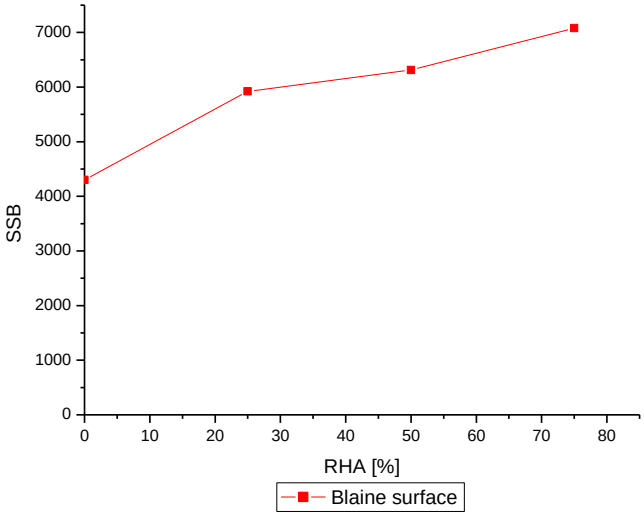

Fig. 10 – Effect of RHA addition rate on Blaine Specific Surface.

It is found that the BSS area of the synthesized cements increases as a function of the increasing rate of clinker substitution, this may be due to the nature of the incorporated substitution (RHA).

The RHA cement density is smaller than that of PC. Consequently, if a portion of cement is replaced with RHA relative to the mass, the volume of the mixture pastes increases. RHA cements prevent cement particles from forming in blocks.

Influence of moisture and fire loss on cement paste used

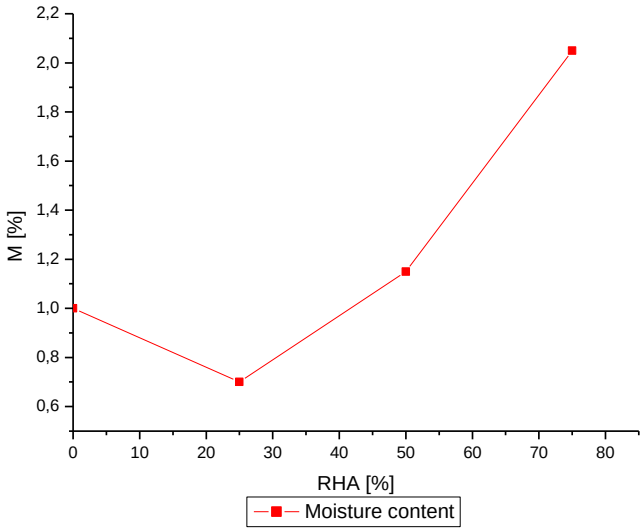

Fig. 11 – Moisture content of synthesized cement.

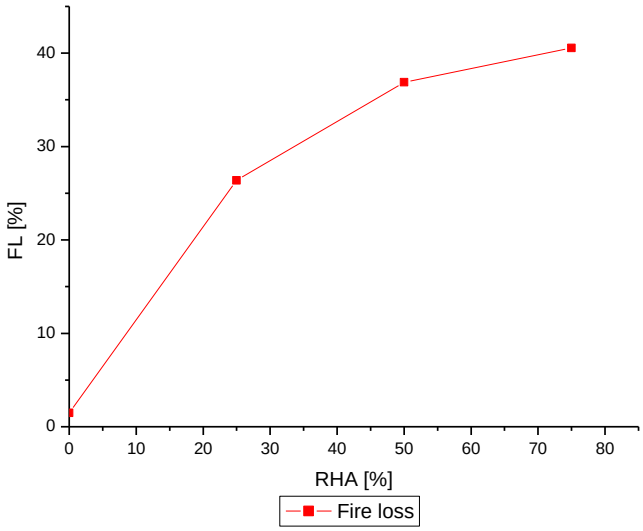

Fig. 12 – Fire loss of synthesized cement.

The moisture content accelerates the hydration kinetics of the C_2S, which is particularly slow in the heart of the synthesized cements. Thus, the effect of the large specific surface area on the pozzolanic reaction reacts with the $Ca[OH]_2$ Portlandite released during the hydration of the cement to form other additional crystals of CSH in large quantities.

The cellulose/lignin matrix of the rice husk is destroyed by fire, represents only 20-25% of the initial weight and leaves behind irregular and angular particles consisting of a porous siliceous skeleton. Although the ash particles of rice husks are not very small, they have a very large specific surface mainly internal due to their porosity. However, this again depends on the calcination conditions, i.e. temperature and duration, since the crystallization of the silica leads to the agglomeration of the particles and to the transformation into a granular compact structure [46]. After grinding, the porous structure breaks and gives rise to fine porous particles having properties similar to those of silica fumes [48].

Mechanical behaviour of mortars

Crushing tests of the 4x4x16 cubic specimens were carried out in order to determine the average resistance of three specimens at different hardening ages.

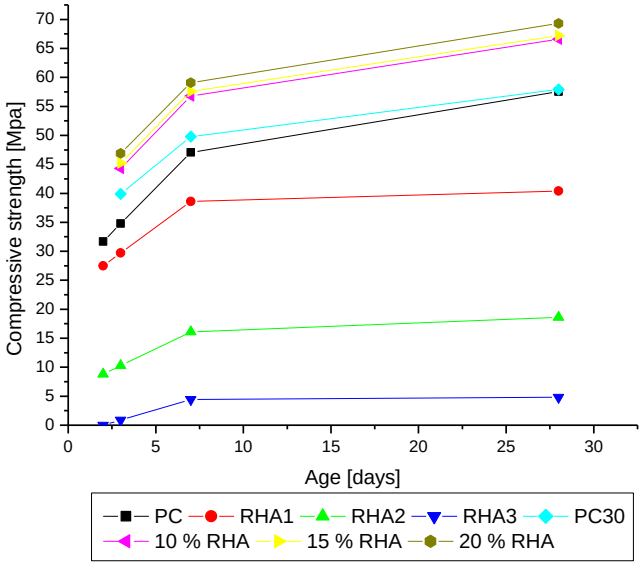

Fig. 13 – Compression test results.

Our PC mortar has compressive strength almost the same as the PC30 manufactured by D.D.Bui et al. [47] see even a little more, but other concretes made by the same authors including 10%RHA, 15%RHA and 20%RHA for their high resistance, are mainly due to the use of superplasticizer and in addition the W/B ratio is taken equal to 0.34.

The RHA1 mixture has a compressive strength at 28 days (40.40Mpa) equivalent almost to 3/4 that of the PC control mortar (57.55Mpa), with a water / binder ratio having been kept equal to 0.5.

Similarly, tensile tests on three supports of standardized 4x4x16 specimens were also carried out in order to determine the average tensile strength of three specimens at different hardening ages.

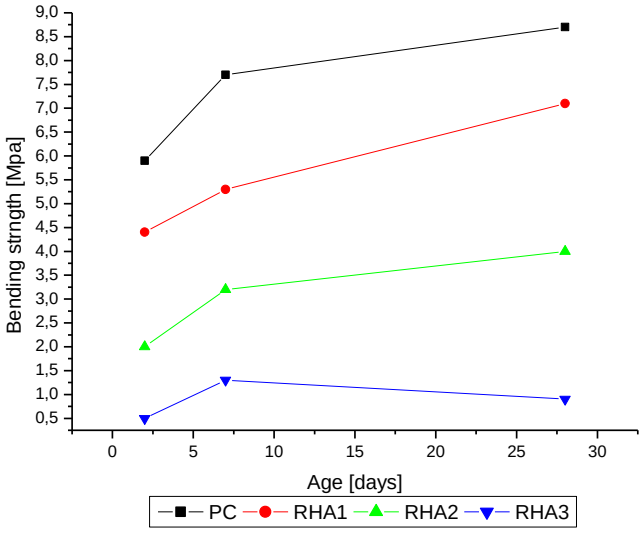

Fig. 14 – Bending test results.

The two preceding figures place in certainty that the resistances of the mortars evolve increasing with time and have no fall apart from RHA3 which has 75% of clinker substitution. These evolutions are clearly visible on the graphs of the flexural and compressive resistances. It can be seen that the control mortar, the first mixture with 100% artificial Portland cement PC, has for each of the ages a resistance higher than those of other mortars. At 28 days, it complies well with the strength stated in the data sheet i.e. a minimum of 50.3MPa in compression.

It should be noted that the increase in compression and bending resistance as a function of the hardening age is practically identical for all mortars tested except for the RHA3 compound cement which remains monotonous between 7 and 28 days in compression and decreases in traction by bending.

Figure 13 shows us that at a young age the cements synthesized with RHA have a low resistance except for the cement with 25% RHA which has an acceptable resistance with respect to the PC cement, while those synthesized with 50% and 75% RHA have lower or even insufficient resistance especially for the RHA3 compound cement.

The short-term resistances (2, and 7 days) are due to the tricalcium silicate (C_3S) contained in the cements and the 28-day resistance is due mainly to the belite (C_2S).

In fact, the evolution of the resistors depends on the RHA content and the storage time of the test pieces, as well as on the C_3S. Thus, RHA could have an effect on the clinker reactivity in the short term, manifested by an increase in setting time and a decrease in resistance.

To provide such a mortar with acceptable mechanical resistance, the water / cement ratio must be considered.

CONCLUSIONS

This article has undeniable technical, economic, and ecological interests.

Indeed, the study undertaken in the latter, tells us:

- that it is possible to exploit the rice husks ash that has proven qualitatively that it could be a good artificial pozzolan,
- that it was revealed that after calcination and following an X-ray diffractometry study showed that the ash was partially amorphous and partially crystalline with visible cristobalite traces.
- that is allowed us to study the influence of rice husk ash as a substitute on the Portland cement manufacturing process,
- that the results allowed us to limit the percentage of RHA in cement and to find new types of cement with different substitution percentages.
- that only 25% RHA cement has a standardized resistance,
- this 25% substitution of clinker reduces the energy consumption of the clinker almost to half of 1450 degrees Celsius to 750 degrees Celsius,
- that it contributes accordingly to the improvement of the environment by reducing CO_2 emissions.

This approach of uniting various cement materials (clinker, RHA) is becoming increasingly receptive to the new way of developing mortars and can be improved and enriched in the near future by recommendations which are:

- The water / binder ratio will have to be increased to allow greater workability.
- Experimentally find the optimum content of the synthesized gypsum cement.
- Improve the density of the mixture-mortar by improving the filling of particles by adding a superplasticizer.
- Influence of pozzolanic activity as a function of grinding time and therefore of the specific surface area of the ash particles.
- Calcine the rice husk and use the residues resulting from this calcination as a complement to a binder such as lime for example.

REFERENCES

[1] Boden, T., Andres, B., Marland, G., 2016. Global CO2 Emissions From Fossil-fuel Burning (Cement Manufacture, and Gas Flaring).
[2] Parrott, L. J., 2002. Cement, concrete and sustainability. A report on the progress of the UK cement and concrete industry towards sustainability (British Cement Association).
[3] Flower, D. J. M., Sanjayan, J. G., 2007. Green House Gas Emissions due to Concrete Manufacture, (International Journal of Life Cycle Assessment), 12 (5), 282-288.
[4] Habert, G., Roussel, N., June 4-6, 2008. How to design concrete with a low environmental impact? (XXVIth University Meetings of Civil Engineering), Nancy, France.
[5] Collins, F., 2010. Inclusion of Carbonation during the Life Cycle of Built and Recycled Concrete: Influence on their Carbon Footprint (International Journal of Life Cycle Assessment), 15 (6), 549-556.
[6] Emad, B., Gholamreza, Z., Ezzatollah, S., et Alireza, B., 2013. Global strategies and potentials to curb CO2 emissions in cement industry (Journal of Cleaner Production), vol. 51, pp. 142-161.
[7] Scrivener, K.L., John, V., Gartner, E.M., 2016. Eco-efficient cements: potential, economically viable solutions for a low-CO2, cement-based materials industry, in: United Nations Environmental Programme UNEP.
[8] Scrivener, K., Martirena, F., Bishnoi, S., Maity, S., 2017. Calcined clay limestone cements (LC3), Cem. Concr. Res. 1 – 8, https://doi.org/10.1016/j.cemconres.2017.08.17.
[9] Scrivener, K., Avet, F., Maraghechi, H., Zunino, F., Ston, J., Hanpongpun, W., et al., 2019. Impacting factors and properties of limestone calcined clay cements (LC3), Green Mater. 7 3 – 14, https://doi.org/10.1680/jgrma.18.00029.
[10] Zunino, F., Martirena, F., Scrivener, K., 2020. Limestone Calcined Clay Cements (LC3), ACI Mater. J, Submitted.
[11] Zunino, F., Scrivener, K., 2020. Assessing the effect of alkanolamine grinding aids in limestone calcined clay cements hydration, Constr. Build. Mater. https://doi.org/10.1016/j.conbuildmat.2020.121293.
[12] Zunino, F., 2020. Limestone calcined clay cements (LC3): raw material processing, sulfate balance and hydration kinetics (EPFL Thesis), 8173.
[13] Zunino, F., Scrivener, K., 2020. Increasing the kaolinite content of raw clays using particle classification techniques for use as supplementary cementitious materials, Constr. Build. Mater. 244. Doi: https://doi.org/10.1016/j.conbuildmat.2020.118335.
[14] Martirena Hernandez, J.F., Almenares-Reyes, R., Zunino, F., Alujas-Diaz, A., Scrivener, K.L., 2020. Color control in industrial clay calcination (RILEM Tech), Lett. 5 1 – 7. Doi :10.21809/rilemtechlett.2020.107.
[15] Mokhtaria, B., Fatiha, K. A., et Abdelaziz, S., June, 2009. Durability of mortars based on natural pozzolana and artificial pozzolan (Nature and Technology Review), vol. 01, p. 63 to 73.
[16] Antoni, M., 2011. Investigation of Cement Substitution by Combined Addition of Calcined Clays and Limestone (Federal Institute of Technology in Lausanne).
[17] Rikioui, T., Tafraoui, A., et Mekkaoui, S. L., 2011. Use of metakaolin from the south-west region of Algeria in the formulation of economic concrete, e. A.
[18] Hosseini, M. M., Shao, Y., et Whalen, J. K., 2011. Biocement production from silicon-rich plant residues: Perspectives and future potential in Canada (Biosystems Engineering).
[19] Ayrinhac, F. 2005. Valorization of fluidized bed boiler fly ash circulating in the civil engineering sector, Materials (INSA of Toulouse France).
[20] Cheriaf, M., Cavalcante, J., et Pera, R. J., 1999. Pozzolanic properties of pulverized coal combustion bottom ash, Cem. Concr. Res. 29, p. 1387–1391.
[21] Haldun, K., et Mine, K., 2007. Usage of coal combustion bottom ash in concrete mixture (Construction and Building Materials), pp. 1922-1928.
[22] Habert, Assessing the environmental impact of conventional "green" cement production. In Pacheco-torgal, Cabeza, F., Labrincha, L.J., et De Magalhaes, A., 2014. Echo-efficient Construction and Building Materials: Life cycle assessment (LCA), echo-labelling and case studies (chap. 10, p.199-238). Cambridge, Woodhead Publishing Limited.
[23] Kadri, E., Kenai, S., Ezziane, K., Siddique, R., DE Schutter, G., 2011. Influence of metakaolin and silica fume on the heat of hydration and compressive strength development of mortar (Applied clay science), vol. 53, p. 704-708.

[24] Amato, I., 2013. Green Cement: Concrete Solutions (Nature), vol. 494, n° 7437, p. 300-301.
[25] Setting the Standard for Sustainable Concrete Construction. 2015. In Ceratech. Green Concrete Sustainability.
[26] Aghabaglou, A., MSezer, G.I., Ramyar, K., 2014. Comparison of fly ash, silica fume and metakaolin from mechanical properties and durability performance of mortar mixtures view point (Construction and Building Materials), vol. 70, p. 17-25.
[27] Siline, M., Ghorbel, E., Bibi, M., 2016. Valorization of pozzolanicity of Algerian clay: Optimization of the heat treatment and mechanical characteristics of the involved cement mortars (Applied Clay Science), vol. 132-133, p. 712–721.
[28] Holcim and Lafarge complete merger and create Lafarge Holcim, 10 july 2015. A new leader in the building materials industry. Media Release. In Lafarge Holcim. Media Relations.
[29] Sui, S., Wilson, W., Georget, F., Maraghechi, H., Kazemi-Kamyab, H., Sun, W., et al., 2019. Quantification methods for chloride binding in Portland cement and limestone systems (Cem. Concr. Res.), 125. Doi: https://doi.org/10.1016/jcemconres.2019.105864.
[30] Bentz, D.P., Stutzman, P.E., Zunino, F., 2017. Low-temperature curing strength enhancement in cement-based materials containing limestone powder (Mater. Struct. Constr.), 50, doi: https://doi.org/10.01617/s11527-017-1024-6.
[31] Hoang, K., Justnes, H., Geiker, M., 2016. Early age strength increase of fly ash blended cement by a ternary hardening accelerating admixture (Cem. Concr. Res.), 81 59 – 69, https://doi.org/10.1016/j.cemconres.2015.11.004.
[32] Li, X., Ouzia, A., Scrivener, K., 2018. Laboratory synthesis of C3S on the kilogram scale (Cem. Concr. Res.), 108 201 – 207, https://doi.org/10.1016/6j.cemconres.2018.03.019.
[33] Diana, B., Girts, B., et Liga, U., 2013. Coal Combustion Bottom Ash as Micro filler with Pozzolanic Properties for Traditional Concrete (Procedia Engineering), n° 157, pp. 149-158.
[34] Hüseyin, Y. A., Metin, G., Mustafa, D., et Ilker, T., 2010. Utilization of waste marble dust as an additive in cement production (Materials and Design), vol. 31, p. 4039–4042.
[35] Semcha, A., 2006. Valorization of dredged : Applications in the BPW, case of Fergoug dam (University of Reims Champagne-Ardenne).
[36] Ibrahim Nasr Morsi, M., 2011. Properties of rice straw cementitious composite (Doctoral thesis from the Technical University of Darmstadt, Germany).
[37] Salas Serrano J., and Veras Castro, J., 1985. Building materials with insulating properties based on rice husk (Inf. la Constr.), vol. n°372.
[38] Salas, J., Alvarez, M., and Veras, J., 1986. Lightweight insulating concretes with rice husk (Int. J. Cem. Compos. Light. Concr.), vol. 8, no. 3, pp. 171–180.
[39] Jauberthie, R., Rendell, F., Tamba, S., and Cisse, I., 2003. Properties of cement—rice husk mixture (Constr. Build. Mater.), vol. 17, pp. 239–243.
[40] Ganesan, K., Rajagopal, K., and Thangavel, K., 2008. Rice husk ash blended cement: Assessment of optimal level of replacement for strength and permeability properties of concrete (Constr. Build. Mater.), vol. 22, no. 8, pp. 1675–1683.
[41] Jauberthie, R., Rendell, F., Tamba, S., and Cisse, I., 2000. Origin of the pozzolanic effect of rice husks (Constr. Build. Mater.), vol. 14, no. 8, pp. 419–423.
[42] Xu, W., Lo, Y. T., Ouyang, D., Memon, S. A., Xing, F., Wang, W., and Yuan, X., 2015. Effect of rice husk ash fineness on porosity and hydration reaction of blended cement paste (Constr. Build. Mater.), vol. 89, pp. 90–101.
[43] Johar, N., Ahmad, I., and Dufresne, A., 2012. Extraction, preparation and characterization of cellulose fibres and nanocrystals from rice husk (Ind. Crops Prod.), vol. 37, no. 1, pp. 93–99.
[44] Tran, T. P. T., Benezet, J. C., and Bergeret, A., Jul. 2014. Rice and Einkorn wheat husks reinforced poly (lactic acid) (PLA) biocomposites: Effects of alkaline and silane surface treatments of husks (Ind. Crops Prod.), vol. 58, pp. 111–124.
[45] Siline, M., Omary, S., 2018. Optimization of the SO3 content of an Algerian Portland cement: Study on the effect various amounts of gypsum on cement properties (Construction and Building Materials), vol. 164, p. 259–262.

[46] Jaturapitakkul, C., and Ronngreung, B., 2003. Cementing Material from Calcium Carbide Residue-Rice Husk Ash.
[47] Bui, D. D., 2001. Rice husk Ash as a Mineral Admixture for High Performance Concrete, Pays-Bas.
[48] Sabuni, E., 1995. Research into the potentialities of rice husk ash cement for application in rural Tanzania, Pays-Bas.
[49] Bui, D. D., Hu, J., and Stroeven, P., 2005. Particle size effect on the strenght of rice husk ash blended gap-graded Portland cement concrete.

CIVIL ENGINEERING JOURNAL

Article no. 25

THE CIVIL ENGINEERING JOURNAL 2-2022

STUDY ON THE INFLUENCE OF THE CONFINEMENT EFFECT ON THE BOND STRENGTH RECOVERY IN THE DEFECTIVE GROUTED SLEEVE CONNECTION

Kulondwa Kahama Espoir, Xie Fuzhe, Ali Abdulkadir Aden and Faisal Iliasu Illo

Jiangsu University, Faculty of Civil Engineering and Mechanics, Department of Civil Engineering, Zhenjiang, 301 Xuefu road, China; espoirkulondwa@gmail.com, xiefuzhe@ujs.edu.cn, calidhuux88@outlook.com

ABSTRACT

Defects emanating from the onsite operation of the grouted sleeve connector have a significant impact on the ultimate tensile capacity of the connector. In this research, an experiment on the capacity of the fully grouted sleeve connector considering different configurations of defects was carried out. The experiment results indicated that the connector is highly sensitive to the location of the defects, which engenders a drop of 15% in the ultimate capacity of the connector. Based on the accurate simulation of the experiment model, a series of parametric analyses were conducted to evaluate the interaction of defects with other mechanical properties of the connector. It was found that the different values of the ratio of the sleeve diameter to that of the bar within the design recommended interval significantly influence the connection's performance. The lowest ratio value engenders approximately 10% to 16% of tensile strength recovery in the weakened configuration, while a bigger ratio value engenders a decline in the capacity. This work proposes the incorporation of a safety constant in the average bond expression.

KEYWORDS

Bond strength, Grouting defect, Confinement effect, Interfacial modeling, Grouted sleeve connection

INTRODUCTION

Grouted sleeve connections are one of the frequent ways of connecting precast concrete components in the construction industry [1]. This kind of connection is achieved by the confinement of high-strength, non-shrink grouting materials in the sleeve splice where two reinforcements are connected. Given the relevance of connections in the structural integrity of precast concrete members, various research avenues were undertaken to confirm the reliability of this connection.

Early investigations on the grouted sleeve connector focused on its mechanical properties by subjecting the connector to a tensile loading test [2-4]. It is found that an adequate integration of each of the mechanical properties can sustain the tensile performance of the connector up to the fracture of the bar. This indicates that the connector can achieve and outperform the tensile

resistance of the reinforcement bar [2, 4, 5]. The mechanical properties of the connector are mainly influenced by the embedded length of the rebars, the bond strength, and the diameter of the iron sleeve.

In the quest of expanding research on the reliability of the grouted sleeve connection, studies combined experimental and theoretical approaches to assessing the earthquake performance of the connector [6-9]. It was found that the connector's performance largely depends on a good configuration of its mechanical properties and mainly the bond [10].

Studies on the bond between the bar and the grouting materials have confirmed a strong relationship between the bond strength and the anchorage length[11-15]. In the grouted sleeve connector, the bond strength is the main component of resistance when the connector is subjected to loading [14, 16, 17]. Experimental research on the connector revealed that the mechanical interlocks developed by the deformed bar largely contribute to the bond formulation. At the same time, good chemical adhesion and the high compressive strength of the grouting materials are important characteristics and result in additional enhancement of the bond performance [18].

However, during the onsite grouting process, sometimes an error resulting from the manipulation of the grout inlet or outlet hinges and the manual preparation of grouting materials causes defects within the sleeve. Currently, research interests on grouted sleeves focus on the influence of the defects on the connector's performance.

The investigations on defective grouted sleeve connectors found that the presence of defects within the connector can significantly reduce the tensile and seismic resistance of the connector. Xu uniformly mixed soil and foaming agents as defects in grouting material during his experimental research and found that 30% of defects in the total mixture significantly reduced the bond performance and precipitated the failure of the connector [19]. Most recently, Zheng presumed the defects reduced the bar's embedded length and subjected the defective connector to tensile and cyclic loading. He found that when the embedded length is 4d the tensile performance is compromised, while during the cyclic resistance was compromised when the anchorage length was equal to 5d, where d is the diameter of the bar[20]. Further investigations of defects within the connector used a similar approach of predesigned defects to assess the connector's performance. They confirmed that defects significantly weaken the resistance of the connection even in a post-fire analysis completed by Zhang [5, 21]. However, most of these studies concentrated more on a half-grouted sleeve than a fully grouted sleeve. They either relate embedded length reduction defects and distributed defects to the tensile performance and seldom consider the influence of the location of the defect on the performance of the connector.

Further research on the bond performance of the connector found that the confinement pressure from the sleeve impacts the bond performance [12, 22, 23]. The impact of the confinement effect within the sleeve can vary based on the ratio of the sleeve diameter to that of the reinforcement bar [24, 25]. In summary, provided by Espoir K in his theoretical research, the bond performance of the connector has an inverse proportionality with the sleeve diameter [26, 27]. A comprehensive analysis of the impact of defects requires additional investigation on how the defects interact with the change in the mechanical properties of the connector.

This paper analyses the impact of the confinement effect resulting from the diameter of the sleeve on the bond strength degradation and recovery of a grouted sleeve connection predesigned with defects and the induced consequences on the tensile performance of the connector. This article further studies the influence of the positioning of the defects in interaction with the possible degrees of confinement of grouting materials within the sleeve through a

parametric analysis. The findings of this research aim to enlighten the structural health monitoring process of the defective grouted connection and to propose an optimized configuration for the components of the grouted sleeve connection

THE EXPERIMENT OF FULLY GROUTED SLEEVE CONNECTOR

Material's properties and material's model

The materials properties of the bar are drawn from the tensile experiment of a steel bar used in the experiment of this work. The diameter of the bar in the experiment was constant at 14mm but changed in the proposed parametric study. The materials properties of the bar are listed in Tab. 1.

Tab. 1 - Material model of the reinforcement bar

Material density (kg/m3)	Yield strength (MPa)	Ultimate strength (MPa)	Yield plateau $\Delta\varepsilon_y$ (mm)	Ultimate strain ε_u (mm)	Young's Modulus (Mpa)	Poisson's ratio
7850	470	620	0.017	0.11	206000	0.3

The elastic-plastic behavior of the sleeve connector is carried on using a bilinear model without consideration of the hardening strain of steel material. The ultimate stress of the sleeve duct is given as 550 MPa, and the yield considered in this work is set at 450 MPa from [28]. The manufacturer tested the material model of the sleeve iron duct, which is presented in Tab. 2.

Tab. 2 - Material model of the reinforcement bar

Mass Density (kg/m3)	Elastic		Plastic
	Young's Modulus (MPa)	Poisson's ratio	Ultimate strength (MPa)
7300	203000	0.3	550

The injected grounding materials achieved an average compressive strength of 89 MPa. The grouting materials are modeled using the Concrete Damaged Plasticity (CDP) model available in Abaqus commercial software modified for concrete under active confinement following Lubliner's model [29]. For better accuracy, the post-failure modeling of grouting materials considers tensile stiffeners to allow residual stress through the crack until total failure. The CDP model for the grouting materials is established based on their empirical, experimental verification for each parameter [30-35]. The adopted CDP parameters in this research are presented in Tab. *3*.

Tab. 3 - Grouting material model [30-35]

Parameters	Mass density (kg/m3)	Elastic		Plastic				
		Elastic modulus Mpa	Poisson's ratio	Dilatation angle Ψ	Eccentricity	f_{bo}/f_{co}	K	Viscosity parameter
Model properties	2500	38000	0.2	38	0.1	1.16	0.66	0.0001

Test specimen and defect distribution

The experiment considered in this study aimed at assessing the amplitude of the bond strength degradation induced by the different locations of the defect and resulting consequences on the tensile performance of the grouted sleeve connector. The preset defects in grouting materials within the grout-bar bonding zone were made of a silicon rubber tape of 2mm thickness tied around the bar in different lengths 1d, 2d, and 3d where d is the diameter of the bar respectively in six different locations for each specimen as illustrated in Fig. 1.

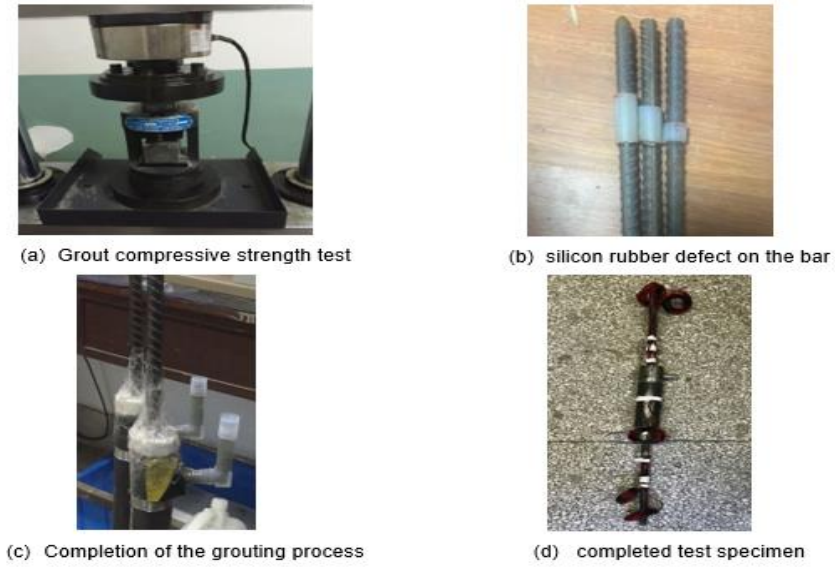

Fig. 1 – overall preparation of the test specimens

A total of 18 test specimens with defects of different sizes were made to test the influence of defects of different sizes in different locations on the tensile performance of the connector. In Fig. 2, the different arrangements of defects in the specimen are presented. The proposed configurations of the defects were based on the probability of occurrence of the defects during

the onsite operations of grouting. The defects are first considered for a single reinforcement and later for both reinforcement bars lapped within the connector, as sketched in Fig. 2.

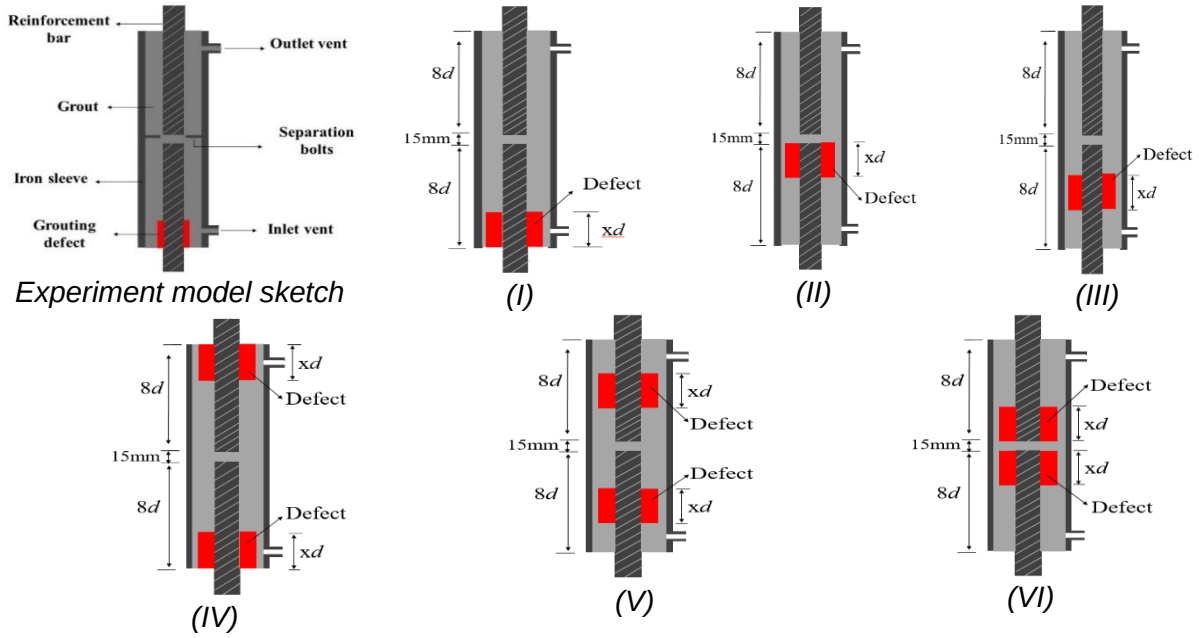

Fig. 2 – overall preparation of the test specimens

The unidirectional static tensile load was applied by the universal hydrostatic tensile loading machine of the maximum capacity of 300KN at a rate of 28KN/min. The loading method based on the JGJ1407-2016 technical regulations for mechanical connections of reinforcement bars with a sleeve and was completed in the following process 0→0.6 f_{yk} (measure residual deformation) →max Tensile force (record the tensile strength) → 0 (determine the total elongation at the maximum force).

Experimental results and discussion

As presented in this work, the tensile experiment of the defective grouted sleeve connector recorded some parameters that inform the analysis of the connector's performance. These parameters include but are not limited to the Yield Force, the Ultimate load, the total elongation and the observed failure mode for each specimen.

The representative Load displacement curves of the experimental results can be portrayed through the specimens of configurations I, II, III, and IV as shown in Fig. 3. To summarize the impact of defects based on their position along the anchorage length of the reinforcement bar.

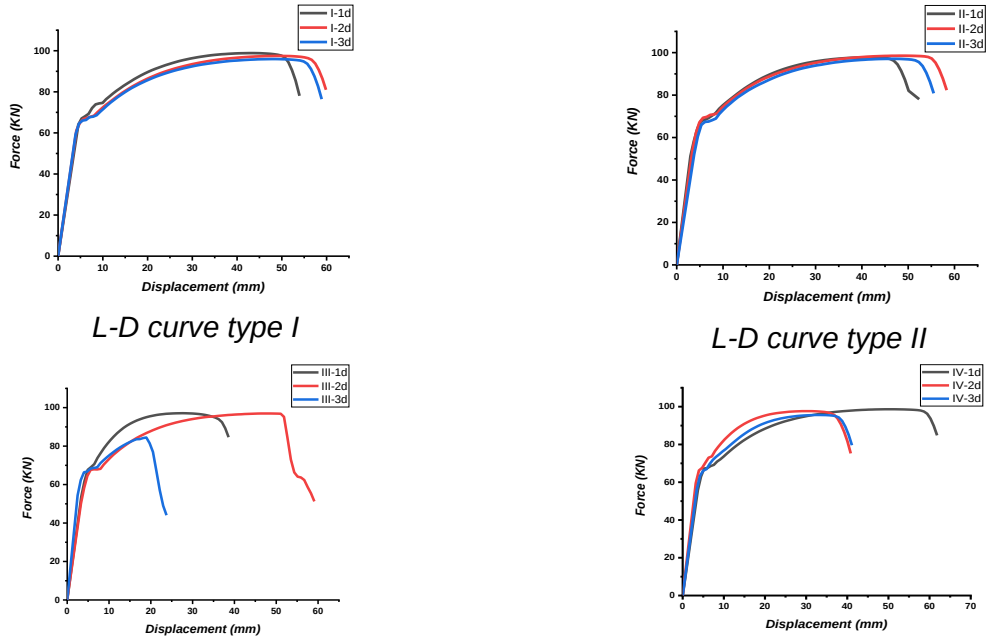

Fig. 3 – Representative L-D plots of tensile test

All specimens considered in this experiment failed in the plastic loading stage of the connector after the yielding point. This reveals that an active anchorage length of the bar of value ≥ 5d can enhance the tensile performance of the connector beyond the yielding point regardless of the location of the defect. However, the ultimate tensile capacity of the connection is considerably affected by the location of the defect when the active anchorage length is 5d. This is further explained by the premature drop of plot III-3d in Fig. 3. Thus, the location of the defect in configuration III threatens the integrity of the connection.

Considering the findings in Fig. 3, the connector's performance shows great sensitivity to the defect location, especially in test specimens where the defect size is 2d and 3d. This indicates that a defect of small size (1d) has a minor impact on the connector's performance regardless of the location and much more when the active anchorage length of the bar is 7d. The impact of the location of the defect is observed when the size of the defect is 2d and 3d. When the defect is of size 3d in arrangement III where the defect is located in the mid-span of the bar, the drop in the ultimate capacity and bond strength of the connector is 19.6%. Whereas, when the same defect is preset on both reinforcement bars within the connector, the resulting drop in capacity is approximately 16%. The bond strength of the connector shows a trend of performance recovery when a similar defect is located on both ends of the reinforcement bars in the specimen. The improved performance also observes a decrease in the total elongation. This phenomenon results from the instability due to the unequal distribution of stresses between the two ends of the connector when the defect is located on one side of the reinforcement resulting in structural instabilities due to the deterioration of the bond capacity of the defective side. The location of defects in bonding zones of both ends of the reinforcements promotes an equal and symmetric response of the connector enhanced by the equal bond capacity of a single reinforcement,

enhancing the stability of the connector. Studies in the subsequent section consider how defects interact with the confinement effect to identify the most suitable configuration of the connection and the risk associated with defects.

VALIDATION OF THE NUMERICAL MODEL

The grout-bar bond constitutes the bonded interface and are modeled in Abaqus using a friction-based interfacial model with contact pressure P. The slip of the bond strength occurs at a critical value of the shear strength τ_{crit} between interfaces and corresponds to the yield value of the actual bond strength.

Model validation

The model's accuracy is established based on its ability to predict the connector's behavior when subjected to similar loading and boundary conditions. The relevant test output of the experiments, including the tensile capacity of the connector and the failure phenomenon, is set as the main indicator to test the model's validity.

Load resistance prediction

To further validate the performance of the proposed models, the load resistance is an important indicator of the good accuracy of the computational model to simulate the experiment. For this purpose, some selected typical load-displacement curves resulting from the numerical models' computation are plotted on the same chart as those resulting from this work's experiment, as presented in Fig. 4.

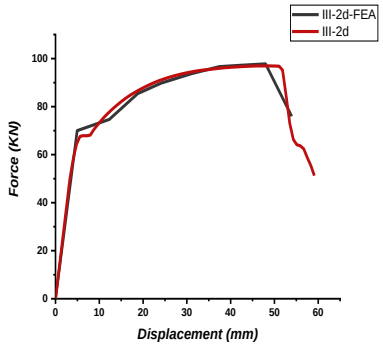

(a) Specimen III-2d L-D comparison

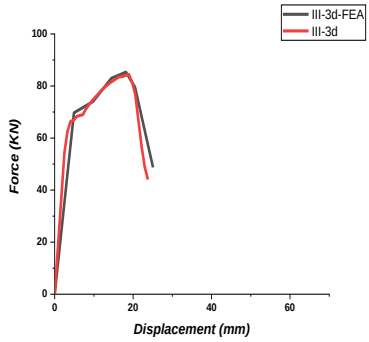

(b) Specimen III-3d L-D comparison

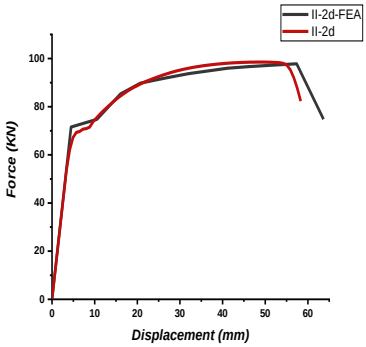

(c) Specimen II-2d L-D comparison

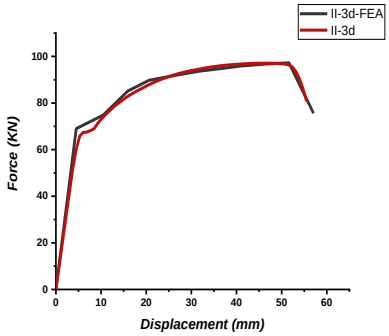

(d) Specimen II-3d L-D comparison

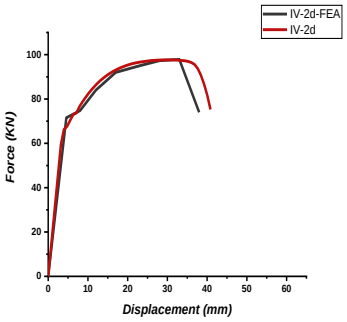

(e) Specimen IV-2d L-D comparison

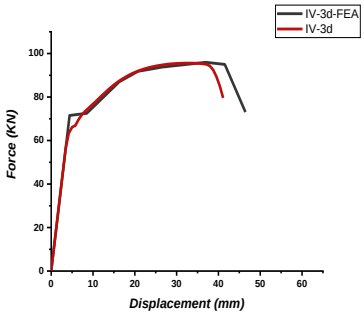

(f)Specimen II-3d L-D comparison

Fig. 4 – Load resistance prediction

The load resistance of the connector is accurately predicted following the similar trend of the load-displacement curves of both FEA and experimental findings. The main points of the load-displacement curves are also located at almost similar loading magnitude and equivalent displacement, which is proof of the proposed model's reliability to adequately predict the mechanical properties of the grouted sleeve connection.

Failure mode prediction

The proposed model has predicted the connector's behavior with a similar trend of materials performance when subjected to tensile loading. Similar to the experiment, the numerical models captured the connector's sensitivity to the defect's location and its induced consequence on the failure modes. Fig. 5 presents the failure mode prediction by the numerical models.

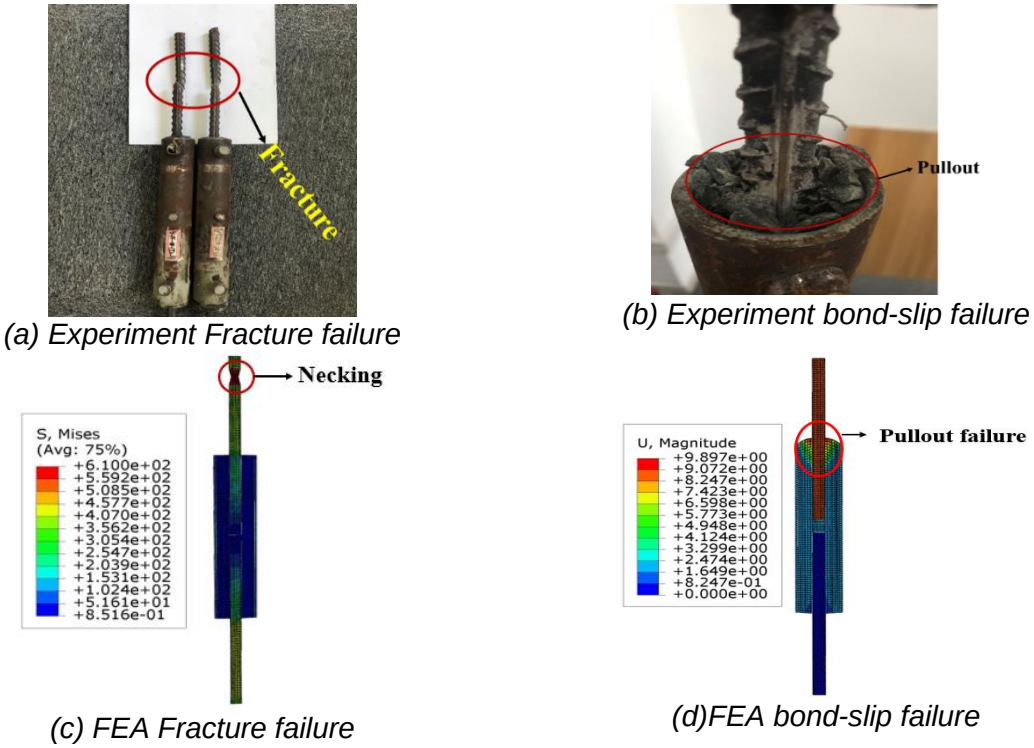

(a) Experiment Fracture failure

(b) Experiment bond-slip failure

(c) FEA Fracture failure

(d)FEA bond-slip failure

Fig. 5 - Failure mode prediction of the model

The fracture failure of the connector indicates the ability of the connector to sustain the overall performance of the reinforcement bar or even better. It's achieved by adequate bond resistance to the tensile pull-out forces until the yielding and the reinforcement fracture. The slip failure on the other end indicates the connector's weakened bond performance, which does not sustain the tensile capacity of the bar to its fracture. Through both numerical analysis and experiment, this failure mode is engendered by the defects and their location, which compromises the resistance of the connector by accumulating stresses in one zone. Based on the findings presented in Tab. 1, all the specimens predesigned with defects of size 1d, and the numerical models with similar defects failed by the fracture of the reinforcement. This indicates that the active bond developed along the anchorage length of 7d sustains the connector's tensile capacity regardless of the defect's location. When the length of the defect is 2d, the specimen with the preset defect in the midspan of one end of the bars in arrangement III experiences a slip failure. The location of the defect in this configuration prompts the slip failure even when the effective anchorage length of the bar is 6d. The bond strength is considerably compromised when the defect's length is 3d and explains most of the pull-out failures. Nevertheless, when the defect is located in both edges of the connector, the influence of the defect of length 3d becomes minor when the defect is located in the edges of the connector. Therefore, the parametric analysis will be conducted on arrangements II, III, and IV models.

PARAMETRIC STUDY

The parametric study proposed in this research evaluates the influence of the confinement effect by changing the ratio of the sleeve diameter to that of the bar (ds/d) from the lower limit to the upper limit of the design specified values {2.66-3.55} [36]. Three degrees of confinement effects are considered. The one established from the experiment in this work is denoted by N with the ratio value of 3.2. The smallest recommended value of the ratio denoted by S has the value of ds/d=2.66, and the biggest allowable value, the ratio ds/d=3.55, is denoted as B. Three diameters of the reinforcement bar, 12, 14, and 16mm, are considered in this parametric. Specimens are labeled based on their configuration (arrangement), the diameter of the bar, ds/d ratio index, and the size of the defect in the following sequence configuration-bar-diameter-confinement index-length of defect i.e. II-16-N-2d.

Effect of the degree of confinement on the load-resistance of the connector

The evaluation of the impact of the confinement effect on the load-bearing capacity of the connection can be assessed by comparing the plots when the diameter of the connector varies for each of the three types of configurations in consideration with different degrees of confinement S, N, and B. The plots in Fig. 6 summarize the behavior of the Load-displacement curves of the connector in different types of configurations.

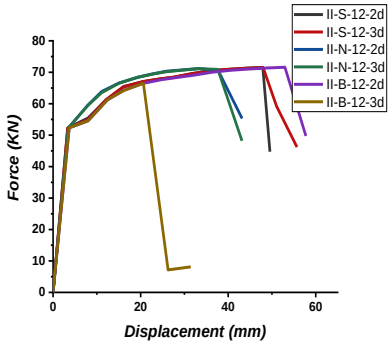

(a) L-D curves for type II-12

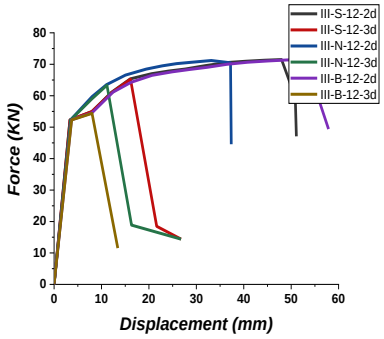

(b) L-D curves for type III-12

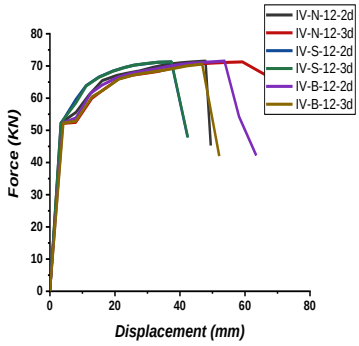

(c) L-D curves for type IV-12

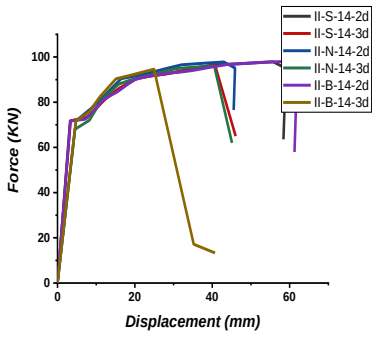

(d) L-D curves for type II-14

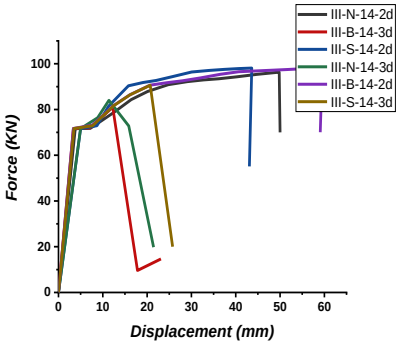

(e) L-D curves for type III-14

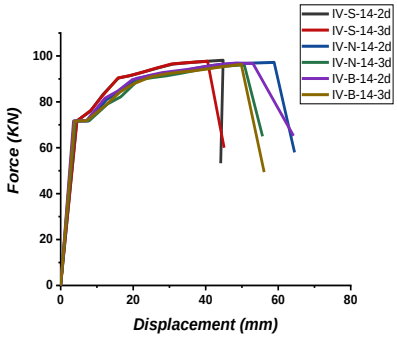

(f) L-D curves for type IV-14

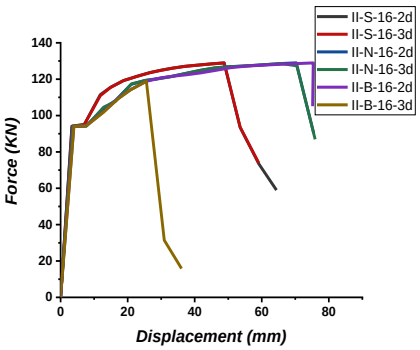

(g) L-D curves for type II-16

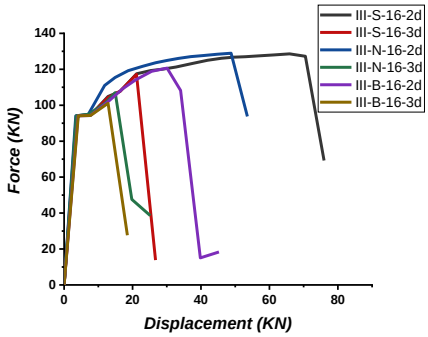

(h) L-D curves for type III-16

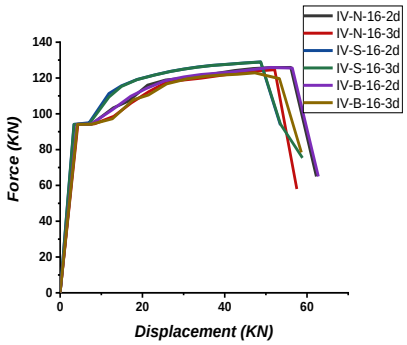

(e) L-D curves for type IV-16

Fig. 6 – Load displacement of the connector for different degrees of confinement

The influence of the confinement effect based on the ds/d ratio is analyzed in combination with the changes of the reinforcement diameter in the configuration of three types of defects as presented earlier. In inference to the outputs presented in Fig. 6, the connectors response presents trends influenced by the location of defects, size of the defects, and the confinement effect, whereas the effect of the diameter of the reinforcement is limited in changing the tensile capacity of the connector but has negligible influence on the trend of the load-displacement response of the connector.

The peak value of the bond performance is registered at the lowest value of the ds/d ratio in all plots. This is due to the sleeve's smaller diameter, which enables a higher impact of the lateral pressures in the effective bonding zone where the resistance of the connector is formulated. The largest value of the ratio experiences the lowest bond resistance as a result of the decreased impact of the confining pressures in the bonding zone. Nevertheless, the significance and impact of the confinement effect on the bond strength shrink as the performance of the connector regains the strength from the smaller size of the defect. Thus, the effect of confinement may be negligible when the bond strength is sustained by an adequate anchorage length of the bar in a normal configuration.

Impact of defects on the stress distribution within the connector

The main way defects can compromise the connector's performance is by changing the distribution of stresses through the components of the connector. The proposed numerical model in this study has sensibly tracked the influence of the location of the defects on the distribution of stresses among the components of the connector. Fig. 7 presents the influence of defects on the distribution of stresses to each part of the connector and the resulting impact on the overall tensile performance of the connector.

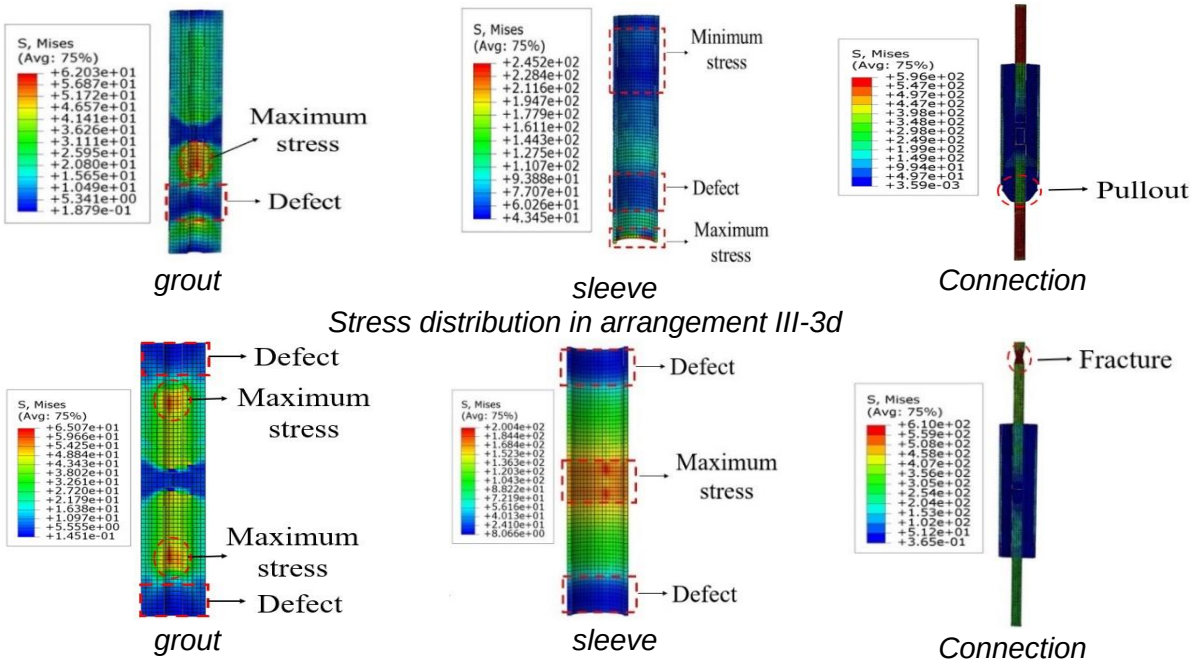

Fig. 7 – Influence of the defect location on the distribution of stresses

Arrangement III provides the sensitive location of the defect. In contrast, arrangement IV enhances the asymmetric distribution of stresses within the connector and improves the connector's performance due to the stability and symmetric loading enhanced in either side of the reinforcement.

Effect of the confinement effect on the failure mode

One of the main influences of the different degrees of confinement on the mechanical performance of the grouted sleeve connection is the modification of the failure mechanisms from slip to fracture and vice-versa. In specimens with the sensitive location of the defects, the premature slip failure can result from a significant drop in the ultimate load-bearing capacity of the connection when subjected to tensile loading. Tab. 4 presents the specimens which registered a change in the failure mechanism from their initial failure modes due to the effect of confinement based on the ds/d ratio.

Tab. 4 - Change of failure mechanism under different confinement effects

Model label	Initial failure mode (N)	New failure mode	ds/d ratio
II-S-12-3d	Slip out	Fracture	S
II-B-12-2d	Fracture	Slip out	B
III-S-12-2d	Slip out	Fracture	S

IV-B-12-3d	Fracture	Slip out	B
II-S-14-3d	Slip out	Fracture	S
II-B-14-2d	Fracture	Slip out	B
III-S-14-2d	Slip out	Fracture	S
IV-B-14-3d	Fracture	Slip out	B
II-S-16-3d	Slip out	Fracture	S
II-B-16-2d	Fracture	Slip out	B
III-S-16-2d	Slip out	Fracture	S
IV-B-16-3d	Fracture	Slip out	B
IV-B-16-2d	Fracture	Slip out	B

Inferring from the data in Tab. 4 models change from the slip failure in the N ratio index specimens to the fracture failure due to a small value of the ds/d ratio, which increases the impact of confinement pressures in the effective bond zone and consequently improves the tensile resistance of the connector leading to the fracture of the reinforcement bar. The contrast of this mechanism is observed within the specimen, which switched from a fracture failure in normal configurations to a pull-out failure in a specimen with a higher value of the ds/d ratio. This aspect is due to the dissipation of the confinement forces in the big layer of grouting materials hence reaching the effective bonding zone with a small magnitude resulting in the slip of the bar due to the declining bond strength compared to the specimen in which the lateral pressures traverse a relatively thin layer of grouting materials and attain the effective bond zone with a higher magnitude. The effect of confinement is empirically reported in related studies to impact the nature of concrete/bar bonds. A similar observation result from the parametric study of the defective grouted sleeve in this work is significant.

The change in the failure mechanism of the connector due to the confinement effects is not affected by the diameter of the reinforcement bar but rather the location of the defect and its size. Therefore, regardless of the diameter of the bar, similar configurations of the models registered an identical impact of the confinement effects on the switch of their failure mechanism. This aspect tends to limit the influential parameters of the mechanical properties of the grouted sleeve connector to the confinement effect, the location, and the size of the defects.

Influence of the confinement effect on the ultimate capacity of the connector

Another impact of the different degrees of confinement on the mechanical performance of the connector is observed in a significant change in the ultimate tensile capacity of the connector when subjected to loading. A significant loss in tensile capacity of the connector was reported in specimen with configurations II as a result of the decrease in the degree of confinement due to the enlargement of the diameters' ratio to the index B. When the defect length is 3d, in all specimens of type (III-3d), regardless of the confining effect, there was a loss in the capacity due to the nature of defects though at different rates as a result of degrees of confinement

In Fig. 8, the highest percentage decrease in the ultimate capacity is 9.8 observed when the diameter of the reinforcement is 12. While keeping a similar configuration, an increase in the diameter of the bar decreases the rate at which the ultimate capacity of the connector drops.

Therefore, the biggest diameter of the bar has the smallest value of the percentage of decrease in ultimate capacity. In respect to this scenario, the bond strength of the larger diameter of the bar deteriorates slower when the confinement pressure decreases.

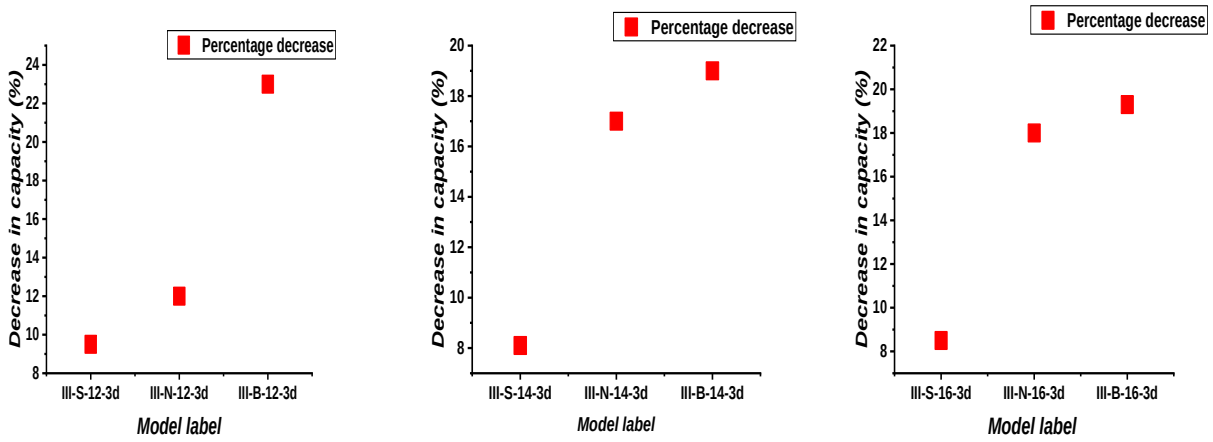

Capacity decrease in III-12-3d Capacity decrease in III-14-3d Capacity decrease in III-16-3d

Fig. 8 – Percentage drop in ultimate capacity due to increased ratio in III-3d configuration

The decrease in the capacity due to the different degrees of confinement in a specimen of configuration III, when the length of defect is 3d, registers a recovery when the ratio is at the smallest value of 2.66, as presented in Fig. 8. The percentage of decrease in capacity is around between 8-10 when the ds/d ratio is in a small range (S) for all reinforcement diameters. In contrast, the biggest ratio leads to the highest percentage of decrease in the ultimate tensile capacity of the connector. The smallest diameter of the reinforcement appears to be more susceptible to the decrease in the confinement pressure of the connector and experiences the highest value of the percentage decrease in the tensile capacity of the connector. In contrast, the enlargement of the diameter of the bar slows down the influence of the decreased confinement pressures. The explanation of this scenario is not straightforward; however, the larger diameter of the bar generates a large bonding zone compared to a small value of the diameter. The contribution of the confinement effect may be therefore decreasing with the enlargement of the bar diameter as well.

Since the embedded length of the connector 5d can sustain the Performance of ultimate Performance of the connector up to fracture in some specimens and yet exhibits a premature failure in other specimens due to the location of the defect, there is a need to modify the bond strength calculation in the structural health monitoring when the effective embedded length is 5d. Considering the changes in the capacity resulting from the connector due to the confinement effects in the design ranges of the ratio ds/d, the equation for the average bond strength, which considers the ultimate load needs to be modified for design optimization when the defects are detected within the connector.

The initial bond strength equation

$$\mu = \frac{F}{\pi d l_e} \quad (1)$$

F is the ultimate applied load, d is the diameter of the bar and l_e is the anchorage length of the reinforcement. For the ultimate state design of the bond resistance of grouted sleeve connection, the effect of confinement effect and the location of the defect when the anchorage length is 5d should be considered in the modified expression for the average bond calculation. The constant of safety design accounting for the confinement pressure and the defect is f_c' . The modified equation for the average bond calculation can be written as

$$\mu' = f_c' \frac{F}{\pi d l_e} \quad (2)$$

The safety constant $f_c' = 0.92$ when the ds/d ratio index is S (2.66) and $f_c' = 0.77$ when the ds/d ratio index is B (3.55).

CONCLUSIONS

This paper analyzes the influence of the degrees of confinements in the allowable interval of the ratio of the sleeve diameter to the diameter of the bar on the bond strength and tensile capacity of the grouted sleeve connector predesigned with defects. This article presents the experimental program subjecting the connector with predesigned defects in different locations to the tensile test, validating the proposed numerical models, and conducting a parametric analysis with the three main degrees of confinements based on the diameters' ratio. The following conclusions are derived.

The grouted sleeve connection is sensitive to the location of the defects, which determines if the defects present a high risk, mild risk, and minor risk to the structural integrity of the connection.

The presence of defects in the connector influences its performance by creating overstressed zones within the connector due to the interruption in the normal symmetric and equal distribution of loading stresses resulting in the early failure in some specimens.

The effect of confinement considerably influences the connector's failure mechanism regardless of the bar's diameter. The lower ratio value switches the failure modes of some specimens from pull-out to fracture, while its value in the upper limits of the ratio's interval engenders the opposite phenomenon.

The lowest recommended value of the diameters' ratio considerably improves the bond strength and results in approximately 10% to 16% recovery of the decreased tensile performance due to defects in the high-risk zone and a low degree of confinement.

For an optimized limit state design, the average bond strength can be improved by a safety constant (f_c'), which incorporates the impact of the defects' location and the effect of confinement on the bond strength of the connector.

The significance and impact of the confinement effect on the performance of the connector shrink become negligible when the bond strength is sustained by an adequate anchorage length of the bar in a normal configuration.

ACKNOWLEDGEMENTS

The study presented in this paper was supported by China's National Natural Science Foundation (Grant No. 51608234) and the Natural Science Foundation of Jiangsu Province of China (Grant No. BK20160534), which are gratefully acknowledged.

REFERENCES

[1] Martin, L.D. and C.J. Perry, *PCI design handbook: precast and prestressed concrete*. 2004: Prestressed Concrete Inst.

[2] Lu, Z., et al., *Mechanical behaviour of grouted sleeve splice under uniaxial tensile loading.* Engineering Structures, 2019. **186**: p. 421-435.

[3] Qiong, Y. and X. Zhiyuan, *Experimental study of grouted sleeve lapping connector under tensile load.* Građevinar, 2017. **69**(06.): p. 453-465.

[4] Yuan, H., et al., *Tensile behavior of half grouted sleeve connections: Experimental study and analytical modeling.* Construction and Building Materials, 2017. **152**: p. 96-104.

[5] Liu, Y.J., C. Li, and W.J. Zhou. *Numerical analysis on tensile properties of grout-filled splice sleeve rebars under ISO 834 standard fire*. in *E3S Web of Conferences*. 2018. EDP Sciences.

[6] Ameli, M., et al., *Seismic column-to-footing connections using grouted splice sleeves.* ACI Structural Journal, 2016. **113**(5): p. 1021.

[7] Ameli, M. and C.P. Pantelides, *Seismic analysis of precast concrete bridge columns connected with grouted splice sleeve connectors.* Journal of Structural Engineering, 2017. **143**(2): p. 04016176.

[8] Haber, Z.B., M.S. Saiidi, and D.H. Sanders, *Seismic Performance of precast columns with mechanically spliced column-footing connections.* ACI Structural Journal, 2014. **111**(3): p. 639-650.

[9] Qu, H., et al., *investigation and verification on seismic behavior of precast concrete frame piers used in real bridge structures: Experimental and numerical study.* Engineering Structures, 2018. **154**: p. 1-9.

[10] Zheng, Y., et al., *performance and confining mechanism of grouted deformed pipe splice under tensile load.* Advances in Structural Engineering, 2016. **19**(1): p. 86-103.

[11] Dancygier, A.N., A. Katz, and U. Wexler, *Bond between deformed reinforcement and normal and high-strength concrete with and without fibers.* Materials and Structures, 2010. **43**(6): p. 839-856.

[12] Hosseini, S.J.A., *Bond Behaviour of Grouted Spiral and Splice Connection Under Direct Axial and Flexural Pullout Load*. 2015, Universiti Teknologi Malaysia.

[13] Lee, J.-Y., et al., *Bond behaviour of GFRP bars in high-strength concrete: bar diameter effect.* Magazine of Concrete Research, 2017. **69**(11): p. 541-554.

[14] Sayadi, A.A., et al., *The relationship between interlocking mechanism and bond strength in elastic and inelastic segment of splice sleeve.* Construction and Building Materials, 2014. **55**: p. 227-237.

[15] Rolland, A., et al., *Analytical and numerical modeling of the bond behavior between FRP reinforcing bars and concrete.* Construction and Building Materials, 2020. **231**: p. 117160.

[16] Kim, H.-K., *Bond strength of mortar-filled steel pipe splices reflecting confining effect.* Journal of Asian Architecture and Building Engineering, 2012. **11**(1): p. 125-132.

[17] Xing, G., et al., *Experimental study on bond behavior between plain reinforcing bars and concrete.* Advances in Materials Science and Engineering, 2015. **2015**.

[18] Jiang, T., et al., *Three-dimensional nonlinear finite element modeling for bond performance of ribbed steel bars in concrete under lateral tensions.* International Journal of Civil Engineering, 2020: p. 1-23.

[19] Xu, F., et al., *Experimental bond behavior of deformed rebars in half-grouted sleeve connections with insufficient grouting defect.* Construction and Building Materials, 2018. **185**: p. 264-274.

[20] Zheng, G., et al., *Mechanical Performance for defective and repaired grouted sleeve connections under uniaxial and cyclic loadings.* Construction and Building Materials, 2020. **233**: p. 117233.

[21] Zhang, W., et al., *Experimental study on post-fire performance of half grouted sleeve connection with construction defect.* Construction and Building Materials, 2020. **244**: p. 118165.

[22] Hosseini, S.J.A. and A.B.A. Rahman, *Effects of spiral confinement to the bond behavior of deformed reinforcement bars subjected to axial tension.* Engineering Structures, 2016. **112**: p. 1-13.

[23] Torre-Casanova, A., et al., *Confinement effects on the steel–concrete bond strength and pull-out failure.* Engineering Fracture Mechanics, 2013. **97**: p. 92-104.

[24] Wang, Z., et al., *Experimental study on a novel UHPC grout-filled pipe sleeve with mechanical interlocking for large-diameter deformed bars.* Engineering Structures, 2021. **226**: p. 111358.
[25] Berra, M., et al., *Steel–concrete bond deterioration due to corrosion: finite-element analysis for different confinement levels.* Magazine of Concrete Research, 2003. **55**(3): p. 237-247.
[26] Espoir, K.K., X. Fuzhe, and G. Haojie, *GROUTED SLEEVE CONNECTION FOR PRECAST CONCRETE MEMBERS.* Civil Engineering Journal, 2020. **28**(4).
[27] Kahama, E.K., X. Fuzhe, and D.-L. M. Anglaaere, *Numerical study on the influence of defects in grouting on the mechanical properties of a full grouted sleeve connector.* The Journal of Adhesion, 2021: p. 1-32.
[28] Guo, H., J. Zhang, and C. Wang, *Experimental Study on Influence of Connection Defects on Joint Strength of Half-Grouted Sleeve Splicing of Rebar.* Advances in Civil Engineering, 2020. **2020**.
[29] Lubliner, J., et al., *A plastic-damage model for concrete.* International Journal of solids and structures, 1989. **25**(3): p. 299-326.
[30] Hany, N.F., E.G. Hantouche, and M.H. Harajli, *Finite element modeling of FRP-confined concrete using modified concrete damaged plasticity.* Engineering Structures, 2016. **125**: p. 1-14.
[31] Kmiecik, P. and M. Kamiński, *Modelling of reinforced concrete structures and composite structures with concrete strength degradation taken into consideration.* Archives of civil and mechanical engineering, 2011. **11**(3): p. 623-636.
[32] Manual, A.S.U.s., *Abaqus 6.11.* http://130.149, 2012. **89**(2080): p. v6.
[33] Ma, Y.-X., O. Zhao, and K.H. Tan, *Experimental and numerical studies of concrete-encased concrete-filled steel tube stub columns under uniaxial and biaxial eccentric compression.* Engineering Structures, 2021. **232**: p. 111796.
[34] Ren, W., et al., *Numerical simulation of prestressed precast concrete bridge deck panels using damage plasticity model.* International Journal of Concrete Structures and Materials, 2015. **9**(1): p. 45-54.
[35] Raza, A., et al. *Finite element modelling and theoretical predictions of FRP-reinforced concrete columns confined with various FRP-tubes*. in *Structures*. 2020. Elsevier.
[36] Brenes, F.J., S.L. Wood, and M.E. Kreger, *Anchorage requirements for grouted vertical-duct connectors in precast bent cap systems*. 2006.

CIVIL ENGINEERING JOURNAL

Article no. 26

THE CIVIL ENGINEERING JOURNAL 2-2022

APPLYING BIOGEOGRAPHY-BASED MULTI-LAYER PERCEPTRON NEURAL NETWORK TO PREDICT CALIFORNIA BEARING RATIO STABILIZED POND ASH'S VALUE WITH LIME SLUDGE AND LIME

Jiaman Li[1], Jundong Wu[2] and Wei Hu[3]

1. *Shaanxi College of Communication Technology, Xi'an, Shaanxi, 710000, China; Jiamanli126163@gmail.com*
2. *China Airport Construction Group Co., Ltd. Northwest Branch, Xi'an, Shaanxi, 710000, China; (corresponding author) lixiaojiaman@126.com*
3. *Shaanxi provincial transport planning design and research institute, Xi'an, Shaanxi, 710000, China; weihucivil126@gmail.com*

ABSTRACT

The California Bearing ratio (CBR) value of pond ash stabilized with lime and lime sludge was predicted in this research using a hybrid biogeography-based multi-layer perceptron neural network (BBO-MLP) with varying numbers of hidden layers (one up to three). In order to do this, the model used five inputs—the maximum dry density, ideal moisture content, lime percentage, lime sludge percentage, and curing period. The best BBO-MLP network, BBO-MLP1, has R^2 values of 0.9977, $RMSE$ values of 0.7397, MAE values of 0.476, and PI values of 0.0104. The predicted CBR values in all three of the created systems show a tolerable level of agreement with empirical findings, demonstrating the viability of the suggested models for very accurate CBR value prediction. Comparisons between the three created models show that BBO-MLP1 performs better than the others. BBO-MLP1 might be identified as the suggested model as a result.

KEYWORDS

California bearing ratio, Pond ash stabilized, Lime, Lime sludge, Hybrid biogeography-based multi-layer Pprceptron neural network

INTRODUCTION

It takes a large area to dispose of fly ash from thermal power plants, which leads to environmental issues, including leaching and dusting. Thermal power plants create three forms of ash [l] 1. Fly ash: this is made of electrostatic precipitators**.** 2. Bottom ash: this is mixed with water to make a sludge, which is subsequently disposed of as 3 . Pond ash in ash ponds [2]. ASTM categorizes coal ash as Class F and Class C ash [3]. Class C ash includes extreme concentrations of calcium and reacts with water without a binder [4].

Class F ash has less calcium and is produced by most of the world's thermal power plants [5]. Class F ash lacks the vital strength for use as a construction material. Numerous studies [6–9] were done to enhance the lime-stabilized Class F fly ash's engineering qualities. Cement and gypsum Lime sludge (LS) is an extra byproduct.

About 4.5 million tons of LS are produced yearly by these sectors in India [10], and their disposal is challenging [11–13]. As LS comprises calcium carbonate [14], researchers have proposed employing it in a range of applications [15-17].

CBR is among the most critical metrics to assess the subgrade of elastic and stiff pavements [18]. The CBR validation may be accomplished in the site construction or a laboratory. In the laboratory, it is often examined on compressed soil models, but on the site, it is performed on the ground surface. In addition to being complicated and time-consuming, the CBR test occasionally yields erroneous results owing to sample disruption and inadequate laboratory testing conditions. So, constructing prediction models could benefit and serve as a foundation for analysis.

An artificial neural network (ANN) is a simplified human brain simulation [19]. It is widely recognized for collecting and expressing abstruse inputs and outputs [20]. Unlike most traditional empirical and statistical methodologies [21], our method does not require such knowledge. Therefore, ANNs are suitable for simulating the complicated behavior of the vast majority of geotechnical engineering materials, which are highly variable [21]. ANNs are superior to most traditional procedures [21] due to their modeling capability and capacity to learn from experience. Recently, ANN has been successfully implemented in virtually every field of geotechnical engineering, including the compressive strength and Young's modulus of frozen sand [21-31].

Despite the wealth of literature on ANN applications, some research has been performed to anticipate the soils' CBR values. Yildirim and Gunaydin [32] created statistical models and an artificial neural network (ANN) using CBR data gathered from various sites along Turkey's public highways. In terms of predicting CBR values, the ANN model outperforms statistical approaches. Sabat [33] generated ANN and MR models for assessing the CBR value. The CBR was accurately predicted by the MR and ANN models; however, the ANN model performed significantly better. The M5P and Random forest RF model tree modeling methodology simulate the pond ash's soaking CBR value. LI and LS were utilized to stabilize pond ash. Utilized CBR data collected by experimental software. Model performance was tested to utilize conventional statistical parameters. Although the performance of both models in forecasting the CBR value is excellent, it is evident from the statistical characteristics that the RF technique performs better than the M5P model [34].

This study's primary purpose was to identify and evaluate the precision of several intelligent techniques [35]. So, a hybrid biogeography-based multi-layer perceptron neural network (BBO-MLP) with varying hidden layers' numbers is constructed to predict CBR values in lime and sludge pond ash. CBR was the starting variable for the model. The input variables for the model were optimal moisture content (OMC), maximum dry density (MDD), the curing period (CP), lime sludge percentage (LS), and lime percentage (LI). Four performance metrics were used to assess the model's accuracy.

DATASET AND METHODOLOGIES

The data set's description

In order to study the influence of lime sludge and lime on the value of CBR, 51 experimental data records were selected from the published document (Table 1) [36] to create a data set. Five unique variables that may affect the CBR's value were investigated. These factors are shown in Table 2**.**

Tab. 1 - The results of CBR and Seventeen mix designs

Mix No.	Lime percentage (LI)	Lime Sludge percentage (LS)	The maximum dry density (MDD(g/cc))	The optimum moisture content (OMC(%))	CBR		
					7.0	28	45
1	0.0	0.0	1.1750	26.80	2.20	3.40	4.30
2	2.0	0.0	1.1940	25.30	10.10	13.40	15.40
3	2.0	5.0	1.2270	25.00	14.60	26.30	29.50
4	2.0	10.0	1.2300	24.80	20.60	33.60	38.50
5	2.0	15.0	1.2380	24.30	24.70	39.50	46.30
6	4.0	0.0	1.2070	24.50	16.20	27.70	31.50
7	4.0	5.0	1.2370	23.80	22.50	32.30	40.50
8	4.0	10.0	1.2510	23.30	28.10	39.40	46.10
9	4.0	15.0	1.2530	23.10	32.40	45.90	52.30
10	6.0	0.0	1.2270	24.20	26.10	42.30	50.60
11	6.0	5.0	1.2590	23.00	33.10	52.60	63.80
12	6.0	10.0	1.2370	23.20	30.40	44.80	54.90
13	6.0	15.0	1.2420	24.00	32.30	47.70	57.40
14	8.0	0.0	1.2560	23.00	29.90	44.80	53.40
15	8.0	5.0	1.2400	22.80	34.20	52.90	61.10
16	8.0	10.0	1.2460	24.70	31.20	46.10	56.30
17	8.0	15.0	1.2410	24.10	32.10	48.90	57.60

Tab. 2: Input and output variable statistical values

VARIABLE	Min	Max	Average	St. deviation
LI	0.00	8.00	4.7060	2.4680
LS	0.00	15.00	7.0590	5.7030
MDD	1.1750	1.2590	1.2330	0.0220
OMC	22.800	26.800	24.1120	1.0080
CP	7.000	45.000	26.6670	15.5420
CBR	2.200	63.800	35.7220	15.4380

Biogeography-based optimization (BBO)

The BBO methodology is Simon's developed meta-heuristic optimization approach [37]. This technique presupposes a restricted number of habitat categories within an ecosystem. Food, water, temperature, and other factors are suitability index variables (SIVs).

The habitat suitability index quantifies the quality of each environment (HSI). When a habitat has a high HIS or is saturated, organisms incline to move and immigrate to environments with a low HIS. Each habitat was a possible solution to the problem, with its appropriateness indices acting as selection criteria (DVs).

Results with minor target values have greater HSI values in the minimization technique. This strategy utilizes the "migration" and "mutation" operators. The HS-sized habitats are ranked according to their respective cost functions. The following equation determines the appropriateness ($\mathrm{HSI_i}$): (1)

$$\mathrm{HSI_i} = -\mathrm{i} + \mathrm{HS} + 1 \tag{1}$$

In Equations. (2)-(3) μ_i indicates the emigration and λ_i is the immigration values which are computed as below:

$$\mu_\mathrm{i} = \frac{\mathrm{HSI_i}}{\mathrm{HS}} \tag{2}$$

$$\lambda_\mathrm{i} = 1 - \frac{\mathrm{HSI_i}}{\mathrm{HS}} \tag{3}$$

The BBO method's migration curve is seen in Figure 1. The transition from the j-th determinant of the r-th habitat to the i-th determinant of the r-th habitat is expressed by equation (4).

$$\mathrm{DV_j^k} = \alpha \mathrm{DV_j^i} + (1-\alpha)\mathrm{DV_j^r} \tag{4}$$

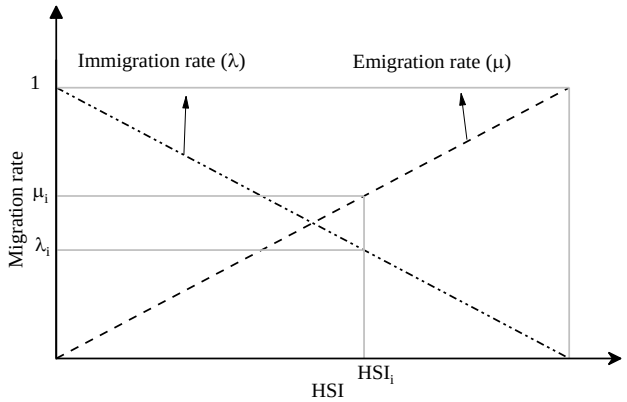

Fig. 1 – The BBO algorithm's migration function

Biogeography-based multi-layer perceptron neural network (BBO-MLP)

A human brain's mathematical process simulation is the basis of an artificial neural network. The key elements of the transfer function, connection pattern, and learning function comprise ANN [38]. These concepts are utilized for training an exclusive network by adjusting its weights according to the structure of the problem [39,40]. Each layer comprises neurons with different mathematical connections; however, neurons number in the output layer through the dataset of interest [41]. The

neurons of the unseen layers are essential for distinguishing and recognizing signal properties [42,43].

Although concealed layers' number is studied, each hidden layer is limited to a maximum of 25. Similarly, the BBO approach determines the ideal neurons' number in each hidden layer for models with various numbers of hidden layers. The ANN training phase studied several methods for determining the weights and biases. In order to, the back-propagation strategy for MLP learning [38,39] is utilized based on its previous success. In this technology, input signals are modified and weighted over several layers of neurons to get an acceptable output. Figure 2 depicts the hybrid BBO- MLP process.

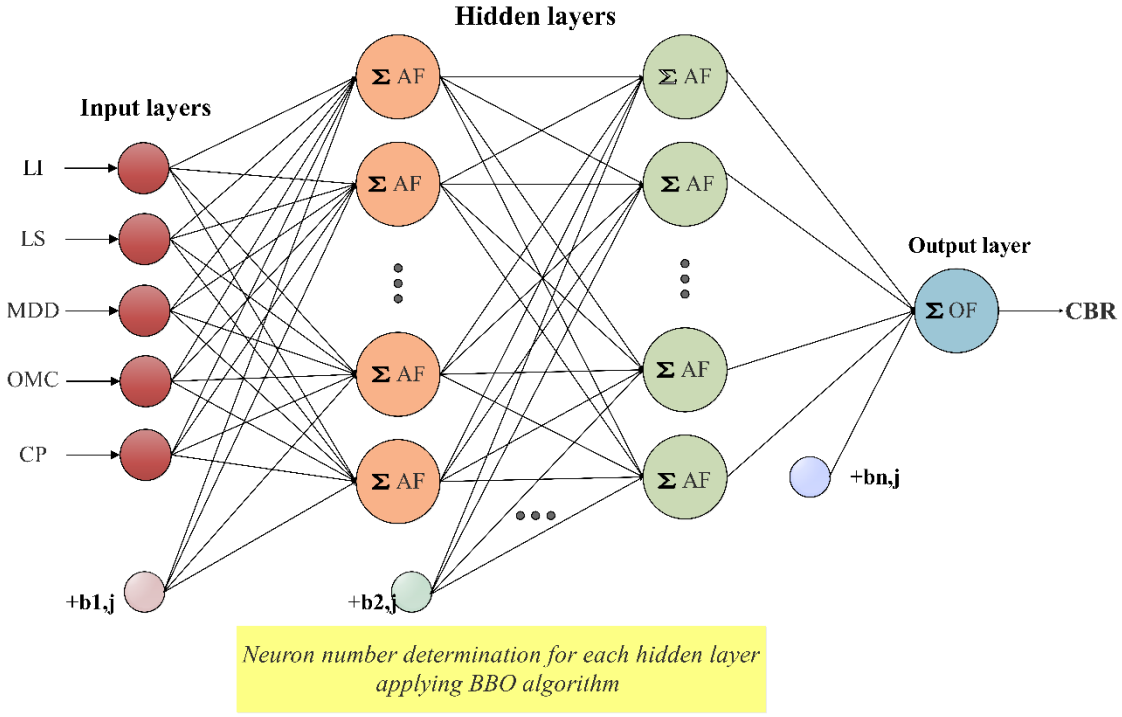

Fig. 2 – BBO-MLP hybridization procedure

Performance evaluators

Various statistical assessors were employed to evaluate the efficacy of hybrid models developed for CS forecasting. As for accuracy measures, R^2, MAE, RMSE, and PI were used (Eqs. (5)-(8)):

$$R^2 = \left(\frac{\sum_{p=1}^{P}(t_P - \bar{t})(y_P - \bar{y})}{\sqrt{\left[\sum_{p=1}^{P}(t_P - \bar{t})^2\right]\left[\sum_{p=1}^{P}(y_P - \bar{y})^2\right]}} \right)^2 \quad (5)$$

$$MAE = \frac{1}{P}\sum_{p=1}^{P}|y_p - t_p| \quad (6)$$

$$RMSE = \sqrt{\frac{1}{P}\sum_{p=1}^{P}(y_p - t_p)^2} \quad (7)$$

$$PI = \frac{1}{|\bar{t}|}\frac{RMSE}{\sqrt{R^2}+1} \quad (8)$$

R^2 : The determination's coefficient

RMSE : Root mean squared error

MAE : Mean absolute error,

PI : Performance index

y_P : The predicted values of P^{th} pattern

t_P : The target values P^{th} pattern

$\bar{t}$: The averages of target values

$\bar{y}$: The averages of predicted values

RESULTS

Below are the findings built to forecast the pond ash's CBR value stabilized with sludge and lime. Figure 3 compares experimentally collected data with results calculated by the BBO-MLP1, BBO-MLP2, and BBO-MLP3 models. Observably, the generated models' R^2 values that exceed 0.99620. It suggests that the relationship between the experimental and forecasted values emanated from the integrated models is about identical, thereby displaying the highest level of accuracy. In addition, a score-based technique is established by using statistical indicators to compare the productivity of the used models, like R^2, RMSE, MAE, and PI. Table 3 contains the consequences.

The BBO-MLP1 model has the maximum score (12), with R^2 of 0.99770, RMSE of 0.73970, MAE of 0.4760, and PI of 0.01040. All indices decrease as the hidden layers' number increases. The RMSE rises from 0.73970 to 0.99040 as the hidden layers' number increases. BBO-MLP1 performs better than BBO-MLP2 and BBO-MLP3 (R^2 =0.9970, RMSE=0.87550, and PI=0.01230). The performance of the non-BB optimization method for calculating the neurons' number in each hidden layer is satisfactory overall.

The time series plots in Figs. 4 demonstrate an adequate match between the measured and anticipated CBR. The calculated CBR values for all applicable models are remarkably near experimental data.

Tab. 3 - The outcome of creating GWMLP models for CBR prediction

Models			*BBO-MLP1*	*BBO-MLP2*	*BBO-MLP3*
Number(s) of hidden layer			*1*	*2*	*3*
Number of Hidden layers of neurons			*[6]*	*[4, 4]*	*[6,11,5]*
Results of network	*All data*	*RMSE*	*0.73970 (3)*	*0.87550 (2)*	*0.99040 (1)*
		R2	*0.99770 (3)*	*0.9970 (2)*	*0.99620 (1)*
		MAE	*0.4760 (3)*	*0.51030 (1)*	*0.48980 (2)*
		PI	*0.01040 (3)*	*0.01230 (2)*	*0.01390 (1)*
TRS			*12.0*	*7.0*	*5.0*
Rank			*1.0*	*2.0*	*3.0*

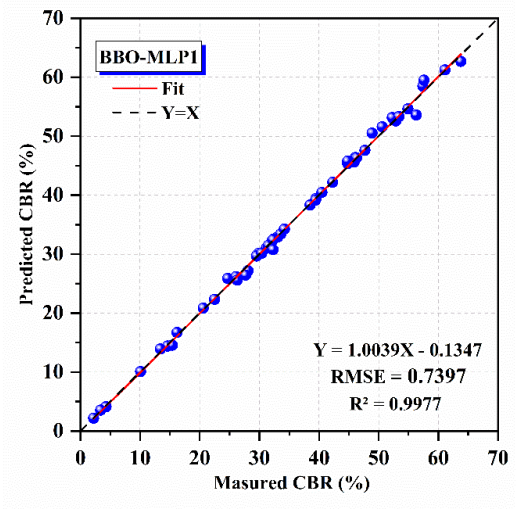

(1A)

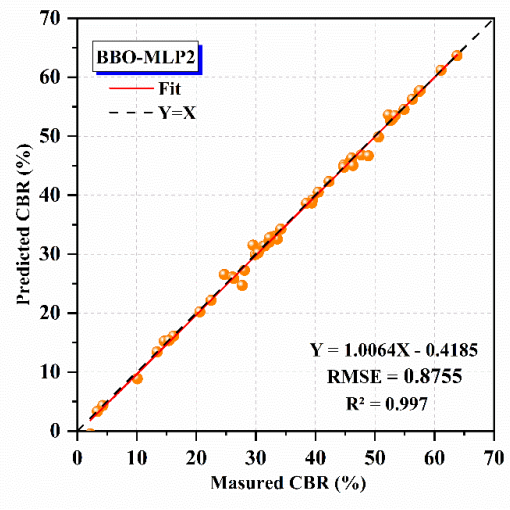

(2B)

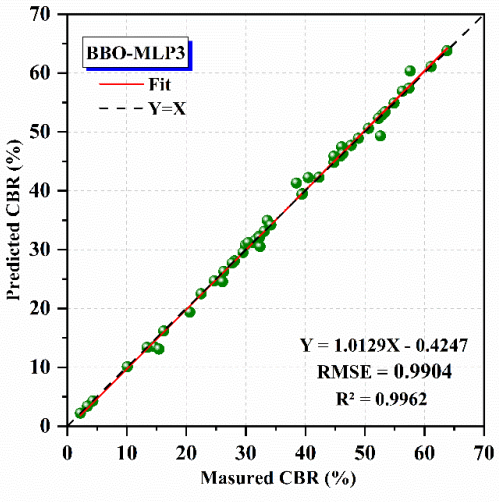

(3C)

Fig. 3 – (1A) BBO-MLP1, (2B) BBO-MLP2, (3 C) BBO-MLP3

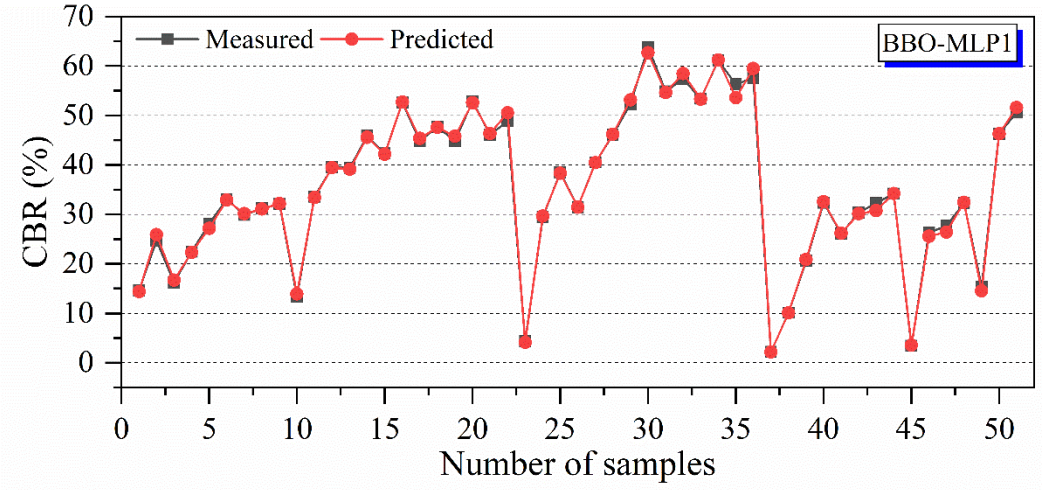

(1) BBO-MLP1 CBR prediction using models

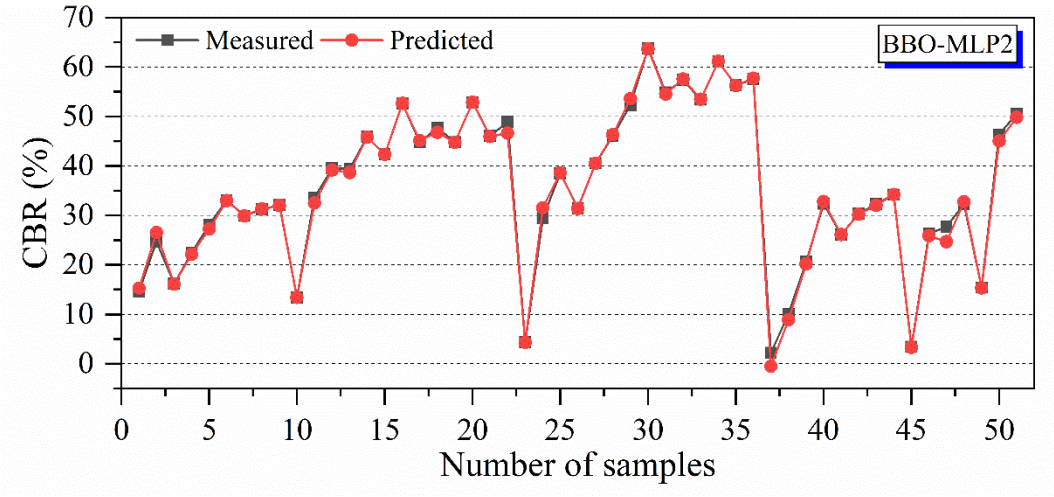

(2)

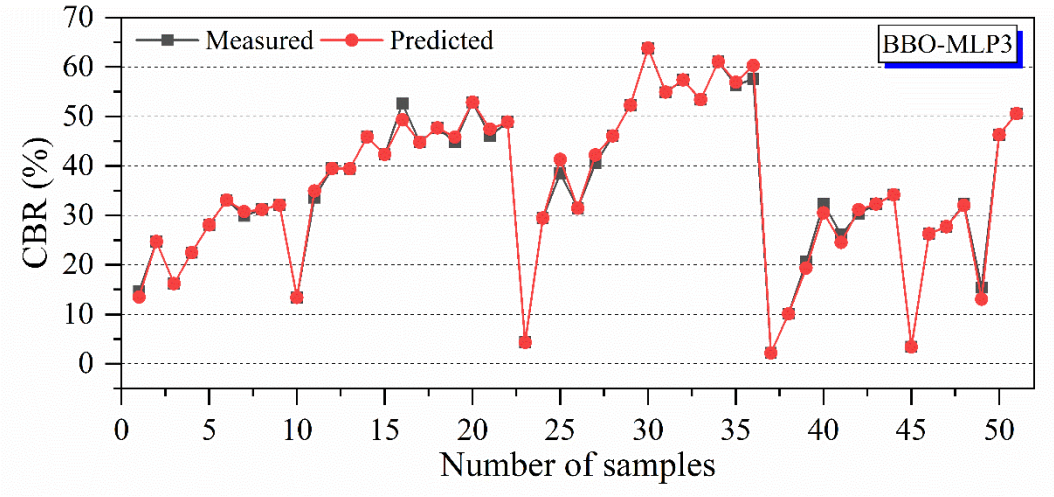

(3)

Fig. 4 – (1) BBO-MLP1, (2) BBO-MLP2, (3) BBO-MLP3; CBR prediction using models

SENSITIVITY ANALYSIS

The hybrid models were analyzed to discover the most significant input elements for computing the CBR. The data was generated by eliminating a single input parameter. Here R^2 Moreover, RMSE were statistical performance metrics. Statistical performance criteria are used to choose the suitable model for sensitivity analysis. The BBO-MLP1 model is chosen for this study because of its remarkable performance. According to Table 4, the CP is the most relevant metric. From this viewpoint, additional inputs have minimal impact on the model's performance. It is important to remember that removing the input parameters can result in a modest reduction in model performance. However, where the analysis was through trial measurements to specify the impressions of stabilized materials, removing variables might reduce the model's generalizability. Since the multicollinearity issue has little effect on the model's fit and, in general, has little effect on forecasts, the current research does not propose removing any variables.

Tab. 4: Analysis of sensitivity with the tree-based Random Forest model

Inputs	Removed parameter	R^2	RMSE	Ranking
MDD, OMC, LI, LS, and CP	-	0.99770	0.73970	-
	MDD	0.99580	1.00950	5.0
	OMC	0.99560	1.030	4.0
	LI	0.99360	1.25120	3.0
	LS	0.99360	1.27840	2.0
	CP	0.66480	7.94610	1.0

CONCLUSION

A hybrid biogeography-based multi-layer perceptron neural network (BBO-MLP) with hidden layers' varying numbers was developed to predict California bearing ratio (CBR) values in lime and lime sludge pond ash. CBR was the starting variable for the model. The model included extreme dry density, optimal humidity, lime sludge percentage, cure duration, and CBR as output variables as input factors.

With R^2 of 0.99770, RMSE of 0.73970, MAE of 0.4760, and PI of 0.01040, BBO-MLP1 gives the greatest performance among the BBO-MLP models. All metrics deteriorate as the number of buried layers is decreased. BBO-MLP1 performs better than BBO-MLP2 and BBO-MLP3 (R^2=0.9970, RMSE=0.87550, and PI=0.01230). In each created model, the predicted CBR values accord satisfactorily with investigated data, proving the validity of the proposed models for properly predicting CBR values. Three generated models are compared, and BBO-MLP1 demonstrates superior performance. Consequently, BBO-MLP1 may be known as the planned model.

This study's main aim and contribution were to develop hybrid multi-layer perceptron neural networks to predict the California bearing ratio of stabilized pond ash. These models could be used in practical applications and in order to decrease the time and cost of experimental efforts. The referred citation was used to select the dataset. However, this article used laborious and cost-needed efforts that can be reduced using prediction models with the same accuracy.

REFERENCES

[1]. Esmaeili-Falak, M., Sarkhani Benemaran, R. and Seifi, R. (2020a), "Improvement of the mechanical and durability parameters of construction concrete of the Qotursuyi Spa", Concrete Res., 13(2), 81-90.

[2]. Bera AK, Ghosh A, Ghosh A (2007) Compaction characteristics of pond ash. J Mater Civ Eng 19(4):349–357

[3]. Suthar M, Aggarwal P (2017) Analysis of heavy metals in pond ash samples from Haryana. In Proceedings of 29th research world international conference, Las Vegas, USA, 16–17 March 2017, ISBN: 978-93-86291-88-2

[4]. Parsa J, Munson-McGee SH, Steiner R (1996) Stabilization/ solidification of hazardous wastes using fly ash. J Environ Eng 122(10):935–940

[5]. Ghosh A, Subbarao C (2006) Tensile strength bearing ratio and slake durability of class F fly ash stabilized with lime and gypsum. J Mater Civ Eng 18(1):18–27

[6]. Ghosh A (1996) Environmental and engineering characteristics of stabilized low lime fly ash. PhD dissertation, Indian Institute of Technology, Kharagpur, India

[7]. Ghosh A, Subbarao C (2007) Strength characteristics of class F fly ash modified with lime and gypsum. J Geotech Geoenviron Eng 1337:757–766

[8]. Pandian NS (2004) Fly ash characterization with reference to geotechnical applications. J Indian Inst Sci 184:189–216

[9]. Suthar M, Aggarwal P (2015) Class-F pond ash a potential highway construction material—a review. Ind Highways IRC 43(8):23–32

[10]. Sahu V, Gayathri V (2014) The use of fly ash and lime sludge as partial replacement of cement in mortar. Int J Eng Technol Innov 4(1):30–37
[11]. Battaglia A, Calace N, Nardi E, Petronio BM, Pietroletti M (2007) Reduction of Pb and Zn bioavailable forms in metal polluted soils due to paper mill sludge addition. Effects on Pb
and Zn transferability to barley. Biores Technol 98:2993–2999
[12]. Calacea N, Campisib T, Iacondinib A, Leonia M, Petronioa BM, Pietroletti M (2005) Metal-contaminated soil remediation by means of paper mill sludges addition: chemical and ecotoxicological evaluation. Environ Poll 136:485–492
[13]. Mahmood T, Elliot A (2006) A review of secondary sludge reduction technology for the pulp and paper industry. Water Res 40(11):2093–2112
[14]. Medhi UJ, Talukdar AK, Deka S (2005) Physicochemical characteristics of lime sludge waste of paper mill and its impact on growth and production of rice. J Ind Pollut Contr 21(1):51–58
[15]. Talukdar DK (2015) A study of paper mill lime sludge for stabilization of village road sub-base. Int J Emerg Technol Adv Eng 5(2):389–393
[16]. Singh M, Garg M (2008) Utilization of waste lime sludge as building materials. J Sci Ind Res 67:161–166
[17]. Ghosh A (2010) Compaction characteristics and bearing ratio of pond ash stabilized with lime and phosphogypsum. J Mater Civ Eng 22(4):343–351
[18]. Day WR (2001) Soil testing manual procedures, classification data, and sampling practices. McGraw Hill, New York, p 619
[19]. Sarkhani Benemaran, R. (2017). Experimental and analytical study of pile-stabilized layered slopes. Civil engineering, Tabriz university, Tabriz, Thesis.
[20]. Benemaran, R. S., & Esmaeili-Falak, M. (2020). Optimization of cost and mechanical properties of concrete with admixtures using MARS and PSO. Computers and Concrete, 26(4), 309-316.
[21]. Kin MW (2006) California bearing ratio correlation with soil index properties master of engineering (civil-geotechnics). Thesis, Faculty of Civil Engineering, University Teknology Malaysia
[22]. Yorulmaz, A., Sivrikaya, O., & Uysal, F. (2021). Evaluation of the bearing capacity of poor subgrade soils stabilized with waste marble powder according to curing time and freeze-thaw cycles. Arabian Journal of Geosciences, 14(5), 1-10.
[23]. Caglar N, Arman H (2007) The applicability of neural networks in the determination of soil profiles. Bull Eng Geol Environ 66(3):295–301
[24]. Zhu, W., Huang, L., Mao, L., & Esmaeili-Falak, M. (2021). Predicting the uniaxial compressive strength of oil palm shell lightweight aggregate concrete using artificial intelligence-based algorithms. Structural Concrete.
[25]. Yuan, J., Zhao, M., & Esmaeili-Falak, M. (2022). A comparative study on predicting the rapid chloride permeability of self-compacting concrete using meta-heuristic algorithm and artificial intelligence techniques. Structural Concrete.
[26]. Yang, C., Feng, H., & Esmaeili-Falak, M. (2022). Predicting the compressive strength of modified recycled aggregate concrete. Structural Concrete.
[27]. Sarkhani Benemaran, R., Esmaeili-Falak, M., & Katebi, H. (2020). Physical and numerical modelling of pile-stabilised saturated layered slopes. Proceedings of the Institution of Civil Engineers-Geotechnical Engineering, 1-16.
[28]. Chen, W., Luo, Q., Liu, J., Wang, T., & Wang, L. (2022). Modeling of frozen soil-structure interface shear behavior by supervised deep learning. *Cold Regions Science and Technology*, 103589.
[29]. Das SK, Basudhar PK (2006) Undrained lateral load capacity of piles in clay using artificial neural network. Comput Geotech 33(8):454–459
[30]. Park HI, Cho CH (2010) Neural network model for predicting the resistance of driven piles. Mar Georesour Geotech 28(4):324–344 30. Cho SE (2009) Probabilistic stability analyses of slopes using the ANN-based response surface. Comput Geotech 36:787–797
[31]. Erzin Y, Cetin T (2013) The prediction of the critical factor of safety of homogeneous finite slopes using neural networks and multiple regressions. Comput Geosci 51:305–313
[32]. Erzin Y, Cetin T (2014) The prediction of the critical factor of safety of homogeneous finite slopes subjected to earthquake forces using neural networks and multiple regressions. Int J Geomech Eng 6(1):1–15
[33]. Zhao HB (2008) Slope reliability analysis using a support vector machine. Comput Geotech 35:459–467

[34] Suthar, M., & Aggarwal, P. (2019, June). Modeling CBR value using RF and M5P techniques. In MENDEL (Vol. 25, No. 1, pp. 73-78).
[35]. Raja, M. N. A., Shukla, S. K., & Khan, M. U. A. (2021). An intelligent approach for predicting the strength of geosynthetic-reinforced subgrade soil. International Journal of Pavement Engineering, 1-17.
[36]. Suthar, M., & Aggarwal, P. (2018). Predicting CBR value of stabilized pond ash with lime and lime sludge using ANN and MR models. International Journal of Geosynthetics and Ground Engineering, 4(1), 1-7.
[37] D. Simon, Biogeography-Based Optimization, IEEE Transactions on Evolutionary 505 Computation. 12 (2008) 702–713. doi:10.1109/TEVC.2008.919004.
[38] Basheer, Imad A, and Maha Hajmeer. 2000. Artificial Neural Networks: Fundamentals, Computing, Design, and Application. Journal of microbiological methods 43(1): 3–31.
[39] Gordan, Behrouz et al. 2019. Estimating and Optimizing Safety Factors of Retaining Wall through Neural Network and Bee Colony Techniques. Engineering with Computers 35(3): 945–54.
[40] Hasanipanah, Mahdi et al. 2018. A Risk-Based Technique to Analyze Flyrock Results through Rock Engineering System. Geotechnical and Geological Engineering 36(4): 2247–60.
[41] Koopialipoor, Mohammadreza, Danial Jahed Armaghani, Mojtaba Haghighi, and Ebrahim Noroozi Ghaleini. 2019. A Neuro-Genetic Predictive Model to Approximate Overbreak Induced by Drilling and Blasting Operation in Tunnels. Bulletin of Engineering Geology and the Environment 78(2): 981–90.
[42] Sarkhani benemaran, Reza, Esmaeili-Falak, Mahzad, Javadi, Akbar. 2022. Predicting resilient modulus of flexible pavement foundation using extreme gradient boosting based optimized models. International Journal of Pavement Engineering. DOI: 10.1080/10298436.2022.2095385
[43] Esmaeili-Falak, Mahzad, Sarkhani benemaran, Reza. 2022. Investigating the stress-strain behavior of frozen clay using triaxial test. Journal of Structural and Construction Engineering. https://doi.org/10.1080/10298436.2022.2095385 .

CIVIL ENGINEERING JOURNAL

Article no. 27

THE CIVIL ENGINEERING JOURNAL 2-2022

NUMERICAL ANALYSIS OF BFRP REINFORCED CONCRETE SLAB EXPOSED TO IMPACT LOADS

Daniel Jindra and Petr Hradil

Brno University of Technology, Faculty of Civil Engineering, Institute of Structural Mechanics, Veveří 331/95, 602 00 Brno, Czech Republic; jindra.d@fce.vutbr.; hradil.p@fce.vutbr.cz

ABSTRACT

This paper describes advanced numerical analysis of a simply supported reinforced concrete slab exposed to close range explosion of a TNT charge. Finite element method (FEM) has been utilized in order to conduct the analysis. Non-linear material model for concrete slab is adopted. Reinforcing bars made of basalt fibre reinforced plastic (BFRP) are considered by elastic-plastic material model. 3D numerical model has been created, and a software with explicit solver (LS-Dyna) has been used in order to conduct analyses. A simplified modelling method of the blast loading has been utilized, which is based on the consideration of the load effects as a time dependent pressure. Several cases with different mesh size or different finite element formulation are investigated. The results are compared with experimental data based on study of fellow researchers. Match between the numerical analyses and measurements is discussed and considered as satisfying.

KEYWORDS

Impact loading, Concrete structure, Numerical analysis, Finite element model, Basalt fibre reinforced plastic (BFRP)

INTRODUCTION AND METHODS

Structures are required to retain its resistance also under severe loading conditions, while exposed to extreme loads, e.g. impacts of various objects. For example, air plane crash modelled by Králik [1], or impacts of projectiles (defence structures for military purposes). Structures are also required to withstand severe damage caused by pressure wave after explosion (different chemical explosives or gas explosion in civil structures). Several different approaches in modelling the effects of blast load are available in order to numerically analyse the response of exposed structures.

The simplest approach to model blast loading of a structure is to consider the pressure wave effects as a time dependent surface load. This approach has been also implemented in LS-Dyna [2], where it is described as "load blast enhanced" (LBE).

Another approach is Arbitrary Lagrangian Eulerian formulation (ALE), where the air domain surrounding the structure and the explosive material itself are included in the background multi material ALE mesh (MMALE) [2]. Blast pressure wave propagation through this environment is being modelled as well. Exposed structure is modelled by Lagrangian elements. Additionally, a fluid structure interaction needs to be established [2], in order to provide a constrain between ALE and Lagrangian meshes.

Coupling of the previous two approaches (LBE and ALE) is another option to consider blast loads. In this variant, the ALE mesh is established only in the closest structure surrounding. The exterior surface of the air domain which faces the blast (a layer of ambient elements [2]) is loaded by the empirical time dependent pressure function. The purpose of these ambient air elements in this edge layer is to convert the load pressure data into a thermodynamic state data, which are subsequently applied to the surrounding ALE air domain as a source. Density and particle velocity

are obtained from Rankine-Hugoniot relations [3]. Several comparative studies have been conducted, e.g. by Tabatabaei et al. [4], or Slavik [5], who compared mentioned methods.

The blast itself could also be modelled using a smooth particle hydrodynamics (SPH) method, which was presented by Monaghan and Lucy independently in 1977 [6,7]. This method has been utilized in large variety of tasks, e.g. by Schwer et al. [8] or Trajkovski [9], who modelled air blasts and compared SPH to previous methods.

Several concrete structures exposed to blast loading have been modelled, e.g. by Tai et al. [10]; Zhao and Chen [11,12], Thiagarajan et al. [13]; Dubec, Maňas, Štoller and Stonis [14]. In this study however, a numerical analysis of one of the physical experiments conducted by Feng et al. [15], who experimentally investigated the response of one-way concrete slab reinforced by basalt fibre reinforced plastic (BFRP) under close-in TNT explosion, has been conducted.

The main objective of this study is to compare the numerical analysis performance of a simply supported concrete slab loaded by a close-range explosion with data based on physical experiment [15] for 2 different mesh sizes and for three different finite element formulations, which are available to be utilized in the used FE software of LS-Dyna [2].

METHODS

In this study, the simplified approach of blast load has been adopted. The effect of the blast wave is considered as a time dependent pressure load applied at the exposed structure surface. This approach has been also implemented in LS-Dyna [2], where it is described as "load blast enhanced" (LBE). Closer details about these features are explained in subsequent chapters. Numerical finite element model has been created and explicit solver has been utilized to conduct the analyses.

For concrete slab, nonlinear material model proposed by Schwer and Murray [16] has been utilized. The parameter values of this model are based on the calibration study by Jiang and Zhao [17]. Basalt fibre reinforced plastic bars are considered with elastic-plastic material model.

PHYSICAL MODEL AND EXPERIMANTAL RESULT OF THE CONCRETE SLAB

The physical experiments are well described in the study by Feng et al. [15]. In this study, a variant of concrete slab noted as "B1-1" [15] is investigated. The concrete class of the slab is C40, with the average strength of concrete cubes cured for 150 days equal to 46.9 MPa [15]. The slab dimensions are: 1100 mm in length, 1000 mm in width, and 40 mm in height. Spacing (axial distance) of the BFRP bars is 50 mm in both directions, diameter is equal to Ø 6 mm. Concrete cover is equal to 5 mm, the effective depth of the slab is 32 mm.

The BFRP bars have been tested in order to establish the material properties [15]. The average tensile strength of 1.53 GPa, and the average elastic modulus of 57.68 GPa have been utilized as material values in this study. The shape of the TNT mass (200 g) is rectangular prism, located in the distance of 400 mm above the mid span of the slab upper surface. The slab is simply supported on a steel frame, with a structural span of 1000 mm. Strain gauges were pre-pasted onto the BFRP bars surface, two at the mid-span and two at the quarter span of the slab, as indicated in the Figure 1. The history of the axial strain of the BFRP bar (along the direction of the structural span) in the mid-span of the slab is depicted in the Figure 1.

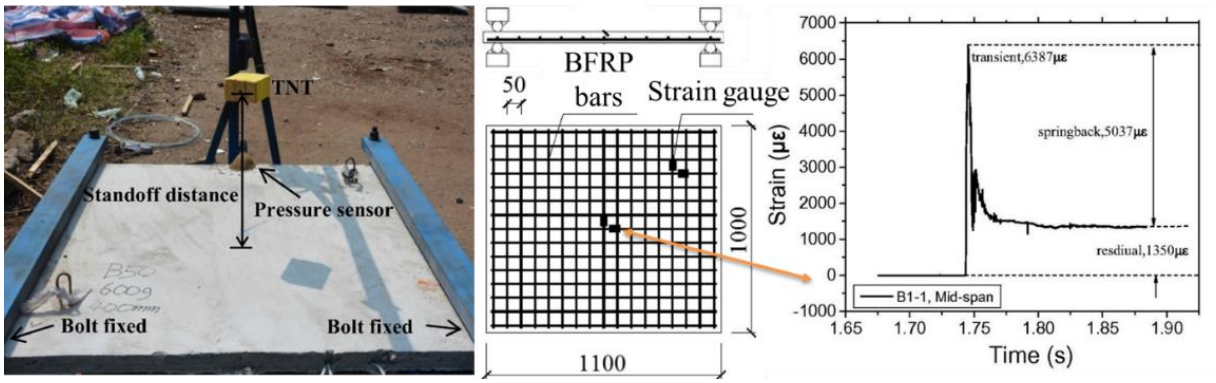

Fig. 1 – Experimental set-up and the mid-span strain history of the BFRP bar [15]

NUMERICAL ANALYSES

Modelling Approach of Blast Loading - Simplified Blast Model (LBE)

A simplified blast model with a pure Lagrangian approach of FEM is used in order to model the effect of a blast wave. The wave effect is considered as a time dependent pressure load, which is applied at the upper surface of the concrete slab, described as "load blast enhanced" (LBE) (LS-Dyna) [2]. It is based on the empirical blast loading function established by Randers-Pehrson and Bannister [18] defined as:

$$P(t) = P_r(t)\,cos^2\,\theta + P_s(t)(1 + cos^2\,\theta - 2cos\,\theta) \tag{1}$$

where θ is the angle of incidence, $P_r(t)$ and $P_s(t)$ are time dependent reflected and incident overpressures respectively, both defined by Friedlander [19] equation. In case of $P_s(t)$ the function is defined as:

$$P_s(t) = P_{so}\left(1 - \frac{t}{t_o}\right) \cdot e^{-b\frac{t}{t_o}} \tag{2}$$

where P_{so} is the peak incident overpressure, b is a decay coefficient of the waveform, and to is the positive phase duration. These parameters are defined in dependence on scaled distance Z introduced by Hopkinson [20] and Cranz [21]:

$$Z = \frac{R}{W^{1/3}} \tag{3}$$

where R is the distance from the epicentre of blast, and W is the equivalent TNT mass. Parameter values in SI units are obtained from JRC report [22]. In this paper, the TNT mass is 200 g, located 400 mm above the upper surface mid span. The scaled distance Z is equal to 0.684 $m \cdot kg^{-1/3}$. The arrival time of the blast wave is approximately 155 μs.

Material model for concrete - Schwer Murray Cap model

In order to describe the behaviour of the concrete slab, nonlinear material model needs to be utilized. Schwer Murray material model [16] is a material model suitable to analyse concrete structures, which is implemented in LS-Dyna material library [2] (MAT 145). The model is based on a yield surface defined by the function:

$$Y(I_1, J_2, J_3, \kappa) = J_2 - R(J_3)^2 {F_f}^2(I_1) F_c(I_1, \kappa) \tag{4}$$

where I1 is the first invariant of the stress tensor. J2 and J3 are invariants of the deviatoric stress tensor. R(J3) is the Rubin strength reduction factor and κ is the cap hardening parameter. The yield surface consists of two parts: the hardening compaction surface $F_c(I_1, \kappa)$, and the shear failure surface $F_f(I_1)$ which is defined as:

$$F_f(I_1) = \alpha - \lambda\, e^{-\beta I_1} + \theta I_1 \tag{5}$$

where parameters α, β, λ and θ are determined by triaxial compression test results. The expression of the hardening compaction surface is defined by equations:

$$F_c(I_1, \kappa) = 1 - \frac{(I_1 - L(\kappa))^2}{(X(\kappa) - L(\kappa))^2} \quad for\ I_1 > L(\kappa) \tag{6}$$

$$F_c(I_1, \kappa) = 1 \quad for\ I_1 \leq L(\kappa) \tag{7}$$

$$L(\kappa) = \kappa \quad for\ \kappa > \kappa_0 \tag{8}$$

$$L(\kappa) = \kappa_0 \quad for\ \kappa \leq \kappa_0 \tag{9}$$

$$X(\kappa) = L(\kappa) + RF_f(I_1) \tag{10}$$

where R is the cap aspect ratio. Hardening compaction surface and the shear failure surface are combined by a multiplicative formulation which allows their continuous and smooth combination at their intersections.

Parameter values utilized for this material model are defined in accordance with the calibration study by Jiang and Zhao [17]. For this process, the uniaxial compression strength of f_{cm} = 46.9 MPa has been considered, which is the average strength of the test specimens as described by Feng et al. [15]. The values are summarized in the Figure 2.

1	MID	RO	SHEAR	BULK	GRUN	SHOCK	PORE	
	1	2400.0000	1.458e+10	1.944e+10	0.0	0.0	1.0	
2	ALPHA	THETA	GAMMA	BETA	EFIT	FFIT	ALPHAN	CALPHA
	1.372e+07	0.3292866	7.153e+06	2.460e-08	1.0000000	0.0	0.0	0.0
3	RO	XO	IROCK	SECP	AFIT	BFIT	RDAMO	
	2.0295680	1.058e+08	1	0.0	1.0000000	0.0018274	250.69104	
4	W	D1	D2	NPLOT	EPSMAX	CFIT	DFIT	TFAIL
	0.0650000	6.110e-10	2.225e-18	5.0000000	0.0	1.0000000	0.0036547	3.500e+06
5	FAILFG	DBETA	DDELTA	VPTAU				
	1	0.0	0.0	0.0				
6	ALPHA1	THETA1	GAMMA1	BETA1	ALPHA2	THETA2	GAMMA2	BETA2
	8.300e+05	0.0	2.407e+05	8.548e-09	7.600e+05	0.0	2.600e+05	7.411e-09

Fig. 2 – Material input card for MAT 145 (in SI units)

Numerical Finite Element Models

Numerical model geometry is based on the experimental model dimensions, and is depicted in the Fig. 3. The geometry of the steel frame supporting the slab is neglected, and simply supported slab is being modelled by utilizing the appropriate boundary conditions. The concrete slab consists of regular hexahedral mesh of solid elements (for 10 mm mesh in a shape of exact cubes). Reinforcing bars are modelled by beam elements with the same mesh size as the solid elements. Two variants of the mesh size are considered, 10 mm and 8 mm, with the total number of finite elements (solid + beam) equal to 48 610 (60 709 nodes) and 92 023 (110 901 nodes) respectively.

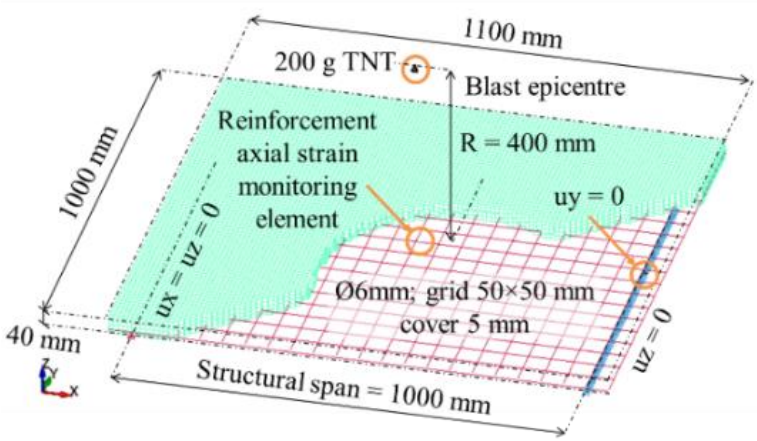

Fig. 3 – Numerical model geometry

Formulation of the beam elements is considered according to Hughes-Liu with cross section integration in all the cases. However various formulations of solid finite elements are adopted, noted as #A, #B and #C:

#A = Solid element with constant stress (along with hourglass control) (option "1" in LS-Dyna [2])
#B = Fully integrated solid intended for poor aspect ratio elements (efficient formulation, option "-1" in LS-Dyna [2])
#C = Fully integrated solid [2] (option "2" in LS-Dyna [2])

The history of axial strain is being monitored in a reinforcing bar located in the mid-span of the slab, in the direction of the structural span (x direction of the GCS).

Reinforcement material (BFRP) has been considered as bilinear material model with negligible hardening, practically linear elastic and ideal plastic behaviour. Material values are based on experimental tests [15], described in the chapter 1 of this study.

ANALYSES RESULTS

Figure 4 depicts the first principal strain at the bottom and top surface of the concrete slab in various times of the numerical analysis. History of axial strain of the reinforcement bar in the mid-span (along the structural length of the slab) is plotted in the Fig. 5 for several cases (as described in the previous chapter), along with the measured reference approximation. This reference is obtained graphically from the picture in Figure 1 right [15].

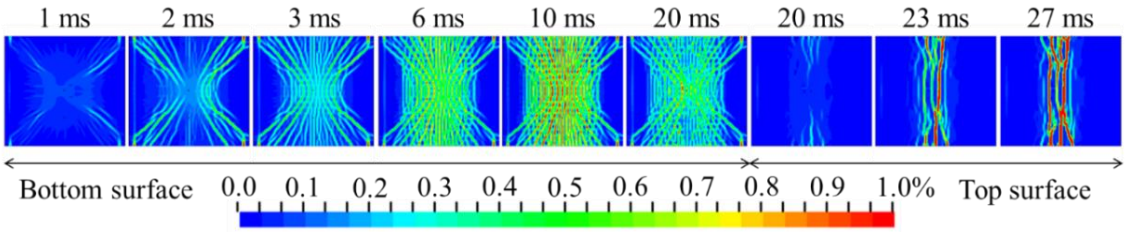

Fig. 4 – First principal strain plots at the top and bottom slab surface in various time (#A, 10 mm mesh)

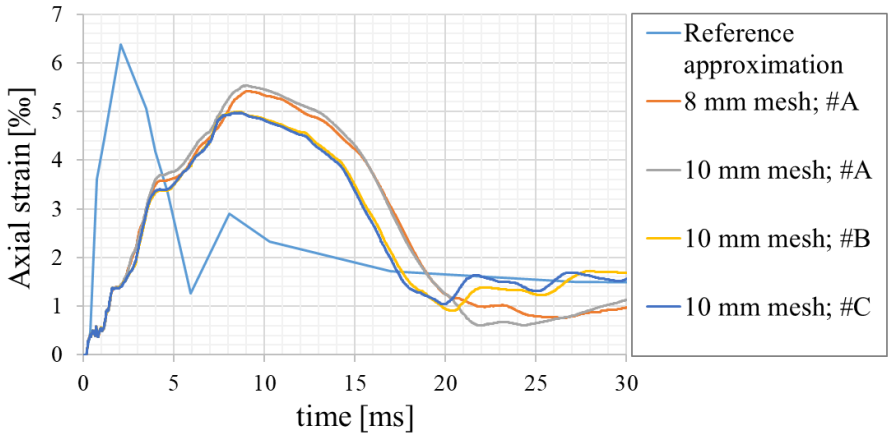

Fig. 5 – History of axial strain in the reinforcement bar.

DISCUSSION

Two mesh sizes have been compared so far, 10 and 8 mm grid. The difference in the results is rather negligible (Figure 5). Coarser mesh has not been investigated, as it is assumed, that for 40 mm thick slab, 10 mm mesh is already coarse enough. More significant difference in the analysis result is observed, when a different solid element formulation has been adopted. For cases with full integration (#B and #C), the maximal axial strain values in the steel bar are 5.0‰, whereas for the single point integration (#A), the peak strain is approx. 5.5‰. The initial strain rate (slope of the graph) is slightly smaller than the reference approximation in all the cases (Figure 5). In order to see this difference more precisely, direct experimental data would be required rather than graphically approximated curve. The axial strain maximums of all the modelled cases (5.0 - 5.5 ‰) are in good match with the measured peak (6.4‰). It is assumed that in order to obtain better match in strain rate (slope of the strain-time curve), the stiffness of the numerical model is required to be calibrated. It is not expected the finer mesh or a different material models (for concrete) would have significant influence on the initial strain rate [23].

The crack patterns at the bottom surface of the concrete slab have developed in the direction parallel to the supports, and also in diagonal directions (Figure 6 right). The first principal strain plots (Figure 4 left part) are of similar patterns. More significant upper surface cracks have evolved in the direction parallel to the slab supports (Figure 6 left). The same patterns are observed in the first principal strains (Figure 4 right part), which were caused by the slab oscillations initiated by the dynamic load.

Fig. 6 – Damage patterns of the slabs after physical experiment at top surface (left) and bottom surface (right) [15].

The simplified blast model considers the spherical source of the explosion from a single point [2], with the validity range of scaled distance Z in interval (0.147; 40) $m \cdot kg^{-1/3}$. The scaled distance value of the experiment set up is 0.684 $m \cdot kg^{-1/3}$, therefore within the validity interval of the

simplified blast approach. However, the shape of the TNT explosive was not spherical (but rectangular prism), what might cause some additional differences between the experimental and numerical results.

CONCLUSION

Explicit finite element numerical analyses (FEA) of the simply supported concrete slab reinforced with basalt fibre reinforced plastic (BFRP) have been conducted. The structure is exposed to a pressure wave caused by a close-range blast of 200 g TNT.

Three different formulations of the concrete solid elements, here referred as #A, #B and #C have been considered. The formulations differed in integration point numbers or other modifications.

Two densities of the mesh have been considered, regular 8 mm and 10 mm mesh of the concrete solid elements. Finer meshes have not been investigated yet. Significant differences in the results of analysed models and possible finer mesh models are not expected. However, computational time would be rapidly increased, hence the number of elements was kept below 125 000 to optimize the performance of the analyses. The difference in the results (crack patterns, axial strain) between 8 mm and 10 mm meshes is also rather negligible. It is assumed that slightly finer mesh would be more suitable (5 mm) in order to capture the concrete crack patterns more precisely, and yet sustain reasonable computational time. This will be tested in the subsequent research studies.

Based on the observed axial strain in the reinforcement bar, the results of the numerical analyses and the experimental data are in a nice match considering the maximums of the strain-time curves, with 5.0 - 5.5 ‰ for numerical analyses and 6.4 ‰ for the experiment. However, the strain rates (slopes of the strain history curves) obtained from the numerical analyses are noticeably smaller than the strain history based on experimental data (Figure 5). Although the reference strain-time data are based on a graphical approximation of raster figure (Figure 1), the approximation error is expected to be smaller than this difference.

Performance of a different material model (for concrete) has not yet been examined for this current setting. Various material models consider strain rate effects slightly differently, and it is possible some might be more suitable. Moreover, the structure stiffness (along with boundary condition stiffness) itself might have significant influence and would require certain calibration. These features could be crucial for a proper strain rates of the reinforcement bar. Further investigation is required.

ACKNOWLEDGEMENTS

This paper has been created with the financial support of the project FAST-J-22-7816 provided by the Brno University of Technology fund for specific university research.

REFERENCES

[1] Králik, J. (2014). Safety of nuclear power plant against the aircraft attack. Applied Mechanics and Materials, vol. 617, p. 76 – 80. ISSN: 1662-7482. DOI: 10.4028/www.scientific.net/AMM.617.76.

[2] Livermore Software Technology Corporation (1997), LS-Dyna® Theoretical Manual. Livermore, CA: Livermore Software Technology Corporation.

[3] Kinney, G. F., Graham K.J. (1985). Explosive shocks in Air. Springer-Verlag Berlin Heidelberg. Online ISBN: 978-3-642-86682-1, 1985. DOI: 10.1007/978-3-642-86682-1.

[4] Tabatabaei, Z.S., Volz J.S. (2012). A comparison between three different blast methods in LS-Dyna®: LBE, MM-ALE, Coupling of LBE and MM-ALE. Paper presented at the 12th International LS-Dyna® Users Conference, Detroit U.S. 2012.

[5] Slavik, T. (2010). A coupling of empirical explosive blast loads to ALE air domains in Ls-Dyna®. Paper presented at the 7th European LS-Dyna® Conference, Salzburg Austria 2009.

[6] Gingold R.A., Monaghan J.J. (1977). Smoothed particle hydrodynamics: theory and application to non-spherical stars. Monthly Notices of the Royal Astronomical Society vol. 181, is. 3, p. 375–389, ISSN (online): 1365-2966. DOI: 10.1093/MNRAS/181.3.375.
[7] Lucy L.B. (1977). A numerical approach to the testing of the fission hypothesis. The Astronomical Journal, vol. 82, p. 1013–24. ISSN: 00046256. DOI: 10.1086/112164.
[8] Schwer, L., Hailong T., Mhamed, S., (2015). LS-Dyna Air Blast Techniques: Comparisons with Experiments for Close-in Charges. Paper presented at the 10th European LS-Dyna® Conference, Würzburg Deutschland 2015.
[9] Trajkovski J. (2017). Comparison of MM-ALE and SPH methods for modelling blast wave reflections of flat and shaped surfaces. Paper presented at the 11th European LS-Dyna® Conference, Salzburg Österreich 2017.
[10] Tai, Y.S., Chu T.L., Hu H.T. and Wu J.Y. (2011). Dynamic response of a reinforced concrete slab subjected to air blast load. Theoretical and Applied Fracture Mechanics. vol. 56, issue. 3, pages.140–147. ISSN 0167-8442. DOI: 10.1016/j.tafmec.2011.11.002.
[11] Zhao, C.F., Chen J.Y. (2013). Damage mechanism and mode of square reinforced slab subjected to blast loading. Theoretical and Applied Fracture Mechanics. vol. 63-64, p. 54-62. ISSN 0167-8442. DOI: 10.1016/j.tafmec.2013.03.006.
[12] Zhao, C.F., Chen J.Y., Wang Y. and Lu S.J. (2012). Damage mechanism and response of reinforced concrete containment structure under internal blast loading. Theoretical and Applied Fracture Mechanics. vol. 61, p. 12-20. ISSN 0167-8442. DOI: 10.1016/j.tafmec.2012.08.002.
[13] Thiagarajan, G., Kadambi A.V., Robert S. and Johnson C.F. (2015). Experimental and finite element analysis of doubly reinforced concrete slabs subjected to blast loads. International Journal of Impact Engineering. vol. 75, p. 162-173. ISSN 0734-743X. DOI: 10.1016/j.ijimpeng.2014.07.018.
[14] Dubec, B., Maňas P., Štoller J. and Stonis P. (2019). Experimental and numerical assessment of fibre reinforced concrete slab under blast load, ICMT 2019 - 7th International Conference on Military Technologies, Proceedings 2019. ISBN: 978-172814593-8. DOI: 10.1109/MILTECHS.2019.8870129.
[15] Feng, J., et al. (2017). Experimental research on blast-resistance of one-way concrete slabs reinforced by BFRP bars under close-in explosion. Engineering Structures, vol. 150 p.550-561. ISSN: 0141-0296. DOI: 10.1016/j.engstruct.2017.07.074.
[16] Schwer, L.E., Murray Y.D. (1994). A three invariant smooth cap model with mixed hardening. International Journal for Numerical and Analytical Methods in Geomechanics, vol. 18, pp. 657-688, DOI: 10.1002/nag.1610181002.
[17] Jiang, H., Zhao J. (2015). Calibration of the continuous surface cap model for concrete, Finite Elements in Analysis and Design. vol. 97, p. 1-19. ISSN 0168-874X. DOI: 10.1016/j.finel.2014.12.002.
[18] Randers-Pehrson, G., and Bannister K.A. (1997). Airblast loading model for DYNA2D and DYNA3D. Army Research Laboratory, Rept. ARL-TR-1310, U.S., 1997.
[19] Friedlander, F.G. (1946). The diffraction of sound pulses I. Diffraction by a semi-infinite plane. Proceedings of the Royal Society A. 1946. ISSN 0080-5630. DOI: 10.1098/rspa.1946.0046.
[20] Hopkinson, B., (1915) British Ordnance board minutes 13565, in: The National Archives, Kew, UK, pp.11.
[21] Cranz, C., (1925) Lehrbuch der Ballistik. Erster Band. AusereBalistik, Springer Verlag, Berlin.
[22] Karlos, V., Solomos G. (2013). Calculation of blast loads for application to structural components. JRC Technical Reports, Report EUR 26456 EN, Luxembourg. ISSN 1831-9424. DOI: 10.2788/61866.
[23] Jindra, D., Hradil P., Kala J., Král P. (2020). Mesh size influence of the concrete slab FE model exposed to impact load for various material models. Transactions of VSB - Technical University of Ostrava, Civil engineering Series, 20(2), 1-7, DOI: 10.35181/tces-2020-0010.

CIVIL ENGINEERING JOURNAL

Article no. 28

THE CIVIL ENGINEERING JOURNAL 2-2022

INTERNAL AND EXTERNAL IMAGE OF HRADČANY AND PRAGUE CASTLE

Martin Šnorbert

Czech Technical University in Prague, Faculty of Civil Engineering, Department of Architecture, Prague, Thákurova 7, 166 29 Prague 6 - Dejvice, Czech Republic; martin.snorbert@fsv.cvut.cz

ABSTRACT

This contribution deals with the urban development of the Hradčany area (it is a district of the capital city Prague, surrounding Prague Castle), within its position in the capital city, but especially within the area itself. Great emphasis is placed on historical development, as it significantly affects the current situation. Prague Castle, perceived as a historical and architectural complex, is unique in its complexity and size, we do not find a similar example in any of the surrounding countries.

Prague Castle, as an important part of Hradčany, was and still is the seat of the monarch, or today the president of the Czech Republic. The development of Czech history influenced the appearance of the Castle (alternation of royal families, growth and decline in the importance of Prague, i.e. the Czech Kingdom in Central Europe). The combination of secular and ecclesiastical power in one place is also remarkable. At the same time, it is possible to find evidence of development in the field of culture, technical conveniences, architectural and engineering arts, over the course of ten centuries.

Based on archival research and the study of references, the reader is acquainted with the gradual change in the formation of the current plan of the city and the Castle. The connection between morphological assumptions and the location of first a Slavic fort, later a stone castle, is pointed out. The castle area was followed by a settlement in the sub-castle, which in the 14th century became a serf town of Hradčany. The alternation of artistic styles over the centuries and the related change in the structure and scale of buildings, but especially the panorama of Hradčany with the silhouette of the Castle, is discussed. In the end, the potential of the Hradčany area and the possibility of modernization interventions are also evaluated.

KEYWORDS

Hradčany, Prague Castle, Town planning, Urban development, Panorama of Hradčany, Silhouette of Prague Castle

INTRODUCTION

The appellation Hradčany is not entirely clear. It is often used for Prague Castle and adjacent places - especially for the originally serf town of Hradčany (area from the Castle to Strahov), Nový Svět and the Royal Garden connected to the Castle by the Powder Bridge. In earlier times, this concept was probably perceived in a broader sense of administrative division, as Prague as a royal capital was made up of four units - Hradčany, the Lesser Town, Old Town and New Town. Today's administrative division (cadastral territory) is limited approximately to the territory defined at the beginning of this paragraph. For an unambiguous determination of the investigated area of Hradčany, a picture (Fig. 1) based on a map application from the company Google (https://www.google.cz/maps) is attached. In common parlance, Hradčany is often confused with Castle, as evidenced by the famous term "Hradčany Panorama," which points to an important terrain

massif above Little Town, ending with Prague Castle with the unmistakable protruding silhouette of the Cathedral of St. Vitus, Wenceslaus and Adalbert.

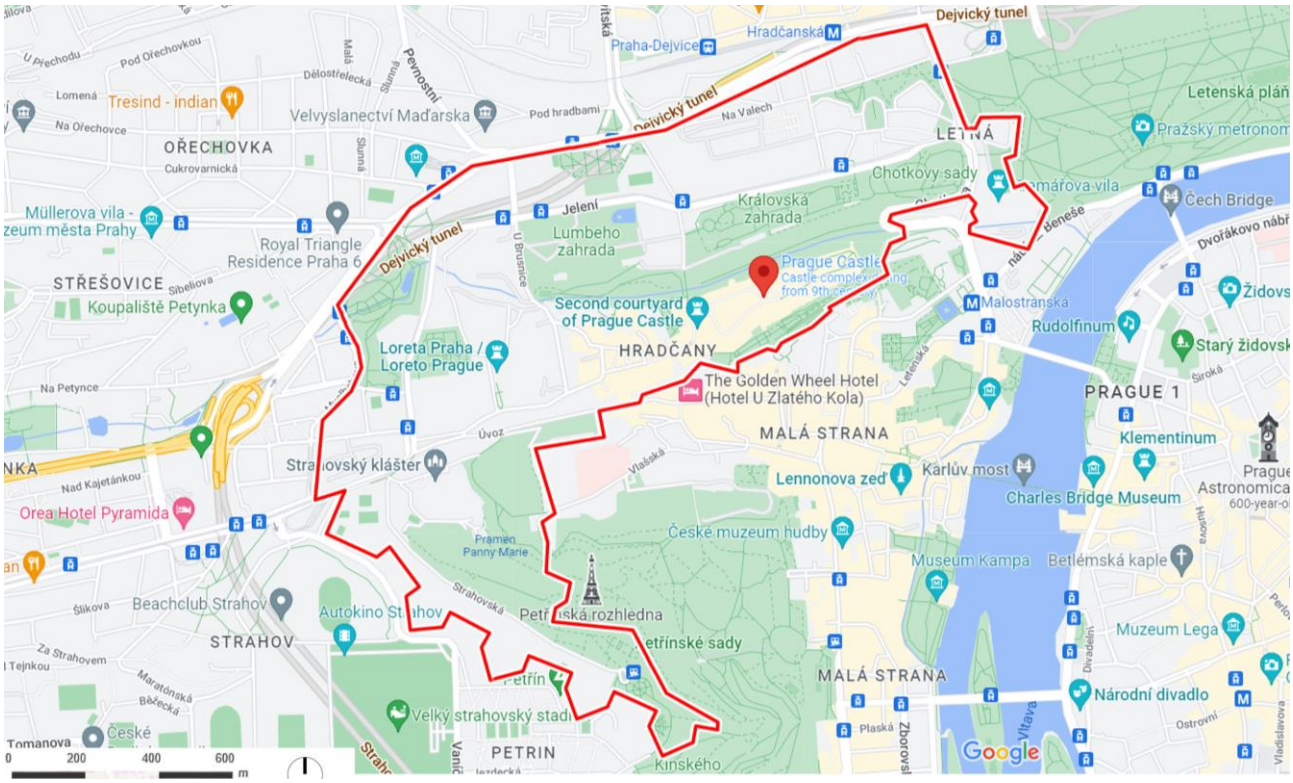

Fig. 1 – Marking of the Hradčany area (red line = border) [1]

The Castle and Hradčany are a remarkable unit, which combines morphological assumptions with the result of the work of a huge number of people. Several foreign artists also worked here, reaching world standards and understanding and supporting the local genius loci. That is why there is a common art base in Hradčany, consisting of a selection of used materials (work with stone, fired clay or plaster), rhythm and height ratio of the windows. On the other hand, there are many contrasts - political even construction. For example, the imprints of the monarchy and the republic, the church and secular power, old and modernist architecture, the opposites of the smallest buildings of houses and the largest palace buildings. In the Hradčany area there are intricate streets, variously wide, curved, small spaces, as well as squares and courtyards, small nooks or beautiful viewing areas, stairs, walls, accessible and only emotionally sensed gardens, freed spaces, but also plots with high-density of buildings; palaces, temples and houses of various sizes and styles.

URBAN DEVELOPMENT OF HRADČANY AND CHANGES IN THE PANORAMA OF THE CASTLE

Romanesque period

Already in the second half of the 9th century, a wooden Přemyslid princely palace was built on the site of the Slavic fort, which acquired the appearance of a stone castle in the Romanesque period. On the Hradčany ridge, it is possible to assume a market settlement in Pohořelec, which in the 11th century approached the Castle. The original simple fortifications of the fort were replaced by a new rampart fortification under Prince Břetislav I. The area in front of the castle in the west was reduced and new walls (up to 5 meters high) were built, and a moat was dug in front of them. The strengthening of the walls consisted of towers, which also served as gates. A stone bishop's palace with the chapel of St. Morice was built and the St. Vitus rotunda was rebuilt into a basilica. Already

at this time (1145-1150) the monastery church of St. George as a three-aisled Romanesque Basilica with two towers was built, and these two towers remind us of the Romanesque period to this day. Soběslav's new two-storey stone palace was seen at the head of the walls. The castle probably also housed the dwellings of a castellan and canons, the houses of the prince's retinue, courtiers and servants and, of course, the relevant economic facilities, warehouses and weapons repair shops. The palace consisted of a large rectangular hall measuring 50 x 10.5 m, supplemented by a heated princely living room. On one side, a castle chapel was added, dedicated to All Saints, on the other side, the southern border was formed by a tower. During the construction of the palace, an effort was made to show the importance of the Czech monarch and to equalize or overcome the level of the imperial Palatinate (Pfalz). Therefore, the facade facing the city was artistically conceived and had a representative character [2].

Prague Castle has preserved the spaciousness and complexity of the old fort. It could be said that it was more of an urban space in which there were several fenced or separate complexes of buildings. There were Basilica of St. Vitus, Basilica George with two towers, with a nunnery with a garden of paradise, the building of the bishop's palace with the chapel of St. Moritz (Mauricius), Church of St. Bartholomew, burgrave's building, chapter of St. Vitus, the court of canons, servants' houses and farm buildings.

In front of the Castle, on the area of the Hradčany ridge, there was probably only a small settlement at that time. Also, in the area of today's Hradčanské Square there was a settlement, but probably not too large, because even after 1300 this square was almost empty. The hills and plateaus around the Castle were forested and after 1140 the Strahov Monastery "in the Black Forest" was founded.

In this epoch, the Hradčany panorama could be observed for the first time, as the Hradčany hill was crowned by the castle palace, the monastery of St. George, and especially the block elevation of the Basilica of St. It welcomes, with its considerable overall length and magnificent mass. The scale was relatively small, but the mass was concentrated and divided only in detail.

Fig. 2 – Hypothetical view of the Slavic fortified settlement of Prague (9th century), the predecessor of today's Castle [3], page 72

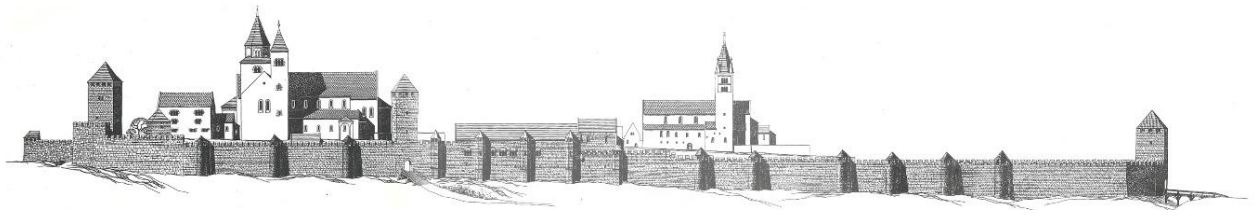

Fig. 3 – Reconstruction of the view of the Romanesque Castle during the reign of the last Přemyslids (13th century) [3], page 72

Gothic period

Přemysl Otakar II. tried to strengthen the walls and partial reconstruction of the Castle and its own seat - the palace and other buildings. On the west side was an undeveloped plain, which was used to build a large fort and restore two moats according to the principles of the Gothic fortification system. Another defensive fortification tower and a new episcopal tower were built on this side. At the other end of the Castle, the entrance through the Black Tower was cancelled and a new fortification gate to the Na Opyši road was established. An open corridor with arcades and nine Gothic arches was added to the Romanesque palace on the upper floor and opened into a new

courtyard. A smaller wing was newly built at the corner of the south gate, and a new chapel of All Saints was added to the chateau. Two short new wings then ran into the north courtyard [4].

A fire in 1303 severely damaged the old royal palace, the accession of John of Luxembourg to the Czech throne meant decay in the area of the Castle, on the contrary, the rule of his son Charles IV. represents a famous chapter in the history of Prague and the Czech lands. On the remains of the ground floor of the Romanesque palace and the building of Přemysl Otakar II. he had a two-storey gothic palace built, there were two halls on the upper floor. This palace was located north of the old Romanesque south tower, and a new court chapel of All Saints was built east of it according to the design of Petr Parléř. The construction of the cathedral began in connection with the promotion of the Prague diocese to archdiocese in 1344. The construction was first led by Matthias of Arras and after his death by Petr Parléř and later by his sons Jan and Václav. The bell tower - the large south tower - remained unfinished due to the Hussite wars. A new wing was built next to the old palace on the site of the transverse wing, and a fortified front courtyard was built. Both towers (White and Black) were rebuilt and the castle fortifications were repaired [5].

Sometime around 1320, the highest burgrave of Prague founded a serf town near the Castle. It was the third city in today's Prague and it was called Hradčany - this name meant in Old Czech a settlement of people who lived around the castle. When the town was founded, one of the oldest town plans was used - the wedge layout (we also observe it near Bechyně or Mladá Boleslav, for example). This disposition opened up towards the Castle and an important part was a long marketplace surrounded by houses and walls, which led to the edge of the hill to Petřín and the Brusnice valley. The area was further divided into two streets (today's Loretánská and Kanovnická) and their transverse bridge (U Kasáren). In addition to the perimeter walls, the city was protected by castle moats in the east and a moat running parallel to Kanovnická Street in the west.

At the time of Charles IV. the seriousness of the Castle grew, but also Hradčany, and therefore craftsmen working for the Castle, as well as many people of lordly and spiritual status, moved to this area. The canons settled on the northern side of Hradčanské náměstí, while the south belonged to the Parléř family. Between the Hradčany walls and the fortifications of Prague Castle, there was a space where people who could not find a place inside the city began to build their homes.

During the reign of Charles IV. the old Romanesque castle, similar to the German Palatinates, was transformed into a castle built according to the principles of French Gothic. Its horizontal design of the walls, the palace and other houses of nobles and church leaders was completed by a vertical in the form of a cathedral rising to the sky. On the contrary, the government of Wenceslas IV. and the Hussite period brought stagnation, cessation of construction activity, and even the relocation of the monarch to the area of the Royal Court in Prague's Old Town.

The Jagiellonian accession to the Czech throne was associated with a new boom and construction activity in the Castle area. First, the Vladislav's bedroom was built, then a short bridge crossing between the castle and the cathedral, in which a royal oratory was built. At that time, the excellent builder Benedikt Ried (Rejt) worked at the Castle, under his leadership a beautiful airy hall with an intertwined ribbed vault in the late Gothic style was created on the floor of Charles Palace, but the windows foreshadowed the arrival of a new style - the Renaissance. The access to this hall was also specific, on one side, riding stairs were created for tournament riders, because knightly competitions took place in the hall.

This time brought a more artistically successful outline to the panorama and the scale of the old royal palace increased. The vertical effect of the cathedral under construction was added.

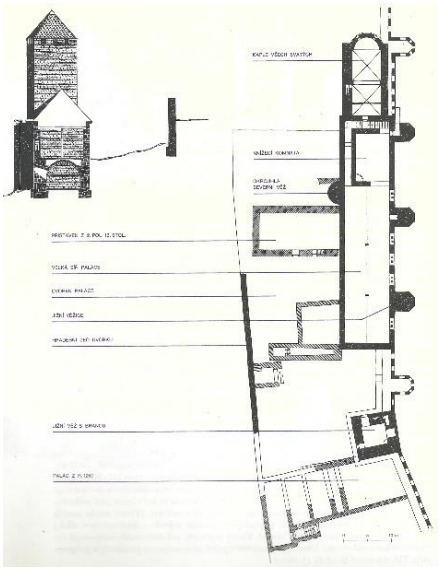

Fig. 4 – Reconstruction of the first floor of a stone Romanesque princely palace [3], page 71

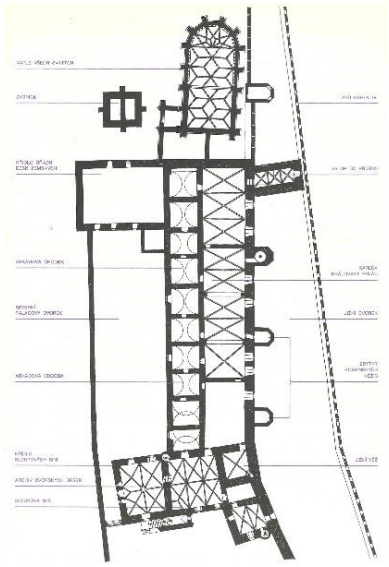

Fig. 5 – Reconstruction of Prague Castle in the time of the Luxembourgs around 1400 [3], page 82

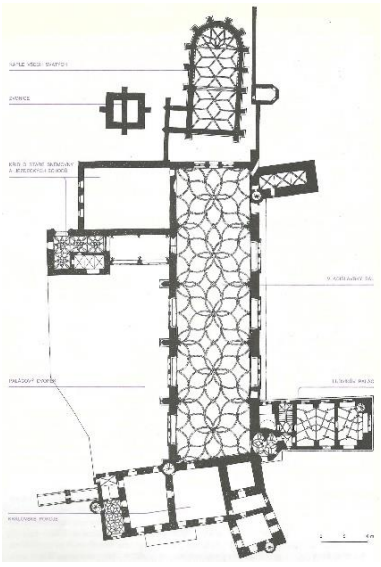

Fig. 6 – Floor plan of the royal palace after reconstructions carried out under Vladislav II. [3], page 83

Renaissance period

Benedikt Ried built the Ludvík's Wing, oriented towards Prague, perpendicular to the Vladislav Hall. The siege tactics also changed, and therefore the construction of several cannon towers (Daliborka, Bílá věž = White Tower and Mihulka) on the northern side, with a significant wall thickness and areas for storing gunpowder and plenty of space for operating cannons.

Hradčany was slowly recovering from heavy wounds during the Hussite wars, the development was made possible by the royal decision so that the village of Hradčany could sell the desolate plots to foreign settlers to build new houses. The aristocracy is trying to get to the Castle at this time, followed by courtiers, servants and craftsmen. In Loretánská Street, land was being merged for the construction of large aristocratic palaces. A Renaissance town hall was built in Hradčany behind the square.

The beginnings of the Habsburgs on the Czech throne were connected with the arrival of Italian artists and craftsmen who brought the Italian concept of the Renaissance to Prague. There was an effort to add, rebuild and modify the castle wings and rooms for the purposes of a comfortable and representative palace. In this respect, the Castle could only expand westwards towards Hradčany. The second goal was the construction of an airy summer residence surrounded by a Renaissance garden with relevant period buildings (Míčovna = Ballroom, Jízdárna = Riding hall, Lví dvůr = Lion's court and other) and equipment. There was no more space for this event on the promontory, and therefore a garden was established behind the Deer Moat, where until then there was a slightly sloping terrain with vineyards, which ran parallel to the axis of the Castle. The Queen Anne's Summer Palace was built in the garden (the beginnings of the construction were connected with Paolo della Stella, the completion of the construction with Bonifác Wohlmut) [6].

The Great Fire of 1541, which occurred on Malostranské Square and spread across the Lesser Town to the Castle and Hradčany. This catastrophe essentially destroyed the Gothic appearance of the Castle and paves the way for the Czech Renaissance. The repairs first focused on the castle fortifications - bastions, gates, the White Tower. Under the leadership of Hans Tirol, a new robbery, a private royal room at the Old Palace, were built, and the queen's rooms were rebuilt. After him, Bonifác Wohlmut began to work at the Castle. He took part in the construction of the new

Chamber of Deputies, the completion of the Renaissance choir loft in the cathedral and the Renaissance helmets of the large south tower, and the construction of small and large ballrooms [7].

The spatial demands of the nobility and church representatives grew and they could not be satisfied in the area of the Castle, but at the same time there was an effort to settle as close as possible to the king, and therefore attention was turned to Hradčany. The aristocracy bought and merged the burnt places of several houses into one plot and built magnificent Renaissance palaces - the Lobkowicz Palace with sgraffito decoration, the Gryspek Palace, and the Sternberg Palace were built on Hradčanské Square. However, the opposite procedure also appeared, when some gardens and larger plots were divided into smaller building plots for the construction of houses - for example in Horní Úvoz, from the Castle to Kanovnická Street, on Loretánské Square. Apart from the palaces and new houses, Hradčany did not change much, or only changed in detail and on the facades. Walls and gates from the time of Charles IV. they were desolate and severely damaged. Other city amenities such as city water supply or paving were in a primitive state. The other streets were not modified at all. Of the whole city, the Renaissance was used the most in the Castle, examples being the Rosenberg Palace, the Lobkowicz Palace, the new burgrave's office and helmet on the cathedral bell tower.

The fate of Prague and Hradčany was greatly influenced by the reign of Rudolf II, who transformed Prague into a European metropolis with great artistic, cultural and research activities. At this time, the imperial residence expanded to almost all sides, private houses were demolished, the third courtyard was paved, water was distributed and several fountains were built. The king moved west from the old castle, where he had a new apartment set up - the summer room of the emperor and empress. A large new stable was built (stable with two floors). Ferdinand's and Rudolf's stables created a plinth for two new halls - the two-winged Spanish Hall and the Gallery (New Hall) for collections of rarities and curiosities. In the middle wing, Rudolf's corridor, which connected the northern and southern parts of the Castle on the first floor, became an important part of communication. The number of courtiers and servants at Prague Castle was also increasing, which is why the development of houses in Jiřská Street (rebuilt in the Baroque style) was increasing. The Great Tower of the Cathedral of St. Vitus received an astronomical clock with a double dial. Rudolf II. was also interested in spaces outside the Castle. A large and long greenhouse was built in the Royal Garden, and an orangery and greenhouse for fig trees were established. On the south side, the Garden of Eden (Rajská zahrada) was established in front of the monarch's room on the site of old vineyards. His successor, King Matthias, had a dignified gate built (the first Baroque building in the Castle).

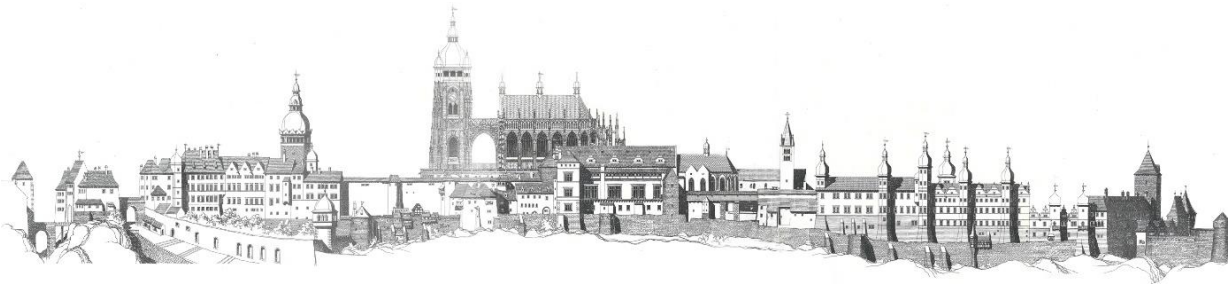

Fig. 7 – Reconstruction of the view of Prague Castle under Rudolf II. A dominant feature of Castle is the unfinished Gothic Cathedral of St. Vitus, whose tower is finished with a Renaissance helmet. (After 1600) [3], page 72

Hradčany became a royal town in 1592, the town hall was rebuilt with sgraffito decoration. Hradčany and Lesser Town became residential towns, where rich domestic and foreign nobles, courtiers, various specialists and court contractors bought land and houses. The social regulation, which stipulated that every nobleman living in Prague lived in their own house, also contributed to this.

The Renaissance brought the city of Hradčany and the Castle to the image of Prague as a compact mass, basically from Strahov to the Belvedere. Compared to the past, a change in the character of the panorama was observed, which was caused by many architectural details, colors, attractions in the silhouettes of some buildings - especially the motif of towers at Rosenberg Palace, almost all castle buildings used beautiful sgraffito decoration, multi-storey volute gables, with two lanterns and colourful roofing.

Baroque period

The Thirty Years' War brought stagnation and war damage - first the Saxons invaded Prague, then the Swedes. Vienna became the capital of the Habsburg monarchy, yet Prague still had a significant position and strategic position, so the construction of a Baroque fortification was started and it was based on a complex system of high brick walls with star bastions and reinforced deep moats. In 1670, all Prague cities were fortified, and the Castle became a separate administrative district, delimited by old fortification walls with five gates and three drawbridges [8].

In 1673, the foundation stone was laid for the completion of the cathedral in a new Baroque concept according to the architect G.D. Orsi. In 1760, a Renaissance helmet was struck and damaged by lightning and acquired the Baroque form it still has today. At the end of the new ramp leading to the Castle, the Church of Our Lady of Einsiedel was built with a facade facing the Castle. The Church of Our Lady Help of Christians in Chances (soon demolished) was built near the Bruska Gate. The Santa Casa, later the cloister, the jewel box and the church of Our Lady were built in Loreta. K. I. Dienzenhofer built a new facade with two side chapels, a square with a staircase, and finally a floor above the cloisters.

In the Baroque period, the Royal Garden was modified according to the rules of the period, supplemented with sculptural decoration, grew and new buildings were built in it - a riding hall and a farmyard. The garden occupied an area approximately as large as the Castle's own area. Another baroque garden was found by the Černín Palace, had an axial connection to the palace's loggia and was finished by a pavilion [9].

Even during the Thirty Years' War, a certain construction activity took place at the Castle - there was a reconstruction, expansion and connection of a part of the Castle along the south side of the third courtyard. Until this time, the second courtyard was perceived more as a place in front of the castle, which is changing and thanks to the Matthias Gate was clearly defined. In addition to palace and large church buildings, several chapels and artistic sculptures were built at the Castle.

In the Hradčany area, the situation was repeated to a certain extent, as it was after the fire in 1541. The nobility buys land ravaged by the war, consolidates plots and builds beautiful palaces. Humprecht Černín of Chudenice had a magnificent palace built at the highest point in Hradčany, the Lobkowicz Palace was rebuilt, and the archbishop's palace was also rebuilt. The Tuscan and Martinique palaces were also built on Hradčanské Square.

Later, the archbishop's palace was rebuilt (this time in the French Rococo style), the Sternberg Palace was built, in Loretanska Street there was a whole front of aristocratic palaces on the left - Dietrichstein, another Sternberg, Kolovrat, Wroclaw and the palace of the imperial court office. The presence of these palaces led to the expulsion of the townspeople on the outskirts of Pohořelec, and gradually this area was also controlled by the nobility and the church, so that the townspeople settled in the New World area.

It was not until the 18th century that the Castle and Hradčany became a building unit with an external optical unity. The old spaces also became squares (conscious urban units) - Hradčanské, Loretánské Square and the whole Loretánská Street. The medieval character was disappearing and Hradčany even stands out over the streets of the Old Town and New Town in certain respects.

Although the above-mentioned spaces are architecturally designed, their surface was rather untidy with mud and dust.

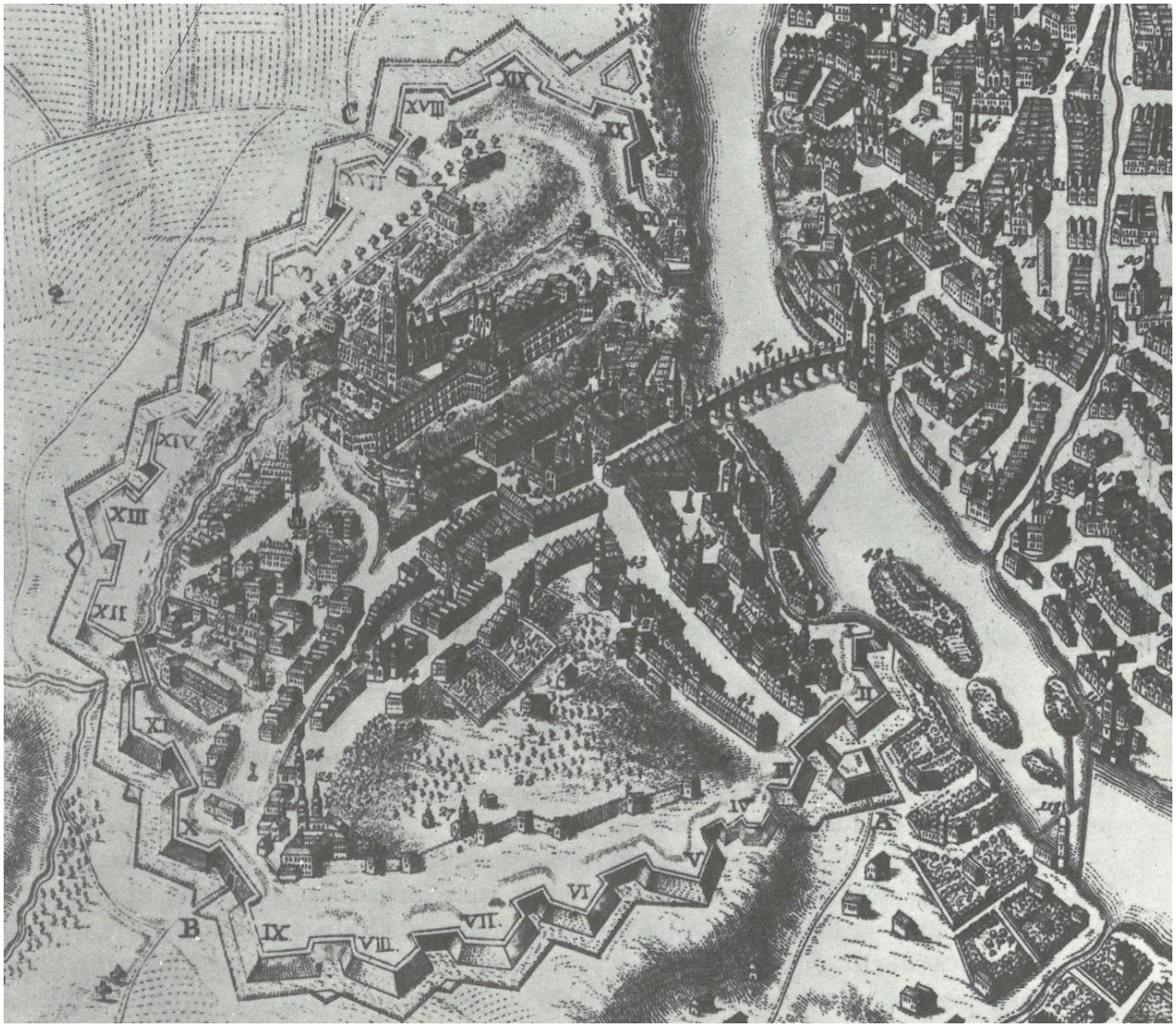

Fig. 8 – An excerpt from an engraving depicting Prague, surrounded by Baroque walls, in an axonometric view [10], page 104

Prague was in the time of Charles VI. one huge construction site and has undergone a huge change in whole and detail. Baroque construction erases the Gothic character of the city and gives it forms that last to the present. Perhaps only due to a lack of funds, some significant medieval buildings were not transformed into a Baroque form. In the panorama, the Castle and the town were united into one building unit. The castle is already gaining a large scale similar to today's state.

Classicist period

This period was characterized by a major reconstruction of the Castle caused by war damage during the battles for Habsburg heritage. The first and second moats (from the time of Přemysl Otakar II) were filled in and a new wall was built above the former third moat at the archbishop's palace. During the alterations, the Castle area was cleaned of various houses and outbuildings, and sometimes, unfortunately, some important buildings. The first major blow was the French occupation (1741 to 1742), which destroyed the entire Pohořelec up to the Capuchin palace, the courtyard and

stables of the Černín Palace and most of the houses in the New World. Even worse was the Prussian siege of 1747, when Prague was bombed for six weeks. A riding hall with a small ballroom, an opera house and the Powder Bridge were burned. The Spanish and New Hall, the monastery of St. George, the Institute of Noblewomen, and especially the church tower and the interior of the cathedral were damaged. The Hradčany area was also not spared and damage occurred at Loreta, the Černín and Schwarzenberg Palaces and a number of burgher houses.

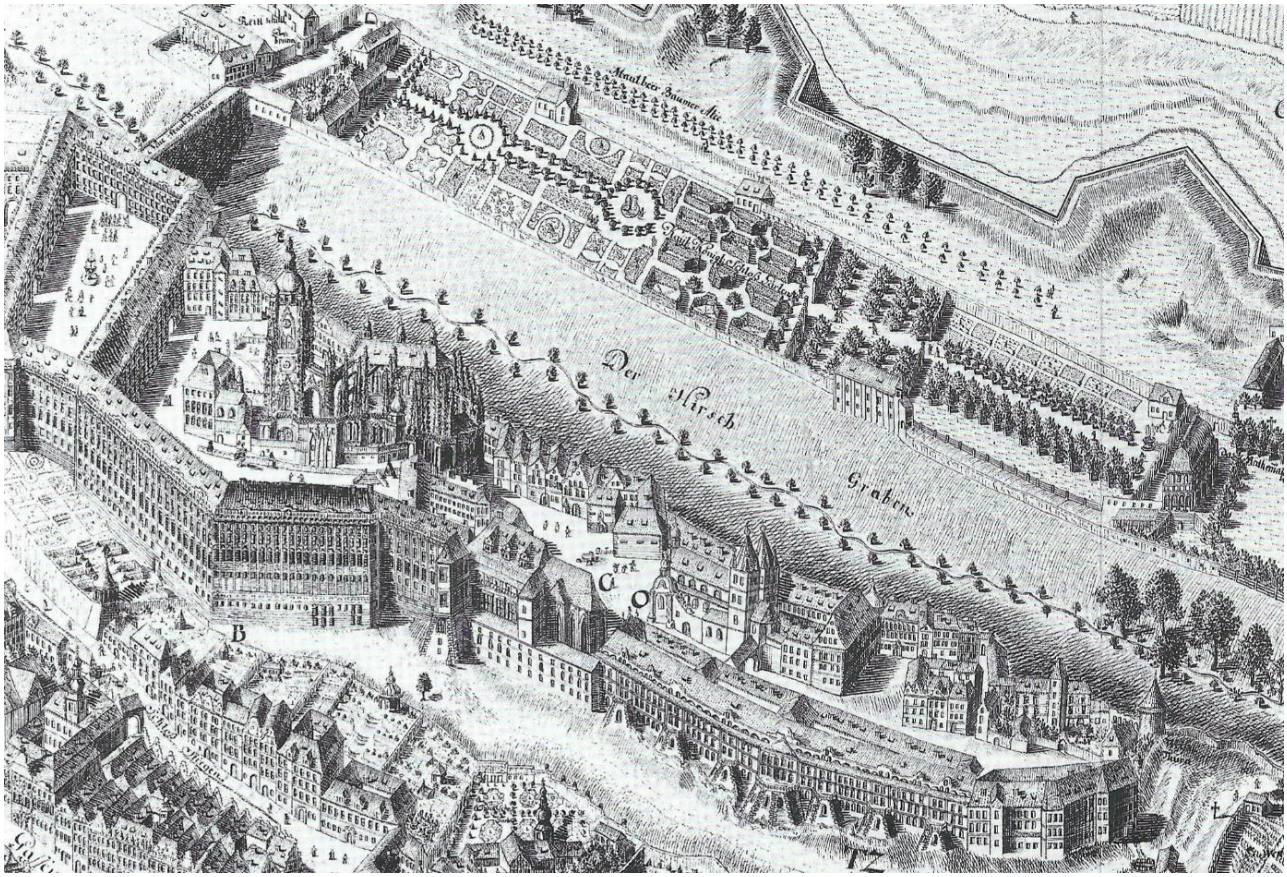

Fig. 9 – Prague Castle from the southeast. Ink pen drawing from 1769 created by Josef Daniel Huber [10], page 33

We would find the beginning of a significant reconstruction in the eastern part of the Castle. The Rosenberg Palace was purchased for the Institute of Noblewomen and completely changed its façade facing the city. Its five typical renaissance towers with onion-shaped roofs were in poor condition and therefore demolished. So, a monotonous long façade was created with three indistinct projections in the style of sober French classicism. As soon as this reconstruction was completed, the Castle was bombed and severely damaged during the Seven Years' War. This led Maria Theresa to order that the entire western part of the castle building should be rebuilt, in particular to unify the disorganized facade facing Prague. Architect Nicolo Pacassi complied with this order in about 20 years. He united the façade under one ledge, incorporating the Matthias Gate into the transverse wing at the western end of the Castle and adding the court of honor. An old moat was filled in, an entrance gate with bars was built in front of the first courtyard and the Castle was optically connected with Hradčany. The Castle changed, lost its defensive character and became a palace. The northern facade of the Castle remained almost unchanged. The sober exterior did not match the interiors, which were decorated with luxurious stucco, beautiful wall and floor finishes and beautiful furniture. The rooms changed their purpose, and many of them were used as offices and warehouses.

During the reign of Joseph II. the centralized government was enforced, so that the castle authorities also ceased their activities and the rooms of the former royal palace remained

abandoned. The castle lost its significance and remained empty. The practical emperor considered using the empty castle secular and church buildings for military purposes. And so it happened. Monastery of St. George, Ballroom, Great Riding Hall, Royal Summer Residence and Monastery of The Ursulines were used as accommodation and technical military facilities.

After the uniform reconstruction of the Castle, when many building alterations from the past were erased or covered, the castle mass began to resemble a single huge block with a modest division, from which only the tower of the cathedral bell tower protrudes. At the same time, however, this horizontal mass further emphasized the dominant position (both in volume and scale) of Prague Castle within the Prague panorama [11].

19th century

In the 19th century, Prague was large, but still a provincial and unpopular city at court. The construction of the Castle inside did not change. Only the preparations for the coronation of Emperor Francis Joseph I as King of Bohemia led to a larger construction project - to the magnificent renovation of the Spanish and New Halls. The highest burgrave of the Czech kingdom, Count Karel Chotek, became an important figure. He improved the connection between Lower Prague and Hradčany on both sides of the castle promontory. The entrance above Ostruhova (Nerudova) Street was very desolate at the time, the count had it re-established and allowed further connection of the town with the Castle to the west. On the other side, he had a modern serpentine road built as part of the Deer Moat, which adjoins Klárov. In a relatively short time, English-style parks have been set up with new views of the old city. Although they were divided by Chotek's serpentine, they were spanned by a bridge like today. He also managed to evict the army from the Royal Summer Palace (soldiers had an artillery laboratory and a warehouse there).

The romantic effort culminated in the second half of the 19th century with the idea of completing the Cathedral of St. Vitus. In 1873, the foundation stone was laid for the building. At that time, there was also a controversy between experts on conversation and restoration of monuments, which was also reflected in the cathedral. The completion of the cathedral was a major construction intervention, which also brought a few smaller demolitions and relocation of some smaller buildings. In Kranner's conception, the cathedral was to fill the space of the third courtyard more significantly than in the ideas of its original creators; the courtyard lost its romance as well as disorder. The west front wall of the cruciform ship on the outside was demolished with the famous painting by Professor Jan Ferdinand Schor called Czech Patrons in Heavenly Glory [12].

At the end of the 19th century, the castle languished structurally and socially. Likewise, Hradčany has become a relatively quiet part of Prague, while the commercial, production and industrial center is moving to new suburbs. The last aristocratic residence Salm Palace was built here in 1810 by the Empire-style. Construction activity could only be recorded in the reconstruction of palaces into buildings used by the Austrian army or officials. Later, new buildings were built here, which, with their scale and style, disrupted the character of the city. An example is the transformation of the Černín Palace into an artillery barracks and Loretánské náměstí into a training ground. Similarly, the small-town character of Pohořelec was suppressed due to the construction of a large mass of land barracks, a large divisional court building and a prison in the vicinity of Loreta and the Capuchin monastery.

Especially in distant views, the Castle gained a different appearance, different conditions and relationships, thanks to the reconstruction from the time of Maria Theresa and the ongoing completion of the cathedral. Before Hilbert's work on the completion of the Church of St. Vitus, the Castle appeared as a continuous horizontal base with the same division by means of hundreds of windows, which, however, suppresses the dominant position of the church, which consisted of a tower and a church body with three small sanctuary towers. The unfinished expression (empty arch of the transept) in contrast to the completed castle line also contributed to this. After the completion, this panorama was no longer perceived as composed of two buildings, but as one complete ensemble with an organic concept, proportionally massive and interesting in the division of four towers in most views, only in the front view three towers were observed. The effect of the bell tower

(large southern tower) was weakened after the completion of the western towers and the increase of the roof.

20th century to the present

The beginning of the 20th century is connected with the completion of the Church of St. Vitus under the leadership of Kamil Hilbert, which was ceremoniously completed in 1929 on the occasion of the 1000th anniversary of the martyrdom of St. Wenceslas. After the establishment of the new republic, Tomáš Garrigue Masaryk became president, and he found himself in a similar situation as Charles IV. The Castle was a large complex, but dilapidated, decrepitude and almost uninhabitable. It was even considered that the first Czechoslovak president would reside in another newly built residence (this idea was discussed again after the first election of President Havel). Masaryk had a lucky hand in choosing the castle architect - he chose the Slovenian professor Josip Plečnik. Plečnik's excellent work should be appreciated - he participated in the modifications of the castle courtyards, the unification and creation of representative gardens, and the adaptation of the interior for the purposes of the president. The Slovenian architect used his sense of monumentality to the grandeur of the space, an example being the Column Hall in the western wing of the New Royal Palace. Ceilings, walls and partitions have been removed in this area. Only the perimeter walls and the roof were left. A hall with a triple row of light columns with Doric and Ionic capitals was created. Plečnik used his favourite column motif here on the axis of the round window. The ceiling was made of copper plates, with a gilded lion in the middle. His castle interventions can be termed modern classicism. His work was followed by other great architects before the Second World War, such as Otto Rothmayer (Plečnik's pupil), Karel Fiala (castle builder), Pavel Janák (in collaboration with urban planner Jan Sokol). Shortly after the war, the architect Janák worked again at the Castle, later Jaroslav Fragner was appointed the castle architect. Over time, one person is not responsible for the modifications of the Castle, but the reconstructions and interventions were decided collectively in various commissions and councils (Idea Council for the Modifications of Prague Castle, etc.). At this time, there were mainly internal modifications, an example being the reconstruction of the middle wing between the second and third courtyards and the creation of the Picture Gallery of Prague Castle. Only the adaptation of the Old Burgrave's Office to the House of Czechoslovak Children affected the external image of the Castle. New quality interventions returned to the Castle with the last Czechoslovak and at the same time the first Czech president Václav Havel, who had a good relationship with architecture. He therefore invited several outstanding architects to renovate the Castle - such as Bořek Šípek, Eva Jiřičná and Josef Pleskot. Again, these were more interventions indoors, except for restoring and acquiring the contemporary appearance of the Orangery building.

The situation was similar in the Hradčany area - it was decided how to open, make accessible and revive the Castle and its surroundings. Tourism and the needs of visitors had a great influence, which is why various restaurant and café establishments and wine bars were established on Hradčanské náměstí. The idea of connecting Letná via the Castle with Petřín, in the form of a round Petřín sightseeing route, was partially fulfilled. Chotkova road was widened for car traffic and it was bridged near Bílek's villa, which connected Letenské and Chotkovy sady. In 1971, the historic centre of Prague (including the Castle and Hradčany) was declared a heritage reservation, so all construction activities are allowed only under certain conditions. Certain construction interventions took place in connection with the construction of the Hradčanská metro station.

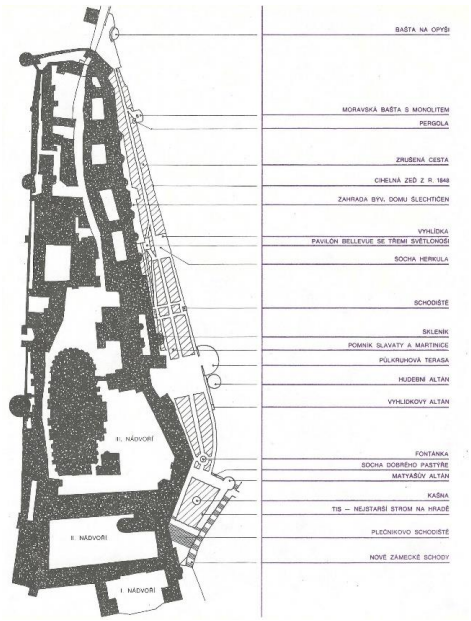

Fig. 10 – Scheme of the southern chateau gardens – Rajská and Na Valech, modifications made by Josip Plečnik in the years 1920 to 1931 [3], page 186

Fig. 11 – Plečnik's Column Hall at the end with a round window with a column [13]

This period did not bring anything new to the Hradčany panorama. Nevertheless, a lot of attention was paid to Hradčany - they appeared on the first postage stamps of the newly formed Czechoslovak Republic (the author was Alfons Mucha), they were a frequent motif for painters and graphic artists.

ANALYSIS OF PANORAMA OF HRADČANY

One of the most beautiful, most famous and most often photographed and reproduced views of Hradčany is the view from Charles Bridge or from the embankment between the National Theater and Charles Bridge; above the river, in a large natural scenery with the axis of the Vltava and above

the bowl-shaped formation of the Lesser Town, lies Hradčany with the dominant feature of Prague Castle and the cathedral. The beauty of Hradčany is reflected in the Vltava mirror [3], page 252.

In distant views, the contrast between the castle silhouette and the natural environment of Petřín on the one hand and Letná on the other is perceived first. The remarkability of this contrasting effect is supported by the differences between the height levels of Petřín and Letná. From the left side, when viewed from the town, Petrin Hill exceeds the Castle and Hradčany, approaching their main axis at an angle. From the right side, there is a lower massif of the Letna ridge, which in view extends approximately the line of Hradčany and the castle itself.

For the part of Hradčany, the two Baroque towers of the Strahov Monastery form the high landmarks, for the Castle it is a richly structured developed silhouette of the Cathedral of St. Vitus, exceeding the horizontal of the roofs of the south castle wing. The accompanying element - the subdominant - is created by the towers of the monastery of St. George over the buildings of the Lobkowicz and Pernštejn palaces. This subdominant is topped by the accent of the Black Tower. Both parts of the secular buildings are connected by a large motif of the Vladislav Hall and the church of All Saints (second part), which differs significantly from the small rhythm of the castle windows and creates a plinth for the Church of St. Vitus. In terms of height, the lowest urban floor (I) is the continuous mass of the castle after Pacassi's reconstruction, above it is the second floor (II) of the cathedral's own mass. The third floor (III) is represented by temple towers. Accompanying subdominant - the monastery of St. George - has only two urban floors. The urban parterre (I) covers the greenery, which is in contrast to the simple division of the continuous mass. The second floor (II) is again formed by towers.

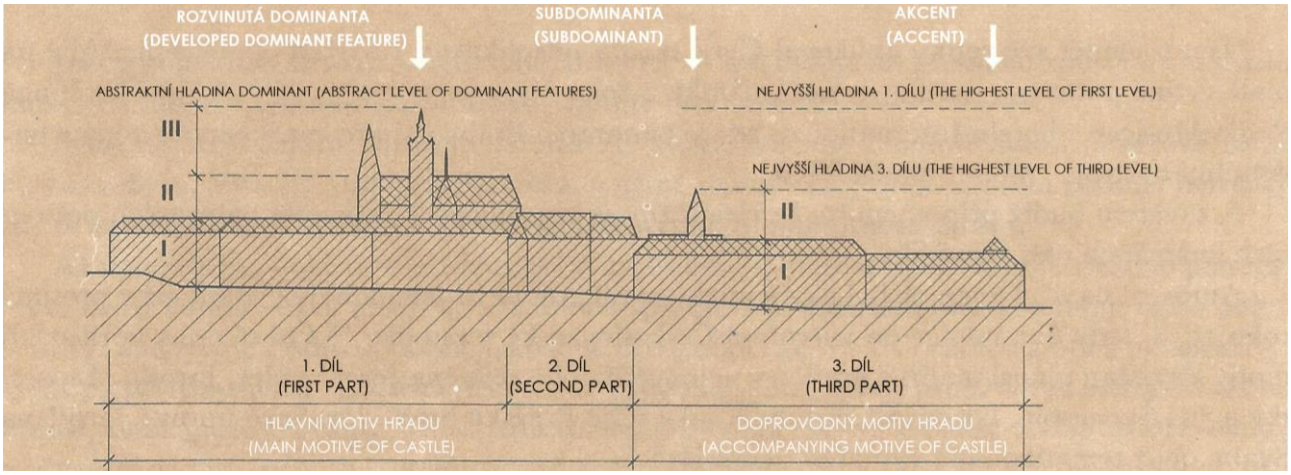

Fig. 12 – Analysis of the artistic effect of Prague Castle (reworked according to [3], page 252)

The view of the entire Hradčany panorama is characterized by the contrasting effects of individual factors. The first contrast can be found in the absolute size of the upper and lower towers - the towers of the Church of St. Vitus, St. Nicholas, Bridge Towers. The second example is different scales - modest civic houses in contrast to monumental medieval buildings. There is also contrast in expressions and diversity of shapes because Gothic buildings (with sharp edges of towers, which are covered with stone slabs or slate) and Baroque buildings with their roofs and domes covered with copper stand side by side or behind each other. Another basic aesthetic component that contributes to the overall image is rhythm. It appears on several levels - from the highest rhythm of

castle windows to the smallest rhythms on the violets of towers, gables of layered roofs, on the teeth of battlements, on the division of windows.

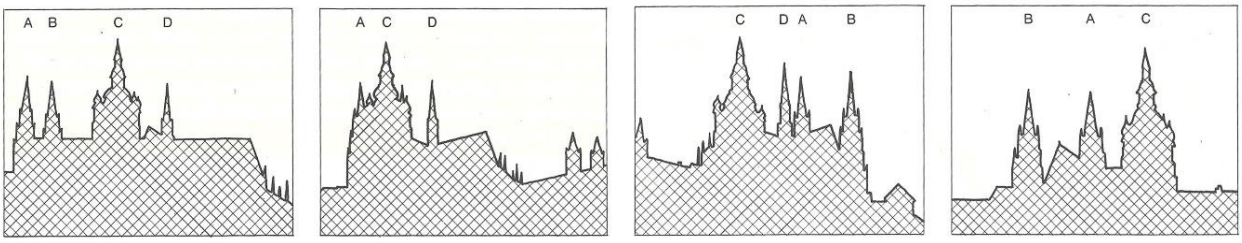

Fig. 13 – Four different forms (views) of the church of St. Vitus according to observer. The first is a view from Jirásek Bridge, the second from Rudolfinum, the third from Summer Residence and the fourth from Hradčanské Square. [3], page 254

Until the time of the Theresian reconstruction, the Cathedral of St. Vitus appeared as a torso that towered over the Castle for many centuries. The bell tower with a renaissance and later baroque helmet had its present appearance, but it was connected to the mass of the church by a large decorative arch, which arched over the empty and unfinished space of the transept. This incomplete and unfinished silhouette of the church was paradoxically not in conflict with the smaller romantic buildings of the castle and aristocratic palaces, which formed a continuous but irregular mass above the walls. On closer inspection, one could see the roof of the church with Baroque turrets, the side chapels were without roofs and several buildings and chapels adjoined the cathedral. So the whole complex seemed like an interesting but unfinished makeshift. After the completion, the Hradčany panorama was no longer perceived as composed of two buildings (horizontal bases and masses of the church), but as one complete body with an organic concept, proportionately powerful and interesting in the division of four towers in most views, only in front view - see the picture, which shows the different forms of the temple according to four different observer views. The changes are mainly due to the asymmetrical location of the main tower in relation to the nave of the cathedral. Other differences are the size and shape of the sanctuary tower from the 19th century above the crossing of ships, as well as two neo-Gothic towers on the western reconstruction of the modern extension.

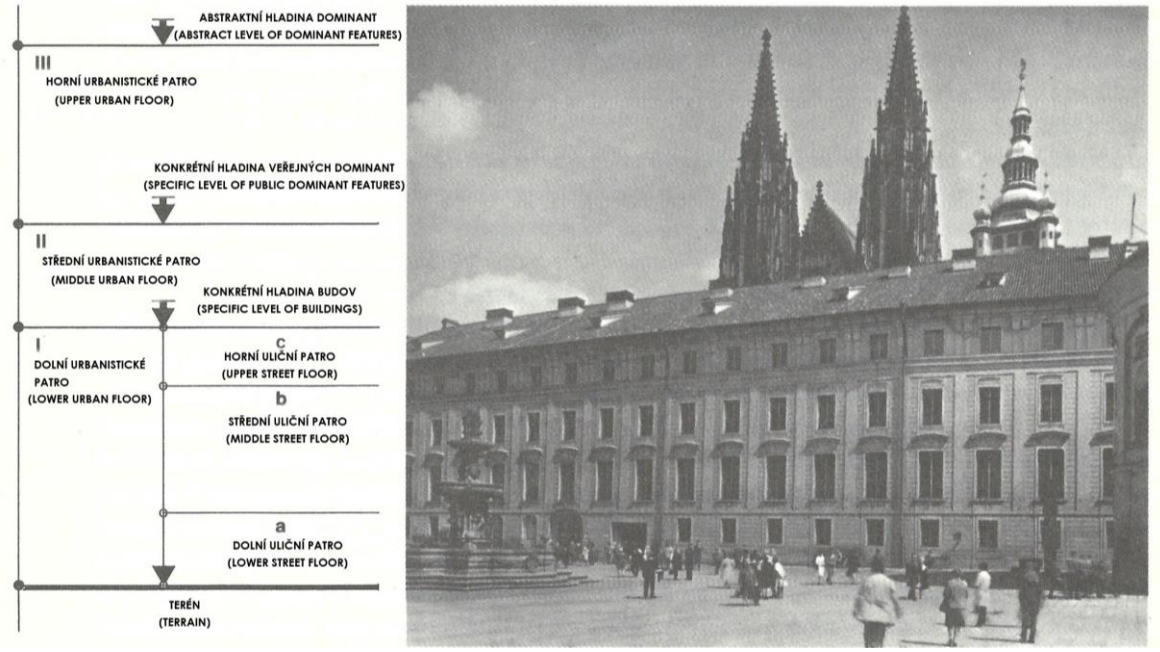

Fig. 14 – The system of urban and street floors applied at the Castle (reworked according to [3], page 257)

If we focus on the Castle itself, we can observe a certain system of urban and street floors seen in the attached picture (Fig. 14). The lower urban floor (I) is built up with buildings and creates a specific urban level. The middle urban floor (II) is made up of towers and public landmarks. The third part (upper urban floor) is very stable, lasts for centuries and creates the main characteristic motif of the urban view of the city, it usually ends with an ideological symbol (cross, eagle, star, lion). The lower urban floor can be divided into three other parts. The first of them is the lower street floor (ground floor - a), which consists of entrances, entrances, shops, portals, statues. It changes rapidly over time. Above it is the middle street floor (b), which is quite durable in appearance, even if the building adapts inside. The upper street floor (c) indicates the roof part, which remains most of the time except for small technical details (antennas, fans, elevator rooms) unchanged.

CONCLUSION

This contribution dealt with the urban development of the Hradčany area. Morphological assumptions influenced the formation of the current town plan and floor plan of the Castle. Initially, there was a settlement related to the Castle in the castle grounds. In the 14th century, this settlement became the serf town of Hradčany. Over the centuries, there was a change of artistic styles and thus changed not only the structure of the buildings, but especially the panorama of Hradčany with the silhouette of the Castle.

Prague Castle is a unique historical and architectural complex, which surprises with its complexity and size. It is very difficult to find a similar example among European capitals. This nature of the Castle is the result of two important factors - one is the special circumstances and the process of creation and the other is the historical and architectural continuity of architects, craftsmen and construction workers over one millennium.

Thanks to its location on a promontory above Prague, Hradčany is now dominating the capital city today and in the past. Even though their isolation has passed, with the abolition of the fortifications and administrative unification with other Prague cities, the material superiority of Hradčany still remains one of the most important components of the city's architectural composition. From the beginning, only the castle itself had this artistic role, only in the 16th century, thanks to the magnificent construction of aristocratic palaces and later church buildings, the serf town became a monumental structure. At that time, the masses of the Castle and the town merge into a common whole crowning the town. To this day, we can perceive the specific atmosphere of noble dignity and peace in the courtyards and alleys of the Castle, as well as the atmosphere of aristocratic residences in the streets and squares of the Hradčany district, even though no aristocrat lives here.

ACKNOWLEDGEMENTS

This article was written within the doctoral course Urban Composition of Settlements, which is taught by senior lecturer Jan Mužík at the Faculty of Civil Engineering of CTU in Prague.

REFERENCES

[1] Google Maps (online). (cit. 2022-07-03). Available from https://www.google.com/maps/@50.0918535,14.3882439,15z

[2] Borkovský I., 1969. Pražský hrad v době přemyslovských knížat (Prague Castle during the Time of Premyslid Princes), 51 (Academia) 162 pp.

[3] Vančura J., 1976. Hradčany, Pražský hrad (Hradčany, Prague Castle), (SNTL) 320 pp.

[4] Čarek J., 1966. K rekonstrukci vývoje a rozlohy raně feudální Prahy (To Reconstruction of Development and Area of Early Feudal Prague), in Pražský sborník historický (Prague Historical Anthology), 40 (Orbis) 166 pp.

[5] Streit J., 1958. Divy staré Prahy (Wonders of Old Prague), 43 (Mladá fronta) 344 pp.

[6] Stefan O., 1964. K dějepisným otázkám naší renesanční architektury (To the Historical Questions of Our Renaissance Architecture), in Umění XII (Art XII), 428-432.

[7] Mencl V., 1969. Praha (Prague), page 109 (Odeon) 378 pp.
[8] Novotný Ant., 1949. Praha v květu baroka (Prague in Bloom of Baroque), 54 (Atlas) 462 pp.
[9] Wirth Z., 1943. Pražské zahrady (Prague Gardens), 35 (Václav Poláček) 88 pp.
[10] Bečková K., 2000. Hradčany a Malá Strana (Hradčany and Little Town), (Paseka) 240 pp.
[11] Hlavsa V., 1959. Hradčany – město a hrad (Hradčany – The Town and the Castle), 38 (STN) 56 pp.
[12] Kozák B., Poche E., Wirth Z., 1964. Hradčany a Malá Strana (Hradčany and Little Town), 20 (Orbis) 233 pp.
[13] Lukeš Z., Podrazil J., 2012. Jože Plečnik – průvodce po stavbách v České republice (Jože Plečnik – Guide to Buildings in the Czech Republic), 52 (Foibos) 320 pp.